Electrochemical studies in soft ionically conducting medium - Deep eutectic solvents and Ionic gels

by

Anu Renjith

Thesis submitted to

Jawaharlal Nehru University

for the award of the degree of

Doctor of Philosophy

December 2015

Raman Research Institute

Bangalore, India – 560 080

CERTIFICATE

This is to certify that the thesis entitled ***"Electrochemical studies in soft ionically conducting medium - Deep eutectic solvents and Ionic gels"*** submitted by Mrs. Anu Renjith, for the award of the degree of DOCTOR OF PHILOSOPHY of Jawaharlal Nehru University, New Delhi, is her original experimental investigation and conclusions. The subject matter of this thesis has not been previously published or submitted to any other university for the award of any other degree or diploma.

Prof. Ravi Subrahmanyan,
Director,
Raman Research Institute,
Bangalore, India -560 080

Prof.V. Lakshminarayanan
(Thesis Supervisor)

DECLARATION

I hereby declare that the entire work embodied in this thesis is the result of the experimental investigation carried out by me independently at Raman Research Institute, Bangalore, under the guidance and supervision of Prof. V. Lakshminarayanan. The experimental work and conclusions presented in this thesis work have not been previously submitted and no part of this thesis work has formed the basis for the award of any other degree, diploma, fellowship or any other similar title. I also declare that I have run the thesis through Turnitin plagiarism detection software.

Prof. V. Lakshminarayanan
(Thesis Supervisor)
Raman Research Institute
Bangalore, India - 560 080

Anu Renjith

ACKNOWLEDGEMENTS

I am grateful to my thesis supervisor Prof. V. Lakshminarayanan for his inspiring guidance throughout my research work. I thank him for all the resourceful discussions which have instilled confidence in me and my research work. His observations and comments helped me to remain focussed and to move forward with research in depth. The enthusiasm shown by him was motivational during the entire span of my Ph.D.

I thank Prof. Sandeep kumar for his valuable suggestions and interests shown in my work. I would like to thank Dr. Arun Roy for sharing his time and knowledge in the SERS studies. I would also like to thank Dr. R. Pratibha, Dr. V. A. Raghunathan and Dr. Ranjini for their help in my experimental work.

I thank Mr. N. Ravisankar for his friendly support and timely help in the lab. I thank Mrs. Vasudha for her help in characterization and for all the conversations on academic and non-academic matters. I would also like to thank Mr. Dhason for his help in SEM imaging and fabricating glass apparatus, Mr. Ram for preparing evaporated gold samples for electrochemical studies, Mr. Mani for his help in fabricating accessories for various experiments and Mr. Sreenivasa for technical helps. I also thank Mr. K. Radhakrishna for availing me all the necessary facilities for my research work.

I thank my labmate Jagadeesh for his constant help and useful discussions. I would also like to thank Swaminathan, Avinash, Rajib, Jyothi, Meera, Sreeja, Santhosh, Madhukar, Shrikrishnan, Chayanika, Tarun and Anitha for all their help. I am grateful to my friends Anju and Srilakshmi for all the cherished moments spent in IISc.

It is a pleasure to thank all the library staffs of RRI who have provided excellent and timely help during my research. I would like to thank various other departments of RRI like the Administration, Computer, Accounts, Workshop, Security, Transport, Canteen, Hostel and Clinic for their constant support throughout my research.

I would like to express my sincere thanks to my husband Mr. Renjith George who took a keen interest in my research progress. His constant support and motivation was always encouraging. I would also like to thank my parents and in laws for their care and constant prayers. Finally I would like to thank my brothers for their interests shown in my work.

CONTENTS

	Contents	v
	Abbreviations	xi
	Synopsis	xiii
	List of publications	xxiii
1.	**Introduction**	1
	1.1. Molecular solvents	3
	1.2. Ionic gels	4
	1.3. Ionic liquids	4
	1.3.1 Structural aspects of ionic liquids	5
	1.3.2 Classification of ionic liquids	5
	1.4. Deep eutectic solvents (DES)	7
	1.4.1 Components and composition of DES	7
	1.4.2 Physical properties of choline chloride based DES	9
	1.4.3 Applications of DES	13
	1.5. Electrochemical methods of preparing nanoparticle modified substrates	18
	1.6. Applications of electrodeposited nanoparticles	19
	1.6.1 Electrochemical sensors	19
	1.6.2 Surface enhanced Raman spectroscopy (SERS)	20
	1.6.3 Electrocatalysis for fuel cells	20
	1.7. Objectives of the work	23
2.	**Materials and Methods**	28
	2.1. Introduction	29
	2.2. Preparation of Deep eutectic solvents (DES)	29
	2.3. Instrumentation	29
	2.4. Electrochemical techniques	30
	2.4.1 Cyclic voltammetry	30
	2.4.2 Electrochemical Impedance Spectroscopy	32
	2.4.3 Chronopotentiometry	38

2.4.4 Chronoamperometry 39
2.4.5 Tafel plot analysis 40
2.5. Scanning electron microscopy (SEM) 41
2.6. Spectroscopy and other techniques 43
2.6.1 UV spectroscopy 43
2.6.2 Raman Spectroscopy 44
2.7. X-ray diffraction 46

3. Electron transfer studies of some redox active species (Cationic, anionic, neutral) in DES 48
3.1. Introduction 49
3.2. Experimental 52
3.2.1 Materials 52
3.2.2 Electrode pretreatment 53
3.2.2 Electrochemical studies 53
3.3. Results and Discussions 53
3.3.1 Cyclic voltammetric studies 53
3.3.1.1 Anionic complex 54
3.3.1.2 Cationic complex 59
3.3.1.3 Neutral redox active species 62
3.3.2 Behaviour of Peak Current vs. Scan Rate 69
3.3.3 Calculation of diffusion coefficients of the redox species 70
3.3.3.1 Calculation of diffusion coefficients from EIS 70
3.3.3.2 Calculation of diffusion coefficients from cyclic voltammetry 75
3.4. Conclusions 76

4. Electrochemically prepared SERS substrates of Ag by anodic dissolution in DES 80
4.1. Introduction 81
4.2. Experimental 82
4.2.1 Material used 82

4.2.2 Electrode Pretreatment 83
4.2.3 Electrochemical synthesis and insitu deposition of silver nanoparticles 83
4.3. Results and discussions 84
4.3.1 Characterization 84
4.3.2 SERS activity of mesoporous substrate 89
4.4 Conclusions 92

5. Electrochemically grown mesoporous metallic substrates of Ag, Au and Pd by anodic dissolution in DES; Synthesis, characterization and electrocatalytic studies 94
5.1. Introduction 95
5.2. Experimental 97
5.2.1 Material used 97
5.2.2 Electrode Pretreatment 97
5.2.3 Electrochemical studies 97
5.2.4 Electrochemical synthesis and *insitu* deposition of metal nanoparticles 97
5.3. Results and discussion 100
5.3.1 Characterization 100
5.3.2 Electrocatalytic activity of the mesoporous metallic substrates to Hydrogen Evolution Reaction in acidic media 108
5.3.2.1 Electrochemical response of AgNP coated W wire 109
5.3.2.2 Electrochemical response of AuNP coated on gold disc electrode 113
5.3.2.3 Electrochemical response of PdNP coated on Pd wire 115
5.4. Conclusions 117

6. One step preparation of 'ready to use' Au@Pd nanoparticle modified surface using DES and its electrocatalytic properties in alcohol oxidation reaction 121

6.1. Introduction 122

6.2. Experimental 124

6.2.1 Materials used 124

6.2.2 Electrochemical studies 125

6.2.3 Electrodeposition of nanoparticles from DES 125

6.3. Results and discussions 126

6.3.1 Characterization 126

6.3.2 Electro-oxidation of methanol in alkaline medium 135

6.3.2.1 Kinetics of methanol electro-oxidation 141

6.3.3 Electro-oxidation of ethanol in alkaline medium 146

6.3.3.1 Kinetics of ethanol electro-oxidation 148

6.4. Conclusions 151

7. Oxygen evolution catalysts of graphite modified with Co and Co-Ni alloys prepared in DES 157

7.1. Introduction 158

7.2. Experimental 160

7.2.1 Materials 160

7.2.2 Electrochemical studies 160

7.3. Results and discussion 161

7.3.1 Electrocatalysts based on porous films of Cobalt 161

7.3.1.1 Optimization of electrodeposition conditions 161

7.3.1.2 Characterization of the electrodeposited films of Co 167

7.3.1.3 Cyclic voltammetric studies of the electrodeposited Co films 168

7.3.1.4 Mechanism of OER on the electrodeposited Co films 170

7.3.1.5 Activation energy measurements 172

7.3.2 Electrocatalysts based on porous films of Cobalt– Nickel 174

7.3.2.1 Electrodeposition of Co-Ni alloys on graphite 174

7.3.2.2 Characterization of the electrodeposited films 175
7.3.2.3 Cyclic voltammetric studies of Co-Ni alloy films 177
7.3.2.4 Mechanism of OER on Co-Ni films 177
7.3.2.5 Activation energy measurements 178
7.4. Conclusions 179

8. A novel colloidal suspension of TBA^+ BF_4^- - EG and its applications as a soft solid electrolyte 183

8.1. Introduction 184
8.2. Experimental section 187
8.2.1 Materials 187
8.2.2 Preparation of the colloidal suspension 187
8.2.3 Instrumentation 188
8.2.4 Cell design 188
8.2.5 Electrochemical procedure followed for monitoring enzyme – substrate reaction 189
8.3 Results and discussion 189
8.3.1 Optimization of the gel components 189
8.3.2 Characterization of the colloidal suspension 191
8.3.2.1 Phase transition studies 191
8.3.2.2 Rheological studies 193
8.3.2.3 Morphological studies 193
8.3.2.4 XRD studies 194
8.3.2.5 Ionic conductivity measurements 195
8.3.2.6 Schematic model of the colloidal suspension and potential applications 198
8.4 Applications of the $TBABF_4$ – EG colloidal suspension 198
8.4.1 Dispersing medium for nanoparticles 199
8.4.2 Electrochemical monitoring of enzyme kinetics in the gel matrix 200
8.4.2.1 Urea - urease reaction 200
8.4.2.2 Glucose oxidase – dextrose 203

8.4.2.3 Alkaline Phosphatase – p-nitrophenyl phosphate 205
8.5 Conclusions 206
9. Summary and Future works 209

ABBREVIATIONS

DES	Deep eutectic solvents
SERS	Surface Enhanced Raman Spectroscopy
RTIL	Room temperature ionic liquid
HBD	Hydrogen bond donor
ChCl	Choline chloride
EG	Ethylene glycol
Ethaline	DES prepared from Choline chloride and Ethylene glycol
Reline	DES prepared from Choline chloride and Urea
Maline	DES prepared from Choline chloride and Malonic acid
ACN	Acetonitrile
PC	Propylene carbonate
DMSO	Dimethyl sulphoxide
HER	Hydrogen evolution reaction
OER	Oxygen evolution reaction
Au@PdNP	Gold-Palladium coreshell nanoparticles
$TBABF_4$	Tetrabutyl ammonium tetrafluoroborate
UV	Ultra violet
FTIR	Fourier transform infrared
SEM	Scanning electron microscope
EDAX	Energy dispersive X-ray analysis
XRD	X-Ray diffraction
EIS	Electrochemical impedance spectroscopy
POM	Polarising optical microscopy
DSC	Differential scanning calorimetry
FTIR	Fourier transform infrared
DSC	Differential scanning calorimetry
D	Diffusion coefficient
η	Viscosity
ν	Scan rate
SCE	Saturated calomel electrode
MMO	Mercury/ mercury oxide electrode

E_p	Peak potential
$E_{1/2}$	Half-peak potential
R_u	solution resistance
C_{dl}	Double layer capacitance
R_{ct}	Charge transfer resistance
Z_W	Warburg impedance
Z'	Real part of impedance
Z''	Imaginary part of impedance
$Fe[(CN)_6]^{4-\|3-}$	Ferrocyanide/ferricyanide
$[Ru(NH_3)_6]^{2+\|3+}$	Hexaammineruthenium II/III
Fc	Ferrocene
$FcBF_4$	Ferrocenium tetrafluoroborate
$FcCH_2OH$	Ferrocene methanol
Cp	Cyclopentadienyl anions
$MMIMBF_4$	1,3-dimethylimidazolium tetrafluoroborate
MV	Methyl viologen
MPBA	4-Mercapto phenyl boronic
$NaBH_4$	Sodium borohydride
Pt/Rh	Platinum-rhodium alloy
ECSA	Electrochemically active surface area
EtOH	Ethanol
MeOH	Methanol
E_a	Activation energy
Co_{Mal}	Electrodeposited Co film prepared in maline medium
Co_{Eth}	Electrodeposited Co film prepared in ethaline medium
Co_{Rel}	Electrodeposited Co film prepared in reline medium
K_m	Michaelis–Menten constant
V_{max}	maximum velocity achieved by the enzyme-substrate reaction
GOx	Glucose oxidase
ALP	Alkaline Phosphatase
pNPP	4-nitrophenylphosphate

SYNOPSIS

Electrochemical studies in soft ionically conducting medium - Deep eutectic solvents and ionic gels

The thesis presents the electrochemical studies carried out in soft ionically conducting media namely, deep eutectic solvents and ionic gels. These solvent media are currently being studied as they have some unique properties vis-a-vis conventional molecular solvents. In recent times, active research to overcome some drawbacks of molecular solvents which are volatile, flammable and often toxic, led to the development of stable, environment friendly, ionically conducting solvents known as ionic liquids. By complexing a quaternary ammonium chloride with a hydrogen bond donor, a new class of ionic liquids known as Deep Eutectic Solvents (DES) was developed recently. They are eutectic mixtures that remain in liquid state at room temperature. The DES can be prepared by a simple thermal mixing of two components viz., choline chloride and a hydrogen bond donor such as urea, ethylene glycol.

Within a short span of its introduction, there is a widespread utilization of DES in industrial processes such as metal deposition and metal oxide dissolution. In spite of considerable work in these aspects of DES, there is a large scope in terms of electrochemical studies in these solvents. Electrochemistry being a powerful tool in understanding electron transfer processes and material synthesis, studies in this area are quite promising.

The thesis attempts to explore the potential of DES as a medium for the electron transfer studies and electrochemical synthesis of nanoparticles. Since the DES medium is devoid of water, hydrogen and oxygen evolution reactions are not limiting factors unlike that in aqueous medium. The components of the DES have the inherent ability to stabilize the nanoparticles formed. A major part of the thesis deals with the electrochemical synthesis of different metal nanoparticles such as Ag, Au, Pd,

Au@Pd core shell, its *insitu* deposition onto conducting substrates in DES and their potential applications.

The nanoparticles modified substrates were suitable for direct use in several applications. The conducting substrates onto which the nanoparticles were deposited were selected keeping in view of the potential application. Therefore, while nanoparticles of Ag were deposited onto Pt/Rh thermocouple metal wires for SERS applications, monometallic and bimetallic nanoparticle of Au and Pd were deposited onto graphite substrate. The preparation of electrocatalysts for hydrogen evolution reaction by modifying Au and Pd wires with dense films of Au and Pd nanoparticles respectively at high current densities was also demonstrated.

Finally a novel non-polymeric colloid suspension was prepared from a predetermined composition of tetra butyl ammonium salt and ethylene glycol. The colloid suspension exhibited certain unique physical properties and was demonstrated as a medium for monitoring enzyme kinetics by electrochemical method. The gel containing a constant amount of enzyme was allowed to react with different concentrations of substrate. The ionic conductivity of the colloid suspension measured by electrochemical impedance spectroscopy was found to vary with the progress of the enzyme-substrate reaction. The rate of the reaction in the colloidal matrix was found to obey Michaelis –Menten equation. The electrochemical method employed here with the colloidal medium acts as a simple robust method to follow enzymatic reactions in a soft medium mimicking biological environment.

In the following, a brief description on the contents of the chapters is presented.

Chapter 1. Introduction

This chapter gives an introduction on ionic liquids, deep eutectic solvents and ionic gels. The components of these soft ionic conducting medium, their physical properties and applications explored till date in literature are discussed. Since the thesis involves the preparation of mesoporous materials in DES medium, a few

applications of the mesoporous metallic substrates especially in the field of fuel cells and SERS are also discussed in the chapter.

Chapter 2. Materials and methods

This chapter deals with the concepts of the various experimental techniques used in the study. Electrochemical techniques such as cyclic voltammetry (CV), electrochemical impedance spectroscopy (EIS), chronopotentiometry, chronoamperometry and Tafel analysis were extensively used in the study. The section also discusses various other characterization techniques such as scanning electron microscopy (SEM), cryo-SEM, X-ray diffraction (XRD), polarizing optical microscopy (POM), differential scanning calorimetry (DSC) and rheological instrumentations used for characterizing the materials prepared in this work.

Chapter 3. Electron transfer studies of some redox active species (Cationic, anionic, neutral) in Deep Eutectic Solvents

The chapter discusses the electrochemical studies of some of the common redox probes carried out in the DES media. The redox properties were compared with that in appropriate aqueous and non aqueous media. The redox species selected for the studies were distinct in terms of their charge (e.g. $Fe(CN_6)^{4-/3-}$, $Ru(NH_3)^{2+/3+}$, ferrocene methanol) or hydrophilic / hydrophobic properties (e.g. methyl viologen, ferrocene).

The cyclic voltammetric studies of the redox species studied showed changes in the electrochemical features (viz., peak potential, peak current) as the medium changes from a molecular solvent to a DES (Fig.1). The shift in the peak potentials were explained based on the preferential interaction of the reactant / product with the medium. The peak currents of all the redox species studied were significantly decreased in DES compared to that in molecular solvents due to the high viscosity of the former. The diffusion coefficients of the redox species in DES were calculated by EIS and also by

cyclic voltammetry. A comparison of the results determined by both of the electrochemical methods were found to be in reasonable agreement.

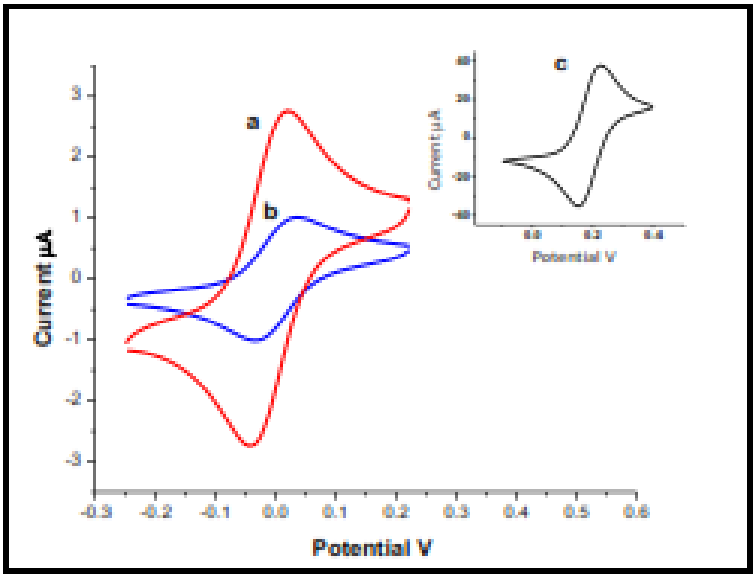

Figure 1. *Cyclic Voltammogram of 5mM* $Fe(CN)_6^{4-/3-}$ *in (a) Ethaline (choline chloride + ethylene glycol) (b) Reline (choline chloride + urea) (c) aqueous medium / 0.1M KCl at a scan rate of 20 mV/s Vs Ag/AgCl*

Chapter 4. Electrochemically prepared SERS substrates of Ag by anodic dissolution in DES

This chapter discusses an electrochemical method of utilizing DES as an effective medium for preparing thin films of silver nanoparticles on metallic substrates. The procedure involved the electrochemical dissolution of a silver wire at a constant current density. The anodic dissolution technique carried out in DES overcomes problems associated with the hydrogen and oxygen evolution in aqueous medium at the cathode and the anode and thereby overcome the problem of the passivation of the silver anode.

In DES, the dissolved metal ions from the Ag wire get simultaneously reduced at the cathodic metal substrate (Pt/Rh wire). These form clusters of nanoparticles stabilized by the Mercaptophenyl boronic acid (MPBA) molecules present in the

medium (Fig.2a). The mesoporous silver films were also characterized by SEM, EDAX and XRD. The presence of the stabilizer ligand on the nanoparticles was confirmed by SERS. The prepared substrate exhibited a strong Raman spectra of the stabilizer (MPBA) with an enhancement factor of 10^6. A SERS substrate with such intense inherent spectra is not desirable as these Raman signals would interfere with those of the analyte species, when used. Hence the mesoporous Ag film on Pt/Rh wire were calcined to get stabilizer free substrates for SERS. The calcined silver nanoparticle film showed highly enhanced Raman signals of the chosen analyte (Methylene blue) (Fig.2b).

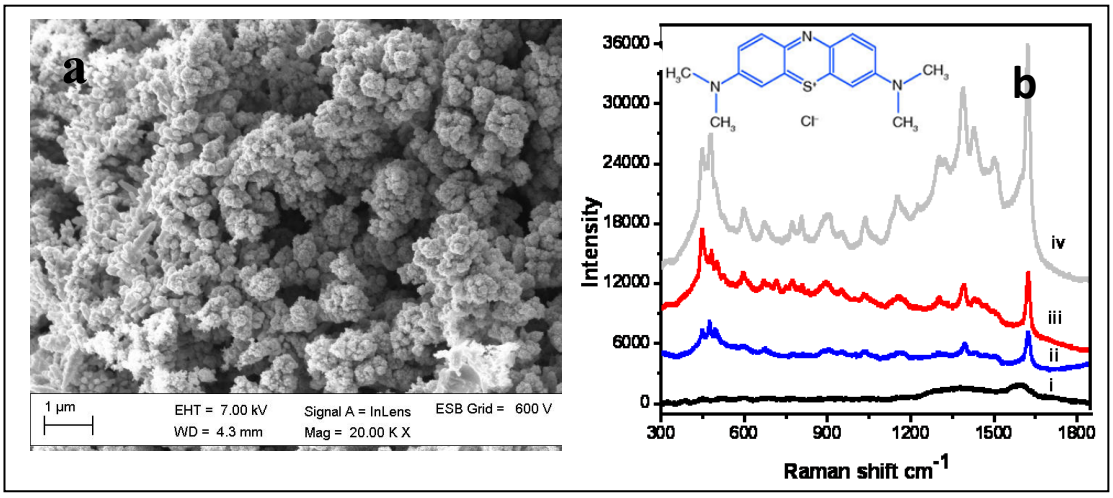

Figure 2. *(a) SEM image of the mesoporous Ag substrate (b) normalised SERS spectra of methylene blue adsorbed on calcined substrate from aqueous solutions of (i) 0 M (ii) 3.7 x10^{-7} M (iii) 3.7 x 10^{-6} M (iv) 37 x 10^{-6} M*

Chapter 5. Electrochemically grown mesoporous metallic substrates of Ag, Au and Pd by anodic dissolution in Deep Eutectic Solvents; Synthesis, characterization and electrocatalytic studies

The chapter discusses the preparation of thin films of monometallic substrates of Au, Pd and Ag nanoparticles respectively in DES using electrochemical methods. The experimental conditions in terms of reagents, current density and deposition time for the three metals were standardized for different systems. While mesoporous silver nanoparticle films could be deposited on tungsten wires at a relatively low current

density, the deposition of Au and Pd nanoparticles on to Au and Pd wires respectively required higher current densities.

The mesoporous metal fims were characterized by SEM, XRD and electrochemical techniques. The highly porous texture of the electrodeposited film as seen in Fig.3 provides superior electro catalytic performance for Hydrogen Evolution Reaction (HER). The mechanisms of HER on the fabricated substrates were studied by chronoamperometry and Electrochemical Impedance Spectroscopy (EIS). The studies showed that while mesoporous Ag substrates followed Volmer - Heyrovski mechanism for HER, the mesoporous Au and Pd substrates followed by Volmer – Tafel mechanism.

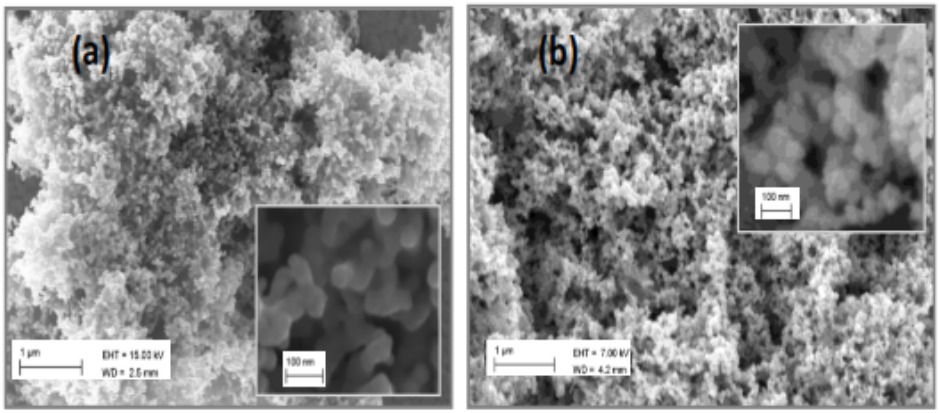

Figure 3. *SEM images of mesoporous (a) AuNP on Au wire (b) PdNP on Pd wire. Inset shows magnified images with 100nm scale-bar*

Chapter 6. One step preparation of 'ready to use' Au@Pd nanoparticle modified surface using Deep eutectic solvents and its electrocatalytic properties in alcohol oxidation reaction

The chapter discusses the method of *insitu* preparation and deposition of bimetallic nanoparticles of Au and Pd. In order to achieve bimetallic nanoparticles, the anodic dissolution process of Au and Pd wires were carried out simultaneously (Fig.4a). An *insitu* deposition of bimetallic nanoparticles was observed on the graphite rod used as the cathode (Fig.4b). The fabrication strategy in ethaline (DES)

avoided the addition of external stabilizers and reducing agents. A systematic electrochemical, elemental and morphological characterization by cyclic voltammetry, EDAX and SEM, confirmed that the bimetallic nanoparticles exhibited a core-shell morphology.

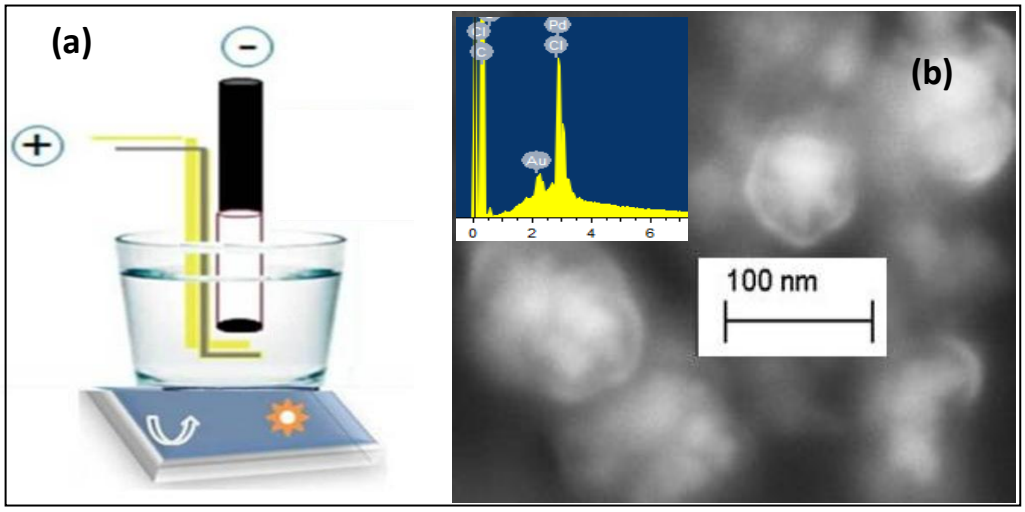

Figure 4. *Schematic representation of anodic dissolution technique for the electrodeposition of Au@Pd nanoparticle in DES medium (b) SEM images of graphite rod modified with Au@Pd NPs*

The electrocatalytic properties of the Au@Pd nanoparticle modified graphite were studied in the electrochemical oxidation of methanol and ethanol by cyclic voltametry, Tafel analysis and activation energy measurements. The Au@Pd NPs exhibited superior electrocatalytic performance over its corresponding monometallic counterparts viz., AuNPs and PdNPs prepared under identical conditions. The activation energy requirements of the Au@Pd NP modified graphite electrodes were also quite low making them a potential anode catalyst in alkaline media based alcohol fuel cells at ambient temperatures. The method suggested here for the synthesis of mesoporous electrocatalysts is simple, effective and environmentally friendly.

Chapter 7. Oxygen evolution catalysts of graphite modified with Co and Co-Ni alloys prepared in DES

The chapter describes the preparation of thin films of porous cobalt and cobalt –nickel alloys on graphite substrates. The metal ion source for the electrodeposition described here was obtained from a dissolved concentration of $CoCl_2$ in DES unlike the anodic dissolution of metal wires described in earlier chapters. The conventional methods of cobalt electrodeposition employ an acidic medium for the process. Therefore, in addition to the ethaline media used before as synthesis media, the possibility of utilizing a DES prepared from a mixture of choline chloride and malonic acid (maline) was also explored. Since the experiment was carried out at room temperature, the problem of high viscosity of maline (1124 cP Vs 36 cP of ethaline) as an electrodeposition medium was solved by using maline-water mixtures. A set of experimental conditions such as solvent composition, current density, metal salt concentration, deposition time were varied and optimum conditions were finalized.

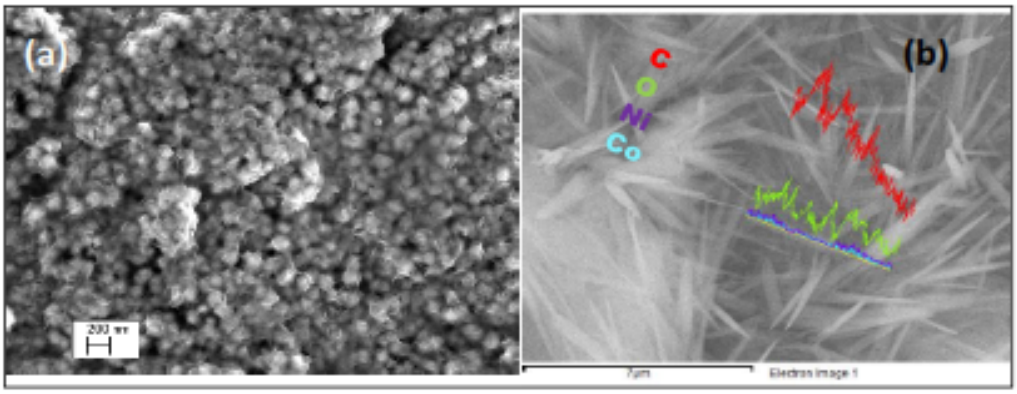

Figure 5. *(a) SEM images of the Co modified porous graphite substrate (b) electron image displaying the line scan of EDAX of the Co - Ni modified graphite.*

The nanomaterials developed using this solvent medium were studied as electrocatalysts for oxygen evolution reaction (OER) in alkaline medium and compared with those prepared in ethaline and reline media. The cobalt modified graphite substrates (Fig.5a) were characterized by SEM, EDAX and cyclic

voltammetry. The bimetallic deposition of Co/Ni onto graphite substrate (Fig.5b) and studied its electrocatalytic properties in OER is also demonstrated here.

Chapter 8. A novel colloidal suspension of TBA^+ $BF4^-$ - EG and its applications as a soft solid electrolyte

The chapter discusses the preparation and characterization of a novel colloidal suspension prepared by a simple thermal mixing of two components viz., tetrabutyl ammonium tetraflouroborate TBA^+ BF_4^- and ethylene glycol. The colloidal suspension obtained from an optimized composition of the components was thoroughly characterized in terms of its thermal, rheological and ionic conducting properties. The colloidal suspension exhibited soft solid properties, sharp thermo reversible sol-gel transitions together with inherent ionic conductivity which has potential applications as a soft solid electrochemical medium (Fig.6a).

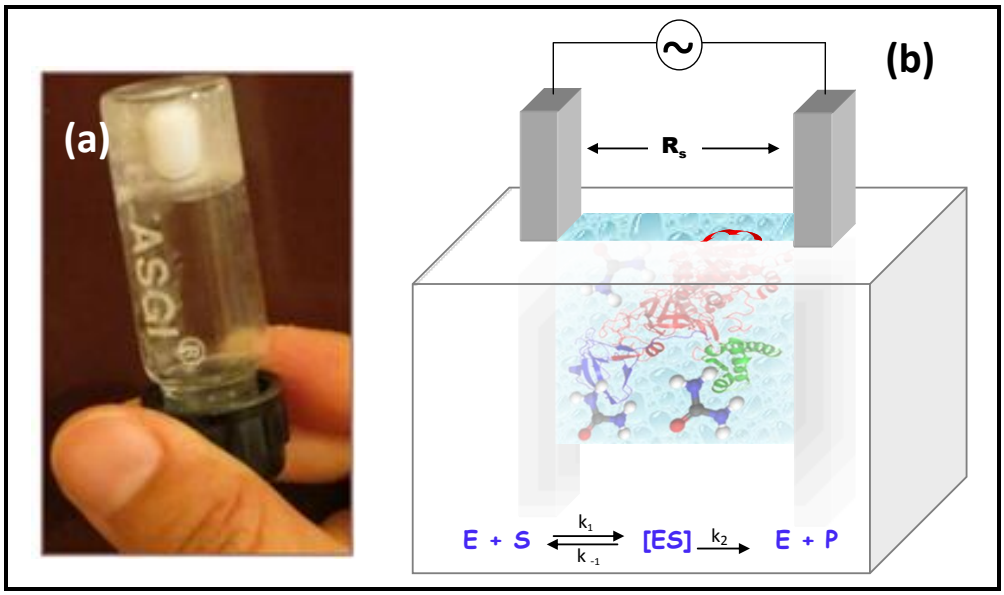

Figure 6. *(a) Photograph of the colloidal suspension in a vial containing a teflon coated magnetic pellet at room temperature (b) schematic representation of the electrochemical method used for the electrochemical monitoring of enzyme kinetics in the colloidal suspension.*

The soft solid nature of the colloidal suspension can be considered as a model system mimicking biological environment and therefore was evaluated as a medium for monitoring enzyme kinetics using an electrochemical impedance method. Further it has been reported earlier that the structure of the protein in its native state is very well preserved in a colloidal matrix vis-a-vis., molecular solvents. In this study, a few micro litres of the sol (colloidal suspension at T > 50 ^{0}C) containing a known concentration of substrate was injected between two parallel Pt electrodes. The sol solidifies immediately to form the gel and the corresponding enzyme (1µL of 1mg/ml aqueous solution) was added to 110 µL of gel. The enzyme-substrate reaction was then allowed to take place in the colloidal suspension (Fig.6b). The technique used for the real time monitoring of enzyme kinetics is based on electrochemical impedance spectroscopy at a constant frequency. A set of enzyme – substrate reactions such as urease - urea, glucose oxidase and L-dextrose, alkaline phosphatase – para- nitro phenyl phosphate were studied in the colloidal matrix. It is shown that in all the cases, the reaction kinetics was found to follow Michaelis-Menten equation.

Chapter 9. Summary and future works

This chapter summarises the results and conclusions of the various electrochemical studies described in the preceding chapters in addition to the possible scope for further work in this area.

LIST OF PUBLICATIONS

1. In situ fabrication of electrochemically grown mesoporous metallic thin films by anodic dissolution in deep eutectic solvents.

Anu Renjith, Arun Roy and V. Lakshminarayan;

J Colloid Interface Sci., 2014, **426**, 270-9.

2. One step preparation of 'ready to use' Au@Pd nanoparticle modified surface using deep eutectic solvents and a study of its electrocatalytic properties in methanol oxidation reaction.

Anu Renjith and V. Lakshminarayan;

J. Mater. Chem. A, 2015, **3**, 3019-3028.

3. A novel colloidal suspension of TBA^{+} $BF4^{-}$ – EG and its applications as a soft solid electrolyte.

Anu Renjith and V. Lakshminarayan;

RSC Adv., 2015, **5**, 87956-87962.

4. Electron transfer studies of some redox active species (Cationic, anionic, neutral) in Deep Eutectic Solvents

Anu Renjith and V. Lakshminarayan;

Manuscript under preparation

5. Oxygen evolution catalysts of graphite modified with Co and Co-Ni alloys prepared in DES

Anu Renjith and V. Lakshminarayan;

Manuscript under preparation

CHAPTER 1

Introduction

The thesis describes the electrochemical studies carried out in soft ionically conducting media namely deep eutectic solvents and ionic gel. In general, the term soft matter denotes materials that exhibit large deformations to small perturbations such as external stresses, electromagnetic fields, and thermal fluctuations. The class of soft condensed matter includes polymers, liquid crystals, colloids, ionic liquids, gels and biological materials. The soft materials when associated with inherent ionic conductivity are interesting as a media for electron transfer studies. Recent entries to this class of materials are deep eutectic solvents and ionic gels.

Deep eutectic solvents (DES) are eutectic mixtures of a quaternary ammonium salt and a hydrogen bond donor such as urea, ethylene glycol, malonic acid etc. These room temperature ionic liquids are associated with certain unique features that can be exploited for electrochemical synthesis and deposition of nanoparticles. The major focus of the thesis is to carry out a detailed study on utilizing DES as a medium for the electrochemical synthesis and deposition of various metal nanoparticles. The nanoparticle modified conducting substrates prepared here are capable of being used directly in various applications especially as high surface area materials or as electrocatalysts. The thesis discusses the applications of these substrates in surface enhanced Raman spectroscopy (SERS) and in the electrocatalysis of hydrogen evolution reaction, oxygen evolution reaction and alcohol oxidation reactions.

The physical properties of the DES differ considerably from the conventional molecular solvents in many aspects. The high viscosity of DES media affects the diffusion behaviour of the solute species. The solvation mechanism itself may be quite different from the molecular solvents composed of uniformly distributed oriented solvent molecule dipoles vis-à-vis the DES which are composed of only anions and cations. These changes in the solvation are expected to affect the electrochemical characteristics of redox processes occurring in the DES media. Therefore the thesis also attempts to study the electron transfer and transport properties of some redox species in DES as electrolytic medium.

The soft ionically conducting media cover an ever-widening range of materials. There is ample scope of material development by the innumerable possible combinations of existing components. A simple preparation of a gel electrolyte exhibiting sharp thermo-reversible transitions has also been demonstrated here. The gel electrolyte was thoroughly characterized in terms of its soft matter nature and electrochemical characteristics. The unique features of the gel were utilized as a dispersion media for nanoparticles and also as an electrochemical media for carrying out enzymatic reactions.

This chapter presents an introduction to the concept of ionic liquids especially DES, the rationale for the choice of components of DES, their physical properties and a brief discussion on the variety of potential applications of DES explored in literature. This will be followed by a narration of the objectives of the work which introduces the applications of nanoparticle supported substrates in surface enhanced Raman spectroscopy and electrocatalysis for fuel cell reactions.

1.1. Molecular solvents

Molecular solvents comprising water, organic solvents and inorganic solvents are the most common electrochemical media. In spite of the fact that electrochemical experiments can be performed in any of these molecular solvents, the solubility of analyte in the solvent, volatility and stability of the solvent to the applied potential (electrochemical potential window) are usually considered while choosing a solvent medium. Compared to organic solvents, water is non-flammable, inexpensive, abundant and has excellent solvent properties making them the universal solvent in electrochemistry. Further, aqueous salt solutions are usually associated with very high ionic conductivities. However, for applications requiring hydrophobic solutes, organic solvents remain the only choice.

For electrochemical studies on reactions involving wider potential range, molecular solvents including aqueous medium are not ideal candidates. This is because these solvents undergo oxidation/reduction at very high positive/negative potentials.

1.2. Ionic gels

Ionic gels are prepared by the quasi-solidification of ionic liquids and organic solvents. The process is carried out by the addition of either polymers, inorganic nanoparticles or low molecular weight gelators to ionic liquids and organic solvents [1-4]. The polymeric analogues of gels have already been extensively studied for various applications. The reversible thermal transitions observed in polymer based ionic gels are attributed to the reversible cross linking of the polymer with temperature.

Gels can also be formed by various secondary interactions such as Van der waals, hydrogen bonding, π- π interactions occurring within the components. These gels possess thermal reversibility much better than their polymeric counterpart. Most of these ionic gel preparation techniques require an initial multistep synthesis of a molecule capable of gelating an ionic liquid. A low concentration of the gelator is added to the bulk solvent medium to promote the formation of three dimensional network structures based on secondary interactions [5]. The organic solvent molecules get trapped within the three dimensional structures causing gelation [6].

1.3. Ionic liquids

Ionic liquids can be defined as salts that exists in liquid state at temperatures less than 100 ^{0}C. Therefore, it is very much different from the molten salts that are liquids only at high temperatures (eg. NaCl at T $\geq$801 ^{0}C, a mixture of 60% $NaNO_3$ - 40% KNO_3 at T = 265-550 ^{0}C). The high melting points of molten salts limit their use in wide number of applications.

Room temperature ionic liquids (RTIL) have been known ever since 1914 when Walden *et al.*, prepared the first ionic liquid ethyl ammonium nitrate with a melting point of 13 ^{0}C [7]. RTIL are considered green solvents as they are environmentally benign, non toxic and non volatile. The studies till date have shown that the use of RTIL have cut down the use of chemical reagents in organic synthesis, stabilizing agents in nanoparticles and supporting electrolytes in electrochemical solvent media [8-9]. Ionic liquids are associated with high cost

and moisture sensitivity and there have been many efforts recently to counter these issues.

1.3.1. Structural aspects of ionic liquids

The structural aspects of the ionic components have to be carefully identified to achieve room temperature ionic liquids. The melting point of an ionic compound is usually related to the lattice enthalpy that comes from the symmetry, size and charge of the ionic components. In order to bring down the melting point of a salt, the size of the ion has to be made large. In addition, the charge on the ions has to be low to decrease the electrostatic force of attraction. Hence, while designing RTIL, non-symmetrical ions that cannot fit into a lattice are usually optimized so that lattice energy and melting point of the compound would be less.

A few of the ionic components that are used for the preparation of ionic liquid is shown in scheme-1. A comparison of the properties of ionic liquids Vs conventional molecular solvents is given in Table-1.

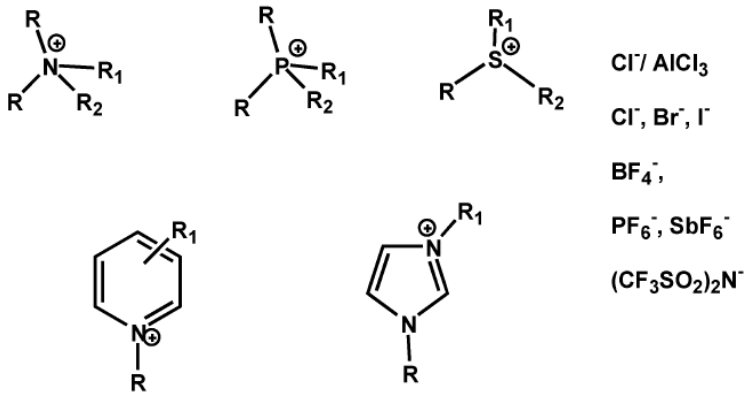

Scheme 1. *Some typical IL cations and anions*

1.3.2. Classification of ionic liquids

Metal based ionic liquids are composed of metal salt and a quaternary ammonium cation. The metal salts such as $ZnBr_2$, $ZnCl_2$, $SnCl_2$, $FeCl_3$ can form ionic liquids with quaternary ammonium salts. The use of these ionic liquids resulted in higher current efficiency and the electroplated metals are generally free from any crack even at micrometer range.

Table 1. *Comparison of the properties of molten salts, ionic liquids and 0.1M KCl*

Compound	**MP T ^{0}C**	**Molar conductivity Scm^{2}mol^{-1}**	**Viscosity cP**
Molten salts			
NaCl	450	154	1.05
$NaNO_3$	900	34	6.9
LiCl-KCl	450	53	2.44
$AlCl_3$(60%)-NaCl	175	41	3.85
Ionic liquids			
emimCl-$AlCl_3$	25	5.3	1.2
emimAl_2Cl_7	25	4.4	14
Bupy BF_4	25	0.3	103
emim[$(CF_3SO_2)_2N$]	25	1.5	31
others			
0.1M aq. KCl	25	129	0.9

The first non - metal based ionic liquid is known to be ethyl ammonium nitrate with a melting point of 12 ^{0}C. The non-metal based ionic liquid utilizes bulky anions such as triflamide, hexaflourophosphate as anions in place of the chlorometallate anions seen in the previous section. The ionic liquids based on these anions are less reactive to air as well as moisture compared to their metal ionic liquid counterparts. This class of ionic liquids can be utilized for several

applications. However they are very much expensive and are quite difficult to prepare.

A recent entry to this class of ionic liquids is the deep eutectic solvents put forward by Abbott *et al.*[10]. The concept behind the preparation of deep eutectic solvents also aims to prepare large unsymmetrical ions as seen in earlier sections. However in this case, the bulky ions are prepared by complexing a simple quaternary ammonium chloride with a hydrogen bond donor. The term 'Deep eutectic solvent' was coined so as to differentiate it from other classes of ionic liquids.

1.4. Deep eutectic solvents

A eutectic mixture is defined as a mixture of two components that has a freezing point lower than its components. Deep eutectic solvents are prepared by simple thermal mixing of the two components viz., quaternary ammonium halide and a hydrogen bond donor (HBD). The depression in freezing point in DES is too drastic that they remain as liquids at room temperature. The hydrogen bonding interaction between the halide anion and the hydrogen bond donor decreases the electrostatic interaction within the quaternary ammonium cation and chloride ion as in scheme 2. This causes a large depression in the freezing point of the mixture.

Scheme 2. *Formation of DES from quaternary ammonium salt and hydrogen bond donor*

1.4.1. Components and composition of DES

Choline chloride is the most commonly used quaternary ammonium salt for the preparation of DES. The structure of choline chloride is provided in scheme-3a. Along with the low symmetry of the compound, the presence of a hydroxyl group on the alkyl chain also contributes to the depression in the freezing point of the mixture [11]. On a commercial scale, choline chloride (2-hydroxyethyl trimethylammonium chloride) is produced in million tonnes per annum scale as an additive for chicken feed. Thus, choline chloride is cheap, abundant, non-toxic

and even biodegradable. The concept of DES was initially demonstrated for mixtures of quaternary ammonium salts with a range of amides but was later extended to a wide variety of hydrogen bond donors.

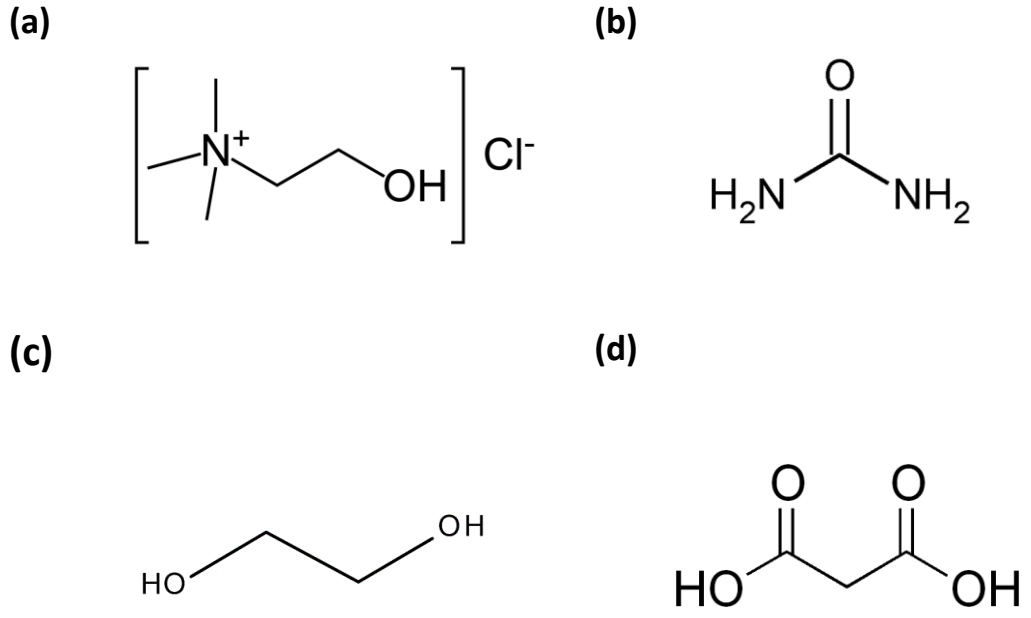

Scheme 3. *Components of DES (a) choline chloride (b) urea (c) ethylene glycol (d) malonic acid*

A variety of acids, amides, diols can be used as hydrogen bond donors and so there is a huge potential for designing a plethora of DES. The eutectic composition of the hydrogen bond donors such as amides, diols, monocarboxylic acids with respect to choline chloride is usually 67 mol % (molar ratio 1:2). The crystallographic data, NMR (HOESY spectra) and mass spectrometry by fast atom bombardment have also confirmed the existence of a 1:2 adduct [11]. However in the case of dicarboxylic acid such as oxalic acid, malonic acid, the eutectic occurs at 50 mol % suggesting a 1:1 complex with choline chloride [10]. Recently, natural DES are also being prepared from biorenewable natural products, such as organic acids, sugars and artificial sweeteners, and amino acids [12]. The components of the DES that are commonly used are given in the scheme-3.

1.4.2. Physical properties of choline chloride based DES

1.4.2.1. Freezing point

As mentioned before, DES is based on the hydrogen bonding interaction between the components viz., choline chloride and a hydrogen bond donor. The freezing point of the mixture is considerably lower than their individual components and often remains as room temperature ionic liquids. The formation of these eutectic mixtures brings about entropy changes which can be correlated to the depression in freezing point. The depression in the freezing point of some of the eutectic mixtures is given in Table-2.

For any hydrogen bonding functional group, the largest depression in freezing point is observed for the mixture associated with strongest hydrogen bonding interaction. For example, urea exhibits largest depression of >122 ^{0}C in freezing point compared to other amides when mixed with choline chloride. The depression in freezing point is also a function of halide anions of the choline salt. Abbott *et al.* measured the depression in freezing point by keeping the HBD constant (urea) and varied the anions of the choline salt [13]. The depression in freezing point was found to follow the order $F^- > NO_3^- > Cl^- > BF_4^-$. Another parameter affecting the freezing point of the mixture is the relative ratio of the choline chloride and hydrogen bond donor. As the ratio of HBD increases, the freezing point of mixture decreases.

Table 2. *Freezing points of DES and its components*

QAS	MP (^{0}C)	HBD	MP (^{0}C)	DES QAS + HBD	FP (^{0}C)
Choline chloride	303	Urea	134	Reline	12
		Ethylene glycol	-12.9	Ethaline	-31
		Glycerol	17.8	Glyceline	-1
		Malonic acid	134	Maline	10

1.4.2.2. Viscosity

Viscosity of an electrochemical medium is extremely important as it affects the rate of mass transport. The diffusion coefficients of ions/molecules are inversely related to the viscosity as shown by the Stokes-Einstein equation.

$$D = \frac{kT}{6\pi\eta R}$$

Where k is the Boltzmann constant, T is the absolute temperature and R is the hydrodynamic radius of the species. The viscosity of the DES is significantly higher compared to the molecular solvents which is an important concern for electrochemical application. The choline chloride based DES exhibits varied viscosities ranging between 37- 6000 cP as compared to a viscosity of 0.89 cP for water. Thus it is evident that the viscosity characteristics of DES depend on the hydrogen bond donor and its extent of hydrogen bonding with the chloride anion. For example, while ethaline medium prepared from choline chloride-ethylene glycol mixture exhibits the lowest viscosity of 37 cP, DES based on derived sugar and carboxylic acids has viscosities in the range 1000 - 6000 cP. A list of DES and their viscosities is provided in the table 3. The addition of water and glycerol disrupts the hydrogen bonded structure of DES and hence are known to decrease the viscosity of DES (Fig. 1a) [14].

Table 3. *Viscosities of DES* at 25 ^{0}C

DES	**Viscosity (cP)**
Reline	750
Ethaline	37
Glyceline	259
Maline	1124

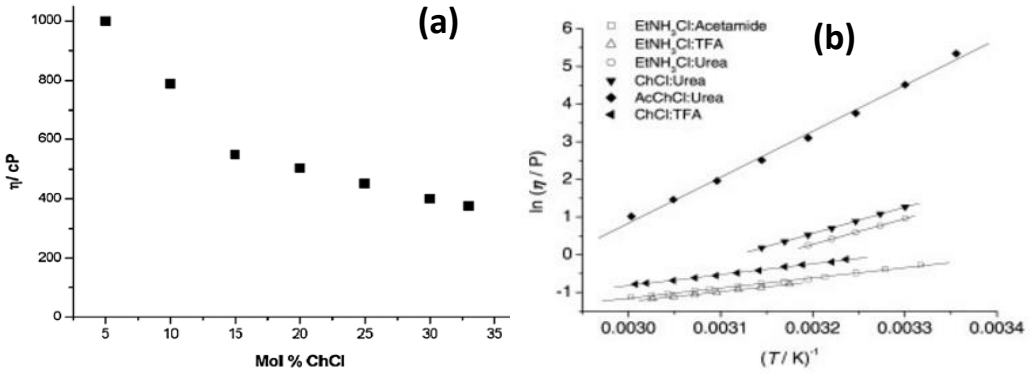

Figure 1. *(a) Variation in the viscosity of glycerol as a function of choline chloride composition (b) Plot of ln η vs 1/T for a variety of DES*

The viscosity, η of the DES also decreases with temperature and obeys the equation,

$$\ln(\eta) = \ln(\eta_0) + \frac{E_\eta}{RT}$$

Where, η_0 is a constant and E_η is the activation energy of the viscous flow. The variation in the viscosity of a set of DES with temperature is given in Fig. 1b.

Recently, the concept of 'hole theory' was used to interpret the high viscosity of ionic liquids and deep eutectic solvents [15]. The theory assumes that ionic materials contain empty spaces or holes due to thermally generated fluctuations in local density. To achieve low viscosity as seen in molecular solvents and molten salts, the dimensions of these holes should match the radii of the ions in the medium. However, in the case of ionic liquids and DES, the size of the ions are relatively larger (3-4Å) compared to the size of the holes (~2Å). This makes the ionic motion through the holes difficult, causing high viscosity.

The viscosity of DES can be lowered by increasing the size of the voids [15]. The radius of an average sized void, < r > is related to the surface tension of the liquid, γ by equation (2).

$$4\pi < r^2 > = 3.5kT / \gamma \qquad (2)$$

Abbott *et al.* proposed that the surface tension and hence the viscosity of DES can be decreased by the introduction of fluorinated hydrogen bond donors [15].

1.4.2.3. Polarity

The polarity of an electrochemical medium signifies the ability of a medium to solvate polar redox species. Infact, the solubility of metal oxides in DES have been found to correlate well with an aqueous HCl solution of 3.14M [16]. A detailed study on the polarity of the commonly used DES viz., ethaline, glyceline, reline, and maline has been studied by Pandey *et al*. [17]. The studies were based on the local environment of the solvatochromic pobes. The polarity was found to vary with the nature of the probe. The order of polarity was found to be glyceline > ethaline > reline, when a hydrogen bonding solvatochromic probe was used. The studies were also conducted based on the response of the solvent to a fluorescence probe Pyrene, which is not affected by the hydrogen bonding interactions. The reline medium with a carbonyl group and amine groups exhibited the highest polarity in terms of static dielectric constant and the refractive index. The results also showed that the polarity of all the four DES were comparatively higher than that of molecular solvents such as ACN, PC, DMSO and common ionic liquids.

1.4.2.4. Ionic conductivity

The ionic conductivity of choline chloride based DES is mainly affected by the viscosity characteristics of the medium and therefore increase significantly with temperature as the viscosity decreases. Similar to the viscosity characteristics which follow Arrhenius equation, the conductivity of DES also follows the same behaviour. The ionic conductivity varies within a range of 0.1-8 mS/cm with ethaline exhibiting the highest ionic conductivity due to its low viscosity. It is apparent that the ionic contribution of DES arises mostly from choline chloride salt rather than the HBD molecule and hence the ionic conductivity of DES increases with the composition of choline chloride. Table 4 provides a list of ionic conductivities of common DES.

Table 4. *Ionic conductivities of DES at 25 ^{0}C* [18]

DES	Ionic conductivity ($mS\ cm^{-1}$)
Reline	0.75
Ethaline	7.61
Glyceline	1.05
Maline	0.55

1.4.2.5. Electrochemical potential window

A wider electrochemical potential window of an ionically conducting medium provides a larger potential range for several electrochemical applications. Ionic liquids and DES exhibit wide electrochemical potential window as they are quite stable to oxidation / reduction processes unlike that of aqueous media. The electrochemical potential window of aqueous medium for example, is typically restricted to 1.23 V on a platinum electrode due to the hydrogen and oxygen evolution processes. The electrochemical potential window of ethaline and reline are 2.1 V and 2.2V respectively [19]. The presence of impurities and water content can decrease this range.

1.4.3. Applications of DES

The deep eutectic solvents were initially utilized mostly in electrochemical applications owing to their inherent ionic conductivity, non-aqueous but polar nature and wider electrochemical potential windows. However within a short span of time, DES is widely accepted in a plethora of applications due to their excellent solvent properties, biocompatibility and inexpensive nature. A few of the applications are discussed below.

1.4.3.1. Electrodeposition of metals

The conventional solvent for electrodeposition applications is water although in some special cases non aqueous molecular solvents are also employed. An ideal electroplating media is expected to be associated with good solvent properties, wide electrochemical potential window and high inherent ionic conductivity. Water is undoubtedly the most accepted solvent for electrodeposition, yet the hydrogen and oxygen evolution reactions occurring in aqueous media during electrodeposition is afflicted with problems such as hydrogen embrittlement, spongy and porous deposition, passivation of electrodes and substrates etc [20]. Passivation is brought about by the formation of metal oxides/hydroxides on the anode preventing the progress of dissolution thereby decreasing the current efficiency of deposition.

The DES addresses some of the issues associated with aqueous electroplating medium. In addition to the high electrochemical stability and high inherent ionic conductivity, DES can solvate metal oxides considerably well which counters the passivation process. This is because any metal oxide/hydroxide that is formed during anodic dissolution gets dissolved off in the DES medium allowing further process to occur. Further, the need of toxic complexing agents can also be minimized by the use of DES.

The electroplating of Aluminium requires non-aqueous medium due to the formation of oxide layer when exposed to water. Therefore the conventional Al electroplating is done in non-aqueous solvent media which are hazardous both during operation and for environment. The eutectic mixtures with its non-aqueous polar nature are suitable for the Al electrodeposition despite a slow deposition rate as reported by Abood *et al.* [21]. Super hydrophobic coatings of Nickel could be achieved without any prior surface treatments in the DES media of reline and ethaline media [22]. Further, $NiCl_2 \cdot 6H_2O$ dissolved in the DES media exhibited a stable thermochromic behaviour over a wide range of temperature [23]. Even in the absence of strong base additives, Zinc electrodeposition carried out in DES was not mass transport limited and exhibited fine microcrystalline features whereas dendritic textures are formed in aqueous medium [17].

The electrodeposition of other metals such as Cu, Ag and Pd and their corresponding electrodeposition mechanism have also been reported in DES medium [24-27]. The physical characteristics of DES media have been proved beneficial for metal alloy deposition too. It is known that in aqueous medium, the differences in the redox potentials of the metal components cause a preferential deposition and therefore increased composition of one metal over another. However in DES, the redox potentials of the metal ions in DES are considerably different from that in aqueous medium due to the complex formation of metal ions with chloride anions. These differences in redox potential wrt aqueous medium make it possible to deposit alloys of variable compositions in DES [28].

1.4.3.2. Synthesis of nanoparticles

The DES is increasingly preferred in the synthesis of metal nanoparticles also. For example, nanoparticles of Au, Pd, Cu and Pt have already been prepared in ethaline and reline media [29-32]. The components of DES by itself are capable of stabilizing the nanoparticles formed. Further, the surface tension of the medium of nanoparticle synthesis determines the nucleation rates and hence the size of nanoparticles. The surface tension values of DES are lower compared to aqueous medium (49 - 52 mNm^{-1} Vs 73 mNm^{-1}) and hence a high nucleation rate with the formation of small sized nanoparticles can be predicted in DES [33]. The synthesis procedures carried out in DES can yield nanoparticles in solution by wet chemical methods as well as nanoparticle films on electrode surface by electrochemical methods. A number of reports on shape selective synthesis of nanoparticles associated with high index planes have been reported by Sun *et al.* in DES [34]. The synthesis is carried out by potential cycling at fast sweep rates in DES containing metal salts at temperatures of 60-80 ^{0}C. The activities of high index planes nanoparticles are superior to ordinary nanoparticles as the former possess a higher density of atomic edges and corners. Chirea *et al.* synthesised gold nanowires in DES by using sodium borohydride as the reducing agent [29]. The synthesized gold nanowires exhibited a large number of corners and edges and exhibited superior catalytic activity in the chemical reduction of p-nitrophenol to aniline.

1.4.3.3. Organic synthesis, polymerization and enzymatic processes

The increasing interest in using environmentally benign solvents as reaction media makes DES accepted even in applications that do not particularly need an ionic conducting medium. This is due to the fact that it is possible to tune novel DES media that specifically solvates a reactant and not the product which simplifies the product extraction process. Even though there are no extensive toxicological studies on DES, it is still considered as a green solvent in organic synthesis due to its recyclability. The DES media can be reused for atleast 3-4 times once the reaction products are extracted using an immiscible organic solvent followed by a brief drying in vacuum. An alternative method of product separation is to dissolve the DES in water. The DES is later recovered in vacuum by removing water.

Many organic synthesis such as alkylation, substitution, reduction, halogenation have been carried out in DES. There are several reports that the use of DES medium increases the product yield with minimal organic reagents necessary for the reaction. For example, Singh *et al.* reported the simple alkylation of aniline using only alkyl bromides in reline medium [35]. The yields obtained were quite high at short reaction time. Azizi *et al.* carried out 1,2 reduction of carbonyls in DES medium using sodium borohydride as reducing agent at room temperature [36]. Pawar *et al.* carried out Perkin condensation reaction of benzaldehyde and acetic anhydride in DES at room temperature for 4-9 hours as against $\geq$16 hours at 140 °C using conventional methods [37]. The DES medium could be reused for about 4 reactions in this procedure.

The DES is also emerging as a preferred media for carrying out different polymerization reactions. Besides being a solvent, the DES components can also act as precursors and structure directing agents in polymerization reactions. The resorcinol-formaldehyde resins prepared in DES containing urea could yield high surface area carbon (100 m^2/g) on carbonization [38]. The high porosity was attributed to the evolution of urea during the carbonization process. DES also seems to be well-suited for frontal polymerization reactions. This is because the

rate of polymerization in this case depends on the viscosity of the medium and with DES and there is a large scope of tailoring viscosities [39].

Enzymatic processes involving hydrophobic substrates often exhibit poor solubility in water and hence are used in organic solvent such as DMSO, acetone that often denature enzymes. Currently, these polar organic solvents are being replaced by ionic liquids and DES that dissolves substrate without deactivating enzymes. Monhemi *et al*. observed remarkable conformational stability of the enzyme lipase in reline medium [40]. This is quite surprising as complete denaturation of enzyme occurs in 8M aqueous urea solution. The results were accounted by the fact that urea molecules have a low diffusion coefficient in DES compared to that in water and hence cannot reach the protein domains. The activity of epoxide hydrolases was found to increase by almost 20-fold with the addition of 25 vol% glyceline compared to that in buffer alone [41]. The study showed that on adding 25 vol% DMSO or acetonitrile, the enzyme activity decreased by 2-6 times. Candida antarctica lipase B catalyzed polymerization of ε-caprolactone have also been carried out in deep eutectic solvents [42].

1.4.3.4. Solubility of gases and metal oxide solutes

Solubility of gases in solvent media is utilized in gas separation and absorption applications. This method can find applications in treating harmful gases from industrial exhaust. The conventional methods of CO_2 absorption employ aqueous amine technology which is associated with high cost and amine volatility. With the advent of DES, these solvents are being studied as cost effective potential candidates for gas absorption owing to the low vapour pressures, non-flammable nature and excellent solvent properties. The presence of large amount of ionic species causes good solubility of gases in DES and ionic liquids. The solubility of CO_2 in reline (choline chloride – urea) was demonstrated in detail at different temperatures and pressures by Su *et al.* [43]. However the presence of water in DES has been found to adversely affect the solubility of CO_2.

Another aspect of the solvent properties of DES is the solubility of metal oxides in DES which provide greener alternatives to acids and alkalis which are normally used for metal recovery. The separation of metal in DES is carried out using the

preferential solvation of certain metal oxides. Abbott *et al.* studied the solubility of over 17 metal oxides in reline, ethaline and maline [16]. The solubility was found to be high in maline medium due to the oxygen accepting nature of protons. The dissolution properties of DES depend on the complexation abilities of the hydrogen bond donor and the chloride anion. The ZnO dissolution in reline medium was attributed to the formation of $[ZnClO.urea]^-$ anion, which has been confirmed by the electronspray mass spectrometry (MS) and FTIR. These features have been observed in the case of CuO too. DES is also used in metal surface treatment prior to metal finishing and depositions in order to dissolve off the surface metal oxide and improve the adhesion of the coating.

1.5. Electrochemical methods of preparing nanoparticle modified substrates

The deposition of nanoparticles on solid substrates in the form of thin films is extremely important for the fabrication of sensors, electrocatalysts and as substrates for surface enhanced Raman spectroscopy (SERS). For electrochemical applications, the nanoparticles synthesized by wet chemical methods are usually immobilized onto a conductive substrate by dropcasting the nanoparticles dispersion or by means of carbon paste or nafion film as binders. However, the deposit prepared by these methods can often effectively decrease the catalytic active sites of the nanoparticles. The stability of the electrodes often pose problems during long term use, especially in electrocatalytic applications. The modified nanoparticles often peel off from the substrate under electrochemical conditions of high current density and vigorous gas evolution.

Electrodeposition is a versatile technique that requires simple instrumentation, yet ensures precise control of the nucleation and growth processes. The thickness of the nanoparticle films deposited on the substrate can be increased by manipulating the electrodeposition time. Recent studies have shown that the morphology of the deposited nanoparticles can also be controlled by varying electrochemical conditions [44].

The electrochemical synthesis and insitu deposition of nanoparticles can be carried out by applying constant potential, potential pulse, potential sweep or a

constant current for a period of time. The metal ion source for the preparation of metal nanoparticles can be either brought about by dissolving the corresponding metal salt in the medium or by the dissolution of the corresponding metal anode. The electrodeposition by anodic dissolution in aqueous medium is associated with gas evolution at the cathode surface affecting the adhesion of the nanoparticles film onto the surface of the substrate.

1.6. Applications of electrodeposited nanoparticles

1.6.1. Electrochemical sensors

Electrochemical sensors have been utilized extensively in practical applications mainly in gas sensing, detection of toxic metal ions and medical diagnostics [45-48]. A majority of the sensors are amperometric, which are based on the oxidation/reduction taking place on the electrode surface causing a flow of electrons (current). The resultant current is measured and often used for quantifying the analyte concentration. The use of nanoparticles modified substrates have proved beneficial in these applications. The high surface area of nanoparticle modified surface amplifies the electrochemical response of the analyte, leading to an increased sensitivity. The use of nanoparticles in electrochemical sensors of analytes such as nitric oxide, organophosphate pesticides, hydrogen peroxide, alcohols, dissolved oxygen have shown to increase the sensitivity.

The surface functionalities of the nanoparticles can be modified to bind enzymes, so as to prepare biosensors of high specificity. The nanoparticles of gold and silver are considered to be biocompatible and hence a large extent of biological processes have been electrochemically monitored on these surfaces. The integration of gold nanoparticles in glucose oxidase based sensors have been shown to enhance the activity of glucose determination [49]. Current studies are not only intended to improve the sensitivities of existing sensors but are also extended towards wearable electrochemical sensors suitable for medical diagnostics.

1.6.2. Surface enhanced Raman spectroscopy (SERS)

The Raman signals of analyte that are inherently weak can be enhanced by adsorbing analyte onto nanoparticle modified substrates. The enhancement of the signal is caused by the interaction of the surface plasmons of nanoparticles modified substrate with the electromagnetic field of the incident laser radiation. SERS is carried out on metallic surface with 10-100 nm roughness fabricated by sputtering of metal over polymer particles, electrodeposition, electrochemical etching, dropcasting nanoparticle dispersions on solid substrates. Of these, the electrodeposited nanoparticles exhibit commendable stability to continuous exposure of laser light and organic solvents vis-à-vis other substrates. An enormous enhancement of Raman signals of the order of 10^{12} was achieved on stable nanostructured thin films of silver prepared electrochemically [50].

1.6.3. Electrocatalysis for fuel cells

The design and fabrication of electrocatalysts for fuel cell applications is of immense interest in research as well as in industries. An electrocatalyst is required in, thermodynamically favourable electrochemical reactions proceeding with poor kinetics. An electrocatalyst increases the rate of a reaction by several orders of magnitude. The presence of an electrocatalyst also brings down the overpotential required for a reaction close to thermodynamic equilibrium potential. Thus in general, the objective of an electrocatalyst is to lower the activation energy barrier of an electrochemical reaction, thereby allowing the reaction to occur at high current densities at potentials close to equilibrium. Most of the fuel cell reaction in practical application utilizes Pt as the electrocatalyst due to its unique ability to bring about reaction near thermodynamic potential. Research efforts to develop cost effective, abundant alternatives to platinum have resulted in electrocatalytic materials of nanostructured nickel, cobalt, palladium, gold [51].

In a fuel cell, an electrolytic medium containing an ionically conducting membrane is sandwiched between two electrode viz., anodes and cathode. The electrochemical oxidation of the fuel taking place at the anode generates ions and electrons. The ions permeate through the ionically conducting membrane towards the cathodic compartment while the electron passes through the external circuit to

the cathode. An electrochemical reduction occurs at the cathode and this flow of electrons causes a current. Thus catalytic materials that are capable of decreasing the overpotential for both the cathodic and anodic reactions are required.

The reaction occurring in fuel cells such as hydrogen and oxygen evolution reactions, alcohol oxidation reaction and oxygen reduction reaction have been studied on a wide range of nanostructured materials. The high surface area of the nanoparticles renders innmumerable active sites for an electrochemical reaction to occur. In addition to the high surface area, the morphology, presence of stabilizers and certain specific crystal planes of the nanoparticles surface are known to impart enhanced activity on to the electrocatalysts.

A brief introduction to the fuel cell reactions catalysed by the metals discussed in the thesis is given below.

(a) Hydrogen evolution reaction

The HER in acidic media has been studied on almost all the metals, though Pt is most commonly used. However, the electrocatalytic activity of Pt is extremely sensitive to adsorbed impurities. The high cost of platinum pose challenge in its use in low-cost systems. Numerous non - Pt based catalysts such as Au, Pd, and mixtures of inexpensive transition metals Fe, Co, Ni are currently being studied.

The mechanism involves primarily a proton discharge step on the metal surface also known as Volmer step [52]. The subsequent step varies with the material used and it can be either Tafel step (chemical combination of adsorbed hydrogen atom on metal) or Heyrovsky step (electrochemical desorption of adsorbed hydrogen atoms).

$$M + H_3O^+ + e^- \rightarrow MH_{ads} + H_2O \text{ (Volmer step)}$$

$$2MH_{ads} \rightarrow M + H_2 \text{ (Tafel step)}$$

$$MH_{ads} + H^+ + e^- \rightarrow 2M + H_2 \text{ (Heyrovsky step)}$$

Where, M represents free metal sites at the electrode, MH_{ads} represents the adsorbed hydrogen atom on the metal surface.

(b) Oxygen evolution reaction

The production of H_2 at the cathode in a water electrolysis cell is severely constrained by the slow kinetics of oxygen evolution reaction (OER) taking place at the anode. To address this issue, highly efficient OER catalysts are required to reduce the overpotential and enhance the energy efficiency of the process. Till date, IrO_2 and RuO_2 are the commonly used OER catalysts due to their high catalytic activity. However, the high cost and their unsustainable supply of these materials makes them unsuitable for large-scale applications. Recent research interest are aimed at developing low-cost OER electrocatalysts on the basis of first-row transition metals and their oxides such as cobalt phosphate composites, nickel borate composites, cobalt oxide nanoparticles and manganese oxide thin films [53-55].

The mechanism of OER is usually represented by Krasil' schchikov reaction scheme [56] given below,

$$S + OH^- \rightarrow SOH + e^-$$

$$SOH + OH^- \rightarrow SO^- + H_2O$$

$$SO^- \rightarrow SO + e^-$$

$$2SO \rightarrow 2S + O_2$$

(c) Alcohol oxidation reaction

The alcohol oxidation reaction carried out in acid media utilizes Pt based catalysts. However, with the development of alkaline media fuel cells, non- noble metals, are also being considered as electrocatalysts for the oxidation of alcohol. Another approach is to decrease the Pt metal loading in catalysts by using Pt in combination with other metals. While optimizing electrocatalysts for practical applications such as in fuel cells, factors such as catalytic poisoning effects, cost and availability are considered. For example, while the activity of Platinum gets diminished due to carbon monoxide poisoning, incorporating a small percentage of Au /Ru /W in the catalysts imparts CO tolerant characteristics to the catalyst.

The alcohol oxidation in alkaline media is known to be catalyzed by hydroxyl ions. The mechanism of alcohol oxidation on gold has been proposed by Kwon *et*

al. [57]. The initial deprotonation is found to be base catalyzed while the second deprotonation is characteristic of the electrode material.

$$RCH_2OH + OH^- \rightarrow RCH_2O- + H_2O$$

$$RCH_2O^- + OH^- \rightarrow RCHO + H_2O$$

The primary deprotonation is usually considered to be the rate determining step. Though the studies were performed on a gold surface, a similar mechanism can be applied for Pt and Pd based catalyst in alkaline media [57].

1.7. Objectives of the work

The objective of the thesis work is to explore the electrochemical aspects of Deep eutectic solvents as an electrolytic medium. The first part of the chapter deals with the electron transfer studies in DES medium. As mentioned earlier, DES is composed of ions unlike the oriented molecular dipoles in water and organic solvents. The electron transfer studies of standard redox species carried out in DES is aimed at understanding the solvation mechanism and mass transfer properties in the medium. This is crucial to explore DES as a medium for electrochemical processes. The use of distinct redox species in the study in terms of charge and polarity intends to identify the differences in the solvation mechanism according to nature of the redox species. The half peak potentials obtained from the cyclic voltammetric studies indicates the preferential solvation of the oxidized/reduced species in the DES medium. The high viscosity of DES affects the mass transport properties of the redox species which is reflected in the diffusion coefficients calculated from electrochemical impedance spectroscopy and cyclic voltammetry.

A significant part of the thesis deals with the studies on potential application of DES as a medium for the *insitu* preparation and electrodeposition of metal nanoparticles. Even though, electrodeposition of metallic films and nanoparticles have been carried out in DES medium by potential sweep and pulse techniques, there are no reports on nanoparticle deposition by anodic dissolution in DES. A study in this area is extremely

important in DES due to the fact that anodic dissolution of certain metals in aqueous medium is associated with passivation problems. Our studies have shown that the metal oxide films causing passivation are soluble in DES medium and hence facile electrodeposition of mesoporous films of metal nanoparticles could be achieved in the medium. Further, it was also seen that the inherent ionic conductivity together with the ability of DES to stabilize nanoparticles minimized the material requirements for the electrodeposition. In this work, the electrodeposition of metal nanoparticles of Au, Ag, Co, Pd and Au@Pd is demonstrated.

Another important objective of the thesis is to design a novel ionically conducting soft medium for electrochemical studies. Such a soft media is of primary interest due to their resemblance with biological media. The soft matrix prepared from $TBABF_4$ and ethylene glycol was explored as a medium for electrochemical monitoring of enzyme kinetics.

References

1. S. Washiro, M. Yoshizawa, H. Nakajima and H. Ohno, *Polymer*, 2004, **45**, 1577.
2. P. Wang, S. M. Zakeeruddin, P. Comte, I. Exnar and M. Gratzel, *J. Am. Chem. Soc*., 2003, **125**, 1166.
3. J. C. Ribot, C. G. Sanchez, R. Hoogenboom and U. S. Schubert, *J. Mater. Chem.*, 2010, **20**, 8279.
4. K. Hanabusa, H. Fukui, M. Suzuki and H. Shirai, *Langmuir*, 2005, **21**, 10383.
5. J. Bonnet, G. Suissa, M. Raynal and L. Bouteiller, *Soft Matter*, 2014, **10**, 3154.
6. N. W. Smith, J. Knowles, J. G. Albright and S. V. Dzyuba, *J. Mol. Liq*., 2010, **157**, 83.
7. M. Freemantle, An Introduction to Ionic Liquids, Royal Society of Chemistry, 2010, 12.
8. W. Miao and T. H. Chan, *Acc. Chem. Res*., 2006, **39**, 897.
9. A. S. Pensado and A. A. H. Pádua, *Angew. Chem.*, 2011, 8683.
10. A. P. Abbott, D. Boothby, G. Capper, D. L. Davies and R. K. Rasheed, *J Am. Chem. Soc*., 2004, **126**, 9142.

11. A. P. Abbott, G. Capper, D. L., R. K. Rasheed and V. Tambyrajah, *Chem. Commun.*, 2003, 70.

12. A. Paiva, R. Craveiro, I. Aroso, M. Martins, R. L. Reis and A. R. C. Duarte, *ACS Sustainable Chem. Eng.*, 2014, **2**, 1063.

13. A. P. Abbott, G. Capper, D. L. Davies, H. L. Munro, R. K. Rasheed and V. Tambyrajah, *Chem. Commun.*, 2001, 2010.

14. A. P. Abbott, R. C. Harris, K. S. Ryder, C. D'Agostino, L. F. Gladden and M. D. Mantle, *Green Chem.*, 2011, **13**, 82.

15. A. P. Abbott, G. Capper and S. Gray, *Chem. Phys. Chem*., 2006, **7**, 803.

16. A. P. Abbott, G. Capper, D. L. Davies, K. J. McKenzie and S. U. Obi, *J. Chem. Eng. Data*, 2006, **51**, 1280.

17. A. Pandey, R. Rai, M. Pal and S. Pandey, *Phys. Chem. Chem. Phys.*, 2014, **16**, 1559.

18. E. L. Smith, A. P. Abbott and K. S. Ryder, *Chem. Rev*., 2014, **114**, 11060.

19. M. L. M. Badea, A. Cojocaru and L. Anicai, *U.P.B. Sci. Bull.*, Series B, 2014, **76**, 21.

20. Electrodeposition from Ionic Liquids. Edited by F. Endres, D. M. Farlane, A. Abbott, 1-13.

21. H. M. Abood, A. P. Abbott, A. D. Ballantyne and K. S. Ryder, *Chem. Commun. (Camb).*, 2011, **47**, 3523.

22. C. Gu and J. Tu, *Langmuir*, 2011, **27**, 10132.

23. C. Gu and J. Tu, *RSC Adv.*, 2011, **1**, 1220.

24. M. J. Popescu, V. Constantin, M. Olteanu, O. Demidenko and K. Yanushkevich, *Rev. Chim.*, 2011, **62**, 626

25. H. Wang, Y. Jia, X. Wang, Y. Yao, D. Yue and Y. Jing, *Electrochim. Acta*., 2013, **108**, 384.

26. P. Sebastian, E. Valles and E. Gomez, *Electrochim. Acta.*, 2013, **112**,149.

27. G. Lanzinger, R. Bock, R. Freudenberger, T. Mehner, I. Scharf and T. Lampke, *Trans. Inst. Met. Finish.*, 2013, **91**, 133.
28. A. P. Abbott, G. Capper, K. McKenzie and K. S. J. Ryder, *Electroanal. Chem.*, 2007, **599**, 288.
29. M. Chirea, A. Freitas, B. S. Vasile, C. Ghitulica, C. M. Pereira and F. Silva, *Langmuir*, 2011, **27**, 3906.
30. J. A. Hammons, T. Muselle, J. Ustarroz, M. Tzedaki, M. Raes, A. Hubin and H. Terryn, *J. Phys. Chem. C*, 2013, **117**, 14381.
31. Q. B. Zhang and Y. X. Hua, *Phys. Chem. Chem. Phys.*, 2014, **16**, 27088.
32. L. Wei, Y. Fan, N. Tian, Z. Zhou, X. Zhao, B. Mao and S. Sun, *J. Phys. Chem. C*, 2012, **116**, 2040.
33. D. Agostino, R. C. Harris, A. P. Abbott, L. F. Gladden and M. D. Mantle, *Phys. Chem. Chem. Phys.*, 2011, **13**, 21383.
34. H. Liao, Y. Jiang, Z. Zhou, S. Chen and S. Sun, *Angew. Chem. Int. Ed. Engl.* 2008, **47**, 9100.
35. B. Singh, H. Lobo and G. Shankarling, *Catal. Lett.*, 2011, **141**,178.
36. N. Azizi and E. Gholibegio, *RSC Advances*, 2012, **2**, 2289.
37. P. M. Pawar, K. J. Jarag and G. S. Sharkarling, *Green Chem*. 2011, **13**, 2130.
38. D. Carriazo, M. C. Gutie´rrez, M. L. Ferrer and F. del Monte, *Chem. Mater.*, 2010, **22**, 6146.
39. J. D. Mota-Morales, M. C. Gutierrez, I. C. Sanchez, G. Luna-Barcenas and F. del Monte, *Chem. Commun*., 2011, **47**, 5328.
40. H. Monhemi, M. R. Housaindokht, A. A. Moosavi-Movahedi and M. R. Bozorgmehr, *Phys. Chem. Chem. Phys.*, 2014, **16**, 14882.
41. J. T. Gorke, F. Srienc and R. J. Kazlauskas, *Chem. Commun*., 2008, **14**, 1235.
42. J. T. Gorke, F. Srienc and R. J. Kazlauskas, *ACS Symposium Series*, Vol. 1038, Chapter 14, 169.

43. W. C. Su, D. S. H. Wong and M. H. Li, *J. Chem. Eng. Data*, 2009, **54**, 1951.

44. N. Tian, Z. Zhou, S. Sun, Y. Ding and Z. L. Wang, *Science*, 2007, **316**, 732.

45. Y. M. Liu, C. Punckt, M. A. Pope, A. Gelperin and I. A. Aksay, *ACS Appl. Mater. Interfaces*, 2013, **23**, 12624.

46. G. Liu and Y. Lin, *Anal. Chem.*, 2005, **77**, 5894.

47. Y. Zhu, G. Zeng, Y. Zhang, L. Tang, J. Chen, M. Cheng, L. Zhang, L. He, Y. Guo, X. He, M. Lai and Y. He, *Analyst***,** 2014, **139**, 5014.

48. H. Yu, M. Xu, S. Yu and G. Zhao, *Int. J. Electrochem. Sci*., 2013, **8**, 8050.

49. J. T. Holland, C. Lau, S. Brozik, P. Atanassov and S. Banta, *J. Am. Chem. Soc*., 2011, **133**, 19262.

50. L. A. Lane, X. Qian and S. Nie, *Chem. Rev.*, 2015, **115**, 10489.

51. S. Zhang, Y. Shao, G. Yin and Y. Lin, *J. Mater. Chem. A*, 2013, **1**, 4631.

52. J. O. M. Bockris, I. A. Ammar and A. K. M. S. Huq, *J. Phys.chem.*, 1957, **61**, 879.

53. M. W. Kanan and D. G. Nocera, *Science*, 2008, **321**, 1072.

54. J. Esswein, M. J. McMurdo, P. N. Ross, A. T. Bell and T. D. Tilley, *J. Phys. Chem. C*, 2009, **113**, 15068.

55. M. Dinca, Y. Surendranath and D. G. Nocera, *Proc. Natl Acad. Sci. USA*, 2010, **107**, 10337.

56. I. Krasil'shchikov, *Zh. Fiz. Khim*., 1963, **37**, 531.

57. Y. Kwon, S. C. S. Lai, P. Rodriguez and M. T. M. Koper, *J. Am. Chem. Soc*., 2011, **133**, 6914.

CHAPTER 2

Materials and Methods

2.1. Introduction

This chapter describes the experimental techniques used for the characterization of the nanomaterials and electrocatalysts prepared in this work. The surface studies of the nanoparticle catalysts were carried out using UV spectroscopy, SERS and XRD. The morphological characterization of the surface was carried out by SEM. The electrocatalytic performance of prepared materials were analysed by cyclic voltammetry, Tafel analysis and electrochemical impedance spectroscopy. FTIR and DSC were used for the characterization of some of the bulk samples used in the study.

2.2. Preparation of Deep eutectic solvents (DES)

DES is a room temperature eutectic mixture of choline chloride and a hydrogen bond donor (HBD). The DES used in this study are maline, ethaline and reline. The names of these DES media are based on the hydrogen bond donors used in the preparation [1]. For example, malonic acid, ethylene glycol and urea were used as HBD for the preparation of maline, ethaline and reline respectively with a molar ratio of 1:2. Choline chloride purchased from Aldrich was dried for one hour in a hot air oven at 50 ^{0}C prior to use. The components were magnetically stirred at 80^{o} C until a homogeneous colorless liquid was formed.

2.3. Instrumentation

EG&G potentiostat (model 263A) which is interfaced to a PC through a GPIB card (National instruments) was used for galvanostatic deposition, cyclic voltammetry and chronoamperometry. EIS was performed using a model 5210 lock-in amplifier (Perkin-Elmer instruments) with Powersuite software (EG&G) interfaced with a PC. UV-vis absorption spectra of nanoparticles were measured using Perkin Elmer-Lambda 35 spectrophotometer. X-ray diffraction studies (XRD) were carried out using Cu-Kα (l = 1.54 Å) radiation from a Rigaku Ultrax 18 rotating anode generator (5.4 kW) monochromated with a graphite crystal.

SEM images and EDAX were recorded with Ultra plus field emission scanning electron microscope (FESEM).

Raman spectra were obtained with a high resolution triple Raman spectrometer (T64000, Horiba JobinYvon), using a He–Ne Laser (λ=632.8 nm) with a 50 x objective. Laser power was maintained at 23mW. Prior to acquiring spectra, spectrometer was calibrated using a standard Si wafer.

2.4. Electrochemical techniques

2.4.1. Cyclic voltammetry

Cyclic voltammetry is often the first experiment performed in an electroanalytical study for acquiring qualitative information about electrochemical reactions. The technique provides considerable amount of information on the thermodynamics and diffusion characteristics of redox processes. In cyclic voltammetry, the potential of a working electrode (*wrt* a reference electrode) is swept as a function of time between the limits E_1 and E_2 in a triangular waveform and the resulting current at the working electrode is measured (Fig.1). By varying the rate at which potential is swept, information regarding the kinetics of mass transport and the heterogeneous reaction kinetics can determined.

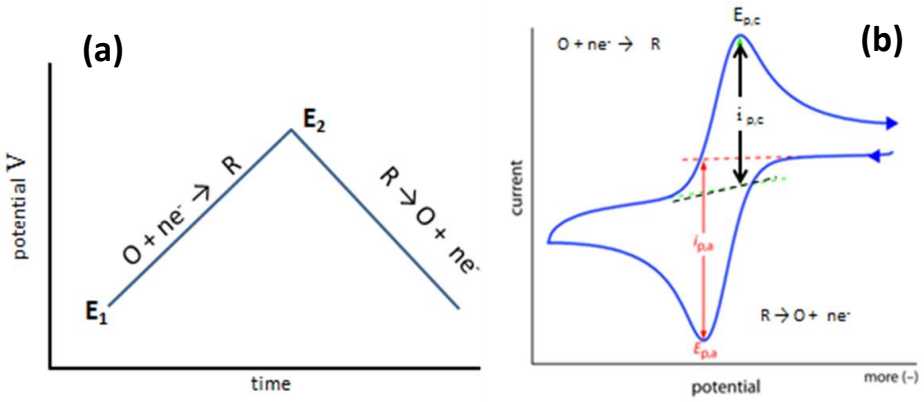

Figure 1. *(a) Potential-time wave form applied (b) current-potential profile in a cyclic voltammetric experiment*

The current arises due to two reasons [2-3]

i) Capacitive current due to double layer charging of the electrode|electrolyte interface leading to the capacitance current. The capacitive current exists even in a test solution that contains no electroactive analyte.

ii) Faradaic current resulting from various electrochemical processes like redox reactions, adsorption.

For a typical reversible one-electron redox reaction of the type;

$$O + ne^- \leftrightharpoons R$$

The ratio of the concentration of oxidized C_o and reduced species C_R is given by the Nernst equation,

$$E = E^0 + \frac{RT}{nF} \ln \frac{C_o}{C_R}$$

Within the region next to the electrode surface known as Nernst diffusion layer, the concentration gradient of the electroactive species is linear. As the potential is swept negative, the surface concentration of the oxidized species decreases progressively due to reduction. This increase in the concentration gradient, causes an increase in the current. As the potential is being is being continuously made negative, the surface concentration of the oxidized species decreases and eventually becomes zero. The concentration gradient is maximum at this point and and hence gives the maximum current. Beyond this potential, the concentration gradient starts to decrease due to relaxation effect, causing a decrease in current. The initial increase in current followed by a decrease owing to the concentration gradient gives rise to a peak shaped response in the cyclic voltammogram. The reverse sweep towards the positive potentials also gives similar current-potential profile but with an opposite sign.

The size of the diffusion layer depends on the scan rate used. At slow scan rates, the diffusion layer will grow much further from the electrode. Consequently the diffusion to the electrode surface is considerably smaller at slow scan rates than it is at faster rates. Thus the magnitude of the current will be lower at slow scan rates. At high scan rates, the diffusion layer does not have sufficient time to relax and hence the concentration gradient as well as the current resulting from it also increases.

The peak current in cyclic voltammetry is given by the Randles-Sevcik equation

$$i_p = (2.69 \times 10^5) n^{3/2} A D^{1/2} v^{1/2} C$$

where *n* is the number of electrons in the redox reaction, *A* is the area of the working electrode, *D* is the diffusion coefficient for the electroactive species, ν is the scan rate, and *C* is the concentration of the electroactive species at the electrode. If the analyte concentration is known, then cyclic voltammetry can be used to measure the analyte's diffusion coefficient.

The cyclic voltammogram of a reversible redox reaction is characterized by, [3]

1. $\Delta E_p = | E_p^A - E_p^C | = 59/n$ mV
2. $| E_p - E_{p/2} | = 59/n$ mV
3. $| I_p^A / I_p^C | = 1$
4. $I_p \ \alpha \ \nu^{1/2}$
5. E_p is independent of ν

Where E_p^A and E_p^C are the peak potentials of anodic and cathodic reactions respectively

I_p^A and I_p^C are the peak currents of anodic and cathodic reactions respectively.

2.4.2. Electrochemical Impedance Spectroscopy

Electrochemical impedance spectroscopy (EIS) is an ac technique that gives accurate, error-free kinetic and mechanistic information on redox reactions. EIS involves the application of a very small perturbation voltage of 5 to 10 mV peak-to-peak in a range of frequencies onto a system which is close to the steady state equilibrium. The response of the electrochemical system in terms of current is

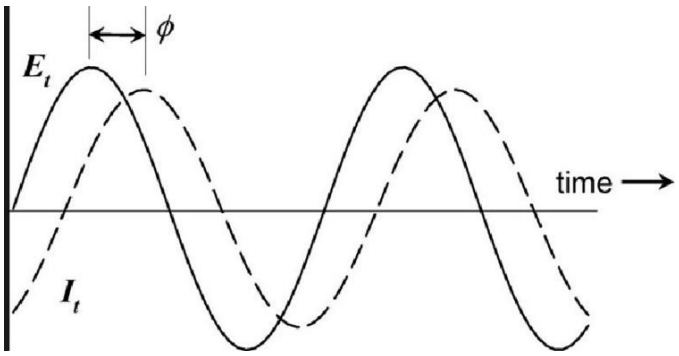

Figure 2. *Schematic representation of a small sinusoidal applied perturbation (E) and the current response (I)*

measured. The current response differs in phase and amplitude from the applied voltage signal. Fig.2 shows the sinusoidal signal of perturbation (E_t) and response (I_t) of the electrochemical system. The measurement of phase difference and amplitude of the response signal with respect to the applied signal over a wide frequency range can provide data on electrode capacitance and charge-transfer kinetics and also on the diffusion of the redox probes. For this reason, EIS has become a powerful tool in the study of corrosion, semiconductors, batteries, electroplating, and electro-organic synthesis.

Principle of AC circuits

The knowledge of the principles of ac circuits is essential to analyse the electrochemical response of a cell to an ac perturbation. On applying a sinusoidal signal of voltage $V = V_0 sin(\omega t)$ to an electrical circuit that contains a combination of resistors and capacitors, a current response, given by $I = I_0 sin(\omega t + \phi)$ is obtained. Here V_o is the maximum amplitude, I_o is the maximum current, ω is the angular frequency and ϕ is the phase angle between the perturbation and response. The potential V and current I are proportional by a factor known as impedance Z. In terms of phasor, the rotating vectors are separated in the polar diagram by the angle.

For a pure resistor, R the phase angle ϕ is zero. This means that there is no phase difference between the applied potential and the response current. Thus for a resistor, the relation $I = V_0 sin\omega t$ / R is obtained from the Ohm's law, V = IR.

For a pure capacitor, C, the current I is given by, $I = CdV/dt$. On substituting the value of V as $V_0 sin(\omega t)$ followed by differentiating, the equation becomes,

$$I = \omega C V_0 sin\,(\omega t + \pi/2)$$

$$I = V_0 sin\,(\omega t + \pi/2)/X_C$$

where $X_C = (\omega C)^{-1}$ is known as the capacitive reactance. Thus in the case of a pure capacitor, the current leads the potential by 90°or $\pi/2$. By a similar calculation, for a circuit element containing a pure inductance, the potential leads the current by 90°or $\pi/2$.

Equivalent Circuit of an electrochemical Cell

An electrode interface undergoing an electrochemical reaction is typically analogous to an electronic circuit consisting of a specific combination of resistors and capacitors. The values are determined by analysing these analogous circuits, in terms of the interfacial phenomena occurring at the electrode-solution interface. For an electrochemical reaction,

$$O + ne^{-} \rightarrow R$$

The electron is transferred across the electrified interface, as illustrated in Fig. 3*a*. The charge transfer leads to both faradaic and non-faradaic components.

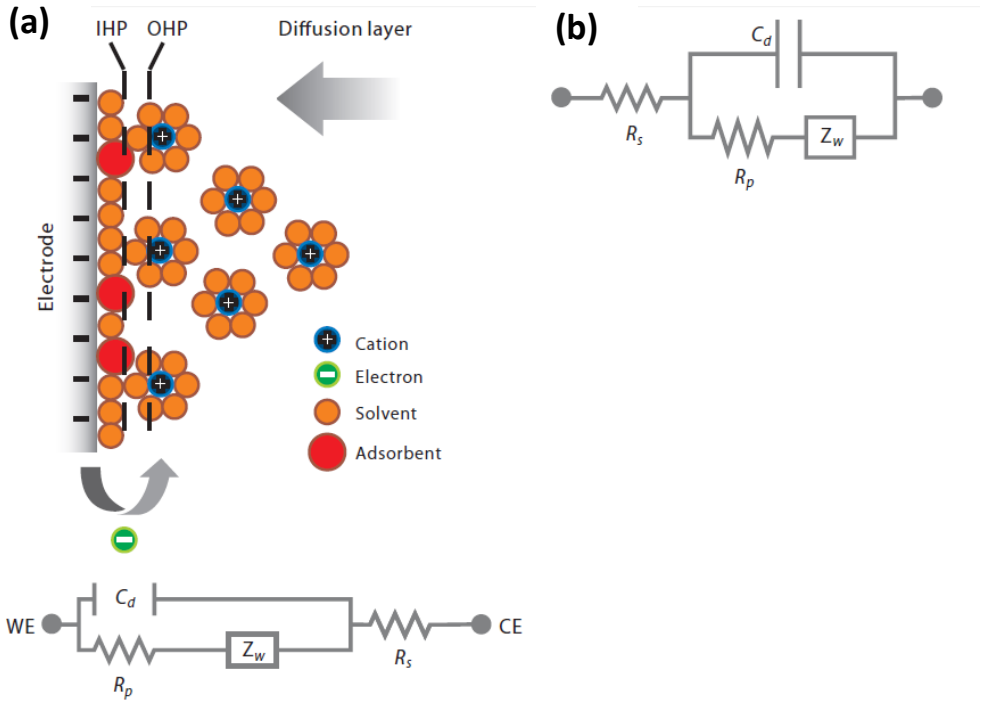

Figure 3*(a). Electrified interface with a negatively charged electrode; countercations are aligned along the electrified surface. At bottom are the electrical circuit elements corresponding to each interface component (b)An idealized Randles electrical equivalent circuit for the interface*

An electrode|solution interface can be considered as an impedance to a small sinusoidal excitation. The impedance of the electrochemical interface is a complex function, Z(ω) that can be expressed either by cartesian or polar coordinates,

$Z(\omega) = Z'(\omega) + j\,Z''(\omega)$

$Z(\omega) = |Z|e^{j}$

$|Z|^2 = |Z'_{re}|^2 + |Z''_{im}|^2$

where Z'_{re} and Z''_{im} are the real and imaginary components of the impedance.

The phase angle ϕ can be expressed as,

$$\phi = \text{Arc tan} \quad = \text{Arc tan} \quad \frac{Z_{im}}{Z_{re}} \quad \text{and} \quad \frac{Z''(\omega)}{Z'(\omega)}$$

Z_{re} or $Z'(\omega) = |Z|\cos\phi$; Z_{im} or $Z''(\omega) = |Z|\sin\phi$

An equivalent circuit for a diffusion controlled electron transfer reaction (Randles equivalent circuit) is shown in Fig. 3b. The components of the circuit are solution resistance, R*s*, double layer capacitance C_{dl}, the charge transfer resistance, R_{ct} and the Warburg impedance Z_W.

The total current on the working electrode is obtained by the sum of the individual contributions of the Faradaic current I_f and the double layer charging current I_c. The charges at the electrode|electrolyte interface contribute to the double layer capacitance. The double layer structure closely is analogous to a pure capacitor and hence it is denoted by C_{dl} in the equivalent circuit. The Faradaic impedance Z_f had two components namely, the charge transfer resistance, R_{ct} and the Warburg impedance, Z_W. While, the resistance offered to the electron transfer is given by charge transfer resistance (R_{ct}), the impedance to the diffusion of the redox probe is given by the term Z_W.

The Warburg impedance is small at high frequencies due to the fact that the reactants do not have to diffuse very far away from the interface. However, at low frequencies, the diffusing reactants have to move very far towards or away from the interface during each cycle and hence the Warburg impedance is very high at these frequencies. The uncompensated solution resistance denoted by R*s* exists between the working electrode and the reference electrode. In the equivalent circuit representation, the uncompensated solution resistance, R_s (existing between the working and the reference electrodes) is inserted as a series element since all

the current has to pass through this element. For a planar diffusion, the value of R_{ct} is given by,

$$R_{ct} = \frac{RT}{nFI_0}$$

where I_0 is the exchange current density.

The solution resistance R_s is expressed as,

$$R_S = \frac{x}{\kappa A}$$

where x is the distance of the capillary tip from the electrode, κ is the conductivity of the solution and A is the area of the electrode.

The relative magnitude of R_{ct} and Z_W at any frequency is a measure of the balance between kinetic and diffusion control. If I_o is very large, $R_{ct} \rightarrow 0$ and will be too small to measure so that only Z_W will be observed. In other case, a very sluggish electrochemical reaction will have very high value of R_{ct} which will be dominant compared to Z_W. The total analysis of the impedance is known as complex plane impedance analysis. Randles equivalent circuits are used for the representation of the elements involved in the circuits which are series and parallel combination of the different elements like capacitors and resistors. This has two limiting cases.

At low frequencies, as $\omega \rightarrow 0$, the real and imaginary parts of impedance are given by,

$$Z' = R_s + R_{ct} + \sigma\omega^{-1/2}$$

$$Z'' = \sigma\omega^{-1/2} + 2\sigma^2 C_{dl}$$

Where

$$\sigma = \frac{RT}{\sqrt{2}n^2F^2\sqrt{D}A}\left(\frac{1}{C_O} + \frac{1}{C_R}\right)$$

in which, D is the diffusion coefficient of the species in solution, A is the area of the electrode, C_0 and C_R are the bulk concentrations of the oxidised and reduced species. On rearranging these equations, we get,

$$Z'' = Z' - Rs - R_{ct} + 2\sigma^2 C_{dl}$$

$$Z'' = Z' - [Rs + R_{ct} - 2\sigma^2 C_{dl}]$$

This corresponds to an equation of a straight line of unit slope. The intercept on the real $Z^{'}$ axis is given by $R_s + R_{ct} - 2\sigma^2 C_{dl}$.

At high frequencies where the Warburg impedance is negligible in comparison to R_{ct}, the two components are represented by,

$Z^{'} = R_S + R_{ct} / (1+\omega^2 R^2_{ct} C^2_{dl})$ and

$Z'' = C_{dl} R^2_{ct} \omega / (1+\omega^2 R^2_{ct} C^2_{dl})$

Eliminating ω from these two equations gives,

$$(Z' - R_s - R_{ct}/2)^2 + (Z'')^2 = (R_{ct}/2)^2$$

which is the equation of a circle with centre at $Z' = Rs + R_{ct}/2$ and a radius of $R_{ct}/2$. A plot of the whole expression for Z' verses Z", which is known as Cole-Cole plot or a Nyquist plot, for a kinetically controlled and a diffusion controlled reactions are shown in the Fig. 4. For a charge transfer controlled reaction, the plot of Z' and Z" at different frequencies (Cole-Cole plot) gives a semicircle.

At infinite frequency, the capacitance in the equivalent circuit offers a very little impedance and hence Z" approaches zero. At low frequencies, the impedance is purely resistive, because the reactance of C is very large. The real axis value at the high frequency intercept corresponds to R_s. The maximum value of Z" in the semicircular region where $\omega = 1/R_{ct} C_{dl}$ gives the value of C_{dl}. The diameter of the semicircle provides the value of R_{ct}. The Warburg impedance term observed for a diffusion-controlled reaction, varies inversely with frequency.

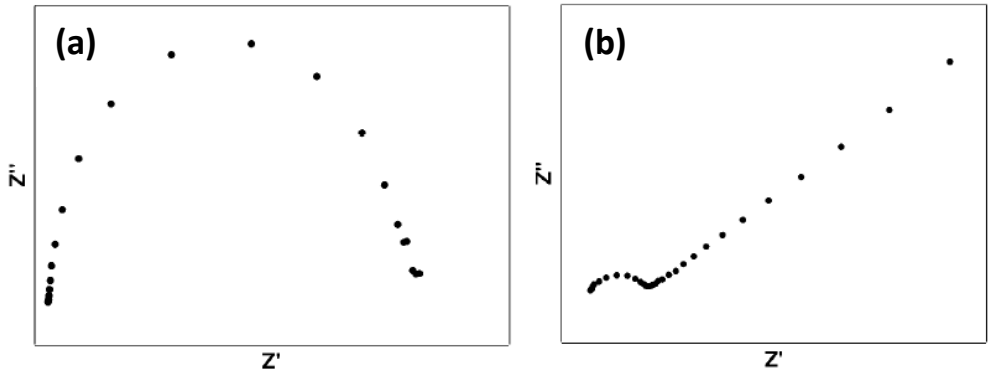

Figure 4. *Nyquist plots for a) kinetically controlled reaction and b) diffusion controlled reaction*

At very low frequencies, Z_w increases and dominates and gives a straight line with a phase angle of 45°.

A plot of logarithm of the modulus of impedance plotted against frequency is known as Bode plot. The plot also has the phase angle component in the y-axis. Thus information regarding the magnitude and phase angle at a frequency can be obtained from a Bode plot. A resistor and capacitor are associated with a phase angles of 0° and 90°, as mentioned earlier. Therefore the Bode plot for a pure resistor and capacitor is characterized by a horizontal line and straight line of unit slope respectively.

A phase sensitive detection method was employed for the measurement of the impedance of the electrochemical cell above 5 Hz using a single-sine technique that provides the highest accuracy. Below 5 Hz, the measurement of impedance was performed using a fast Fourier transform technique based on multi sine experiments that avoids any drift or change in the impedance value of the electrochemical system. The potential of the working electrode is held at a desired DC potential of interest using a potentiostat. A small amplitude of sinusoidal ac voltage with 5-10 mV peak-to-peak is applied to the cell from a lock-in amplifier. The lock-in amplifier measures the phase difference of the current output with respect to the input voltage and the amplitude of the current response, which can be converted to the real and imaginary part of the impedance.

2.4.3. Chronopotentiometry

In chronopotentiometry, an instantaneous current step is applied across an electrochemical to a finite value and the potential at the working electrode is monitored continuously as a function of time. The potential response as a function of time known as chronopotentiogram is shown in Fig. 5. The characteristics of the chronopotentiogram can be explained by considering the concentration profiles of the redox species as a function of time.

Consider the electron transfer reaction

$$O + ne^- \rightleftharpoons R,$$

The initial potential is the rest potential or the open circuit potential (E_{OCP}). Once the (reducing) current step has been applied, there is an initial sharp decrease in the potential due

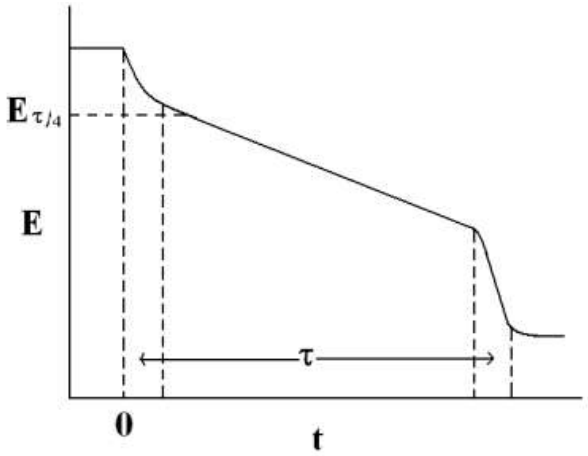

Figure 5. *Schematic diagram of a chronopotentiogram for a reversible system*

to the charging of the double layer capacitance. This continues until a potential at which the species O is reduced to R is reached. Subsequently, a slow decrease in the potential determined by the Nernst equation, is observed until the surface concentration of O essentially reaches zero. Once the concentration of O at the electrode surface is zero, the reactant species O can no longer diffuse for the concentration gradient to the electrode surface to be maintained at the applied current. As a result, the electrode potential falls off sharply.

2.4.4. Chronoamperometry

Chronoamperometry is an electrochemical technique in which the potential of the working electrode is stepped and the resulting current from faradic processes occurring at the electrode (caused by the potential step) is monitored as a function of time. Fig. 6 shows the typical potential-time profile applied and the current response measured as a function of time. The current response of the electrochemical system can be explained by the Cottrell equation.

$$I = nFA\, c_o \sqrt{\frac{D}{\pi t}}$$

The initial sharp increase in current is due to the double layer charging. However

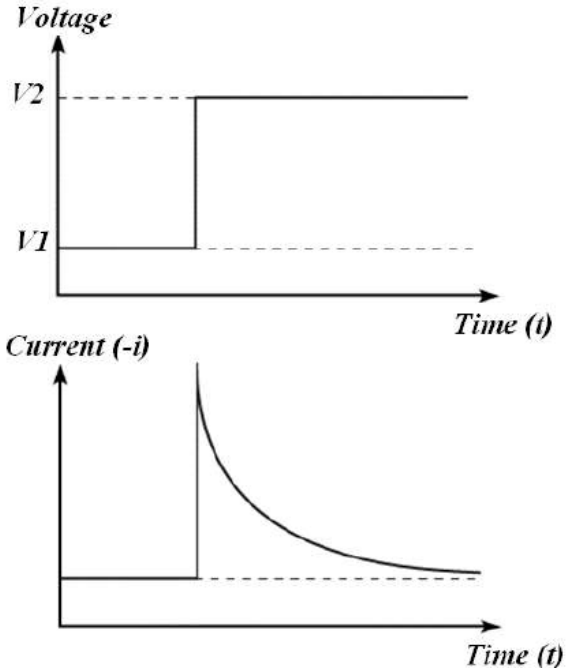

Figure 6. *Schematic representation of potential step applied during chronoamperometry*

the current is significant only during the initial period. Once the faradaic process begins, the current measurements and the response in terms of current as a function of time decreases with time as a function of $1/t^{1/2}$ due to its dependence on concentration gradient. In this work, chronoamperometry was used to calculate currents at different overpotentials to carry out Tafel analysis of the electrocatalytic reactions on the materials prepared.

2.4.5. Tafel plot analysis

A plot of logarithmic current density Vs overpotential is known as Tafel plot (Fig. 7). The overpotential is defined as the deviation of applied potential from the equilibrium potential. While the slope of the lines obtained from the Tafel slopes indicates the rate determining step involved in the process, the intercept gives the value of the exchange current density. Tafel analysis is usually carried out extensively in corrosion studies and in electrocatalysis. In our studies, Tafel studies were performed only for the evaluation of electrocatalysts. In general, it is always desirable to have a low value of the Tafel slope to achieve high electrocatalysis currents at low overpotentials. Therefore the electrocatalytic activity of different materials can be compared from their respective Tafel slope

values. The value of the Tafel slopes hints at the rate determining step and reaction mechanism in the hydrogen and oxygen evolution reactions. In the case of alcohol oxidation reaction, Tafel slopes give a measure of the extent of poisoning by carbonaceous impurities on the electrocatalysts during the reaction [4-6].

The general form of the Tafel equations, are given as follows:

For a cathodic reaction,

$$\log |I| = \log I_0 - \alpha_C \, n \, F\eta / 2.303 \, RT$$

while for an anodic reaction,

$$\log |I| = \log I_0 + \alpha_A \, n \, F\eta / 2.303 \, RT$$

where I is the total current density, I_0 is the exchange current density, α_C and α_A are the respective cathodic and anodic Tafel slopes and η is the overpotential.

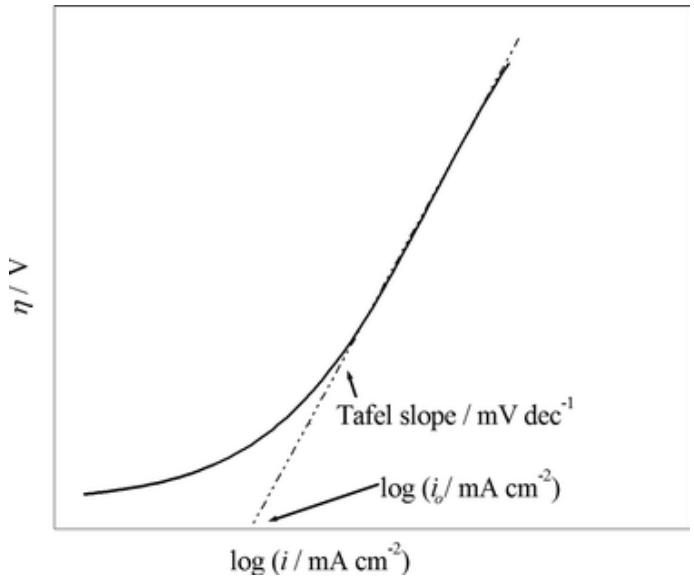

Figure 7. *Tafel plot for an anodic process*

2.5. Scanning electron microscopy (SEM)

The morphological characterization of the electrodeposited nanoparticles was carried out by FESEM. The scanning electron microscope (SEM) uses a focused beam of high-energy electrons to generate a variety of signals at the surface of

solid specimens. The signals that derive reveal information about the sample including external morphology (texture), chemical composition, and crystalline structure and orientation of materials making up the sample.

Highly accelerated electrons generated in an SEM carry significant amounts of kinetic energy. Once the incident electrons are decelerated into the solid sample, this energy is dissipated as a variety of signals produced by electron-sample interactions. These signals include secondary electrons, backscattered electrons (BSE) and photons and heat. Secondary electrons and backscattered electrons are useful for imaging samples. While secondary electrons give essential information on morphology and topography of the samples, the backscattered electrons illustrate contrasts in composition in multiphase samples. In our experiments, SEM images and EDAX were recorded with Zeiss (Ultra plus) field emission scanning electron microscope (FESEM).

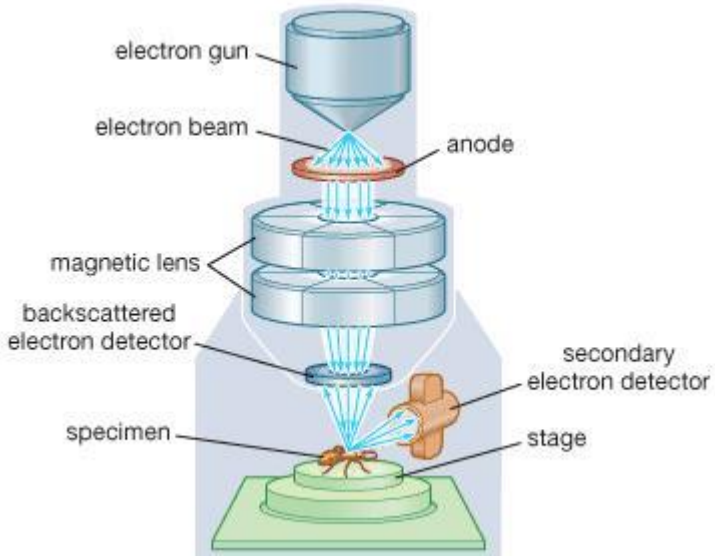

Figure 8. *Schematic representation of a SEM*

Components of SEM

A schematic representation of SEM is given in Fig. 8. The electron gun generates a beam of electrons using a thermal emission source such as a tungsten tip. In conventional thermionic emitters evaporation of cathode material and thermal drift during operation are the major problems which cause less contrast in the images. Recently, FESEM is being increasingly used owing to their better spatial resolution than SEM. In FESEM, a field emission source called cold cathode field

emitter which is not associated with heating is used. The energy of the incident electrons can be as low as 100 eV or as high as 30 keV depending on the evaluation objectives.

The electrons are attracted through the anode and are then focused into a small beam by a series of electromagnetic lenses in the SEM column. Scanning coils near the end of the column direct and position the focused beam onto the sample surface. The electron beam is scanned in a raster pattern over the surface for imaging. The beam can also be focused at a single point or scanned along a line for x-ray analysis. The beam can be focused to a final probe diameter as small as about 10 Å. Finally, when the beam hits the sample surface, the electron signals produced are collected by the secondary electron detector or the backscatter detector. Any interaction of the electron beam with the other gaseous molecules would result in the lower contrast images. To avoid this problem, SEM is usually carried out in vaccum. Besides the imaging features, SEM can also be used for the elemental analysis of the sample.

This is achieved by analysing the X-rays emitted from the sample when the sample is exposed to electron beam. Since every element is associated with a distinct atomic structure, the X-rays characteristic of the element's atomic structure varies from one another.

2.6. Spectroscopy and other techniques

2.6.1. UV spectroscopy

UV spectroscopy is a type of absorption spectroscopy in which light of certain frequency in the ultra-violet region (200-400 nm.) is absorbed by the molecule. Absorption of the ultra-violet radiations results in the excitation of the electrons from the ground state to higher energy state. The energy of the ultra-violet radiation that are absorbed is equal to the energy difference between the ground state and higher energy states.

Nanoparticles have optical properties that are sensitive to size, shape, concentration, agglomeration state, and refractive index near the nanoparticle surface, which makes UV/Vis spectroscopy a valuable tool for identifying, characterizing, and studying these materials. Nanomaterials of silver and gold are

characterized by absorption maximum in the range of 400 nm and 500 nm respectively depending on the size.

2.6.2. Raman Spectroscopy

Raman spectroscopy provides information about molecular vibrations that can be used for sample identification and quantitation. The technique involves shining a monochromatic light source (i.e. laser) on a sample and detecting the scattered light. The majority of the scattered light is of the same frequency as the excitation source; this is known as Rayleigh or elastic scattering. A very small amount of the scattered light is shifted in energy from the laser frequency due to interactions between the incident electromagnetic waves and the vibrational energy levels of the molecules in the sample. Plotting the intensity of this "shifted" light versus frequency results in a Raman spectrum of the sample. The band positions will lie at frequencies that correspond to the energy levels of different functional group vibrations. The Raman spectrum can thus be interpreted similar to the infrared absorption spectrum. As in infrared spectroscopy, band areas are proportional to concentration, making Raman amenable to quantitative analysis.

Surface enhanced Raman spectroscopy

The signals obtained by Raman scattering are usually weak. Under normal conditions, the intensities of the Raman scattered peaks are only 0.001% of the incident light. Therefore it is extremely difficult to attain a Raman spectrum of a sample at a very small concentration. This limitation can be overcome by employing methods to enhance the signal. One such method of enhancing the scattering signal is to adsorb the analyte sample onto a certain rough metal surfaces such as Ag and Au (Fig. 9) [7]. This method of enhancing the Raman signal is known as surface enhanced Raman spectroscopy (SERS).

The mechanism of signal enhancement is explained by two theories

Electromagnetic enhancement theory

It is known that an incident laser light generates surface plasmons on the rough metallic surface. The generation of surface plasmons greatly enhances the electromagnetic field near the metal surface. This would enhance the strength of Raman scattered light [8].

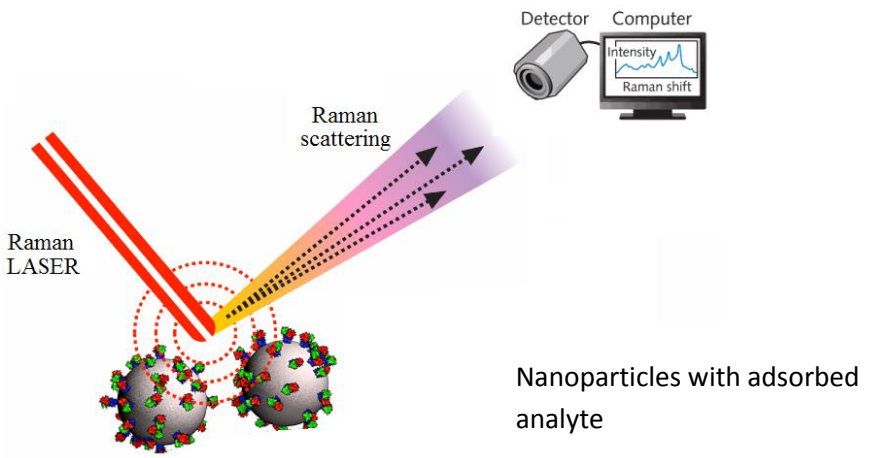

Figure 9. *Schematic representation of the SERS phenomena*

Chemical enhancement theory

By this theory, the enhancement of the Raman signal is brought by a charge-transfer between the metal and the analyte which result in an increase in the polarisability of the molecule. Therefore, for a chemical enhancement to occur, a surface complex between the analyte and the metal must form. As a result of the formation of the complex new electronic states arise, which serve as new resonant intermediate states in Raman scattering. This would lower the energy requirements for the molecule to be excited, thereby Raman scattering occurs more readily and signal enhancement occurs.

SERS substrates

SERS is carried out on metallic surfaces with roughness of the order of 10-100nm. Such rough surfaces are obtained by sputtering of metal onto a substrate, electrochemical roughening by repeated reduction – oxidation cycles. Colloidal solutions of metal nanoparticles are also used as SERS after the solutions are dropcast and dried on glass slides. Though studies till date have shown several metals exhibiting SERS characteristics, silver and gold are the most commonly used metals.

2.7. X-ray diffraction

X-ray powder diffraction (XRD) is a rapid analytical technique primarily used for phase identification of a crystalline material and can provide information on unit cell dimensions. Diffraction occurs when X-rays interact with a regular structure whose repeat distance is about the same as the wavelength of X-rays. The X-rays scattered from a crystalline solid constructively interfere to produce a diffracted beam. In a crystalline sample, the wavelength of an electromagnetic radiation is related to the diffraction angle and the lattice spacing by Bragg's law

$$n\lambda = 2d\sin\theta$$

where, λ is the wavelength of the X-ray used, d is the distance between two crystal planes and q is the scattering angle. The schematic representation of this law is shown in the Fig. 10.

In our studies, XRD studies were used mainly in the characterization of the metal nanoparticles. Information on the phase composition, crystallite size and crystallographic orientation can be obtained from the XRD of the nanoparticle. The Scherrer equation relates the size of crystallites in a solid to the broadening of a peak in a diffraction pattern.

$$d = \frac{0.9\,\lambda}{\beta\cos\theta}$$

d is the crystallite size, λ is wavelength of the radiation, θ is the Bragg's angle and β is the full width at half maximum of the broadened peak.

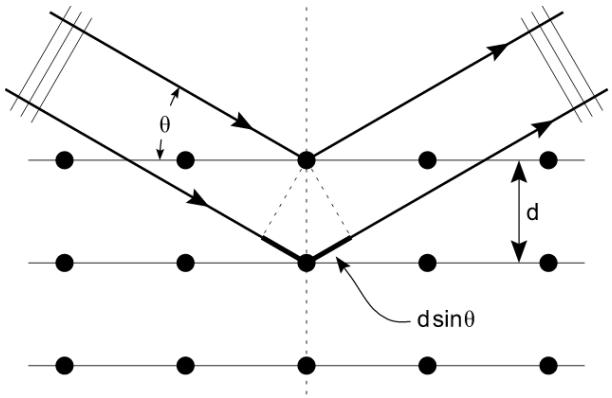

Figure 10. *Schematic representation of the scattering of X-ray leading to the Bragg's law*

References

1. C. D. Agostino, R. C. Harris, A. P. Abbott, L. F. Gladden and M. D. Mantle, *Phys. Chem. Chem. Phys.*, 2011, **13**, 21383.

2. A.J. Bard and L. R. Faulkner, *Electrochemical Methods Fundamentals and Applications*, John Wiley and Sons, Noida, 2nd edn., 2004.

3. R. Greef, R. Peat, L. M. Peter, D. Pletcher and J. Robinson, *Instrumental Methods in Electrochemistry*, Ellis Horwood Ltd., Chichester, Great Britain, 1990.

4. W. Chrzanowski and A. Wieckowski, *Langmuir*, 1998, **14**, 1967.

5. J.O'M. Bockris, *J. Serb. Chem. Soc.* 2005, **70**, 475.

6. Z. X. Liang, T. S. Zhao, J. B. Xu and L. D. Zhu, *Electrochim. Acta*, 2009, **54,** 2203.

7. M. Fleischmann, P. J. Hendra and A.J. McQuillan, *Chem. Phys. Lett.*, 1974, **26,** 163.

8. M. S. Johal, Understanding Nanomaterials, CRC Press, Boca Raton Florida, 2011.

CHAPTER 3

Electron transfer studies of some redox active species (cationic, anionic, neutral) in Deep Eutectic Solvents (DES)

3.1. Introduction

Ionic liquids and deep eutectic solvents (DES) are recently being used as novel electrolytic media as they possess inherent ionic conductivity, wide electrochemical potential window and excellent solubilizing properties. Because of these advantages DES has already found wide ranging applications as a media for metal finishing/plating, nanoparticle synthesis, organic reactions, biocatalysis and enzymatic studies. In spite of considerable work in the above aspects, electron transfer and transport properties of redox species in DES, have not been fully explored. The electrochemical behavior of DES differs considerably from the conventional molecular solvents due to their high viscosity and the ionic composition. While the viscosity affects the mass transport properties of the medium, the ionic composition can influence the redox potentials of electroactive species. A detailed study on the mechanistic aspects in these solvents, therefore will be advantageous for applications involving electron transfer processes. In this chapter, the redox potentials and diffusion characteristics of a set of standard redox species in DES medium are studied by cyclic voltammetry and electrochemical impedance spectroscopy. The shifts in the peak potentials of redox species in DES *wrt* aqueous medium are analyzed based on possible solvation models.

The viscosity of DES varies between 37- 6000 cP depending upon the size and hydrogen bonding nature of the DES components. The diffusional properties of solutes in the medium are significantly affected by the high viscosity. The conventional theories on the diffusion of redox species in an electrolytic medium are often valid only for molecular solvents. The experimental values of diffusion coefficients have also been reported to deviate significantly from the predicted values. The deviations are due to the fact that the diffusing species are in concentrated ionic solutions, a situation much different from that of molecular solvents. The excess ions also exhibit significant ion-ion interactions against the assumptions of non-interacting solvents in theory. Abbott *et al.* used the hole theory to explain the viscosity and diffusion of ions in DES [1]. According to this theory, ionic transport occurs only when the size of the diffusing ions match the holes within the solvent structure. Till date, only the diffusion coefficients of

ferrocene methanol and $Cu^{+/2+}$ have been reported in DES [2,3]. Ionic liquids resemble closely with the DES, in terms of ionic composition and high viscosity and hence the results of diffusion coefficient measurements of redox species in ionic liquids are relevant to understand the mass transfer properties in DES. The diffusion coefficients of redox species in ionic liquids are typical in the range of 10^{-8} - 10^{-7} cm^2/s, which is two to three orders smaller than that of 10^{-4}-10^{-5} cm^2/s in molecular solvents [4].

The solvation mechanism of redox species in DES and ionic liquids are quite different from that normally observed in molecular solvents. The knowledge of the solvation mechanism in DES is essential to understand the redox behavior of electroactive compounds in their electrolytic medium. The Marcus theory on electron transfer processes is based on the reorganization of solvent dipoles. However in the case of ionic liquids/DES, the solvent species is constituted entirely of anions and cations. The solvent reorganization in ionic liquids occurs by ionic translation unlike the solvent dipole reorientation in molecular solvents. Therefore in the case of ionic liquids, the self-diffusion of ions/molecules plays a more significant role in the reorganization process. A model of the solvation structure of a charged species in molecular solvents and ionic liquids is depicted in scheme-1.

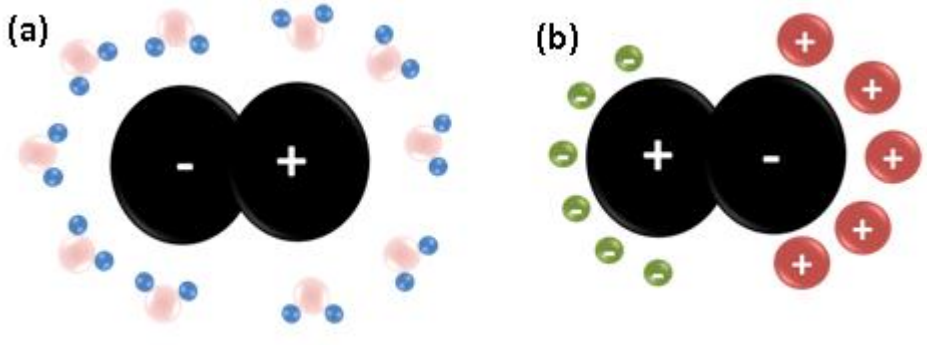

Scheme 1. *Solvation structure of a charged species in (a) polar molecular solvents (b) ionic liquids*

The differences in the solvent reorganization mechanism in DES are expected to cause drastic shifts in the redox potentials of electroactive species *wrt* that observed in molecular solvents. The redox potential is a direct measure of the thermodynamic feasibility of an electrochemical process. The free energy changes

(ΔG°) associated with the redox process is related to the redox potential (ΔE°) by the equation,

$$\Delta G^\circ = -nF\,(\Delta E^\circ) \qquad (1)$$

The changes in the free energy associated with a redox reaction are obviously affected by the solvation structure of the redox species by the solvent. The reduction and oxidation processes are accompanied by solvent reorganizations causing entropy/enthalpy changes. The shift in redox potential depends on the extent of the reorganization which in turn depends on the ability of the oxidized/reduced complex to make/break the solvation structure. The solvation in aqueous medium is associated with drastic changes in entropy due to the fact that a redox process involving changes in the charge of the redox species often disrupts the highly ordered solvation structure of water molecules. As compared to aqueous medium, organic solvents, ionic liquids/DES have much less ordered structure and hence free energy changes associated with redox reactions in organic solvents are significantly lower [5].

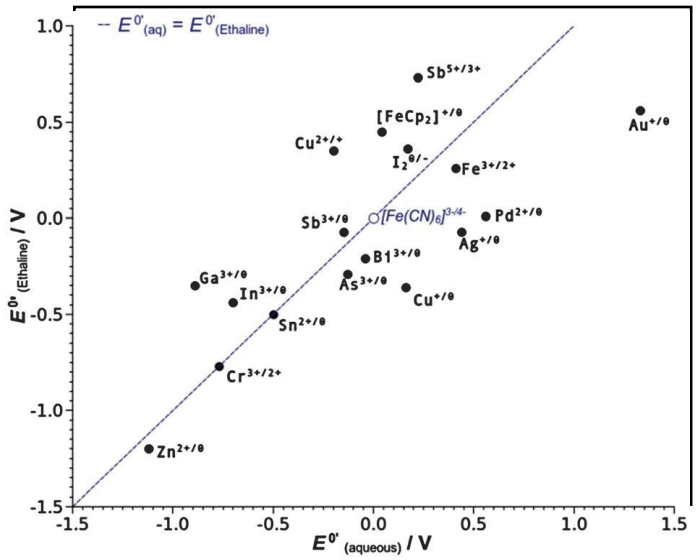

Figure 1. *Electrochemical series for metallic redox couples in a model deep eutectic solvent of ethaline* [6]

Abbott *et al.* established an electrochemical series for metallic redox couples in a model deep eutectic solvent of ethaline [6]. The electrochemical series hints at the preferential stabilization of an oxidation state of a redox species over another. The electrochemical series proposed in DES is given in Fig.1. The higher oxidation state of the redox species spotted above the line of equivalence is better stabilized relative to the lower oxidation state. The variations in the electrochemical behavior of redox species in DES *wrt* aqueous medium was attributed to the speciation effects in the high chloride medium of DES. A detailed study on the shift in redox potentials observed in DES based on the differences in solvation structure has not been carried out till date.

3.2. Experimental

3.2.1. Materials

Potassium ferrocyanide (Loba), potassium ferricyanide (Qualigens), hexaammineruthenium (II) and (III) chloride (Alfa Aesar) ferrocene (Acros Organics), ferrocenium tetrafluoroborate (Aldrich), ferrocene methanol (Aldrich), methyl viologen (Aldrich) were used as received without further purification.

The DES used as medium for the electrochemical studies of redox species were prepared from the components choline chloride and urea / ethylene glycol. The hydrogen bond donors for the preparation of DES, viz., ethylene glycol and urea from Merck were used as received.

Millipore water having a resistivity of 18 MΩ cm was used for the preparation of aqueous solutions of redox species with potassium chloride (Merck) as supporting electrolyte. The electrochemical studies of hydrophobic redox species were done in propylene carbonate (Spectrochem) with Tetrabutylammonium tetrafluoroborate (Alfa Aesar) as supporting electrolyte.

3.2.2. Electrode pretreatment

A gold disc electrode of diameter 1mm (CH instruments) was polished with 1µm, 0.3 µm, and finally 0.05 µm alumina slurries, and cleaned thoroughly with water. Further, the disc electrode was cleaned in Piranha solution and washed in water.

3.2.3. Electrochemical studies

The cyclic voltammetric studies were performed with a three electrode system, Ag/AgCl/3M NaCl (reference electrode), gold disc electrode (working electrode) and Platinum foil (counter electrode). The electrochemical cell of capacity 10 ml was maintained at specific temperatures for kinetic studies using Julabo temperature control systems (F25). All the cyclic voltammetric plots shown in the chapter corresponds to the second cycle of the cyclic voltammetric scan.

The impedance measurements were carried out over a wide frequency range from 100 mHz to 100 kHz and at an AC amplitude of 10 mV. The ac signal was applied to the electrochemical cell containing redox species maintained at the half peak potential (dc) of the redox species. The electrochemical impedance spectroscopy data was analysed using Zman 3.2 software.

3.3. Results and Discussions

3.3.1. Cyclic voltammetric studies

Cyclic voltammetric studies of some of the common redox probes were carried out in DES and molecular solvents such as water and propylene carbonate. The electrochemical characteristics observed in both the cases were compared and analyzed thoroughly. The redox species that are distinct in terms of its charge (positive, negative or neutral) and hydrophilicity / hydrophobicity were selected for the studies. Prior to the addition of redox species, cyclic voltammetric scan of the medium was done in different electrochemical potential ranges to ensure the absence of any redox processes. The cyclic voltammetric behaviour in the

medium exhibits the normal capacitive features (Fig.2). In the following sections, the changes observed in the electrochemical features (viz., peak potential, peak current) of the redox species as the medium changes from a molecular solvent to a DES will be discussed.

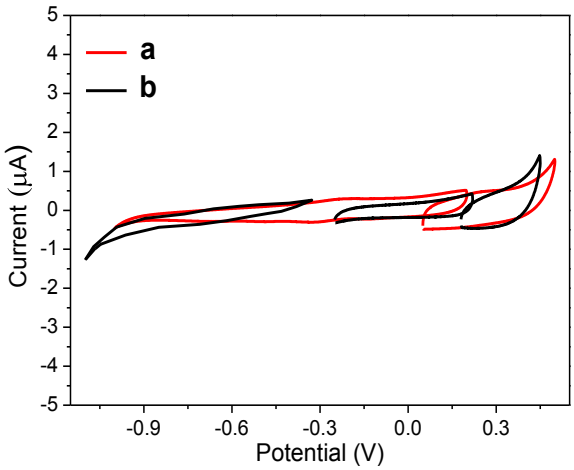

Figure 2. *Cyclic voltammograms of blank (a) reline (b) ethaline carried out in different potential ranges at a scan rate of 20 mV/s*

3.3.1.1. Anionic complex [Ferrocyanide/Ferricyanide System]

$$[Fe(CN)_6]^{4-} \underset{+e^-}{\overset{-e^-}{\rightleftharpoons}} Fe(CN)_6]^{3-}$$

The cyclic voltammogram of $[Fe(CN)_6]^{4-/3-}$ is displayed in the Fig. 3 corresponds to a scan rate of 20mV for an analyte concentration of 5mM. It can be observed from the cyclic voltammogram that the peak currents decrease significantly as the solvent medium changes from aqueous to DES. Both the peak potentials corresponding to the redox process in aqueous medium are shifted to more negative potentials in DES medium.

Discussion on shift in half peak potential of $[Fe(CN)_6]^{4-/3-}$

The redox couple $[Fe(CN)_6]^{4-/3-}$ is highly stable in a chloride rich medium as that of DES. Owing to this Abbott *et al.* utilized the system as an internal reference standard in the calculation of electrochemical series [6]. It is evident from Table

3.1 that the half peak potentials of $[Fe(CN)_6]^{4-/3-}$ in reline as well as ethaline differ only by 12 mV. The half peak potential ($E_{1/2}$) in the DES medium is considerably negative than that observed in an aqueous medium by about 192mV.

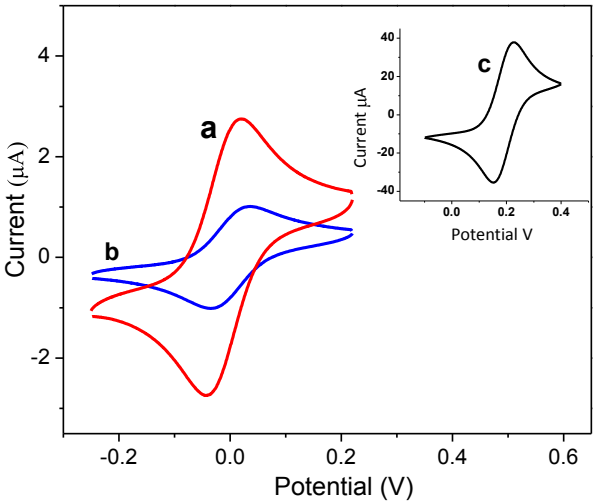

Figure 3. *Cyclic voltammogram of 5 mM* $Fe[(CN)_6]^{4-/3-}$ *in a)ethaline (b)reline (c)aqueous medium/0.1M KCl at a scan rate of 20 mV/s*

The more positive redox potential in aqueous medium indicates that the reduced species $[Fe(CN)_6]^{4-}$ is better stabilized than the oxidized species $[Fe(CN)_6]^{3-}$ making the oxidation process difficult. The drastic reduction in the redox potential of $[Fe(CN)_6]^{4-/3-}$ in DES is brought about by the nature of the solvation

Table 1. *Anodic and cathodic peak potentials (E^p_a and E^p_c), peak separation (ΔE_p), half-peak potentials ($E_{1/2}$) and peak currents (i^p_a and i^p_c) for the 5 mM* $[Fe(CN)_6]^{4-/3-}$ *redox reaction*

Solvent medium	$\mathbf{E^P_a}$ **mV**	$\mathbf{E^P_c}$ **mV**	$\mathbf{\Delta E_p}$ **m V**	$\mathbf{E_{1/2}}$ **mV**	$\mathbf{i_a^p}$ **μA**	$\mathbf{-i_c^p}$ **μA**
Ethaline	18.4	-40.9	59.3	-11	2.76	2.72
Reline	33	-32	65	1	1.02	1.01
Aqueous	222	155	67	189	37.9	35.2

medium which is markedly different in DES compared to that in aqueous medium. The charges of the redox complex are also expected to cause differences in the hydrogen bonding interaction with the solvent. Hence, in order to understand the differences in the solvation features, separate FTIR studies of $[Fe(CN)_6]^{4-}$ and $[Fe(CN)_6]^{3-}$ were carried out in DES as well as in aqueous media. The aim of the study is to correlate the shift in individual FTIR bands of $[Fe(CN)_6]^{4-}$ and $[Fe(CN)_6]^{3-}$ in the solvent to the preferential solvation of one oxidation state over the other.

Yu *et al*. has compared the solvation and hydration dynamics of cyanoferrate anions ($[Fe(CN)_6]^{4-}$ and $[Fe(CN)_6]^{3-}$) by ultrafast infrared spectroscopy [7]. The results obtained from the frequency-frequency correlation function extracted from the 2D IR spectra indicate that hydration shell interacts well to the ferro- species than to the ferri-species and hence the hydration shell of the former is more tightly bound to the -C≡N than the latter. The linear IR spectra of C≡N stretch of $[Fe(CN)_6]^{4-}$ and $[Fe(CN)_6]^{3-}$ carried out in the study appears at 2039 cm^{-1} and 2115 cm^{-1} respectively. The relative shift in the C≡N stretching band was attributed to the excessive hydrogen bonding interactions of C≡N ····· HOH in the $[Fe(CN)_6]^{4-}$ species. Fig. 4 shows the FTIR studies of $[Fe(CN)_6]^{4-}$ and $[Fe(CN)_6]^{3-}$ carried out in water.

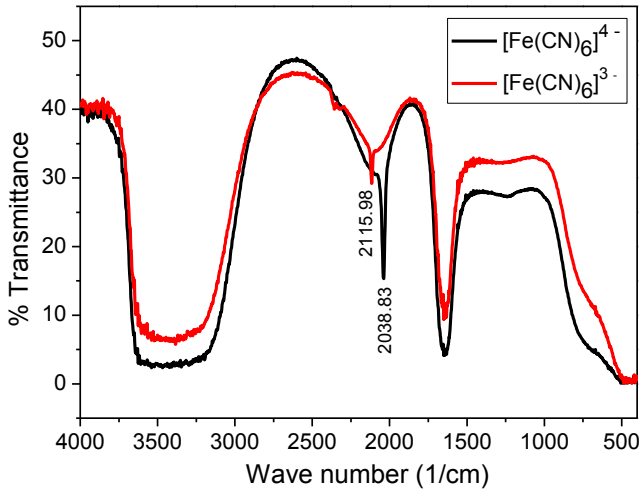

Figure 4. *FTIR spectra of $[Fe(CN)_6]^{4-}$ and $[Fe(CN)_6]^{3-}$ in water*

The ionic hydrogen bond length of N ····· H was found to be shorter in the ferro species than in the ferri species. The hydrogen bonding stabilization energy of $[Fe(CN)_6]^{4-}$ and $[Fe(CN)_6]^{3-}$ in water was found to be -10.4 and -6.9 kcal/mol respectively [7]. These results from the FTIR studies clearly give important indications to the electrochemical redox potentials observed in cyclic voltammetry. The preferential hydrogen bonding interactions of $[Fe(CN)_6]^{4-}$ over $[Fe(CN)_6]^{3-}$ in water implies that the reduced form is preferred in aqueous medium and therefore requires excess applied positive potential for the electrochemical oxidation of the former. The electrochemical oxidation of the ferrocyanide species occurs at 189mV in aqueous medium as seen in Table 1.

The solvation features in DES are completely different from that observed in the aqueous medium. While the uniformly distributed molecular dipoles solvate the redox species in aqueous medium, in the case of DES, the solvation is brought

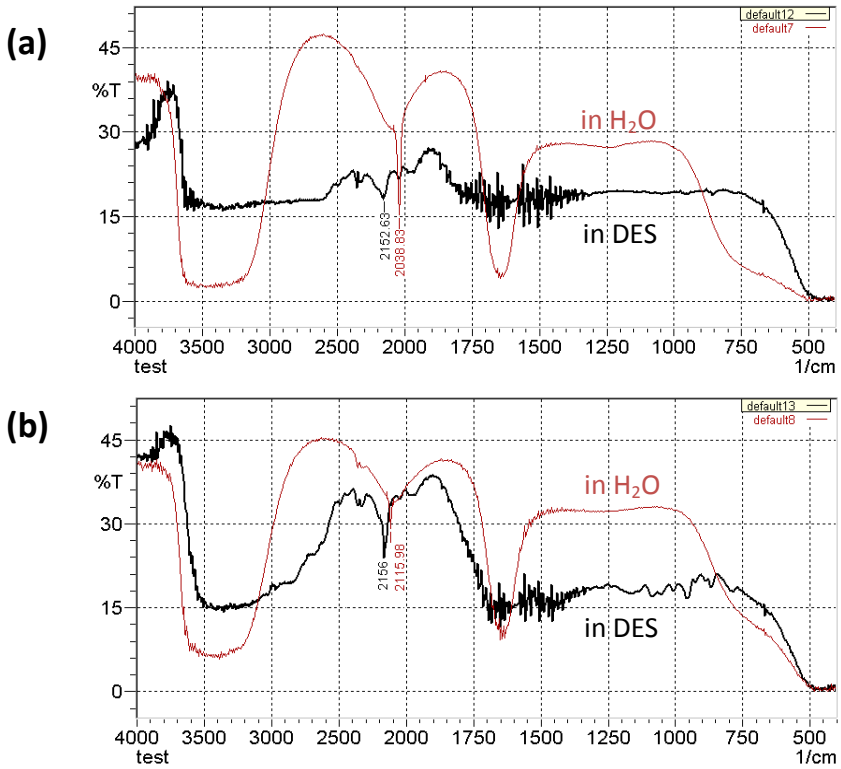

Figure 5. *A comparison of FTIR spectra of (a) $[Fe(CN)_6]^{4-}$ (b) $[Fe(CN)_6]^{3-}$ in water and DES*

about mainly by individual ions. In order to study the solvation features of $[Fe(CN)_6]^{4-/3-}$ in DES, FTIR studies of the same were carried out similar to that done earlier in aqueous medium. Reline medium prepared from choline chloride and urea was used as model system for FTIR studies. The linear IR spectra of C≡N stretch of $[Fe(CN)_6]^{4-}$ and $[Fe(CN)_6]^{3-}$ carried out in DES appears very close at 2152 cm^{-1} and 2156 cm^{-1} respectively (Fig. 5). This indicates that there is no preferential solvation of the ferro-species over the ferri-species in DES as being observed in the aqueous medium. Thus the electrochemical oxidation of $[Fe(CN)_6]^{4-}$ occurs at relatively lower potential than that observed in the aqueous medium. The results can be very well correlated to the redox peak potential of

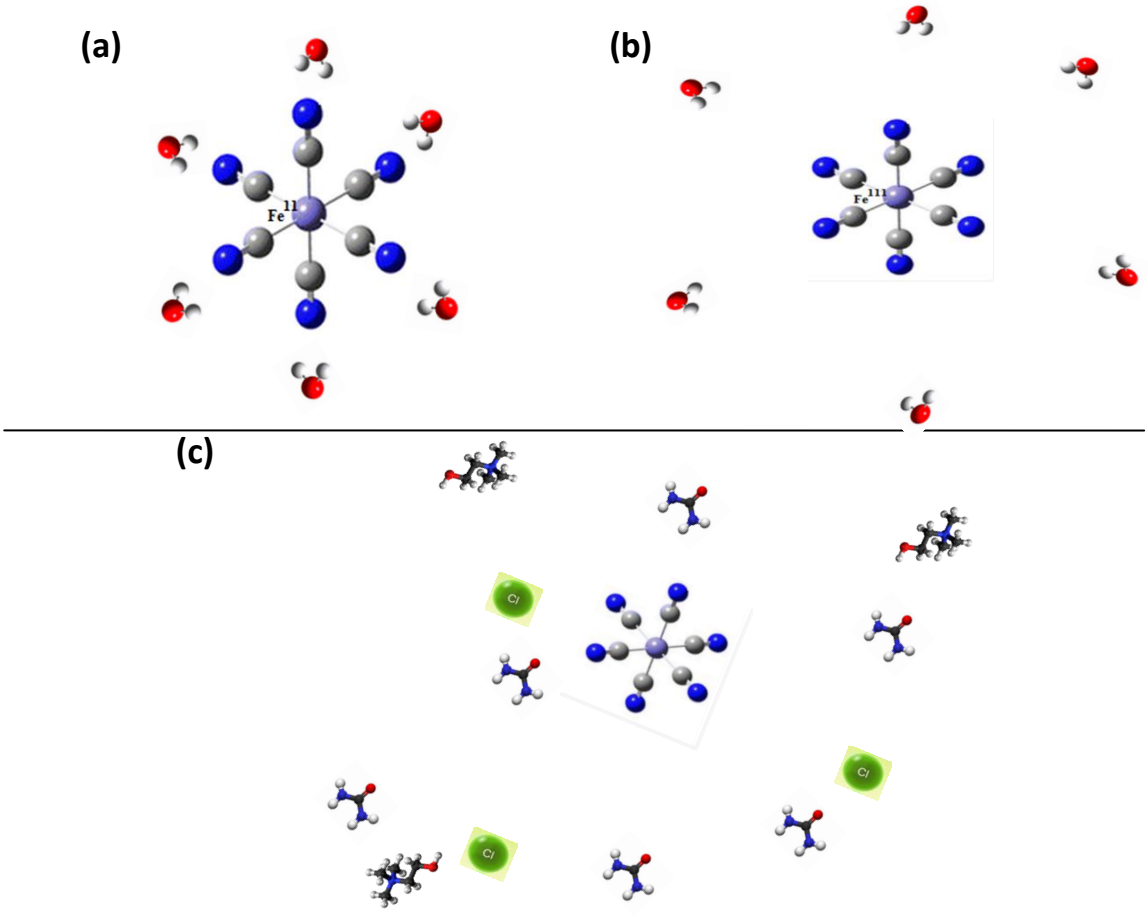

Scheme 2 *.Proposed solvation structure of (a)$[Fe(CN)_6]^{4-}$ (b))$[Fe(CN)_6]^{3-}$ in aqueous medium (c)$[Fe(CN)_6]^{4-/3-}$ in DES (model not to scale)*

$[Fe(CN)_6]^{4-/3-}$ which is ~190 mV lower in DES compared to aqueous medium. A pictorial representation of the probable solvation of the $[Fe(CN)_6]^{4-/3-}$ in aqueous medium and DES is depicted in scheme-2. An organized solvation shell can be seen in the aqueous medium which is tightly bound in $[Fe(CN)_6]^{4-}$ compared to $[Fe(CN)_6]^{3-}$ while in the case of DES, the ions are completely scattered around the redox species giving rise to a disorganized solvation pattern.

3.3.1.2. Cationic complex [Hexaammineruthenium (II / III) system]

$$[Ru(NH_3)_6]^{2+} \underset{+e^-}{\overset{-e^-}{\rightleftharpoons}} [Ru(NH_3)_6]^{3+}$$

Fig.6 shows the cyclic voltammograms of the positively charged complex $[Ru(NH_3)_6]^{2+/3+}$ in ethaline and reline. The inset shows the cyclic voltammogram of the same in aqueous medium. It can be observed that the change in the cyclic voltammetric features with the change in medium is identical to previous study. The peak potentials shift more negative ~100 mV *wrt* aqueous and also the peak currents in reline are almost halved *wrt* to ethaline. And again, the peak potential for the redox process does not shift significantly in reline or ethaline. The results are tabulated in Table 2.

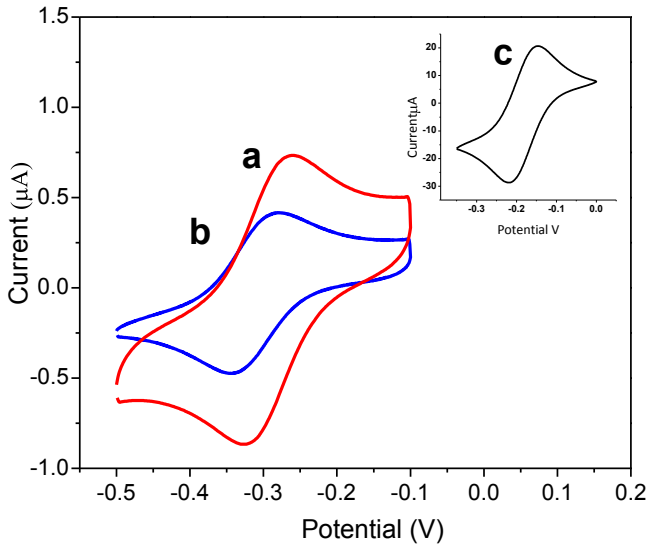

Figure 6. *Cyclic voltammogram of 5 mM* $[Ru(NH_3)_6]^{2+/3+}$ *in a)ethaline (b)reline (c) aqueous medium/0.1M KCl at a scan rate of 20 mV/s*

Table 2. *Anodic and cathodic peak potentials (E^P_a and E^P_c), peak separation (ΔE_p), half peak potential ($E_{1/2}$) and peak currents ($i_a{}^p$ and $i_c{}^p$) of [Ru $(NH_3)_6]^{2+/3+}$*

Solvent medium	$\mathbf{E^P_a}$ **mV**	$\mathbf{E^P_C}$ **mV**	$\mathbf{\Delta E_p}$ **m V**	$\mathbf{E_{1/2}}$ **mV**	$\mathbf{i_a{}^p}$ **µA**	$\mathbf{-i_c{}^p}$ **µA**
Ethaline	-262	-323	61	-292	0.74	0.87
Reline	-282	-344	62	-313	0.42	0.47
Aqueous	-149	-217	68	-183	20.7	28.7

Discussion on shift in half peak potentials of $[Ru(NH_3)_6]^{2+/3+}$

The redox potential of an electroactive species depends mainly on the reorganization energy, λ i.e., the energy required to change the structure of the reactants from that of equilibrium to that of the products. The reorganization energy is contributed by an inner sphere component, λ_i, and an outer sphere component, λ_o. While the inner sphere component is associated with the changing bond lengths and geometries within a molecule, the outer sphere component is concerned with the alignment of a polar solvent's dipole moments.

The electron exchange involved in the redox reaction $[Ru(NH_3)_6]^{2+/3+}$ in aqueous medium is considered to be extremely fast. The reorganization energy contribution to the fast redox reactions is expected to be mainly from the outer sphere component λ_o [8]. Brown *et al*. reported the free energy component of inner sphere (λ_i) and an outer sphere (λ_o) reorganization of the $[Ru(NH_3)_6]^{2+/3+}$ in water [9]. Thus the factors associated with the reorganization of the solvent dipoles plays a crucial role in the electron transfer reaction rather than the change in the bond lengths/geometry of the redox complex.

Yee *et al.* studied the nature of the ion-solvent interactions in terms of entropy factors associated with the solvent reorganization [10]. A large degree of solvent ordering is observed for the tripositive aqua complexes of Ru in aqueous medium

$[Ru(H_2O)_6]^{3+}$. Thus oxidation of Ru^{2+} causes a significant decrease in entropy (35 cal/ K/mole). In the case of $[Ru(NH_3)_6]^{3+}$, the weakly acidic ammine protons to form hydrogen bonds with surrounding water molecules to bring about solvent ordering. The entropy change in this case is found to be 18 cal/ K/mole. The decrease in entropy is lower in the case of $[Ru(NH_3)_6]^{2+/3+}$ compared to the aqua complexes due to the differential acidity of the aqua protons *Vs* ammine protons. This significant entropic cost involved in the oxidation of $[Ru(NH_3)_6]^{2+}$ increases the redox potential requirement for the process in the aqueous electrolyte vis-à-vis DES.

The solvation mechanism of redox species in ionic liquids and DES is quite

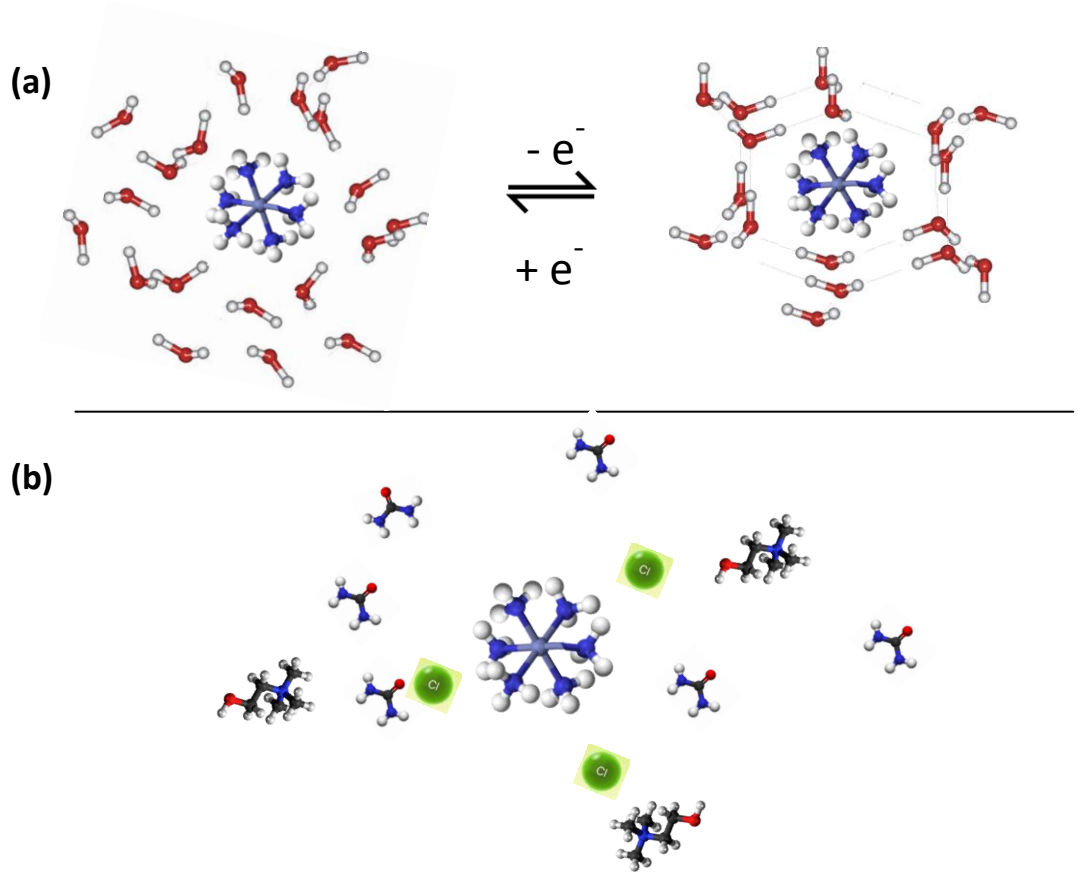

Scheme 3. *A pictorial representation of the (a) proposed solvation shell of* $[Ru(NH_3)_6]^{2+}$ *and* $[Ru(NH_3)_6]^{3+}$ *in aqueous medium (b) solvation of* $[Ru(NH_3)_6]^{2+/3+}$ *in DES (model not to scale)*

different from that observed in molecular solvents. The solvent reorganization energy in ionic liquids has been calculated to be lower than that observed in molecular solvents [11]. The components of DES comprising of hydrogen bonded anionic complex and a bulky choline cation does not form an organized solvation shell unlike the oriented molecular dipoles observed in molecular solvents (scheme-3). Thus there is no preferential solvation of the oxidized/reduced redox species and hence no significant changes in entropy on oxidation/reduction. The electrochemical oxidation of $[Ru(NH_3)_6]^{2+}$ in DES occurs at a more negative potential (-120 mV) compared to that in aqueous medium. The redox potentials of $[Ru(NH_3)_6]^{2+/3+}$ in reline is shifted more positive by just 20 mV *wrt* ethaline.

3.3.1.3. Neutral redox active species

(a) Ferrocene compounds

$$Fc^0 \underset{+e^-}{\overset{-e^-}{\rightleftharpoons}} Fc^+$$

Ferrocene (Fc), a neutral hydrophobic molecule with two cyclopentadienyl anions undergoes an one electron oxidation of its central metal ion Fe^{II} resulting in a ferrocenium (Fe^{III}) ion, which makes the compound polar and hydrophilic. The cyclic voltammetric studies of neutral redox species are studied here with some examples of ferrocene derivatives. Water soluble ferrocene derivative such as ferrocene methanol, FcMeOH and ferrocenium tetraflouroborate, $FcBF_4$ are also studied here. These compounds are chosen such that they are soluble and stable in both the DES media as well as in aqueous media. The trend observed in the shifts of the redox peak potentials of the neutral compounds Fc, $FcBF_4$ and FcMeOH in both the media is in contrast to that observed in the positive $[Ru(NH_3)_6^{2+/3+}]$ and negative $[Fe(CN)_6^{4-/3-}]$ charged complexes discussed earlier. For example, the half peak potentials of FcMeOH were observed to be more positive in DES by ~ 130 mV compared to that in aqueous medium (Table 3). The redox currents were found to be dependent on viscosity as seen before. The peak current which is more related to the viscosity characteristics of the medium follows the same trend

in all the ferrocene compounds studied in this work similar to that of the charged complexes discussed in the earlier sections.

Discussion on shift in half peak potential of $Fc^{0/+}$ (Ferrocene/Ferrocenium)

Ferrocene is a hydrophobic redox species composed of Fe^{2+} ion sandwiched by two cyclopentadienyl anions (Cp) giving an overall neutral charge. Since the central metal ion is sandwiched amidst the bulky cyclopentadienyl ligands, solvent effects are more pronounced at the Cp ligands than at the metal ion centre. On oxidation, the hydrophobic ferrocene converts to hydrophilic ferrocenium cation and the electron density at the cyclopentadienyl ligands decrease causing

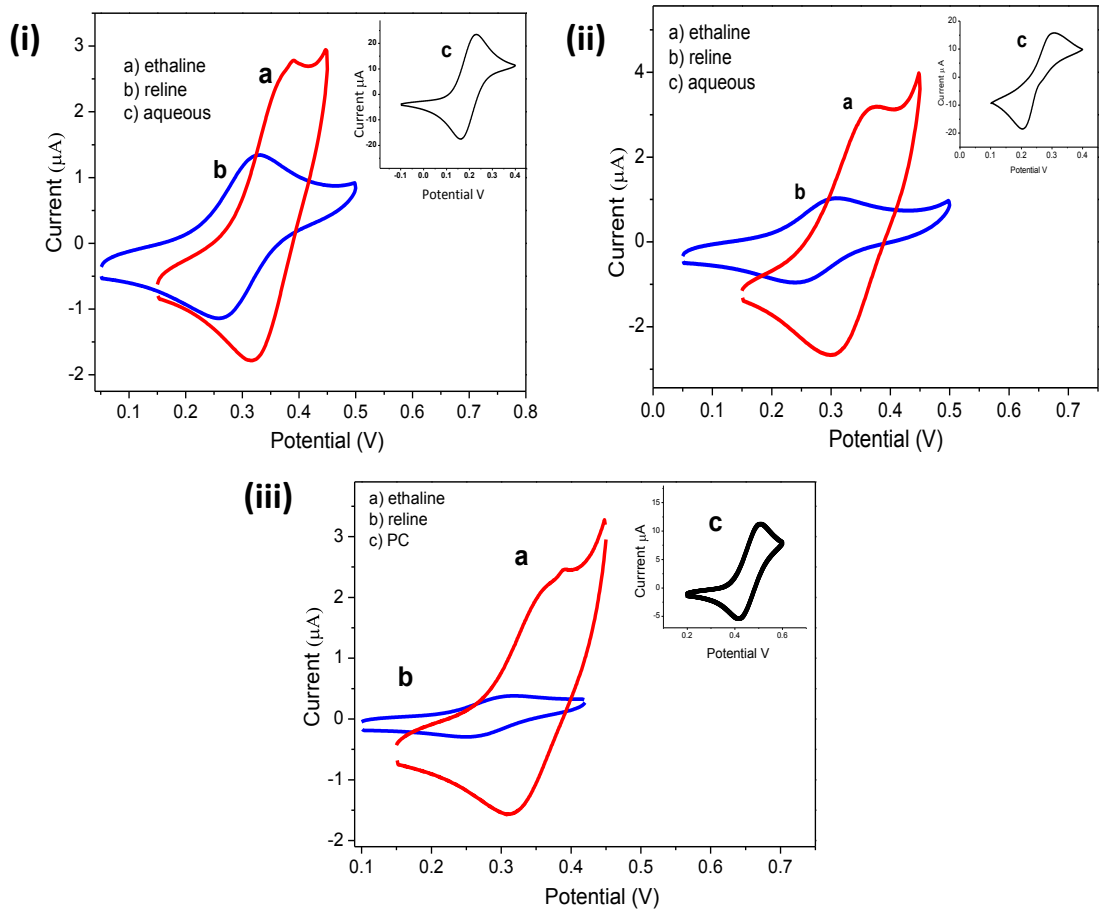

Figure 7. *Cyclic voltammograms of (i) FcMeOH (ii) $FcBF_4$ (iii) Fc a)ethaline (b)reline (c) molecular solvent at a scan rate of 20 mV/s*

drastic changes in the solvation properties. This change in the nature of the molecule from non-polar to polar, makes the electron transfer process dependent on the dielectric constant of the medium. A preferential solvation of Fc^+ drives the electrochemical oxidation of Fc with minimal potential requirements.

The solvation free energies of Fc and Fc^+ were computed in five polar solvents namely water, acetonitrile, methanol, acetone, and dimethylsulfoxide by Kuznetsov *et al* [12]. It was found that the solvation in polar solvents was more favorable for ferrocenium (Fc^+) compared to ferrocene (Fc) as expected. In aqueous medium, the solvation free energy was found to be -46.1 kcal/mol and +0.1kcal/mol for Fc^+ and Fc respectively. The positive solvation free energy of Fc in water is due to the hydrophobic character of Fc. The solvation free energy of Fc increases with the hydrophobic nature of the compound as seen in the case of acetone (-3.1kcal/mol). Such an increase in the solvation energy of Fc when it gets oxidized is reflected in the positive shift of the oxidation potential of Fc. For example, the half peak potential of Fc/Fc^+ in water and acetone are 212mV and 483mV Vs SCE respectively [13].

In contrast to the systems studied previously, $[Fe(CN)_6]^{4-/3-}$ and $[Ru(NH_3)_6]^{2+/3+}$ the half peak potentials of ferrocene is shifted to more positive values in DES when compared to that in aqueous medium (Fig.7). This phenomenon can be attributed to the preferential solvation of Fc by DES components compared to water (in aqueous electrolyte). While, water molecules can stabilize the oxidized product (Fc^+) which is polar and hydrophilic, the DES does not solvate and stabilize Fc^+ species. The redox potentials of Fc in propylene carbonate can be seen to be shifted to more positive potential *wrt* to water due to the same reasons. In general, a decrease in the polarity of the solvent is accompanied by a positive shift in the $E_{1/2.}$ For example, the dielectric constant of water is 80 while that of propylene carbonate is 64.

Table 3. *Anodic and cathodic peak potentials (E^P_a and E^P_c), peak separation (ΔE_p) , half peak potential ($E_{1/2}$) and peak currents (i_a and i_c) of ferrocene compounds in different solvent media*

Redox species	**Solvent**	$\mathbf{E^P_a}$ **mV**	$\boldsymbol{E^P_c}$ **mV**	$\mathbf{\Delta E_p}$ **mV**	$\mathbf{E_{1/2}}$ **mV**	$\mathbf{i_a^p}$ **µA**	$\mathbf{-\ i_c^p}$ **µA**
	Ethaline	381	318	63	350	2.77	1.78
FcMeOH	Reline	330	260	70	295	1.35	1.13
	Aqueous	261	196	65	229	8.08	5.88
	Ethaline	370	300	70	335	3.19	2.66
$FcBF_4$	Reline	303	242	61	273	1.03	0.94
	Aqueous	306	206	100	256	15.77	18.48
	Ethaline	378	302	76	336	2.38	1.54
Fc	Reline	312	246	66	276	0.4	0.29
	PC (Vs Ag/Ag^+)	505	418	87	484	11.2	5.408

On comparing the $E_{1/2}$ of Fc and FcMeOH within the ethaline (ChCl + EG) medium and reline (ChCl + urea) medium, it is apparent that the $E_{1/2}$ values differ by 50-70 mV. This suggests that the solvation characteristics of Fc in DES are different in reline and ethaline. Choline chloride being the common component in both these solvents, the characteristics of the HBD components (EG and urea) in both the cases can be compared. Urea contains more polar components ($-NH_2$ groups) compared to the ethyl chain backbone of EG. Thus EG can solvate and stabilize ferrocene better than urea and water and hence the oxidation of Fc requires more positive potential in this case.

The absolute polarity of DES has not been calculated till date. The most commonly approach to describe solvent polarity in DES is Reichardt's scale where the values are reported *wrt* water in terms of E_T^N. According to the Reichardt's scale of polarity, ethaline (ChCl + EG) and reline (ChCl + Urea) are associated with E_T^N of 0.80 and 0.84 respectively *wrt* aqueous medium ($E_T^N = 1$) and tetramethyl silane ($E_T^N = 0$) [14]. The shift in the redox potentials of Fc in ethaline, reline and aqueous medium can also be explained based on the polarity scales. Ethaline with lower E_T^N of 0.80 can solvate Fc better when compared to reline with E_T^N of 0.84.

Theoretical investigations on the solvation of ferrocene in a model system of 1,3-dimethylimidazolium tetrafluoroborate ($MMIMBF_4$) have been carried out by Yang *et al* [15]. Results obtained in the studies showed interactions of ferrocene in neutral state with both $MMIM^+$ cations and BF_4^- anions from the top and side respectively (thermodynamic stabilization by -11~ -14 kcal/mol). There were no π-π interactions between the cyclopentadienyl ligands (Cp) and $MMIM^+$ cation. Multiple interactions were observed between the Fe atom and $MMIM^+$ cation. On oxidation, the $MMIM^+$ cations experience strong electrostatic repulsion to Fc^+ and moves away, while the BF_4^- anions gets tightly bound to Fc^+, with a binding energy of -72 ~ -86 kcal/mol. Thus in the case of MMIM BF_4, the Fc^+ is better stabilized than the neutral Fc due to the strong binding energy of Fc^+ - BF_4^-.

Even though there have been no reports on the solvation of Fc/Fc^+ in a DES medium, certain implications can be derived from the above solvation model in ionic liquids. As discussed earlier, the absence of π-π interactions between $MMIM^+$ cation and cyclopentadienyl ligands, indicates that the Cp – $MMIM^+$ binding was purely due to hydrophobic interaction. Such an interaction is possible in the DES, between the Cp ligands of neutral Fc and the choline cation (Ch^+). On oxidation, the Fc^+ undergoes electrostatic repulsion with the Ch^+ (scheme-4). However, the chloride anions of DES does not interact and stabilize the Fc^+ due to the weak ion-pair formation of Cl^- - Fc^+ compared to BF_4^- - Fc^+ in the ionic liquid $MMIMBF_4$ [16]. Thus it can be concluded

that the neutral Fc is better stabilized in DES than the Fc^+ and hence Fc undergoes oxidation at higher positive potentials.

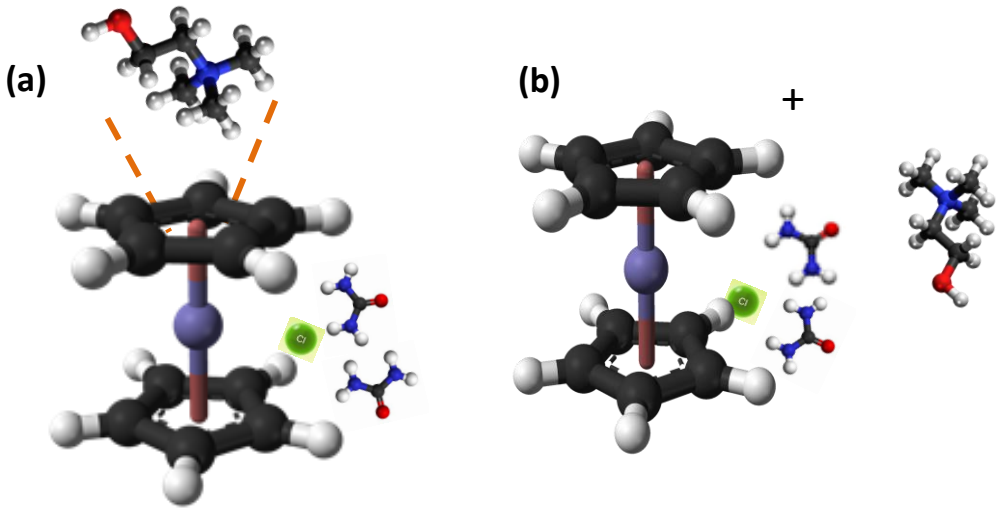

Scheme 4. *A pictorial representation of the solvation shell of (a) Fc (b) Fc^+ in DES (model not to scale)*

(b) Methyl viologen

Methyl viologen (1,1′-Dimethyl-4,4′-bipyridinium dichloride) is an example for a water soluble organic redox active compound exhibiting three oxidation states (MV, MV^+, MV^{2+}). The three oxidation states of MV are given in scheme-5.

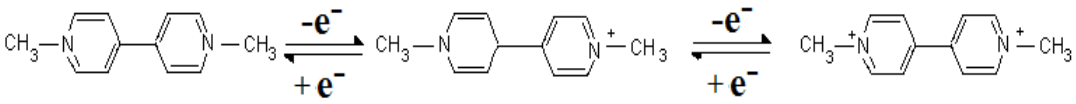

Scheme 5. *Redox reaction of methyl viologen*

Fig. 8 shows the cyclic voltammogram of methyl viologen in aqueous medium, ethaline and reline. The two redox peaks observed in the voltammogram corresponds to the successive electron transfer processes shown in the above scheme. The peak separation observed in all the three solvent media studied here corresponds to a typical reversible redox reaction. The first anodic peak in aqueous medium corresponds to the adsorption of methyl viologen onto the electrode surface as reported. Since the nature of redox peaks are different in DES and aqueous medium, the first cathodic peak is considered for comparison. The half peak potentials of MV have shifted considerably by + 130mV

in DES compared to aqueous medium similar to that observed for the ferrocene compounds (Table 4). In the aqueous medium, while the neutral methyl viologen cannot be adequately solvated, the oxidized hydrophilic species are very well solvated thereby facilitating oxidation process. In DES, the neutral MV^0 can have secondary interactions with the alkyl components. On electrochemical oxidation of MV, the choline cation begins to move away from the oxidized species due to the electrostatic repulsion. The positive shift in the peak potentials in DES compared to that in aqueous medium can be attributed to the preferential solvation of neutral MV compared to the oxidized MV^+, MV^{2+} species.

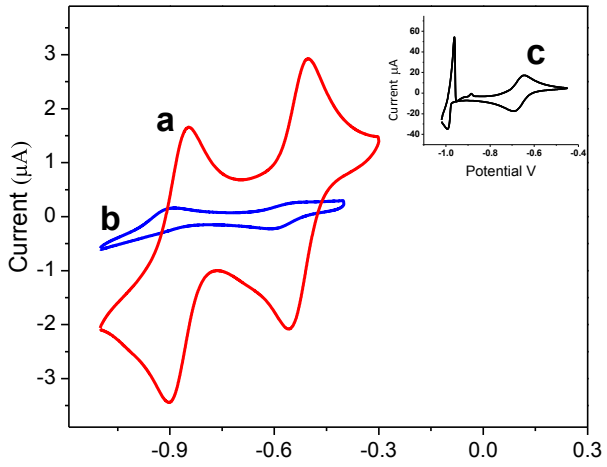

Figure 8. *Cyclic voltammogram of 5 mM MV in a)ethaline (b)reline (c)aqueous medium/0.1M KCl at a scan rate of 20 mV/s*

Table 4. *Anodic and cathodic peak potentials (E^P_a and E^P_c), peak separation (ΔE_p) , half peak potential ($E_{1/2}$) and peak currents (i_a and i_c) of MV in different solvent media.*

	E^2_a mV	E^2_c mV	ΔEp^2 m V	$E^2_{1/2}$ mV	i_a^p µA	$-i_c^p$ µA
Ethaline	-503	-558	55	-531	2.91	2.07
Reline	-536	-603	67	-570	0.262	0.227
Aqueous	-645	-692	47	-668	20.37	17.76

3.3.2. Behaviour of Peak Current vs. Scan Rate

The peak currents of the charged redox species are almost an order of magnitude lower in DES compared to the aqueous medium. Among the DES, the peak currents are almost halved in reline as compared to the ethaline. This is attributed to the decreased viscosity of the ethaline compared to reline ($\eta_{ethaline}$ (37cP) η_{reline}(750cP).

The scan rate dependence of the redox species was studied in reline and ethaline systems. The plot $\nu^{1/2}$ Vs i_p exhibited a linear relationship following the Randles - Sevcik equation for a diffusion controlled process. This indicates that the redox reactions follow the planar semi-infinite linear diffusion in the DES media also. Fig. 9 and 10 shows the plots of square root of scan rate Vs i_p of $[Fe(CN)_6]^{4-/3-}$,$[Ru(NH_3)_6]^{2+/3+}$, FcMeOH, $FcBF_4$ and MV.

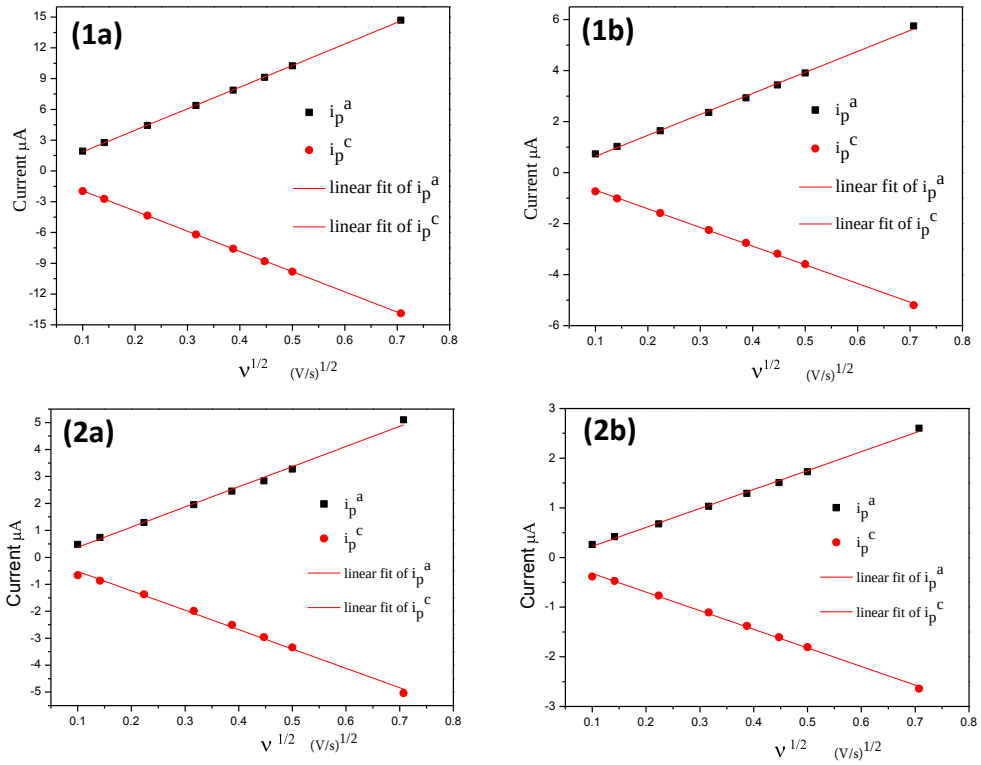

Figure 9. *Plot of average peak current vs. square root of scan rate (1) $[Fe(CN)_6]^{4-/3-}$ (2) $[Ru(NH_3)_6]^{2+/3+}$ in (a) ethaline (b) reline*

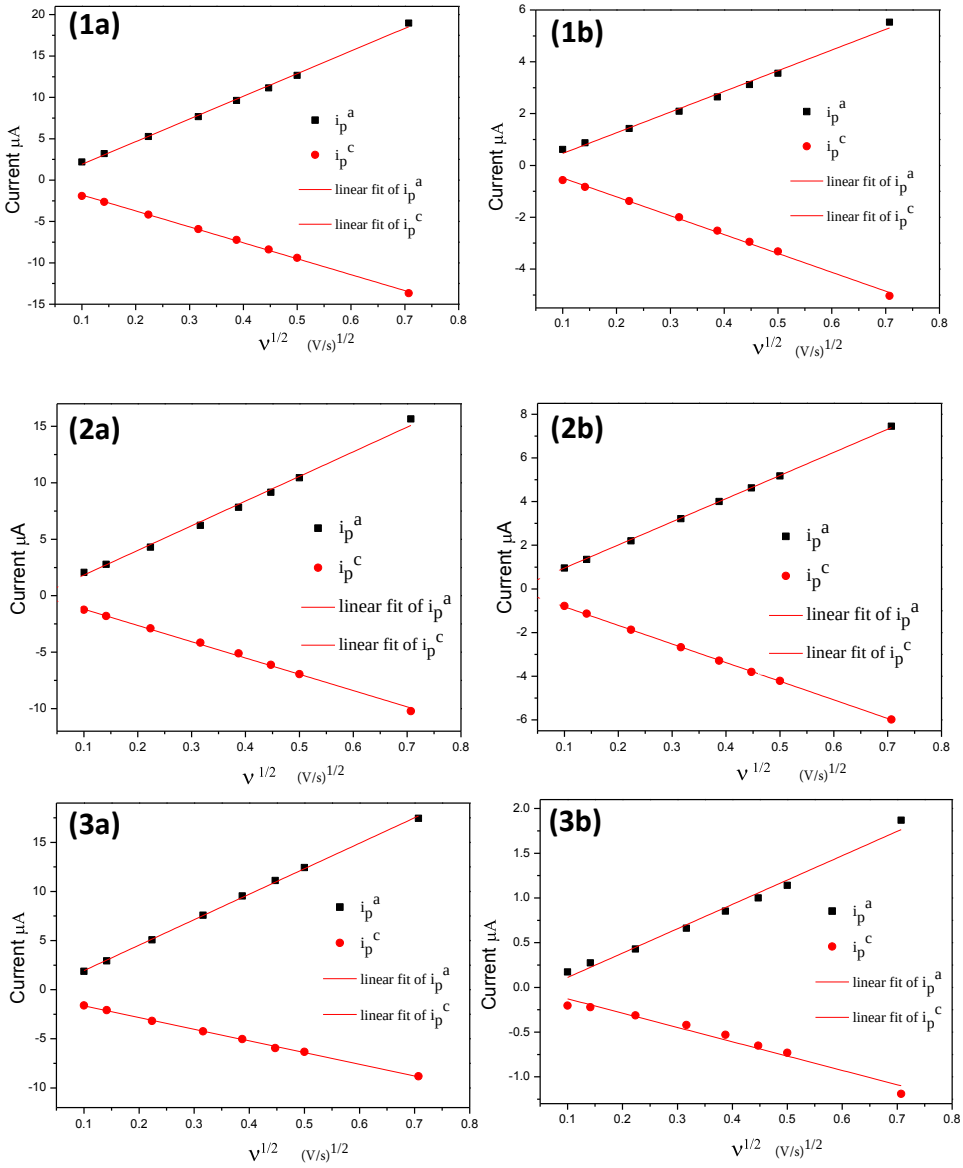

Figure 10. *Plot of average peak current vs. square root of scan rate (1) $FcBF_4$ (2) FcMeOH (3) MV in (a) ethaline (b) reline*

3.3.3. Calculation of diffusion coefficients of the redox species

3.3.3.1. Calculation of diffusion coefficients from EIS

Electrochemical impedance spectroscopic (EIS) studies were conducted for the redox probes $[Fe(CN)_6]^{4-/3-}$, $[Ru(NH_3)_6]^{2+/3+}$, Fc|Fc+, FcMeOH and methyl viologen in the DES media as well as in aqueous medium. The EIS studies were carried out at the

half-peak potentials of the redox probes that were measured from their respective cyclic voltammograms. The results obtained from the EIS were analysed by fitting to an equivalent circuit model. The Randles equivalent circuit R(C(RW)) consisting of an active electrolyte resistance R_S in series with the parallel combination of the double- layer capacitance C_{dl} and an impedance of a faradaic reaction Rct with Warburg impedance Zw in series was used for fitting the EIS data (scheme-6). Fig. 11 and 12 shows the equivalent circuit fitting of the impedance plots for the redox reactions carried out in DES.

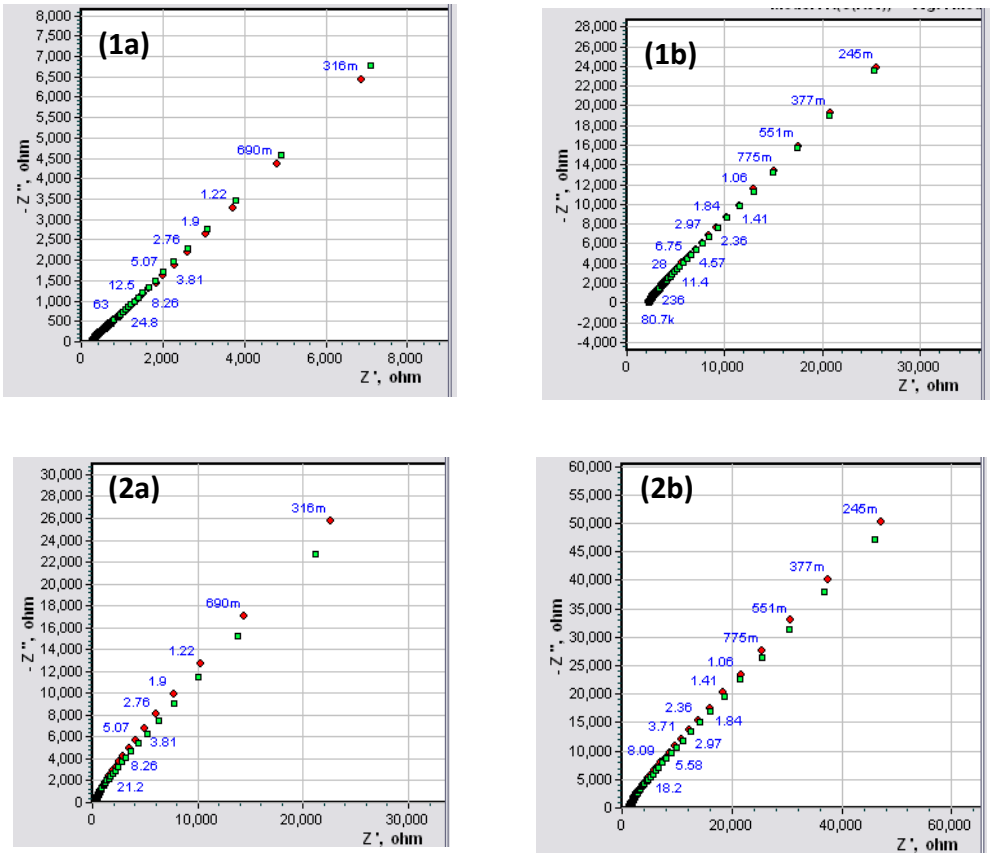

Figure 11. *Equivalent circuit fitting of the Nyquist plots of the EIS studies done at the half peak potential of the redox systems (1) $[Fe(CN)_6]^{4-/3-}$ (2) $[Ru(NH_3)_6]^{2+/3+}$ in (a) ethaline (b) reline*

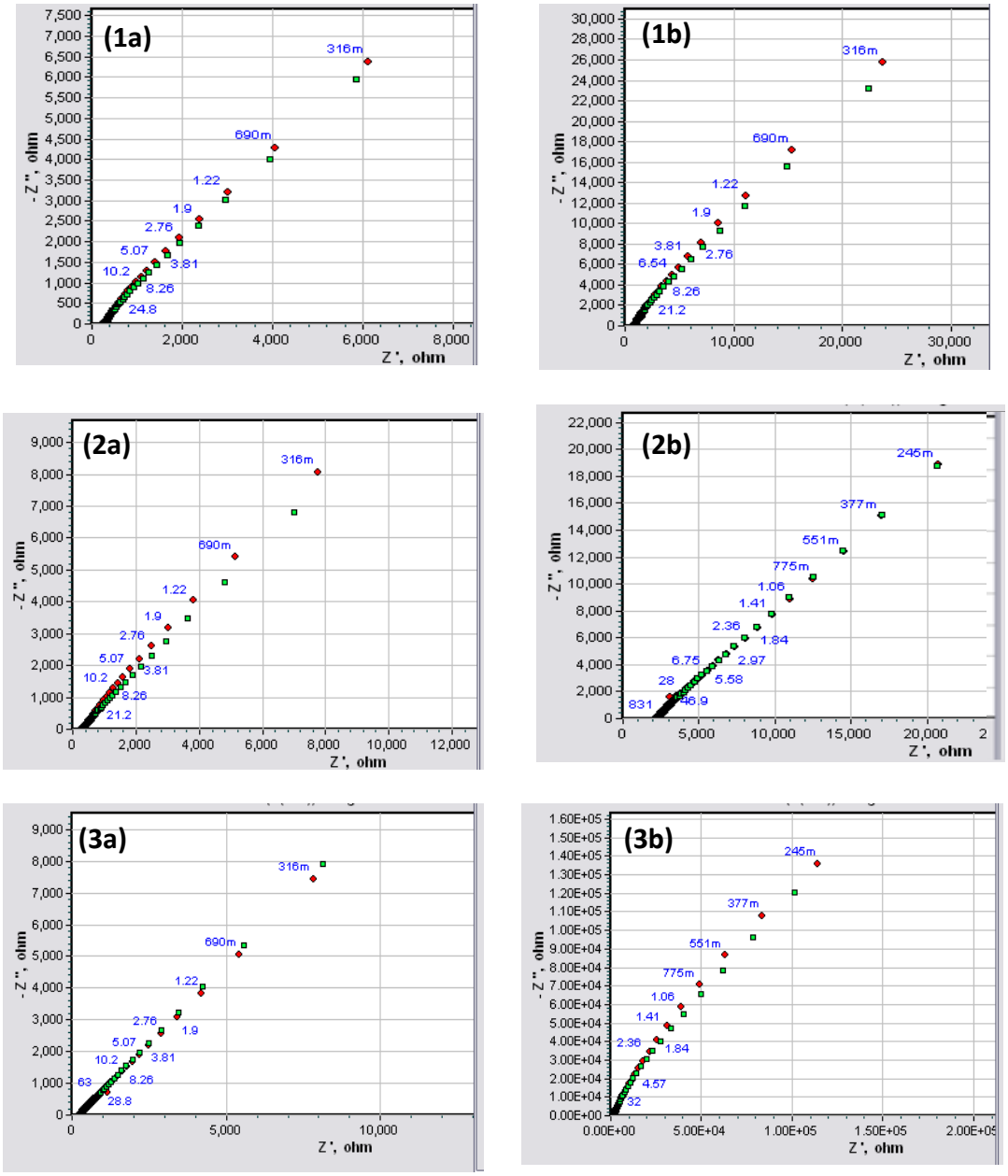

Figure 12. *Equivalent circuit fitting of the Nyquist plots of EIS studies done at the half peak potential of the redox systems (1) $FcBF_4$ (2) FcMeOH (3) MV in (a) ethaline (b) reline*

.

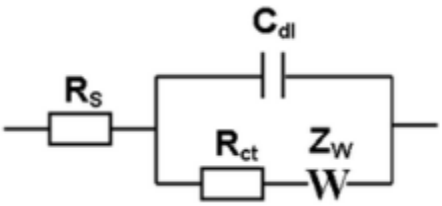

Scheme 6. *Randles circuit used for equivalent circuit fitting of EIS data*

It is evident from the Table 5 that the solution resistance R_u is higher in the DES media compared to the aqueous media. Warburg admittance which is a measure of the diffusion of the redox species in a media is also considerably low by almost an order of magnitude in DES compared to the aqueous medium. The high solution resistance and low Warburg admittance are attributed to the high viscosity of DES.

The diffusion coefficient of the redox species can be calculated from the Warburg impedance by the equation,

$$Z_w = \sqrt{\frac{2}{\omega}} . \sigma \qquad (2)$$

$$\sigma = \frac{RT}{\sqrt{2}n^2F^2\sqrt{D}A} \left(\frac{1}{C_O} + \frac{1}{C_R} \right) \qquad (3)$$

where Z_w is the Warburg impedance, ω is the angular frequency applied, R is the universal gas constant, T is the temperature (in K), n is the number of electrons involved in the redox reaction, F is the Faraday constant, D is the diffusion coefficient of the redox species, A is the area of the electrode, and C_O and C_R are the bulk concentrations of the oxidised and reduced species in the solution, respectively. Warburg impedance is given by ($Z_w = 1 / Y_0$). The square root of diffusion coefficients calculated from the EIS studies are given in Table 5.

Table 5. *Values of the solution resistance (R_u), Warburg admittance (Y_0) and diffusion coefficients of various redox species from equivalent circuit fit of the impedance data*

System	**Solvent**	**R_u (Ω)**	**Y_0 x10^{-5} (S.√sec)**	**$\sqrt{D_{EIS}}$ (cm/√s)**
$[Fe(CN)_6]^{4-/3-}$	Ethaline	283	7.39	6.268 x10^{-4}
	Reline	2255	2.41	2.042 x10^{-4}
	Aqueous	131	106	8.980 x10^{-3}
$[Ru(NH_3)_6]^{2+/3+}$	Ethaline	289	2.205	1.867 x10^{-4}
	Reline	1387	1.205	1.021 x10^{-4}
	Aqueous	139	74.3	5.270 x10^{-3}
FcMeOH	Ethaline	343	7.356	6.234 x10^{-4}
	Reline	2289	3.031	2.568 x10^{-4}
	Aqueous	136	60.1	5.080 x10^{-3}
$FcBF_4$	Ethaline	305	8.411	7.128 x10^{-4}
	Reline	917	2.156	1.827 x10^{-4}
	Aqueous	289	17.67	1.520 x10^{-3}
MV	Ethaline	272	6.329	5.363 x10^{-4}
	Reline	2273	0.4656	3.940 x10^{-5}
	Aqueous	-	50.55	4.280 x10^{-3}

The effect of viscosity on the diffusion coefficents is clear by comparing the √D values of redox species obtained in ethaline (η - 37cP) and reline (η - 750cP). The diffusion

coefficient of a compound is related to the viscosity of the solvent by the Stokes-Einstein equation given by,

$$D = \frac{k_B T}{6\pi\eta r} \qquad (4)$$

Where k_B is the Boltzmann constant, T is the absolute temperature, η is the viscosity and r is the hydrodynamic radius. However in the case of DES, the values calculated from electrochemical experiments were found to deviate from the predicted values. This is because of the fact that the equation assumes a non-interacting solvent which is not the case in DES. The coulombic interactions between the excess ions in DES / ionic liquids and the redox species cannot be neglected. Due to the same reasons, the diffusion coefficients of ferrocene calculated in DES (η-120cP) was found to be 2.7 $x10^{-8}$ cm^2 s^{-1} which is almost two times lower than that predicted by the equation (6 $x10^{-8}$ cm^2 s^{-1}) [2]. The diffusion coefficients of ferrocene and ferrocene methanol obtained in our studies agree well with the literature reported in DES (η - 120cP) and ionic liquid (η - 27cP) respectively [17].

3.3.3.2. Calculation of diffusion coefficients from cyclic voltammetry

The diffusion coefficients obtained from the EIS studies were compared with the results obtained from cyclic voltammetry. The relationship between the peak current and the diffusion coefficient is given by the Randles-Sevcik equation [18],

$$i_p = (2.69 \times 10^5)\ n^{\frac{3}{2}} A\ D^{\frac{1}{2}} C_0\ v^{\frac{1}{2}} \qquad (5)$$

Where n is the number of electrons involved in the redox reaction, A is the electrode area, D is the diffusion coefficient, ν is the scan rate. The electrode area, scan rate, number of electrons and concentration of the redox species involved are all known. Hence the slope obtained from the linear fit of the plot of i_p Vs $\nu^{1/2}$ gives the diffusion coefficient of the redox species studied. A comparison of the diffusion coefficients obtained from cyclic voltammetry and EIS is provided in Table 6. It is apparent that the values obtained from cyclic voltammetry are in reasonable agreement with that obtained in EIS considering the assumption of simple Randles

equivalent circuit model used for fitting EIS data and the neglect of double layer capacitance in the case of cyclic voltammetry.

Table 6. *Comparison of the diffusion coefficients of different redox species calculated from EIS and CV technique*

System	**Solvent**	$\sqrt{D_{EIS}}$ **x10^{-4}** (cm/$\sqrt{s}$)	$\sqrt{D_{CV}}$ **x10^{-4}** (cm/$\sqrt{s}$)
$[Fe(CN)_6]^{4-/3-}$	Ethaline	6.268	4.667
	Reline	2.042	1.733
$[Ru(NH_3)_6]^{2+/3+}$	Ethaline	1.867	1.666
	Reline	1.021	0.877
FcMeOH	Ethaline	6.234	3.413
	Reline	2.568	2.018
$FcBF_4$	Ethaline	7.128	4.537
	Reline	1.827	1.725
MV	Ethaline	5.363	2.813
	Reline	0.394	0.379

3.4. Conclusions

Electron transfer studies of anionic, cationic and neutral redox species have been extensively studied in DES by cyclic voltammetry and electrochemical impedance spectroscopy. The results obtained from the electrochemical studies were compared with that in molecular solvents. Considerable differences in terms of peak current and peak potentials of redox species were observed in DES *wrt* molecular solvents.

The decrease in magnitude of peak current in DES *wrt* molecular solvents is due to the increased viscosity of DES (η – 37 cP and 750 cP for the DES studied). The relative decrease in the peak current within the DES systems studied was also attributed to the same reasons. The plot of square root of scan rate Vs peak current exhibited a linear relationship following the Randles - Sevcik equation for a diffusion controlled process.

The shift in peak potentials of the redox species in DES *wrt* aqueous medium was found to be dependent on the nature of the redox species. While a negative shift in peak potential wrt to aqueous medium was observed in charged redox complexes of $Fe[(CN)_6]^{4-/3-}$ and $Ru[(NH_3)_6]^{2+/3+}$, the trend was found to be opposite in the neutral redox species of FcMeOH, $FcBF_4$ and MV. In the case of $Fe[(CN)_6]^{4-/3-}$ and $Ru[(NH_3)_6]^{2+/3+}$, the corresponding reduced species is preferentially stabilized in aqueous medium compared to DES. The preferential stabilization was rationalized by hydrogen bonding interactions and entropic factors. Contrary to the charged species, the neutral redox probes in their reduced states were stabilized in DES compared to aqueous medium. The non polar components of DES can interact well with the neutral non-polar redox species compared to their oxidized state. The shift in redox potentials followed the electrochemical series proposed by Abbott *et al*. for redox species in DES.

The diffusion coefficients of the redox species in DES were calculated by cyclic voltammetry and electrochemical impedance spectroscopy. The results obtained from the two different techniques were in reasonable agreement. The diffusion coefficient of redox species in DES was found to be less than that observed in aqueous medium by an order of magnitude. The electron transfer studies carried out in DES medium with a set of standard redox species provides adequate information on the solvation features, diffusion coefficients and redox potentials which would be useful for further studies in biological and physiological media.

References

1. P. Abbott, G. Capper and S. Gray, *Chem. Phys. Chem*., 2006, 7, 803.
2. A. Nkuku and R. J. LeSuer, *J. Phys. Chem. B*, 2007, **111,** 13271.
3. Lloyd, T. Vainikka, L. Murtomäki, K. Kontturi and E. Ahlberg, *Electrochim.Acta.*, 2011, **56**, 4942.
4. S. Silvester and R. G. Compton, *Z. Phys. Chem*., 2006, **220**, 1247.
5. D. Aurbach, Nonaqueous Electrochemistry, CRC Press, 1999
6. A. P. Abbott, G. Frisch, S. J. Gurman, A. R. Hillman, J. Hartley, F. Holyoak and K. S. Ryder, *Chem. Commun*., 2011, **47**, 10031.
7. P. Yu, F. Yang, J. Zhao and J. Wang, *J. Phys. Chem. B*, 2014, **118**, 3104.
8. M. Muzikar and W. R. Fawcett, *J. Phys. Chem. B*, 2006, **110**, 2710.
9. M. Brown and N. Sutin, *J. Am. Chem. Soc*., *1979,***101**, 883.
10. E. L. Yee, R. J. Cave, K. L. Guyer, P. D. Tyma and M. J. Weaver, *J. Am. Chem. Soc*., 1979, **101**, 1131.
11. V. A. Nikitina, S. A. Kislenko, R. R. Nazmutdinov, M. D. Bronshtein and G. A. Tsirlina, *J. Phys. Chem. C*, 2014, **118**, 6151.
12. M. Kuznetsov, A. N. Maslii and L. I. Krishtalik, *Russ. J. Electrochem*., 2009, **45**, 87.
13. V. Conte, B. Floris, P. Galloni and C. Bizzarri, *J. Phys. Org. Chem.*, 2010, **24**, 327.
14. J. T. Gorke, R. J. Kazlauskas and F. Srienc, *US 20090117628 A1*
15. Y. Yang and L. Yu , *Phys. Chem. Chem. Phys.*, 2013, **15**, 2669.
16. H. Ju and D. Leech, *Phys. Chem. Chem. Phys.*, 1999, **1**, 1549.

17. K. R. J. Lovelock, A. Ejigu, S. F. Loh, S. Men, P. Licence and D. A. Walsh, *Phys. Chem. Chem. Phys.*, 2011,**13**, 10155.

18. A.J. Bard, L.R. Faulkner, Electrochemical Methods Fundamentals and Applications, John Wiley and Sons, Noida, 2nd edn., 2004.

CHAPTER 4

Electrochemically prepared SERS substrates of Ag by anodic dissolution in Deep Eutectic Solvents (DES)

4.1. Introduction

With the emergence of surface enhanced Raman scattering (SERS), as a versatile and a powerful analytical technique, a lot of interest has been generated for the development of nanostructured materials of gold and silver with fine tuned morphology. Both gold and silver nanoparticles offer excellent choices as SERS substrates due to their strong localized surface plasmon resonance. The silver nanoparticles (AgNP) have the added advantages over gold due to their lower plasmonic losses in visible spectrum [1] and also due to their proven biocompatibility. Generally, the silver nanoparticle supported substrates are obtained by forming silver film on polystyrene nanospheres, and drop casting the colloidal nanoparticles on glass. Besides, the method of nanoscale lithography, self assembly of nanoparticle onto the substrates is also employed [2-6]. The colloid based substrates often cause irreproducibility in SERS due to aggregation of nanoparticles. Poor adhesion of nanoparticles onto substrate, instability of the active layer of SERS to organic solvents and also degradation due to continuous exposure to the laser beam are some of the limitations of the conventional SERS substrates. The technique of nano scale lithography, though requiring expensive fabrication procedures, produces highly reproducible SERS substrates.

Electrochemical synthesis of nanoparticles and their deposition on suitable substrate for SERS are explored in this work. This is because, the electrodeposited nanoparticles are well adherent onto the substrates and are stable to solvent treatments and continous laser exposure. Bian *et al.* prepared recyclable SERS substrates of silver with concave surfaces by electrodeposition [7]. Choi *et al.* prepared highly reproducible SERS substrates based on dendritic gold rods by a single step electrochemical technique. The technique provided highly faceted sharp edge sites which are advantageous for signal enhancement [8]. Orinakova *et al.* reported electrochemical synthesis of silver island films by cyclic voltammetry [9]. Nanoporous Ag films on copper alloy substrates have been prepared by simple galvanic replacement reaction too [10]. The only constraint is the fact that electrodeposition can be carried out only on conducting substrates such as metals, ITO and carbon based materials.

Though there have been many reports on electrodeposition of silver by electrochemical methods such as cyclic voltammetry and pulse techniques, anodic dissolution of silver and subsequent deposition as nanoparticles on a substrate cathode has not been reported widely. This is due to the fact that there are several challenges involved in anodic dissolution of Ag in aqueous medium. The electrodeposition of AgNPs by anodic dissolution requires aprotic medium for electrodeposition, due to the tendency of the anode to passivate in the presence of protons [11]. The presence of even traces of water in the solvent has also been found to decrease the efficiency of the dissolution process. The mechanism of passivation of silver anode during anodic dissolution in protic solvents had been discussed by Murray *et al.* [12]. In protic medium, the protons are generated at the anode surface as a consequence of processes occurring at anode, ie., dissolution of silver and oxidation of water. These protons cause direct oxidation of Ag to Ag^{+}, AgO and finally Ag_2O_3, an insulating oxide which causes polarization of the electrode and drop in current. Therefore, further progress of the reaction leading to the synthesis of AgNPs is dependent crucially on the complete removal of the passive silver oxide film.

In this chapter, a simple method of preparing nanoparticle by anodic dissolution with the simultaneous formation of mesoporous films on Pt/Rh substrate in the medium of DES is described. The inherent ability of DES to solubilize the metal oxides prevents the passivation problems and thus makes it an excellent medium of choice for anodic dissolution of Ag. The mesoporous film was characterized by UV, SERS, XRD, SEM and EDAX. The application of the mesoporous silver substrate for SERS is explored in this work. Efforts were taken to ensure that a pristine SERS substrate of mesoporous Ag which do not exhibit any inherent SERS signal was obtained.

4.2. Experimental

4.2.1. Materials used

All the chemicals used in this study were analytical grade (AR) reagents. Choline chloride, $((CH_3)_3N$ (Cl) $CH_2CH_20H)$ (Aldrich, 98%) was dried for 1 hour

at 100^{o} C prior to use. Ethylene glycol, (Merck), 4-mercapto phenyl boronic acid (Aldrich), sodium borohydride (Aldrich), ethanol (Merck) were used as received. Methylene blue (MB) was used as analyte species in SERS studies.

Silver and platinum/rhodium thermocouple wire each of 0.5mm diameter of 99.99 % purity were purchased from Advent research materials.

4.2.2. Electrode pretreatment

Metal wires which were used as electrodes were polished in aqueous slurries of grades 1 μm, 0.3 μm, 0.05μm alumina successively, ultrasonicated in Millipore water and dried prior to use.

4.2.3. Electrochemical synthesis and insitu deposition of silver nanoparticles

The silver nanoparticles were deposited onto a Pt/Rh thermocouple wire. In this process, a silver wire was used as a sacrificial anode and Pt/Rh wire as a cathode. The electrodeposition was carried out in ethaline medium at 50^{o}C with 4-mercapto phenyl boronic acid (MPBA, 5mM) as a stabilizer and sodium borohydride (0.15M $NaBH_4$) as a reducing agent. The electrolysis was carried out at a current density of 14 mA cm^{-2}. The reaction was accompanied by the formation of a black film of Ag_2O on the Ag anode which was observed to be dissolving in DES medium subsequently. The solubility of metal oxides in DES has been well known and is

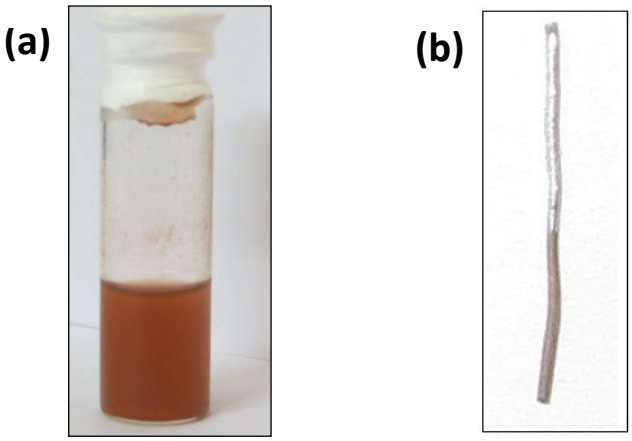

Figure 1*. Photographs of (a)MPBA stabilized silver nanoparticles dispersed in ethanol after purification (b) electrodeposited on Pt/Rh surface for 30 min*

attributed to complexation of the solvent with metal oxides to form soluble species [13]. The color of the medium changes gradually from transparent to reddish brown, indicating the formation of Ag nanoparticles stabilized by MPBA. A simultaneous growth of mesoporous AgNPs was indicated by the formation of a black film at the cathode. The electrodeposition process was carried out for 30 min. The solution turned dark in color with time, which regained the original color after purification with ethanol through repeated sonication and decantation of the solvent. The photographs of the purified silver nanoparticle dispersion in ethanol and the electrodeposited mesoporous film of silver on Pt/Rh wire is provided in Fig.1.

4.3. Results and discussions

4.3.1. Characterization

On applying a suitable current density, the silver wire anode gets dissolved into the medium as ions (Ag^+) which are subsequently reduced at the cathode. In

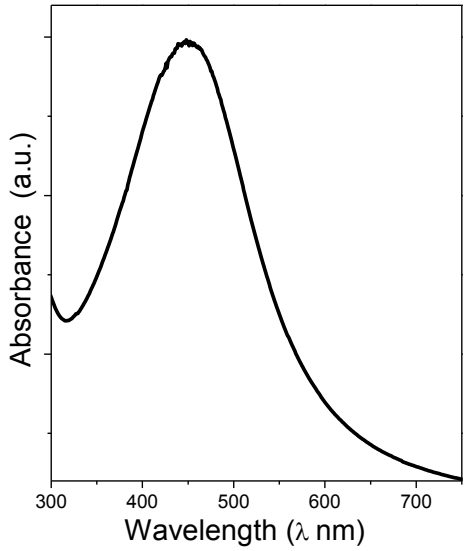

Figure 2. *UV-Vis absorption spectra of purified silver nanoparticles in ethanol*

addition to the electrochemical reduction at cathode surface, the presence of reducing agent in the medium brings about chemical reduction of the silver ions leading to the formation of metal nanoparticles in the solution [14]. The broad

surface plasmon band of silver nanoparticle solution shown in Fig.2 indicates the formation of a polydispersed sample.

The surface enhanced Raman spectra shown in Fig.3a confirm the presence of MPBA monolayer formed on the mesoporous AgNP electrode. The Raman signal at 220 cm^{-1} corresponding to Ag-S bond, which confirms the chemisorption of thiol monolayer on AgNPs [15].-A strong band at 707 cm^{-1} corresponds to the –C-S stretching mode [4]. Raman signals at 999 cm^{-1} (out of plane C-C-C stretch), 1080 cm^{-1}, 1590 cm^{-1} (aromatic ring vibrations) and the weak band at 1180 cm^{-1} (–CH deformations) are characteristic of an aromatic ring. A peak at 1442 cm^{-1} was observed due to the benzene ring vibrations in phenyl-boronic acid group linkage [16]. Raman spectrum of pure MPBA is provided in Fig.3b for comparison. The adsorption of thiol monolayer onto the mesoporous surface was further confirmed by the absence of 2575 cm^{-1} band corresponding to free –SH

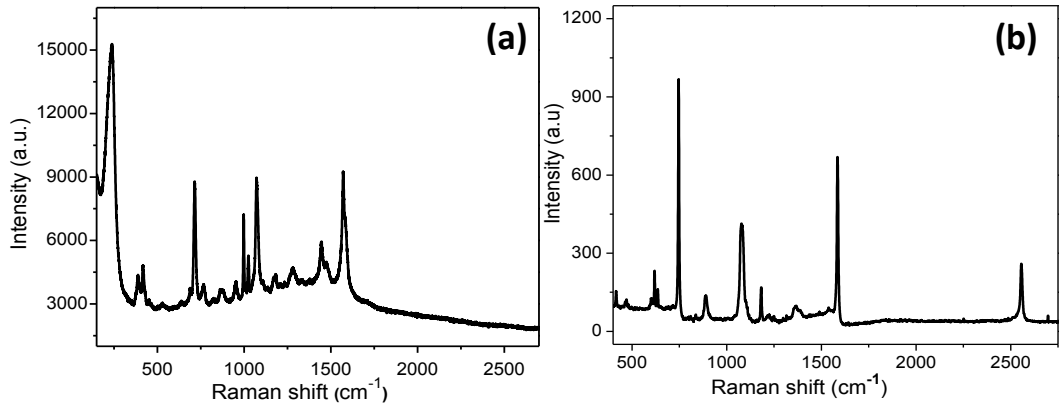

Figure 3. *SERS of the (a) MPBA signals on AgNP Pt/Rh substrate (b) MPBA powder*

groups in Fig.3a. The absence of this band in the SERS spectrum is indicative of the fact that free MPBA molecules do not contribute to the signal intensity in spectra. Assuming a monolayer film of MPBA on the surface of nanoparticles, the SERS signal enhancement due to mesoporous nature of AgNP film was calculated to be 10^6 compared to the normal Raman spectra of known concentration of MPBA dropcasted on a Si wafer. In view of its prospective application in SERS, the mesoporous silver films on Pt/Rh wire were calcined at 250 ^oC for 2.5 hours to remove the organic stabilizers adhering to the nanoparticle. Once the stabilizer molecules are removed, the SERS substrate is free of any interference due to it and provides a pristine surface for the analyte species. The surface

characterization of the sample before and after calcination was performed to confirm that the mesoporous nature of the surface was not affected by calcination.

The surface XRD patterns of the mesoporous substrates were obtained in the 2Ɵ range of 30-80^{o} for an exposure time of 1 hour. Fig.4a displays the diffraction peaks of AgNP modified Pt/Rh substrate. The XRD peak at 38.3^{o} and the humps at 44.5^{o} and 64.5^{o} were assigned to (111), (200) and (220) crystal planes, indicating that the mesoporous Ag film possess face centered cubic structure [17]. The additional sharp peaks observed in the XRD spectra correspond to Pt/Rh wire on which Ag nanoparticles are deposited. The average particle size of the electrodeposited Ag nanoparticles was determined by XRD using Debye-Scherer's equation and was found to be 34.5nm.

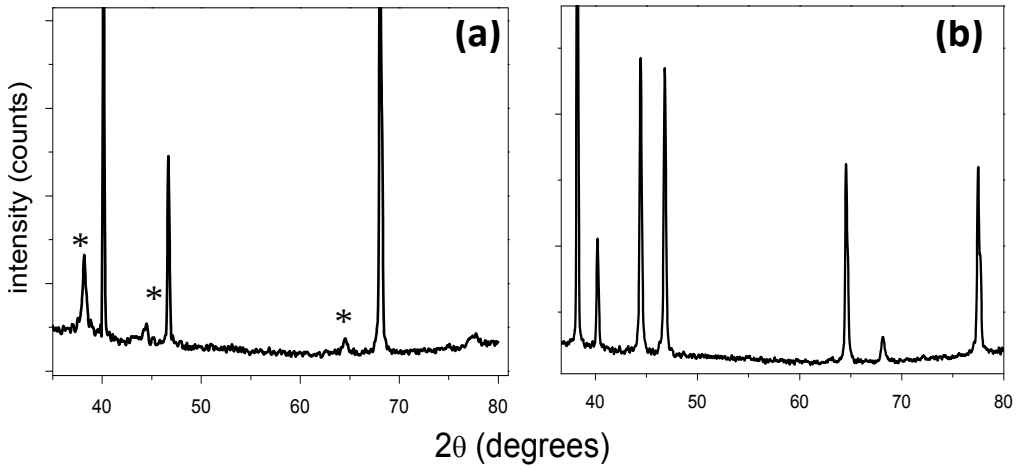

Figure 4. *XRD pattern of the as prepared AgNP (a) calcined AgNP (b) on Pt/Rh wire*

On calcination at 250 ^{o}C for 2.5 hour, as seen in Fig.4b the XRD peaks corresponding to fcc nanostructure of mesoporous Ag became more intense as compared to that prior to calcination. This is evidently due to the surface reorganisation at high temperature during calcination. A similar observation had been reported when AgNPs were calcined to remove organic impurities [18].

SEM images given in Fig. 5 show the as prepared mesoporous deposition of silver on Pt/Rh wire. The dendritic growth of the Ag nanoparticles seen in the interior regions may correspond to initial stages of electrodeposition which grow as clusters in later stages. The elemental composition of the substrate provided in Fig. 6a showed the presence of Pt/Rh along with Ag. This indicates that

underlying substrate is not covered entirely by the mesoporous silver deposit. Fig.7 shows the SEM images of AgNP film on Pt/Rh substrate calcined at 250 ^{o}C for 2.5 hours. The morphology of the nanoparticle changes notably, as AgNPs aggregate to form a network like structure. A comparison of inset images, shows that the smaller nanoparticles coalesce together to form larger clusters of sizes ranging from 200-300 nm. The individual nanoparticles of 10-15 nm coalescing to form larger aggregates

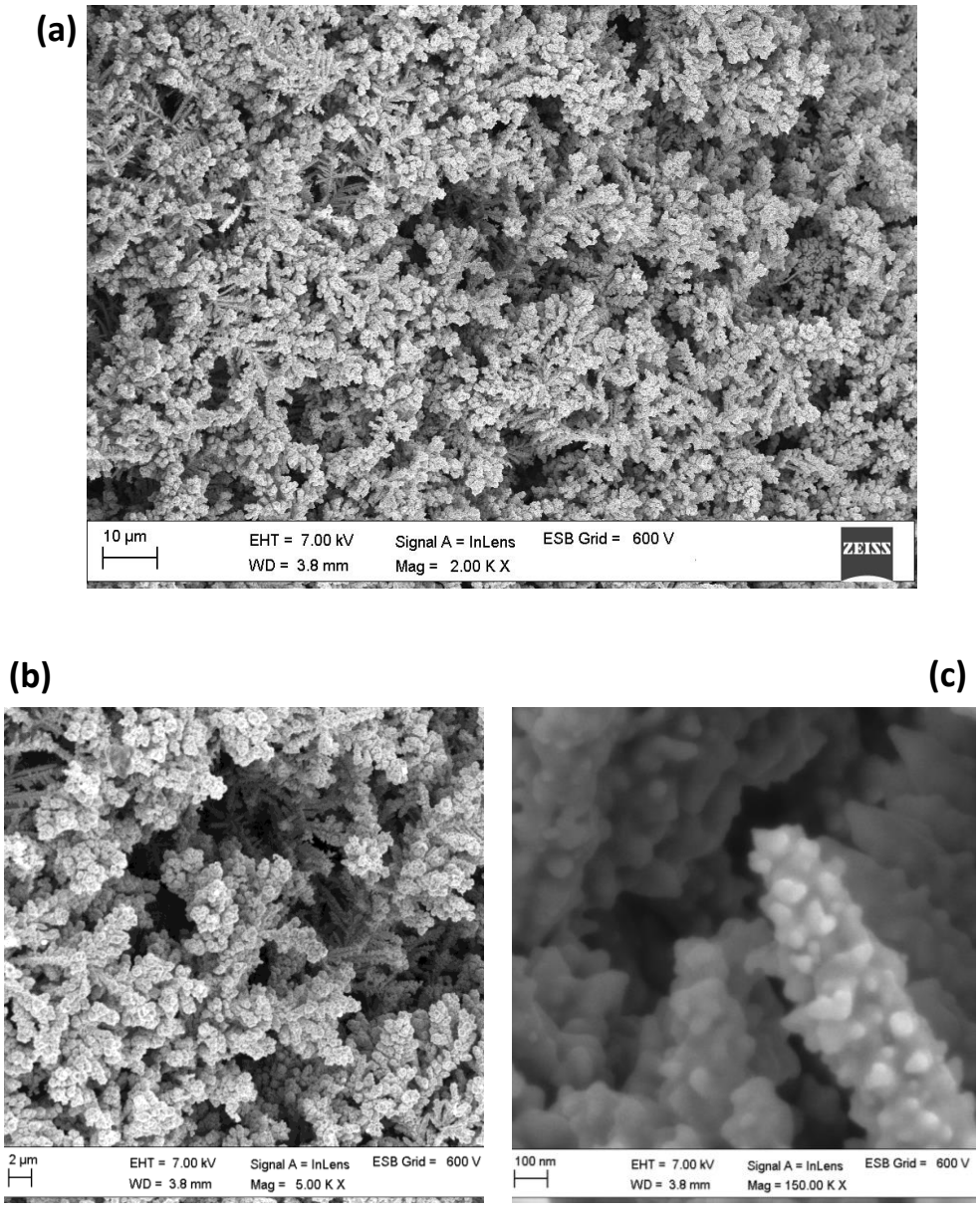

Figure 5. *SEM images of the mesoporous AgNP substrate for an electrodeposition time of 30 min on Pt/Rh before calcination (a) 10 µm (b) 2 µm and (c) 100nm scale-bar*

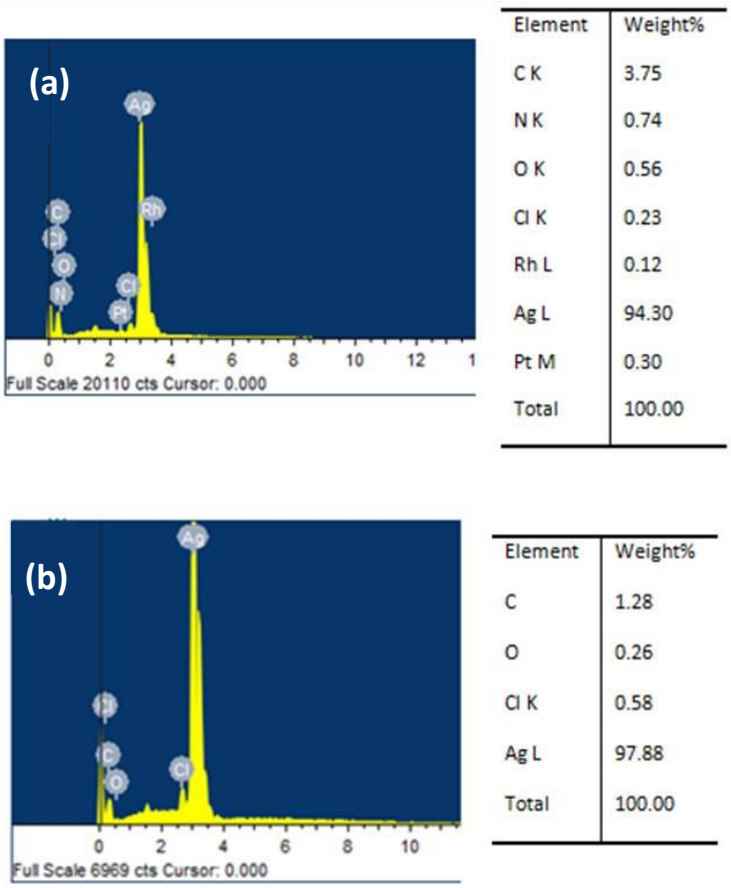

Figure 6. *EDAX results of the mesoporous AgNP film on Pt/Rh (a) before and (b) after calcination*

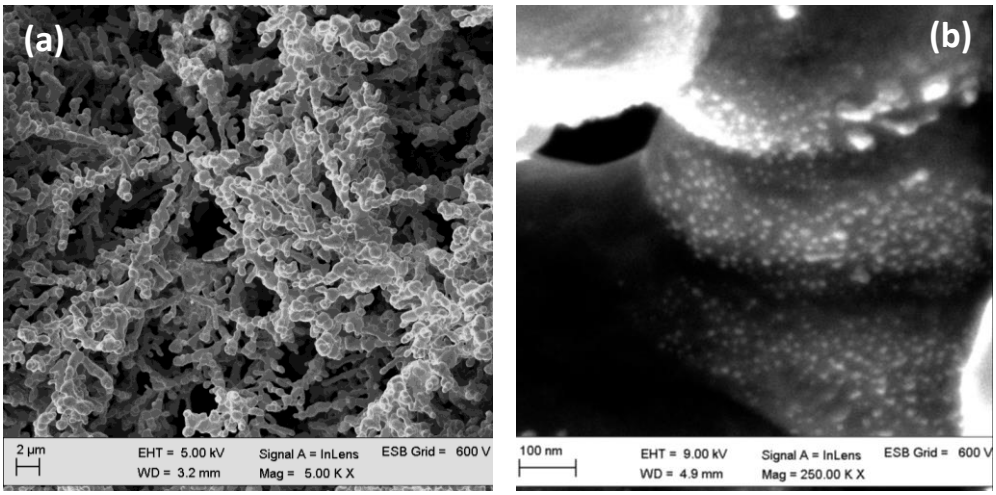

Figure 7. *SEM images of the mesoporous AgNP substrate for an electrodeposition time of 30 min on Pt/Rh after calcination (a) 2 µm scale-bar (b) 100nm scale-bar*

can be seen in the Fig.7b. The EDAX spectra of the calcined substrates shown in Fig.6b confirm that Pt/Rh is extensively covered by the mesoporous AgNP film.

4.3.2. SERS activity of mesoporous substrate

One of the limitations associated with SERS substrates is the signal interference from substrate composition or stabilizer molecules of nanoparticles

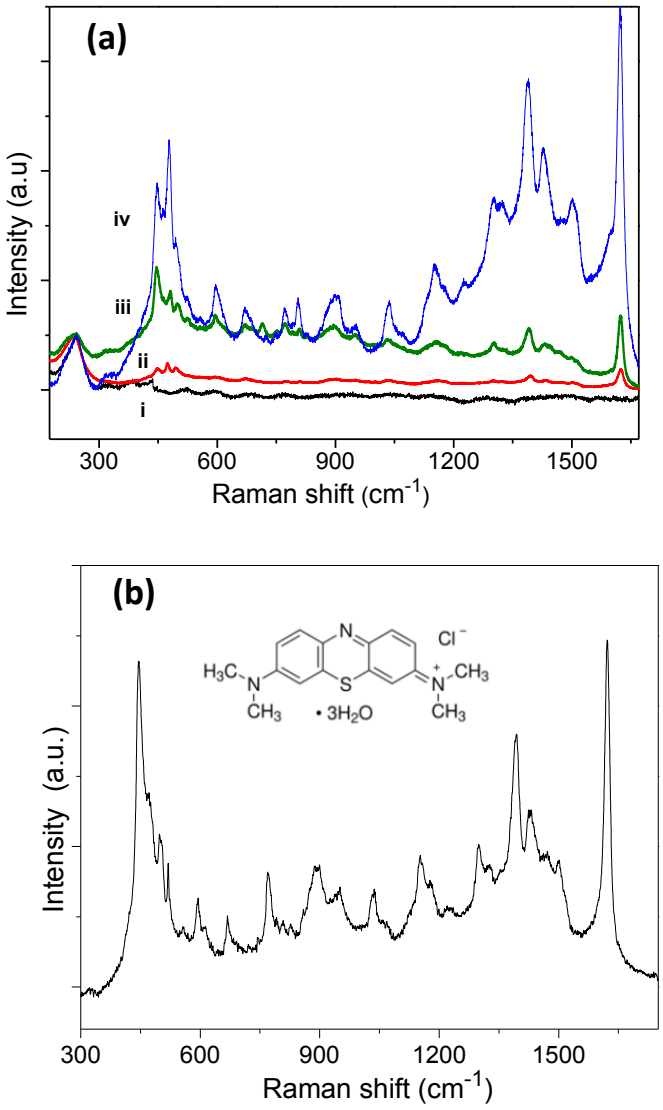

Figure 8. *(a) Normalised SERS spectra of methylene blue adsorbed on calcined substrate from aqueous solutions of (i) 0 M (ii) 3.7 x10^{-7} M (iii) 3.7 x 10^{-6} M (iv) 37 x 10^{-6} M (b) Raman spectra of methylene blue (2µL of 0.1mg/5ml) dropcast on Silicon wafer (inset shows the structure of methylene blue)*

in the SERS spectra. This may impose some constraints in the acquisition of spectra of analyte in a restricted wave number range ie., excluding substrate

signals. In our studies, it was evident from Fig.3a, that the mesoporous AgNP film gives enhanced signals of MPBA, which can interfere with the Raman bands of any analyte species. The possibility of any unspecific molecular interaction between analyte species with the existing MPBA layer on AgNP cannot also be neglected. To overcome this problem as discussed earlier, calcination of the substrate was performed to remove organic moieties present on the mesoporous substrate.

Fig.8a (i) shows the SERS of calcined mesoporous silver substrate exhibiting almost featureless spectra except for the broad band corresponding to Ag-O at ~240cm^{-1}. The AgO is formed on the surface of Ag nanoparticles due to high temperature used during calcination. The absence of any significant peaks in the Raman spectra of the calcined sample confirms the complete removal of the stabilizers adsorbed during the deposition of AgNPs. The utility of the mesoporous substrate in SERS studies has been explored with methylene blue as the analyte. The substrates were dipped in aqueous solutions of methylene blue (3.7 x10^{-7} M - 37 x 10^{-6} M) for 1 hour. A reference sample for acquiring normal Raman spectrum was prepared by drop casting 2µL of 0.1mg/5ml aqueous solution of methylene blue on Si wafer. The SERS substrates and reference samples were allowed to dry at room temperature and the spectra were collected over a range of 100–2000 cm^{-1} with an exposure time of 1 second. The spectral intensity obtained was normalized by the corresponding Ag-O peak intensity for all SERS substrates under study.

A comparison of Fig.8 a and b, shows that the SERS spectra exhibit almost the same features as that present in the normal Raman spectra (NRS) of methylene blue. The SERS spectra are not associated with shifts in band positions, which are usually observed on chemisorption with the substrate. The intensity of the SERS spectra increases as expected with the concentration of methylene blue in the sample. The SERS associated with the lowest concentration (3.7 x10^{-7} M) of the analyte displays only the most prominent peaks of Raman signals of methylene blue. The strong peaks observed in the spectra are 1619 cm^{-1} (stretching vibrations of C-C ring), 1393 cm^{-1} (in-plane ring deformation). The peak observed at 447 cm^{-1} with a shoulder at 476 cm^{-1} in NRS is seen as split peaks at the same

band position in SERS. Raman peak positions obtained in our studies were compared with literature values. Table 1 shows the assignment of the Raman bands in SERS and NRS of methylene blue.

Table 1. *Comparison of Raman peak positions of methylene blue observed in this study along with reported results and spectral assignments [4,19]*

Observed peak position cm^{-1}	**Reported peak positions cm^{-1}**	**Assignments**
1619	1618	ν (C-C ring)
1502	1503	ν(C-C) in plane
1427	1430	ν (C-N)
1390	1396	α (C-H)
1152	1159	β (C-H)
948	948	γ (C-H)
894	890	$CH_{3\ rock}$
768	774	γ (C-H)
596	610	δ (C-S-C)
501	502	δ (C-N-C)

ν stretching α in plane ring vibrations, β in plane bending, δ skeletal deformations

The enhancement factor (G) of the substrate was calculated by the comparison of SERS of methylene blue (37μM) with that of normal Raman spectrum (NRS) at the peak position 1619 cm^{-1} by using the formula

$$G = \frac{N_{ref}\ I_{SERS}}{N_{SERS}\ I_{ref}}$$

where, N_{SERS} and N_{ref} are the number of molecules contributing to the signal on the SERS substrate and reference sample respectively. I_{SERS} and I_{ref} are the

integral area of the Raman signal at 1619 cm^{-1} in SERS and NRS spectra respectively. The enhancement factor was found to be about 2 x 10^6. The value obtained is comparable to the conventionalSERS substrates based on silver using methylene blue as probe molecule [19-20] .

The porous AgNP film fabricated by electrodeposition was found to be well adherent on the surface and could endure electrochemical potential cycling, vigorous heat treatments, rinsing with aqueous and non aqueous solvents. The silver nanoparticle film electrodeposited on metallic substrates provided stable and reproducible SERS signals even upon continuous irradiation with the laser beam, showing a good thermal stability.

4.4. Conclusions

The electrochemical synthesis of silver nanoparticles and their *insitu* deposition on to metallic substrate has been successfully demonstrated using anodic dissolution of pure metal wire. The mesoporous films of silver were quite adherent to electrodeposited substrates and could be effectively subjected to electrochemical treatments, solvent exposure and laser irradiation. The mesoporous silver film shows a SERS enhancement by factor of 10^6. The experiments carried out here shows that the electrodeposition of AgNP in an environmentally benign solvent such as DES and its subsequent sintering at high temperature establishes a simple and efficient technique for the fabrication of stable SERS substrates free from the interference from other associated organic moieties. The method has the potential to be extended to a few other passivating metals in order to fabricate nanoparticle immobilized substrates for different applications.

References

1. W. L. Barnes, A.Dereux and T. W. Ebbesen, *Nature*, 2003, **424**, 824.
2. M. Fan and A.G. Brolo, *Phys. Chem. Chem. Phys*., 2009, **11**, 7381.
3. G. H. Gu and J.S.Suh, *J. Phys. Chem. C*., 2010, **114**, 7258.
4. M. Rycenga, J. M. McLellan and Y. Xia, *Chem. Phys. Lett.*, 2008, **463**, 166.

5. G. D. Fleming, J. J. Finnerty, M. C. Vallette, F. Célis, A. E. Aliaga, C. Fredes and R. Koch, *J. Raman Spectrosc*., 2009, **40**, 632.
6. Y. Bu and S. Lee, *ACS Appl. Mater. Interfaces*, 2012, **4**, 3923.
7. J. Bian, S. Shu, J. Li, C. Huang, Y. Y. Li and R. Q. Zhang, *Appl. Surf. Sci*., 2015, **333**, 126.
8. S. Choi, M. Ahn and J. Kim, *Anal. Chim. Acta*., 2013, **779**, 1.
9. R. Orinakova, L. Skantarova, A. Orinak, J. Demko, M. Kupkova and J. T. Andersson, *Int. J. Electrochem. Sci*., 2013, **8**, 80.
10. C. D. Gu, X. J. Xu and J. P. Tu, *J. Phys. Chem. C*., 2010, **114**, 13614.
11. A. P. Abbott, G. Capper, D. L. Davies, K. J.McKenzie and S. U. Obi, *J. Chem. Eng. Data*., 2006, **51**, 1280.
12. R. Sánchez, M. C. Blanco and M. A. Quintela, *J. Phys. Chem. B*, 2000, **104**, 9683.
13. B. J. Murray, Q. Li, J. T. Newberg, E. J. Menke, J. C. Hemminger and R.M.Penner, *Nano Lett*., 2005, **5**, 2319.
14. D. H. Nagaraju and V. Lakshminarayanan, *Langmuir*, 2008, **24**, 13855.
15. L. Skantarov, A. Orinak, R. Orinakova and F. Lofaj, *Nano-Micro Lett*., 2012, **4**, 184.
16. Y. Erdogdu, M. T. Gulluoglu and M. Kurt, *J. Raman Spectrosc*., 2009, **40**, 1615.
17. S. Gurunathan, K. Kalishwaralal, R.Vaidyanathan, D. Venkataraman, S. R. K. Pandian, J. Muniyandi, N. Hariharan and S. H. Eom, *Colloid Surf. B*, 2009, **74**, 328.
18. P. Mukherjee, M. Roy, B. P. Mandal, G. K. Dey, P. K. Mukherjee, J. Ghatak, A. K. Tyagi and S. P. Kale, *Nanotechnology*, 2008, **19**, 075103.
19. G.N. Xiao and S. Q. Man, *Chem. Phys. Lett.*, 2007, **447**, 305.
20. N. Nuntawong, M.Horprathum, P. Eiamchai and P. Chindaudam, Vacuum, 2010,1.

CHAPTER 5

Electrochemically grown mesoporous metallic substrates of Ag, Au and Pd by anodic dissolution in Deep Eutectic Solvents (DES); Synthesis, characterization and electrocatalytic studies

5.1. Introduction

Deep eutectic solvents (DES) are promising alternatives for conventional aqueous solutions or organic solvents which often require added supporting electrolytes to achieve a desired ionic conductivity [1]. The copious oxygen and hydrogen evolution processes associated with aqueous medium restricts the useful electrochemical potential window. The DES medium is employed in electrochemical processes to counter these limitations of molecular solvents. Further, due to its significant ionic conductivity, DES can be used as a standalone media for electrochemical processes. While these features are also exhibited by ionic liquids, the DES has several advantages for practical applications owing to their insensitivity to water and lower cost.

The wider acceptance of DES in metal/alloy electrodeposition processes has demonstrated its potential to be used for electrodeposition of metal nanoparticles too [1]. With the recent trend towards the development of environment friendly methods of nanoparticle synthesis, there is an increasing interest in DES as a medium of electrochemical nanoparticle synthesis. The DES and their ionic liquid counterparts often act as stabilizers and reducing agents in metal nanoparticle synthesis. This helps to avoid the use of additional stabilizers/reducing agents in the process [2]. Further, the exceptional physical properties of these liquids provide novel routes for the synthesis of metal nanoparticle. Since the DES has relatively low surface tension, it can enhance nucleation rates compared to that in aqueous medium leading to a decreased particle size [3-4]. The choline chloride-based deep eutectic solvents containing AgCl were used for the fabrication of nanoporous Ag films on copper alloy substrates by galvanic replacement reaction [5]. Wei *et al.* demonstrated a shape controlled electrochemical method of synthesis of catalytically active platinum nanoparticles in DES without the addition of surfactants or seeds [6]. The stability of Pd nanoparticles electrodeposited in DES by cathodic reduction of K_2PdCl_4 on glassy carbon was studied recently by Hammons *et al.* [7].

Applications in the field of point of care devices, biosensors, electrocatalysts and SERS require stable and reproducible nanoparticle supported substrates. The

method of electrodeposition of nanoparticles provides a simple straight forward route to fabricate ready to use substrates. The electrodeposited mesoporous films exhibit excellent adhesion on to the substrate and are often tolerant to organic solvents and electrolytes when used for various applications. The process involving anodic dissolution followed by electrodeposition has been well explored in molecular solvents and offers an advantage of obtaining highly pure, well-adherent nanoparticle films on conducting substrates. By manipulating current density and electrodeposition time, the size and the thickness of the nanoparticle film can be controlled. There have been several reports of electrochemical synthesis of nanoclusters of gold, copper, zinc oxide, cobalt, bimetallic nanoclusters of Pd-Pt, Pd-Ni and Ag in molecular solvents [8-11].

The nanostructured materials have easily accessible surface active sites which could be exploited for catalytic applications. The electrocatalytic properties of mesoporous substrates are extensively studied for reactions occurring in fuel cells. With hydrogen being pursued as a promising alternative clean energy source, the electrochemical reduction of water can be an ideal method for the sustainable production of hydrogen. There have been several efforts to identify robust electrocatalyst for hydrogen evolution reaction (HER) to produce large cathodic currents at low over potentials [12-14]. The palladium and gold based materials are being explored as effective alternatives to the existing Pt electrocatalyst [15-16].

In this chapter, the methods of electrodeposition of metal nanoparticles of silver, gold and palladium on to metallic substrates by anodic dissolution in DES medium are presented. The electro catalytic performance of these mesoporous substrates is studied for hydrogen evolution reaction (HER) in acidic medium. Since the electrodeposition in DES is not associated with gas evolution, the mesoporous deposits are well adherent onto the metallic substrate and hence can withstand the vigorous hydrogen evolution reaction. The hydrogen evolution reaction on electrodeposited silver nanoparticle surface has not been reported in literature. Hence a detailed study on the catalyst is quite promising. The mechanisms of HER on Ag, Au and Pd are studied thoroughly by Tafel slopes and electrochemical impedance spectroscopy measurements.

5.2. Experimental

5.2.1. Material used

All the chemicals used in this study were analytical grade (AR) reagents. Choline chloride, ($(CH3)_3N$ (Cl) CH_2CH_20H) (Aldrich, 98%) was dried for 1 hour at 100 ^oC prior to use. Ethylene glycol, urea, sodium hydroxide, (Merck), 4-mercapto phenyl boronic acid (Aldrich), sodium borohydride (Aldrich), ethanol (Merck) were used as received. Methylene blue (MB) was used as analyte species in SERS studies.

Silver, gold, palladium wires each of 0.5mm diameter and tungsten wire (0.25mm diameter) of 99.99 % purity were purchased from Advent research materials.

5.2.2. Electrode pretreatment

Metal wires which were used as electrodes were polished in aqueous slurries of grades 1 μm, 0.3 μm, 0.05μm alumina successively, ultrasonicated in Millipore water and dried prior to use.

The electrochemical synthesis and insitu deposition of metal nanoparticles were carried out in ethaline (choline chloride + ethylene glycol) and reline (choline chloride + urea).

5.2.3. Electrochemical studies

A three compartment electrochemical cell was employed for cyclic voltammetry, electrochemical impedance spectroscopy (EIS) and Tafel analysis. Pt was used as counter electrode and a Saturated Calomel Electrode (SCE) as a reference electrode. The hydrogen evolution reaction on silver was studied using Ag/AgCl/3M NaCl as a reference electrode.

5.2.4. Electrochemical synthesis and *insitu* deposition of metal nanoparticles

The electrodeposition of nanoparticles was carried out in chronopotentiometric mode using two electrodes, kept parallel to each other at a distance of about 5mm. The DES medium was kept under constant magnetic stirring in an electrochemical cell of 10mL capacity. During the process, a mild gas evolution was seen at the

cathode in DES medium. This is in contrast to the vigorous gas evolution occurring in aqueous solutions due to H_2/O_2 evolution at cathode and anode that adversely affects the adhesion of the nanoparticles on the substrate. Evolution of gases in ethaline medium had been previously observed at the cathode during electrolysis under extreme conditions of high current density of 12 A/ dm^2 for a long exposure time and was attributed to the formation of choline base [17-18]. The nanoparticle coated electrodes were scanned in 0.1M H_2SO_4 prior to characterization to remove any organic species trapped within the porous substrates.

(a) Silver

For the formation of mesoporous film of silver, a W wire was used as substrate. A silver wire of diameter 0.5 mm was used as a sacrificial anode and W wire as a cathode. The tungsten wire was scanned in ethaline medium for the removal of tungsten oxide layer prior to electrodeposition. 4-Mercapto phenyl boronic acid (MPBA, 5 mM) was used as a stabilizer and sodium borohydride (0.15 M $NaBH_4$) as a reducing agent for the electrochemical synthesis of silver nanoparticles in ethaline medium maintained at 50 ^{0}C. The electrolysis was carried out at a current density of 14 mA cm^{-2}. The reaction was accompanied by the formation of a black film of Ag_2O on the Ag anode which subsequently dissolved in DES medium. The solubility of metal oxides in DES has been well known and is attributed to complexation of the solvent with metal oxides to form soluble species [19]. The color of the medium changes gradually from transparent to reddish brown, indicating the formation of Ag nanoparticles stabilized by MPBA. A simultaneous growth of mesoporous AgNPs was indicated by the formation of a black film at the cathode. The electrodeposition process was carried out for 1 h. The solution turned dark in color with time, which regained the original color after purification with ethanol through repeated sonication and decantation of the solvent. The mesoporous silver films were calcined at 250 ^{0}C for 2.5 h to remove the organic stabilizers adhering to the nanoparticle.

(b) Gold

Electrodeposition of gold nanoparticles was carried out by using a gold wire of diameter 0.5 mm and gold disk electrode of 1 mm diameter as anode and cathode respectively in reline medium. Sodium borohydride (0.05 M NaBH4) was used as reducing agent for the electrochemical synthesis of gold nanoparticles in reline medium at 50 ^{0}C. The addition of an external stabilizer was avoided due to the intrinsic ability of the medium to stabilize the nanoparticle formed [20]. The electrolysis was carried out at a current density of 0.3 Acm^{-2} for a duration of 30 min. The color of the medium changed rapidly from transparent to grayish blue to black, indicating the formation of gold nanoparticles stabilized by the medium. In situ electrodeposition of AuNPs was apparent from the black film on the cathode. The nanoparticles obtained in the solution were diluted and purified in ethanol for the UV studies.

(c) Palladium

Electrochemical synthesis of Pd nanoparticle in solution and simultaneous electrodeposition on a Pd wire acting as a substrate was carried out in ethaline medium under the room temperature conditions. The medium employed in the method serves to reduce the metal ions to metal nanoparticle and also to stabilize the nanoparticles formed. A Palladium wire of diameter 0.5 mm was used as a sacrificial anode. The process of electrodeposition was carried out at a current density of 1 A/cm^2 for 30 min. The solution turned black in a few minutes indicating the formation of Pd nanoparticles.

The optical properties of the purified nanoparticles dispersed in ethanol were studied by UV–Vis spectroscopy. The surface enhanced Raman studies were carried out on the electrodeposited mesoporous AgNP films for ligand characterization. The morphology and size of electrodeposited nanoparticles films were examined by SEM, EDAX and XRD.

5.3. Results and discussion

5.3.1. Characterization

The mechanism of electrodeposition of metal nanoparticle by anodic dissolution had been earlier reported by Reetz and Helbig [21]. By applying a current density, the metal was dissolved into the medium as ions (M^{n+}) which were subsequently reduced at the cathode. In addition to the electrochemical reduction at cathode surface, the presence of reducing agent in the medium also brings about chemical reduction of the metal ions leading to the formation of metal nano particles in the solution [22]. The broad surface plasmon bands of gold and silver nanoparticle solution shown in Fig. 1 are indicative of a polydispersed sample.

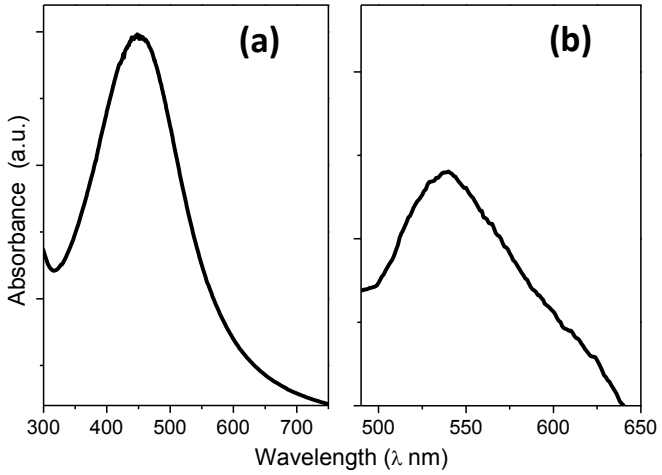

Figure 1. *UV-Vis absorption spectra of purified (a) silver (b) gold nanoparticles in EtOH*

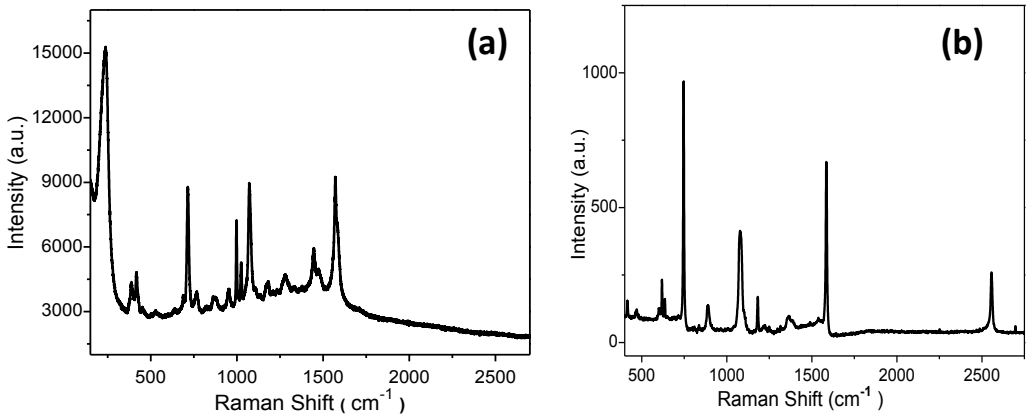

Figure 2. *(a) SERS of the MPBA signals on mesoporous silver substrate (b) normal Raman spectra of MPBA powder*

The surface enhanced Raman spectra shown in Fig. 2a confirm the presence of MPBA monolayer formed on the mesoporous AgNP electrode. Raman spectrum of pure MPBA is provided in Fig. 2b for comparison. The Raman signal at 220 cm^{-1} corresponding to Ag-S bond, confirms the chemisorption of thiol monolayer on AgNPs [23]. The Raman signal at 2575 cm^{-1} band seen in Fig.2b corresponds to free -SH groups. The absence of the band in the SERS spectrum of the mesoporous substrate indicates that free MPBA molecules did not contribute to the signal intensity in spectra. Assuming a monolayer film of MPBA on the surface of nanoparticles, the SERS signal enhancement due to mesoporous nature of AgNP film was calculated to be 10^6 compared to the normal Raman spectra of known concentration of MPBA dropcasted on a Si wafer.

The surface XRD patterns of the mesoporous substrate were obtained in the 2θ range of 30–80 ^{0} for an exposure time of 1 h. A comparison of the xrd pattern of a

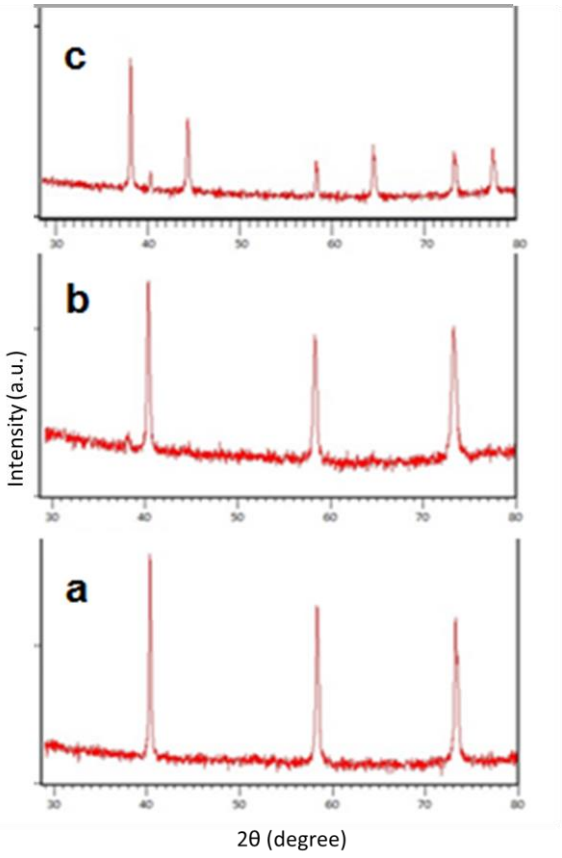

Figure 3. *XRD pattern of (a) W wire (b) AgNP coated W wire (c) AgNP coated W wire calcined at 250 ^{0}C*

bare W wire, AgNP modified W wire and calcined AgNP modified Wwire is given in Fig.3 a, b and c respectively. The XRD peak in Fig.3b at 38.3 ^{0} and the humps at 44.5 ^{0} and 64.5 ^{0} were assigned to (111), (200) and (220) crystal planes, indicating that the mesoporous Ag film possess face centered cubic structure [24]. The additional sharp peaks observed in the XRD spectra correspond to W wire. The average particle size of the electrodeposited Ag nanoparticles was determined by XRD using Debye–Scherer's equation and was found to be 34.5 nm. On calcination at 250 ^{0}C for 2.5 h, the XRD peaks (Fig. 3c) corresponding to fcc nanostructure of mesoporous Ag became more intense *wrt* peaks as compared to that prior to calcination. This is evidently due to the surface reorganization at high temperature during calcination. A similar observation had been reported when AgNPs were calcined to remove organic impurities [25].

The surface XRD pattern of mesoporous gold substrate shown in Fig. 4a can be indexed to fcc nanostructure from the peaks occurring at 38.3^0 (111), 44.5^0 (200), 64.2^0 (220), 77.7^0 (311), 81.8^0 (222) [8]. The average size of nanoparticle was calculated to be 28 nm Fig. 4a displays the surface XRD pattern of Pd nanoparticles deposited on Pd. The mesoporous Pd exhibited face centered cubic (fcc) pattern with peaks at 39.9 ^{0} (111), 46.9^0 (200), 67.9^0 (220). The XRD pattern showed additional peaks at 39 ^{0} and 45 ^{0}, which cannot be indexed to Pd (fcc). These additional peaks were also observed earlier and were attributed to the lattice expansion of Pd on absorbing hydrogen [26-27]. The study also showed that complete desorption of trapped hydrogen from the lattice could not be achieved even by high temperature treatments. In our studies, the nanoparticle synthesis is not accompanied by hydrogen evolution. However, electrochemical scanning in acid medium prior to characterization to remove trapped organic species could have resulted in the formation of surface hydrides [28]. The metal hydride formation observed in the case of Pd nanoparticle, under similar electrochemical pretreatment as that of gold and silver was due to the enhanced hydrogen absorption and adsorption ability of Pd over the latter.

SEM images given in Fig. 5 show the mesoporous deposition of silver on W wire at different magnifications. The dendritic growth of the Ag nanoparticles seen in the interior regions may correspond to initial stages of electrodeposition

which grow as clusters in later stages. Fig. 6 shows the SEM images of AgNP film on Pt/Rh substrate calcined at 250 ^{0}C for 2.5 h. The morphology of the nanoparticle changes notably, as AgNPs aggregate to form a network like structure.

The EDAX data of the as prepared sample is provided in Fig.7a. The results obtained shows that the mesoporous film does not cover the underlying tungsten substrate completely. Further the elemental composition indicates that the stabilizer molecules of 4-Mercapto phenyl boronic acid is bound to the mesoporous film even after the solvent treatment and electrochemical potential scanning in 0.1M H_2SO_4. The EDAX of the calcined substrate provided in Fig.7b, clearly shows that the stabilizer molecules are removed from the substrate. On calcination, the mesoporous film undergoes surface restructuring owing to which the underlying the elemental composition of tungsten is significantly decreased from 7% to 0.33%. The surface restructuring owing to calcination was evident in SEM and XRD also. The prepared mesoporous substrate is intended to be used for electrocatlytic applications. Hence the decreased composition of the underlying W substrate ensures that any observed electrocatalytic activity of the prepared substrate can be attributed only to the mesoporous film.

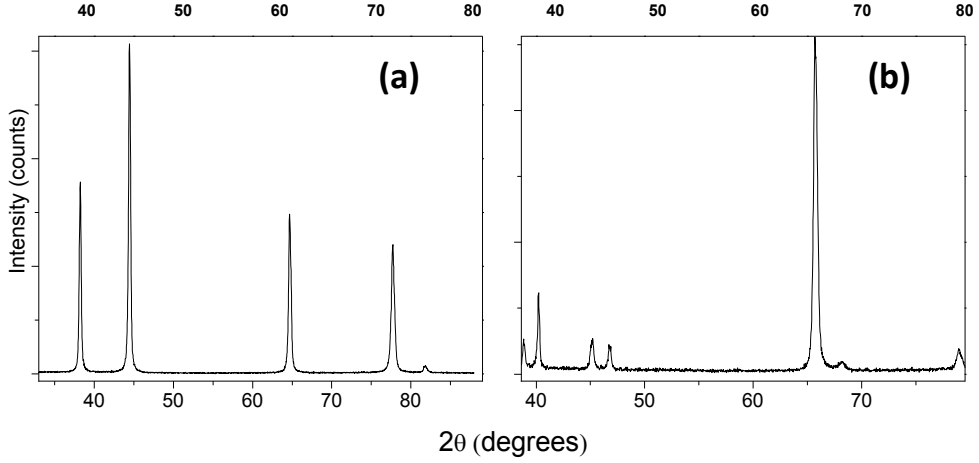

Figure 4. *XRD pattern of (a) AuNP/Au (b) PdNP /Pd*

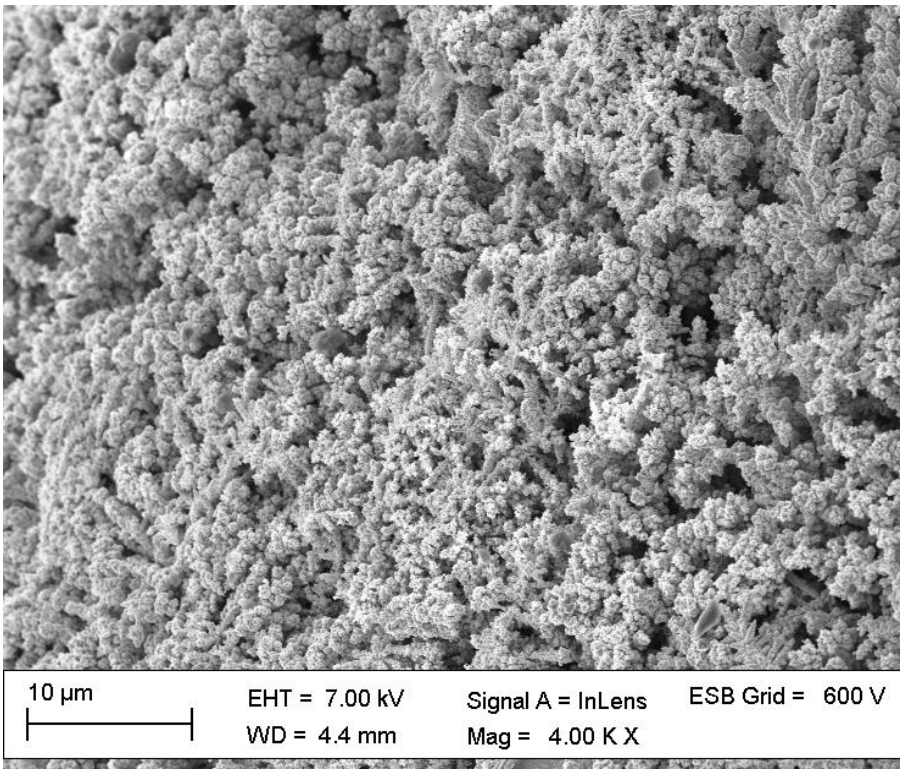

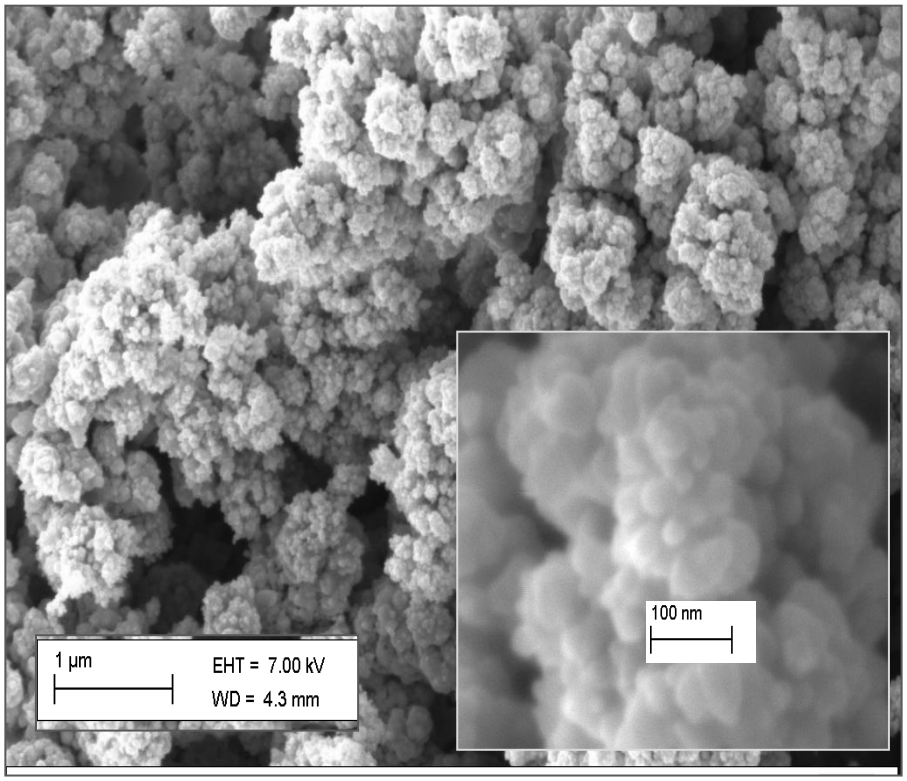

Figure 5. *SEM images of the mesoporous AgNP film on W wire before calcination*

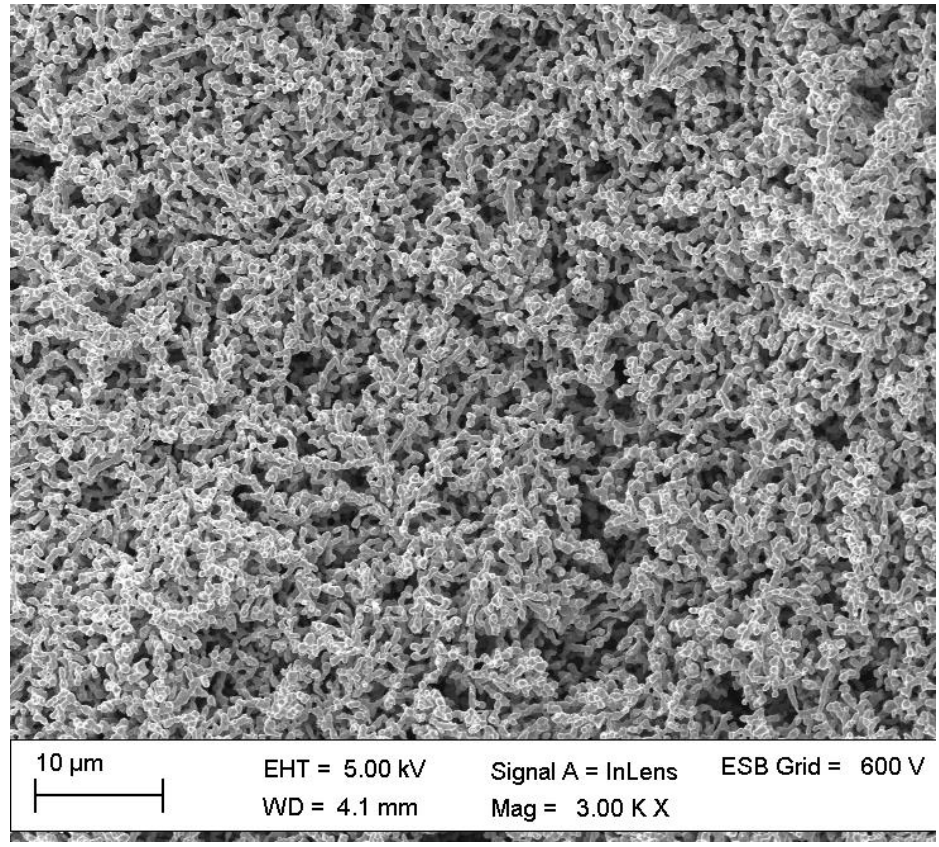

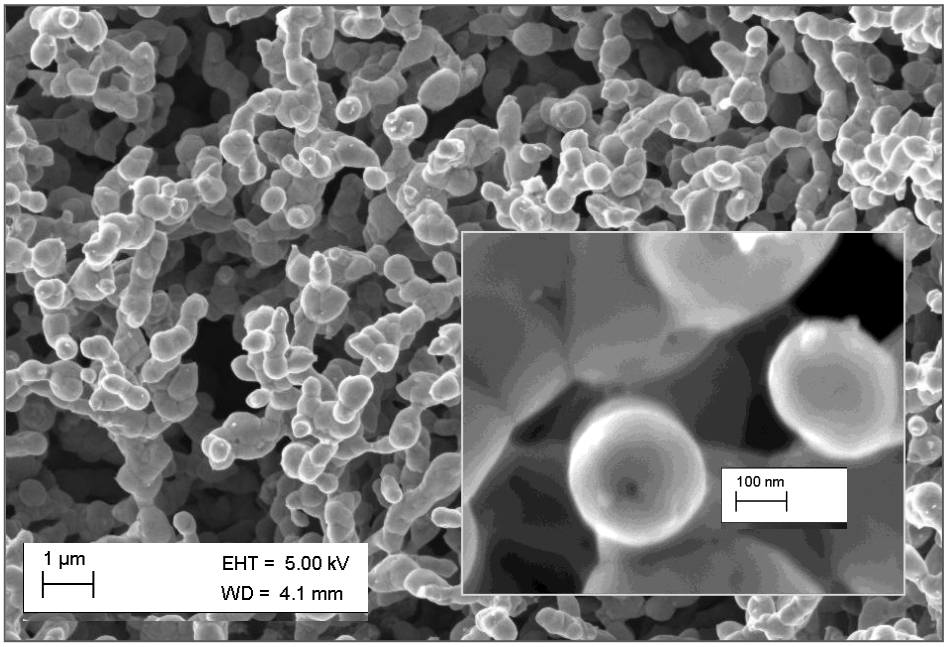

Figure 6. *SEM images of the mesoporous AgNP film on W wire after calcination*

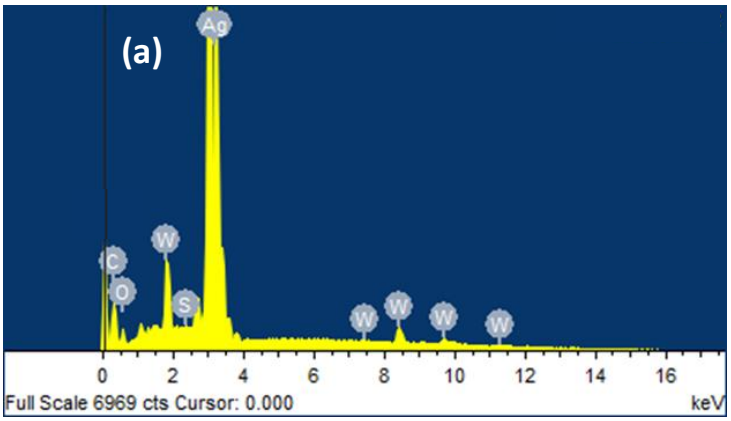

Element	Weight%
C	2.70
O	4.68
S	0.04
Ag	85.42
W	7.16
Totals	100.00

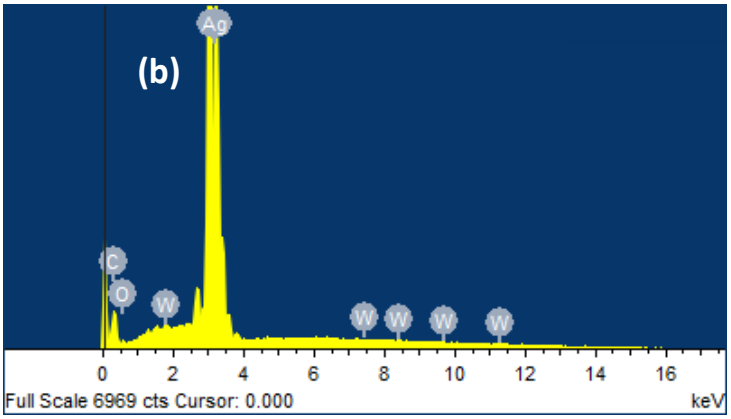

Element	Weight%
C	1.36
O	0.46
Ag	97.85
W	0.33
Totals	100.00

Figure 7. *EDAX of the mesoporous AgNP film on W wire (a) before and (b) after calcination*

Fig. 8a shows the SEM images of gold substrate containing electrodeposited nanoparticles of ~30 nm size. The highly porous nature of the nanostructured Pd film on Pd substrate deposited for an electrodeposition time of 30 min is displayed in Fig. 8b. Pd is a metal well known for its ability to absorb hydrogen and the porous nature of the specimen obtained in our studies puts forth a potential application to be used as a hydrogen storage material. The EDAX spectrum and elemental composition of mesoporous film of Au and Pu are given in Fig. 9 a and b respectively.

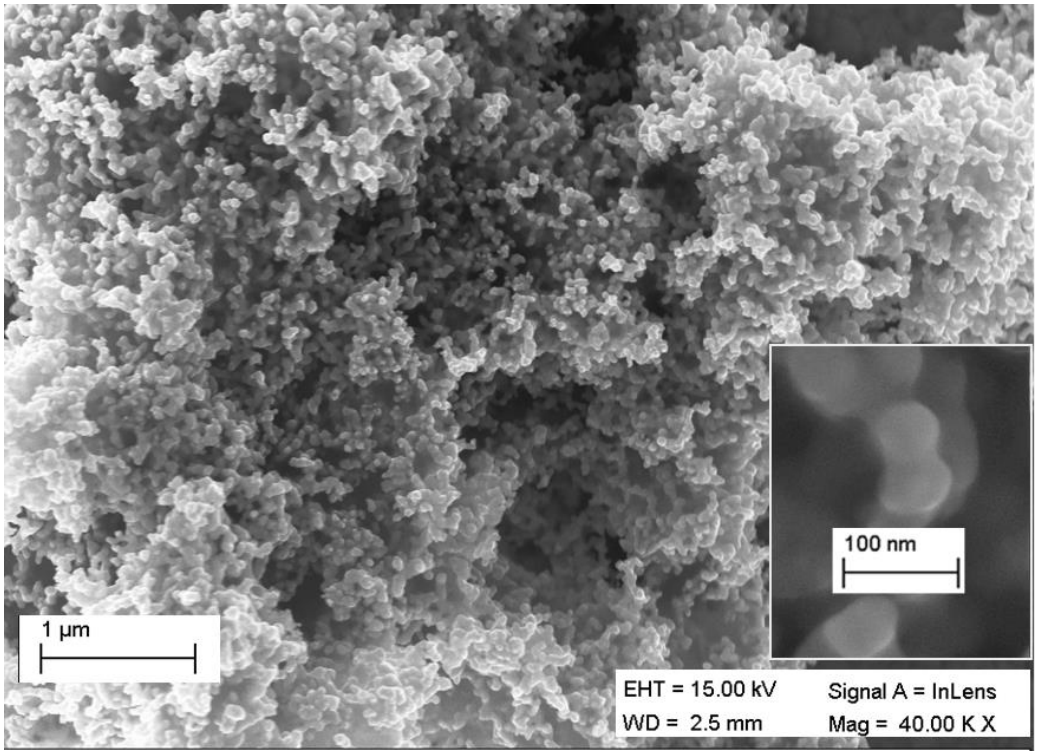

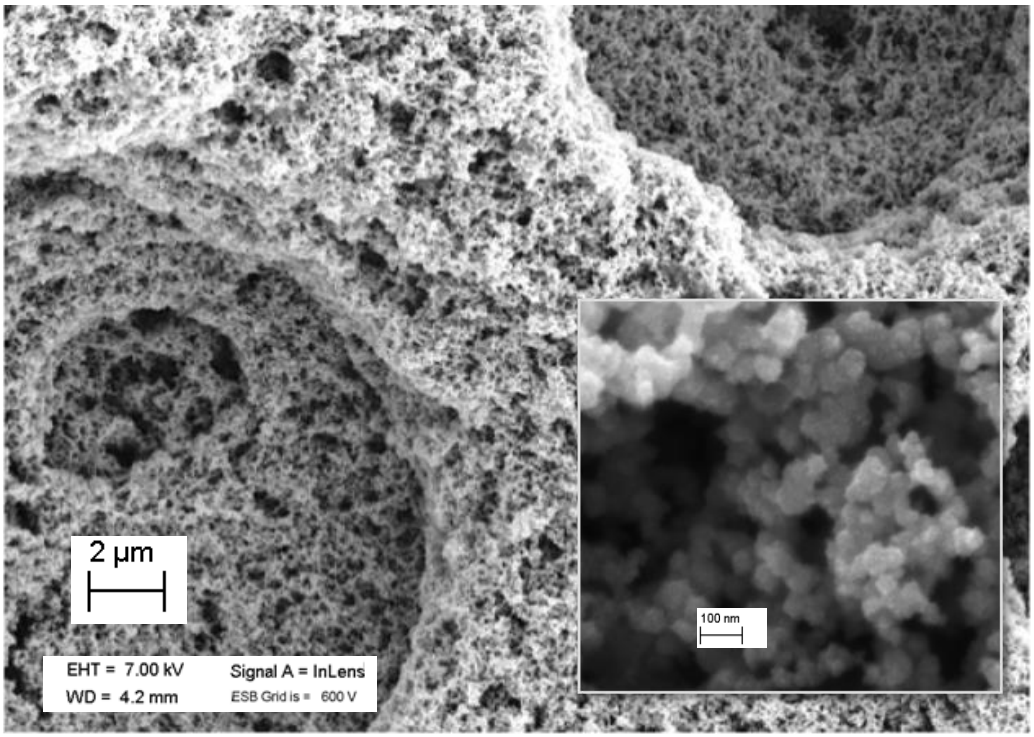

Figure 8. *SEM images of mesoporous (a) AuNP film on Au (b) PdNP film on Pd. Inset shows the magnified images with 100 nm scale-bar.*

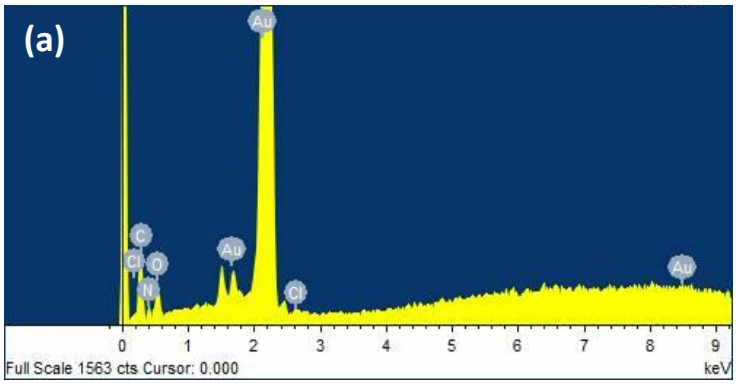

Element	Weight%
C K	6.95
N K	2.30
O K	1.95
Au M	88.8
Totals	100.00

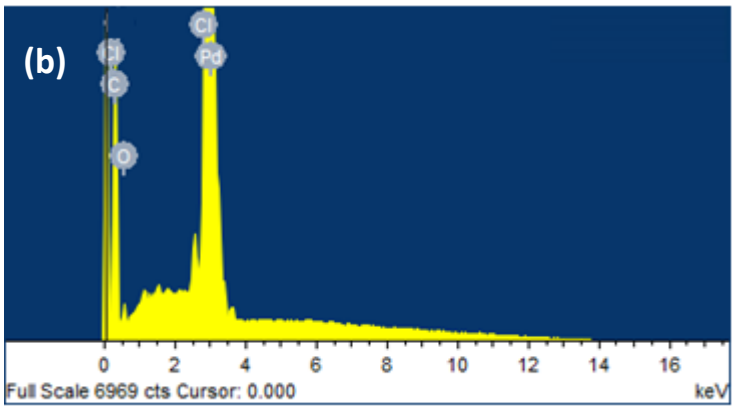

Element	Weight%
C K	4.84
O K	1.22
Pd L	95.53
Totals	100.00

Figure 9. *EDAX results of mesoporous (a)Au NP film on Au (b)PdNP film on Pd*

5.3.2. Electrocatalytic activity of the mesoporous metallic substrates towards hydrogen evolution reaction in acidic media

HER is one of the most investigated electrochemical reaction, which can be performed either in acidic or alkaline medium. Studies carried out till date, on the mechanism of HER in acidic medium involve primarily a proton discharge (Volmer step) at the metal surface, followed by either Tafel or Heyrovsky steps.

$$M + H_3O^+ + e^- \xrightarrow{k_1} MH_{ads} + H_2O \quad (1)$$

Tafel step (2) consists of the chemical combination of adsorbed hydrogen atoms on metal whereas Heyrovsky step (3) involves electrochemical desorption.

$$2MH_{ads} \xrightarrow{k_2} 2M + H_2 \quad (2)$$

$$MH_{ads} + H^+ + e^- \xrightarrow{k_3} 2M + H_2 \quad (3)$$

where, M represents free metal sites at the electrode, MHads represents the adsorbed hydrogen atom on the metal surface, k_1 (eq. 1), k_2 (eq. 2), and k_3 (eq. 3) are the rate constants of the Proton discharge, Tafel and Heyrovsky steps respectively.

Thus, Volmer-Tafel and Volmer –Heyrovsky mechanism are commonly proposed pathways to explain the reduction of protons at the metal surface giving rise to hydrogen evolution. The rate determining step in either of the two pathways can be determined from the Tafel plot of HER (log I Vs E). The slope of the Tafel plot gives an idea on the rate determining step in either of the mechanism while the intercept gives the exchange current density for the reaction. While a Tafel slope of 30mV/dec indicates Tafel mechanism, a slope of 120mV/dec predicts either Volmer or Heyrovsky mechanism to be the rate determining step. Electrochemical Impedance spectroscopy has also been used to study HER, by following impedance changes with applied cathodic potential.

In our work, we have carried out cyclic voltammetry, Tafel Analysis and EIS to evaluate the potential electrocatalytic applications of mesoporous substrates and also to investigate the mechanism of HER followed in the process. Current densities reported in figures are calculated from geometrical area. Nitrogen was purged to remove any dissolved oxygen present.

5.3.2.1. Electrochemical response of AgNP coated W wire

Fig.10 shows the cyclic voltammogram of silver nanoparticle modified W substrate and that of bare W substrate. The peak observed at 0.3V (Vs Ag/AgCl) of mesoporous silver substrate correspond to reduction of silver oxide. The mesoporous Ag film was studied for HER in acidic medium. As a preliminary study, cyclic Voltammetry was performed and the results under identical conditions were compared to that of bulk silver wire. Fig.11 shows that the onset potential for HER with bulk Ag electrode used in our studies occurs almost at -0.620 V.

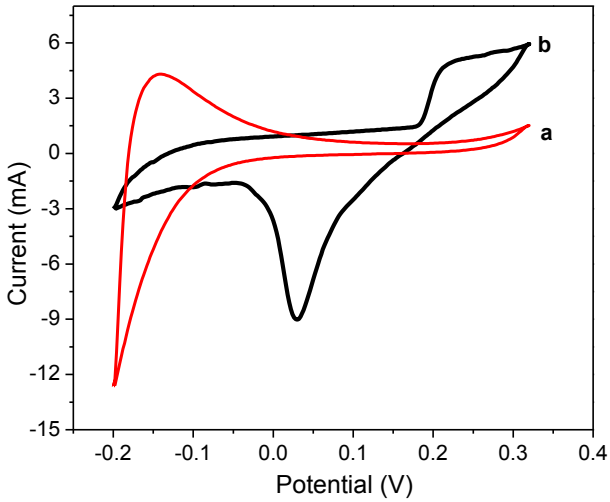

Figure 10. *Cyclic voltammogram of a) bare W wire b) AgNP electrodeposited on W wire at a scan rate of 100m V/s in 0.25M $HClO_4$ Vs Ag/AgCl/3M NaCl Reference electrode*

The voltammograms of porous AgNP film in 0.25M $HClO_4$ shows a lowering of onset potential for HER wrt Ag wire electrode by 100m V. The variation in onset potential of HER with crystallographic orientation of Ag has been earlier studied by Diesing *et al.* in neutral perchlorate medium. The group extended these studies

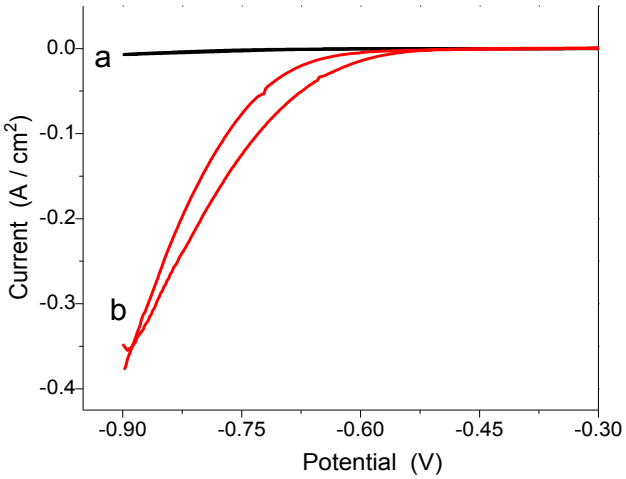

Figure 11. *Cyclic voltammograms of (a) Ag wire (b) AgNP deposited on W wire at a scan rate of 100mV/s in 0.25M $HClO_4$ Vs Ag/AgCl/3M NaCl*

to different pH and observed that onset potentials were not affected with crystallographic orientation in acidic medium [29]. The value of -0.62V Vs Ag/AgCl obtained in our studies agree well with the reports on Ag (111) single crystal electrode in acidic medium of ~ -0.4 V Vs NHE [30].

The electrocatalytic applications of citrate capped AgNP modified basal plane pyrolytic graphite (BPPG) in HER has been studied by Campbell *et al.* [31]. The onset potential reported here is about +0.6V more positive than the values measured by the group which was at -1.25V and was found to be dependent on the surface coverage of AgNP on BPPG. To the best of our knowledge, there has not been any other report on the electrocatalytic applications of AgNPs in acidic medium for HER. The porous AgNP film exhibits a current density of 375mA/cm^2 (normalized to geometrical area) for HER with respect to that of silver wire electrode (7mA/cm^2), an increase by a factor of about 50.

Tafel plots were obtained from the chronoamperometric data at different over potentials of hydrogen evolution for AgNPs coated electode as shown in Fig.12a. A Tafel slope of 110mV /decade was obtained for porous silver nanoparticle coated electrode. The slope indicates that the reaction follows the Volmer-Heyrovsky mechanism involving an initial proton discharge step followed by electrochemical desorption process. Reported results based on Tafel slopes till date also predicts porous AgNP film in our studies follow Volmer-Heyrovsky mechanism, with Volmer step possibly being the rate determining step. Recently, mechanism of hydrogen evolution has been studied on (100) plane of silver by potentiostatic current transients at overpotentials $\eta > 0.7$V in acidic solutions [32]. Mechanism involved in the process was Volmer-Heyrovski with Volmer step being the rate determining step.

Electrochemical Impedance spectroscopy studies were carried out to get further insight onto the kinetics of the process. EIS was performed at -540mV to -660mV for a frequency range of 100 kHz to 100 mHz at an ac amplitude of 10mV. Nyquist plots for HER on porous AgNP electrode in 0.25M $HClO_4$ is shown in Fig.12b.

At high overpotentials and low frequencies, an inductive loop can be seen in Fig.12b. This has been observed in HER of other metal surfaces too and has been attributed to the formation of electrosorbed intermediate layers at the surface [33]. Low frequency inductive loop observed in HER was accounted for by the single adsorbed species mechanism by Harrington [34]. The mechanism proposed

involves two distinct electron transfer steps on the metal sites (eqn 1and 3) consisting of hydride formation and dehydrogenation. Thus, EIS data, in addition to Tafel analysis further confirms that Volmer-Heyrovsky pathway is followed for HER on porous AgNP films on W. The decrease in the diameter of the semicircle is indicative of Rct which decreases with applied cathodic over potential showing faster charge transfer kinetics at higher overpotential. The equivalent circuit fitting of the EIS data provided in Fig.13 shows that R_{ct} lowers from 13000 ohms at -540 mV to a mere 1000 ohms at -660 mV.

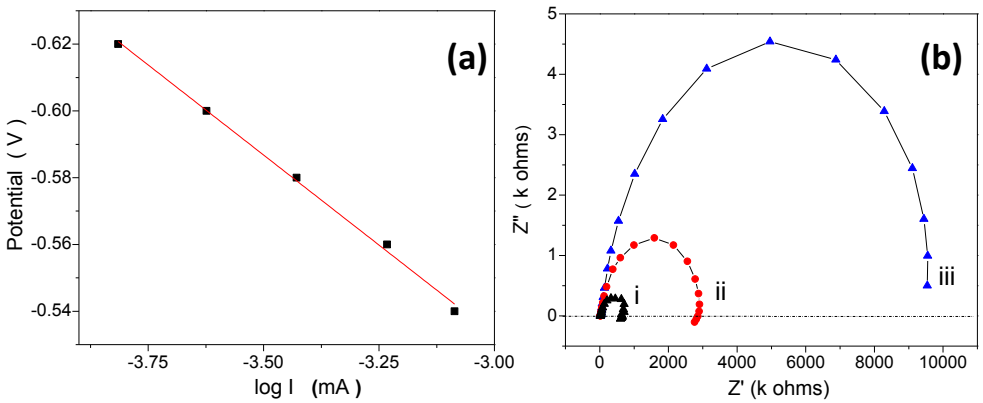

Figure 12. *(a) Tafel plots (b) Nyquist plots for HER of porous AgNP coated W wire at (i)-660mV (ii)-600mV (iii)-540 mV in 0.25M $HClO_4$ under N_2 atmosphere*

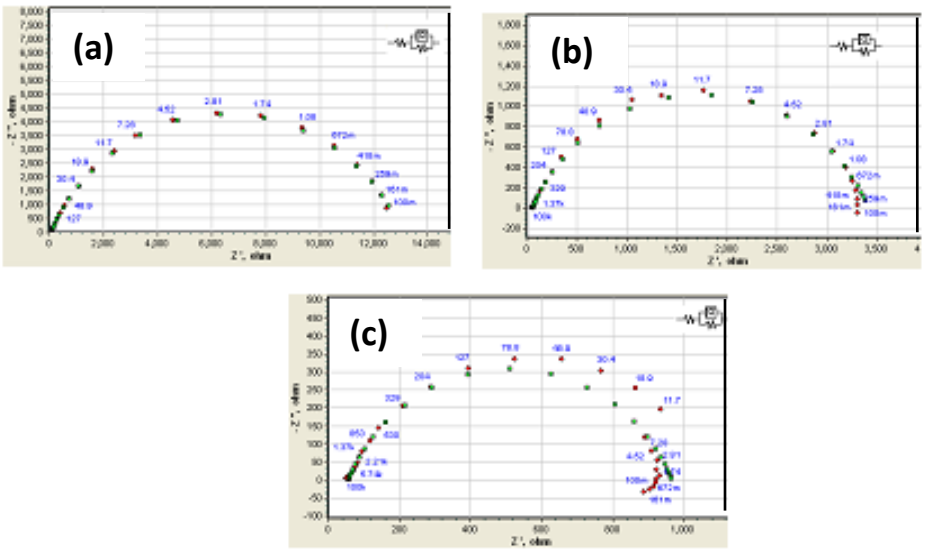

Figure 13. *Equivalent circuit fitting of the Nyquist plots for HER of AgNP modified W wire performed at (a)-540mV (b)-600mV (c)-660 mV.*

5.3.2.2. Electrochemical response of AuNP coated on gold disc electrode

The electroactive surface area (ECSA) of gold nanoparticle coated gold disc electrode was determined from the charge associated with stripping peak of gold oxide in 0.1M H_2SO_4. Fig.14a shows the cyclic voltammograms of mesoporous gold in 0.1M H_2SO_4, with a well defined stripping peak corresponding to gold oxide at 0.82 V (charge associated with stripping peak -550 μC). The highly porous nature of the surface is apparent from the ECSA of 1.45 cm^2 for a geometric area of 0.00785 cm^2. The electrocatalytic activity of mesoporous AuNP film on gold disc electrode in HER was evaluated in comparison to an unmodified gold disc electrode by cyclic voltammetry given in Fig.14b. The mesoporous substrate exhibits distinctly enhanced performance over its unmodified counterpart as evident from positive shift in onset potential and increased current densities.

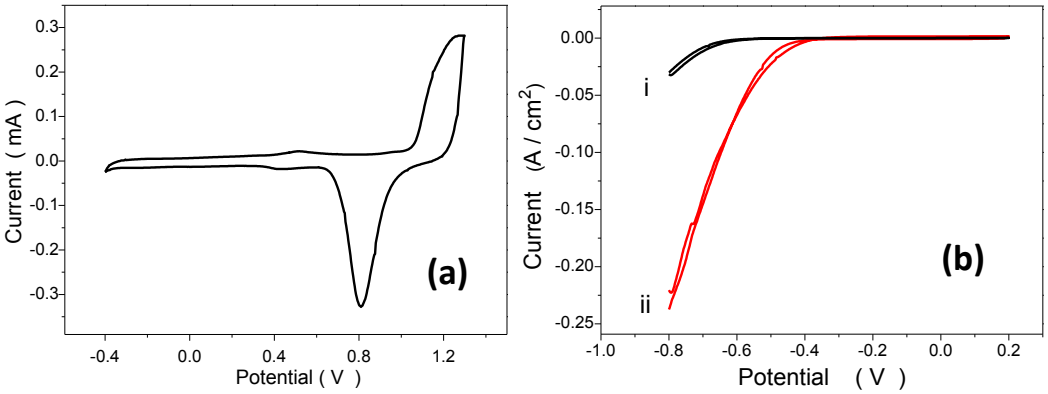

Figure 14. *(a) Cyclic voltammogram of AuNP /Au disc electrode (b) HER at (i) Au disc electrode (ii) AuNP modified Au disc electrode at a scan rate of 100m V/s in 0.1M H_2SO_4 Vs SCE*

The onset potential for hydrogen evolution on mesoporous gold substrate occurs at -360 mV, as compared to -580mV in unmodified gold disc electrode. Current density for HER when normalized to the electroactive surface area corresponds to 1.5 m A/cm^2. The current density measured is about an order of magnitude higher than the value reported earlier by Plowman *et al.* [35]. Plowman *et al*. studied gold nanospikes prepared by electrochemical route and evaluated their catalytic activity in HER in terms of onset potential (-0.3 Vs

Ag/AgCl) and current density (0.16 m A/cm^2). Costa *et al.* also has studied the catalytic effect of AuNP modified on screen printed graphite electrodes by dropcasting varying concentrations of gold nanoparticle in HCl. The onset potential was found to decrease with increasing concentrations of AuNP from pM to nM (-0.8V to -0.3 V Vs Ag/AgCl) [36].

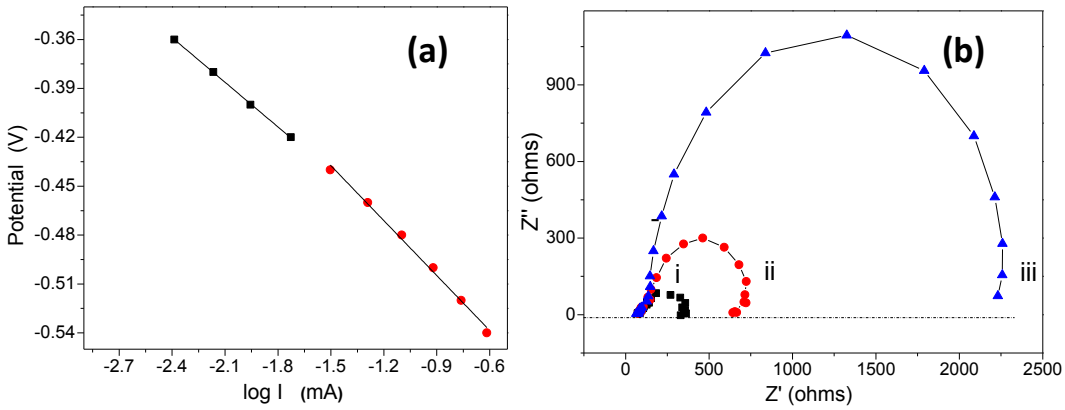

Figure 15. *(a) Tafel plots (b) Nyquist plots at (i) -500 mV (ii) -450mV (iii) -400mV for HER of porous AuNP modified Au disc electrode in 0.1M H_2SO_4 under N_2 atmosphere*

The mechanism of HER on gold has been studied in detail previously by a number of groups with significant consideration on their crystallographic orientation. The catalytic activity of low index planes of gold was compared by Perez *et al.* [37]. The mechanism of HER for all orientations was found to be the same, with (111) plane exhibiting maximum activity. Further, HER studies on gold till date yielded two tafel slopes at low and high overpotentials respectively [38-40]. Volmer – Tafel mechanism has been the proposed pathway for HER, with the discharge process being the rate determining step. Hydrogen adsorption on Au is considered to be energetically unfavorable making the discharge process slow while the weak Au-H bond makes the desorption process fast [41].

In this study, Tafel analysis [Fig.15a] yielded two slopes of 90 mV and 112 mV at low and high overpotentials respectively. The electrochemical impedance studies [Fig.15b] shows the lowering of R_{ct} values with overpotential. A careful analysis of the Nyquist plot given in at lower overpotential confirms the absence of an inductive loop, thus excluding Heyrovsky mechanism as in the case of AgNP described earlier.

The equivalent circuit fitting of the EIS data obtained is presented in Fig.16. The constant phase element obtained by equivalent circuit fitting has an n value 0.8 in all cases with no significant change in CPE values (1x 10^{-5} S sec^{n}). The R_{ct} decreases from 2500 ohms at -400 mV to 350 ohms at -500 mV.

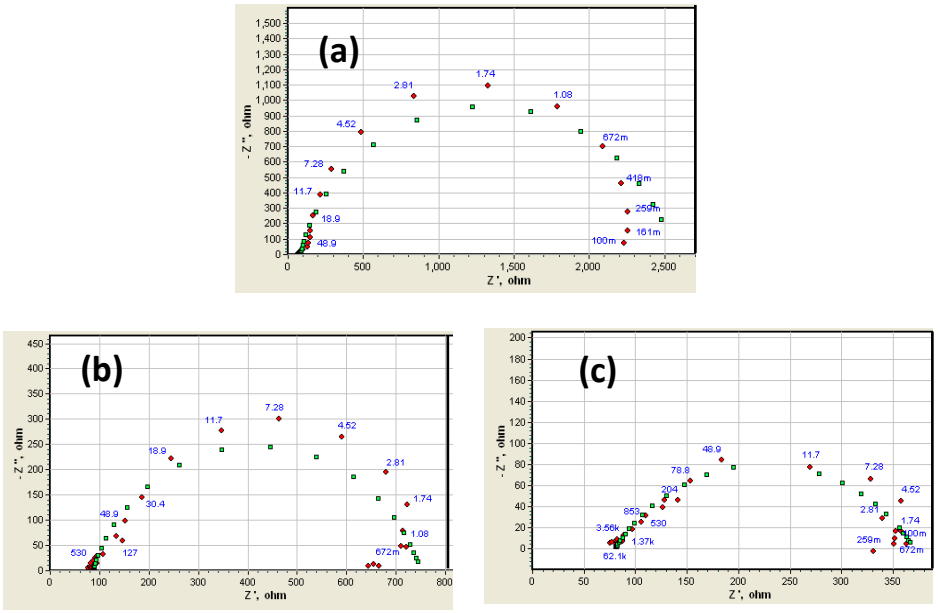

Figure 16. *Equivalent circuit fitting of the Nyquist plots for HER of AuNP modified Au disc electrode performed at a) -400mV b) -450mV c) -500 mV*

5. 3.2.3. Electrochemical response of PdNP coated on Pd wire

Fig.17a shows the cyclic voltammogram of Pd NP modified Pd wire in 0.1M H_2SO_4 in a scan range of -0.4 V to 1 V exhibits peaks in both anodic and cathodic scans. The broad peak extending around 0V is attributed to the oxidation of adsorbed and absorbed hydrogen within the palladium lattice. The formation of PdO extending beyond 0.7 V is accompanied by potential oscillations that continue during the initial stages after the potential reversal. It is probable that the simultaneous oxidation of adsorbed hydrogen and palladium have contributed to the oscillations. A true surface area of 0.35 cm^2 for a geometric area of 0.023 cm^2 indicated the mesoporous nature of Pd substrate.

The onset potential for HER is almost halved in the nanoparticle modified Pd wire compared to bulk Pd wire as seen in Fig.17b. The HER on the mesoporous Pd electrode commences at significantly lower potential (-0.256 V) compared to that

of unmodified Pd wire (-0.52V) Vs SCE. Another striking feature exhibited by these mesoporous substrate is that the overpotential required for the onset of hydrogen evolution is only few mV (50mV) with respect to open circuit potential (-204mV) in 0.1M H_2SO_4.This makes the Pd nanoparticle coated substrate advantageous for the development of highly efficient HER catalyst. The current densities given in the figure are normalized to the true surface area.

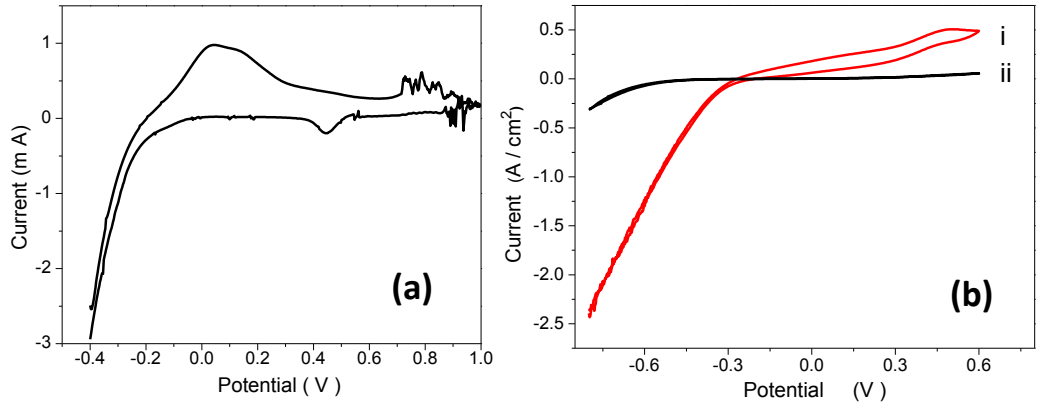

Figure 17. *(a) Cyclic voltammogram of PdNP modified Pd wire (b) HER at (i) Pd wire (ii) PdNP modified Pd wire at a scan rate of 100m V/s in 0.1M H_2SO_4 Vs SCE*

The hydrogen evolution reaction on bulk Pd electrodes has been already been studied elaborately, with many groups proposing Volmer-Tafel mechanism for the process. In our stdies, Tafel analysis were performed in a potential range of -0.24 V to - 0.4 V yielded a slope of 110mV indicating the proton discharge process to be the rate determining step [Fig.18a].

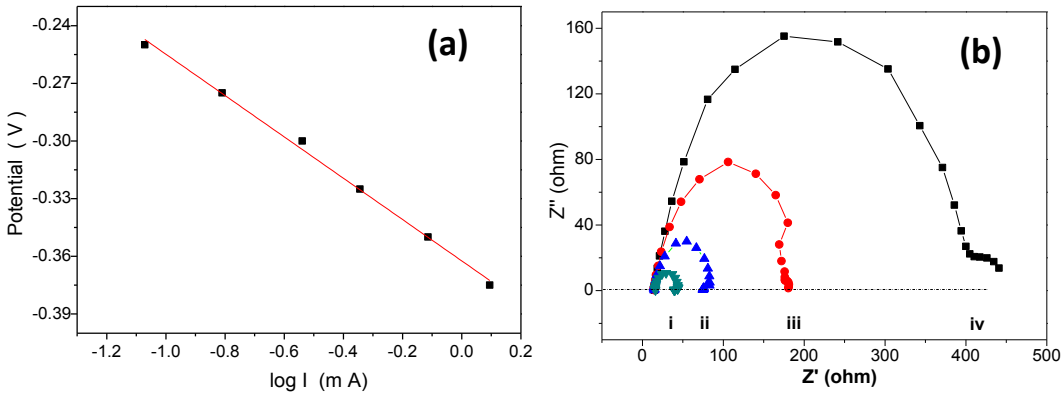

Figure 18. *(a) Tafel plots (b) Nyquist plots at (i) -400 mV (ii) -350mV (iii) -300mV (iv) -250 mV for HER of porous PdNP modified Pd wire electrode in 0.1M H_2SO_4 under N_2 atmosphere*

The EIS analysis further points towards the same, excluding the possibility of Heyrovsky mechanism. A lowering of charge transfer resistance due to the increasing rate of the reaction with overpotential is evident from Fig.18b. The equivalent circuit fitting given in Fig.19 reveals that R_{ct} decreases substantially beyond 50 ohms at an overpotential of mere -400mV. The constant phase element varied between 0.8 - 2x 10^{-5} S sec^{n} with n value corresponding to ~ 0.9.

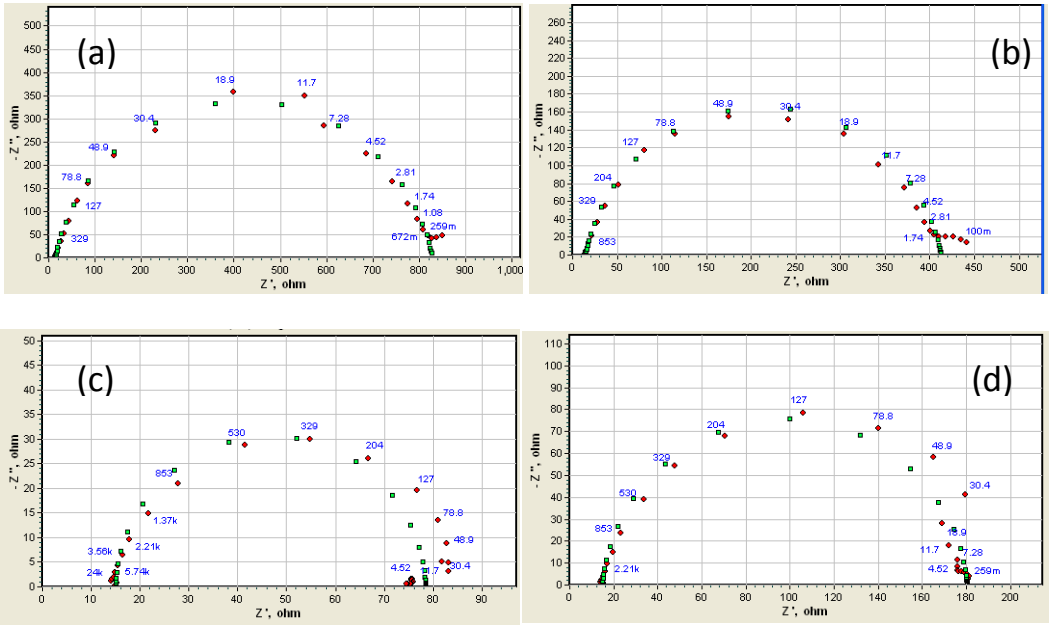

Figure 19. *Equivalent circuit fitting of the Nyquist plots for HER of PdNP modified Pd wire performed at (a) -200mV (b) -250mV (c) -300 mV (d)-350 mV*

5.4. Conclusions

The electrochemical synthesis and deposition of noble metallic particles on to metallic substrate reported here provide a simple and efficient technique to generate well adherent mesoporous films of metal nanoparticles. The passivation of silver usually observed during the anodic dissolution process in aqueous medium was not observed in DES. All the porous nanostructured films of silver, gold and palladium exhibited a good electrocatalytic activity for HER, with substantial lowering of onset potential and increased current densities with respect to the corresponding bulk metals. The overpotential required for HER on PdNP

modified substrate was very small in the order of few millivolts with respect to the open circuit potential. Further applications of these porous metallic films in field of sensors are presently being explored.

References

1. A.P. Abbott, K.E. Ttaib, G. Frisch, K.J. McKenzie and K.S. Ryder, *Phys. Chem. Chem. Phys*., 2009, **11**, 4269.
2. H.G. Liao, Y.X. Jiang, Z.Y. Zhou, S.P. Chen and S.G. Sun, *Angew. Chem. Int. Ed. Engl.*, 2008, **47**, 9100.
3. A.V. Mudring, T. Alammar, T. Bäcker and K. Richter, *ACS Symp. Ser.*; 2010, ch. 12, 177.
4. K. Richter, P.S. Campbell, T. Baecker, A. Schimitzek, D. Yaprak and A.V. Mudring, *Phys. Status Solidi. B*, 2013, **250**, 1152.
5. C.D. Gu, X.J. Xu and J.P. Tu, J. Phys. Chem. C, 2010, **114**, 13614.
6. L. Wei, Y. Fan, N. Tian, Z. Zhou, X. Zhao, B. Mao and S. Sun, *J. Phys. Chem. C*, 2012, **116**, 2040.
7. J. A. Hammons, T. Muselle, J. Ustarroz, Maria Tzedaki, M. Raes, A. Hubin and H. Terryn, *J. Phys. Chem. C*, 2013, **117**, 14381.
8. D. H. Nagaraju and V. Lakshminarayanan, *J. Phys. Chem. C*, 2009, **113**, 14922.
9. B. Stypuła, J. Banas, M. Starowicz, H. Krawiec, A. Bernasik and A. Janas, *J. Appl. Electrochem.*, 2012, **36**, 1407.
10. B. Stypula, M. Starowicz, M. Hajos, E. Olejnik, *Arch. Metall. Mater*., 2011, **56**, 287.
11. J. A. Becker, R. Schäfer, R. Festag, W. Ruland, J.H. Wendorff, J. Pebler, S.A. Quaiser, W. Helbig and M.T. Reetz, *J. Chem. Phys*., 1995, **103**, 2520.

12. J. Yang, D. Voiry, S.J. Ahn, D. Kang, A.Y. Kim, M. Chhowalla and H.S. Shin, *Angew. Chem. Int. Ed. Engl.,* 2013, **52**, 13751.

13. K.R. Koboski, E.F. Nelsen and J.R. Hampton, *Nanoscale Res. Lett.*, 2013, **8**, 528.

14. D. Voiry, M. Salehi, R. Silva, T. Fujita, M. Chen, T. Asefa, V.B. Shenoy, G. Eda and M. Chhowalla, *Nano Lett.,* 2013, **13**, 6222.

15. L. Wang, U. Stimming and M. Eikerling, *Electrocatalysis*, 2010, **1**, 60.

16. A. Safavia, S. H. Kazemic and H. Kazemia, *Fuel*, 2014, **118**, 156.

17. K. Haerens, E. Mathinjs, K. Binnemans and B.V. der Bruggen, *Green Chem.*, 2009, **11**, 1357.

18. K. Haerens, E. Mathinjs, A. Chmielarz and B.V. der Bruggen, *J. Environ. Manage.*, 2009, **90**, 3245.

19. A. P. Abbott, G. Capper, D. L. Davies, K. J. McKenzie and S. U. Obi, *J. Chem. Eng. Data*, 2006, **51**, 1280.

20. M. Chirea, A. Freitas, B.S. Vasile, C. Ghitulica, C.M. Pereira and F. Silva, *Langmuir*, 2011, **27**, 3906.

21. M. T. Reetz and W. Helbig, *J. Am. Chem. Soc.,* 1994, **116**, 7401.

22. D. H. Nagaraju and V. Lakshminarayanan, *Langmuir*, 2008, **24**, 13855.

23. L. Skantarov, A. Orinak, R. Orinakova and F. Lofaj, *Nano-Micro Lett.*, 2012, **4**, 184.

24. S. Gurunathan, K. Kalishwaralal, R. Vaidyanathan, D. Venkataraman, S.R.K. Pandian, J. Muniyandi, N. Hariharan and S.H. Eom, *Colloid Surface B.*, 2009, **74**, 328.

25. P. Mukherjee, M. Roy, B. P. Mandal, G. K. Dey, P. K. Mukherjee, J. Ghatak, A. K. Tyagi and S. P. Kale, *Nanotechnology*, 2008, **19**, 075103.

26. T. H. Phan, R. E. Schaak, *Chem. Commun*., 2009, 3026.

27. D. Jose, B. R. Jagirdar, *Int. J. Hydrogen Energy*, 2010, **35**, 6804.

28. Y. Gimeno, A. H. Creus, S. Gonzalez, R. C. Salvarezza and A. J. Arvia, *Chem. Mater*., 2001, **13**, 1857.

29. D. Diesing, H. Winkes and A. Otto, *Phys. Status Solidi*., 1997, **159**, 243.

30. D. Eberhardt, E. Santos and W. Schmickler, *J. Electroanal. Chem*., 1999, **461**, 76.

31. F. W. Campbell, S. R. Belding, B. Ronan, L. Xiao and R. G. Compton, *J. Phys. Chem. C*, 2009, **113**, 14852.

32. A. Ruderman, M. F. Juareza, G. Soldanoa, L. B. Avalleb, G. Beltramoc, M. Giesenc and E. Santosa, *Electrochim. Acta*., 2013, **109**, 403.

33. D. A. Harrington and B. E. Conway, *Electrochim. Acta*., 1987, **32**, 1703.

34. D. A. Harrington and P. V. Driessche, *J. Electroanal. Chem*., 2001, **501**, 222.

35. B. Plowman, S. J. Ippolito, V. Bansal, Y. M. Sabri, P. Anthony, O'Mullane and S. K. Bhargava, *Chem. Commun*. 2009, 5039.

36. M. M. Costa, A. E. Muniz and A. Merkoci, *Electrochem. Commun*., 2010, **12**, 1501.

37. J. Perez, E.R. Gonzalez and H.M. Villullas, *J. Phys. Chem. B*, 1998, **102**, 10931.

38. A. T. Kuhn and M. Byrne, *Electrochim. Acta*., 1971, **16**, 391.

39. G. J. Brug, M. Sluyters-Rehbach and J.H. Sluyters, *J. Elecroanal. Chem*., 1984, **181**, 245.

40. L. A. Khanova and L.I. Krishtalik, *J. Electroanal. Chem*., 2011, **660**, 224.

41. B. J. Murray, Q. Li, J.T. Newberg, E.J. Menke, J.C. Hemminger and R.M. Penner, *Nano Lett*., 2005, **5**, 2319.

CHAPTER 6

One step preparation of ‘ready to use’ Au@Pd nanoparticle modified surface using Deep eutectic solvents and its electrocatalytic properties in alcohol oxidation reaction

6.1. Introduction

The advent of core shell nanoparticles has led to a variety of applications, especially in the areas of biomedical devices, Li^+ ion storage, SERS, sensors and catalysts [1-5]. In the field of electrocatalyst, the recent studies are focused towards designing novel core-shell nanomaterials from proven catalytically active components. The conventional anode catalysts for the acid medium fuel cells were based on highly expensive and less abundant metal Pt. However, with the recent development in alkaline medium fuel cells (AFCs) owing to improved alcohol oxidation kinetics, non Pt metals are being viewed as alternative catalyst materials [6]. Efforts are also being made to decrease Pt loading in the catalysts by using Pt in combination with other metals. There are several reports of the metallic components such as Pt, Pd and Au in combination with carbon supports such as carbon microspheres, carbon nanotubes, graphene which are extensively studied for electrocatalytic applications in alcohol oxidation [7-10]. The non-platinum based catalyts studied for the design of core shell nanoparticles for AFC include Pd, which has a high catalytic activity in alkaline medium and Au, due to its higher tolerance to oxidative intermediates which act as poison in alcohol based fuel cells.

In this chapter, the studies on the electrochemical synthesis of bimetallic nanoparticles of gold-palladium and their insitu electrodeposition onto a graphite surface are presented. The electrochemical reduction of two different metal ions in DES can lead to different morphologies and electrochemical characteristics. A simultaneous reduction of two different metal ions can lead to the formation of alloy or electrodeposit containing independent clusters of different metals. A preferential reduction of one metal ion over the other can form nanoparticles that can act as nucleation sites for the second metal. This mode of reduction leads to a core-shell morphology, where the nanoparticles of the metal reduced initially forms the core while the second metal nanoparticle

forms a shell. The core-shell nanoparticles are excellent electrocatalysts as they exhibit a synergistic effect due to the coupling of both the metals.

The conventional methods of Au-Pd core shell nanoparticle synthesis (Au@Pd NPs) involve either galvanic replacement reaction or selective chemical reduction of the metal ions. These methods are based on the reduction of metal ions on the surface of a preformed metal core. The galvanic replacement method is based on the higher electrochemical reduction potential of gold over other metals such as Ag, Pt and Pd. This two step method involves the galvanic replacement of preformed nanoparticles of Ag or Co with gold giving hollow gold nanoparticles [11-12]. Through a second step, Pd is allowed to grow over the surface of these Au hollow nanoparticles giving Au@Pd NPs.

Recently, the electrochemical techniques are also employed for the deposition of bimetallic nanoparticles. Kim *et al.* performed an insitu formation and electrochemical deposition of bimetallic nanoparticles of Au and Pd. The deposited bimetallic nanoparticles were detached from the cathode and subsequently coated with gold shell to give PdAu@Au NPs [13]. Yang *et al.* electrodeposited Au@Pd nano composite on a carbon fibre by a two step potential pulse method from metal salt solutions [14]. Earlier, Reetz *et al.* had demonstrated the electrodeposition of nanostructured bimetallic clusters of Ni/Pd, Fe/Ni, Fe/Co onto a Pt sheet by the use of corresponding sacrificial anodes as metal sources [15]. However, the nanoparticles obtained by the method did not exhibit a core-shell morphology. To the best of our knowledge, there are no reports on a single step electrochemical synthesis and *insitu* deposition of core-shell nanoparticles.

Chemical methods are also used for the preparation of Au@Pd NPs. A single step green synthesis of Au@Pd nanoparticles was achieved by utilizing the preferential reducing ability of plant tannins on Au ions over Pd [16]. Hu *et al.* carried out a seed mediated growth of palladium nanoparticles on the preformed nanoparticle of gold acting as a core [17]. Srivastava *et al.* succeeded in synthesizing Au@Pd nanoparticles by the simultaneous reduction

of gold and palladium ions using tryptophan in aqueous medium [18]. Wu *et al.* synthesized Au@Pd NPs by co-reduction of corresponding metal salts in reverse miscellar solutions [19]. However, for electrochemical applications, all of these methods require additional steps to immobilize the prepared nanoparticles on to a suitable substrate. This may provide unstable surface and cannot with stand the harsh electrochemical environment in a cell.

In this study, a facile single step fabrication of Au@Pd core-shell nanoparticles immobilized substrate which can be directly used for different applications is presented. The deep eutectic solvent used here, is associated with adequate ionic conductivity and can be used as a standalone medium for the electrochemical process. The low surface tension of DES implies faster nucleation rates for nanoparticle formation [20]. The inherent reducing ability of ethylene glycol constituting the deep eutectic solvent (ethaline) avoids additional reducing agents. Besides, the components of DES viz., choline chloride and ethylene glycol are known to exhibit a stabilizing effect on the nanoparticles formed and hence avoids the addition of any external stabilizer [21-22]. The green aspects of DES were preserved by the choice of nanoparticle synthesis technique also as the anodic dissolution of Au and Pd wires avoid the addition of any metal ion sources. The process of electrodeposition ensures better adhesion of nanoparticles onto the substrate.

6.2. Experimental

6.2.1. Materials used

The components of DES, namely choline chloride and ethylene glycol were purchased from Aldrich and Merck respectively. Both of the DES components were kept in oven for 30 minutes to remove any traces of moisture. The metal wires of Au (0.5 mm diameter, 99.9%) and Pd (0.5 mm diameter, 99.9%) used for anodic dissolution were purchased from Advent Research Materials (U.K.). The electrochemical studies of the nanoparticle modified electrodes were performed using either sodium hydroxide or sulphuric acid (Merck) as

supporting electrolytes in millipore water of 18MΩcm resistivity. Methanol (AR grade, Merck) was used for alcohol oxidation reaction.

6.2.2. Electrochemical studies

The electrochemical cell was maintained at specific temperatures for kinetic studies using Julabo temperature control systems (F25). For electroanalytical techniques, Pt foil was used as a counter electrode while the nanoparticle modified graphite rod was used as the working electrode. Saturated Calomel Electrode (SCE) and Hg/HgO/1M NaOH (MMO) were used as reference electrodes in acidic and alkaline medium respectively. SEM images and EDAX spectra were recorded with a field emission scanning electron microscope (Ultra plus, Carl Zeiss).

6.2.3. Electrodeposition of nanoparticles from DES

The metal wires of Au and Pd were used together as an anode for the electrodeposition of bimetallic nanoparticles. A graphite rod with a geometrical area of 0.19 cm^2 (circular base of the rod) was used as the cathode. The remaining area of the graphite exposed to the DES medium was sealed by Teflon (scheme-1). The cathode and anode surfaces were kept parallel at a distance of 5 mm. The DES medium was kept at 50^o C under constant magnetic stirring in an electrochemical cell of 10 mL capacity. The anodic dissolution and the simultaneous electrodeposition of bimetallic nanoparticles were carried out at a constant current density of 20 mA/cm^2 on Pd and 40 mA/cm^2 on Au in the ethaline medium for duration of 40 minutes. The variable current density on a single anode containing Au and Pd wires was achieved by exposing double the area of Pd wire *wrt* Au wire dipped in the solution.

The electrodeposition of monometallic nanoparticles (Au and Pd) onto graphite was carried out at a current density (20 mA/cm^2) using the respective metal wire as the sacrificial anode. The amount of Pd dissolved in the medium was considerably higher than that of Au as calculated by the loss in weight of the anode (1 mg of Pd Vs ~0.2 mg of Au) after dissolution. The as prepared

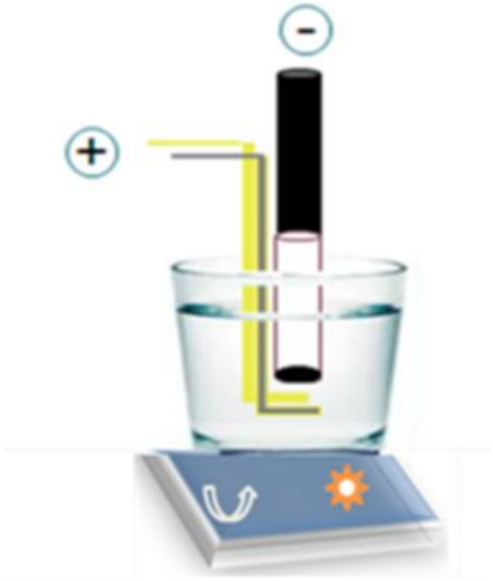

Scheme 1. *Pictorial representation of anodic dissolution technique for the electrodeposition of Au@Pd nanoparticle in DES medium*

nanoparticle modified graphite rods were rinsed thoroughly with millipore water and dried prior to surface characterization and electrocatalytic studies.

6.3. Results and discussions

6.3.1. Characterization

The cyclic voltammetry of the nanoparticle modified electrodes were carried out in 0.5 M H_2SO_4 at a scan rate of 100mV/sec in a scan range of -0.4 V to 1.3 V (Vs SCE). The cyclic voltammogram of Au NP modified graphite given in Fig.1a shows a broad peak in the anodic scan due to the formation of surface oxides of Au and the corresponding metal oxide stripping peak at 0.84 V during the cathodic scan. Palladium is known for its ability to absorb hydrogen and this characteristic response of the mesoporous Pd electrode is apparent from Fig.1b. An intense anodic peak observed at ~ -0.1 V arises due to the oxidation of hydrogen absorbed within the lattice of mesoporous palladium. At potentials beyond 0.9 V palladium oxide is formed, which gets reduced at 0.26 V during the cathodic scan.

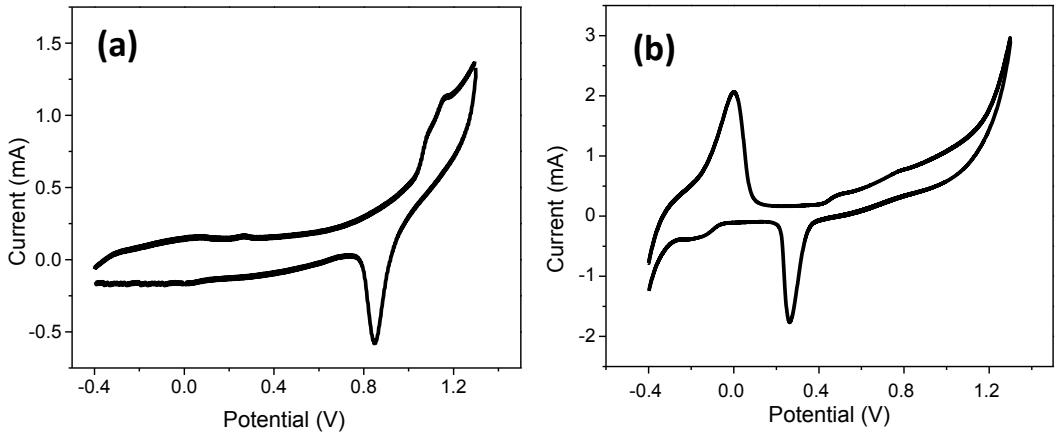

Figure 1. *Cyclic voltammograms of graphite rod modified with nanoparticles of (a) Au (b) Pd in 0.5M H_2SO_4 at a scan rate of 100mV/sec Vs SCE*

The electrochemically active surface area (ECSA) of the mesoporous gold and palladium was calculated from the empirical charge densities associated with the stripping peak of AuO (390 μC/cm^2) and that of PdO (424 μC/cm^2) [23-24]. Thelarge ECSA obtained for the monometallic nanoparticle modified substrates of gold (2.23 cm^2) and Pd (4 cm^2) compared to the geometrical area of graphite substrate (0.19 cm^2) pointed to the fact that nanoparticles are deposited as porous film of high surface area on the solid substrate.

Fig.2 shows the cyclic voltammogram of the Au@Pd film on a graphite substrate. The anodic scan shows the oxidation peak of absorbed hydrogen at around -0.05 V similar to that observed in the case of mesoporous Pd substrate. The first cathodic scan of Au@Pd nanoparticles manifests as a slightly broadened hump for the AuO→Au reduction while the sharp stripping peak corresponds to the reduction of PdO.

On successive scans of cyclic voltammograms, an increasing charge due to AuO reduction is observed with a concomitant decrease in the charge associated with PdO stripping peak. The decreased charge with electrochemical cycling is attributed to dissolution of PdO in acidic medium in presence of a more noble metal Au [25]. Deplanche *et al.* had earlier reported a

similar observation on the Au@Pd core shell nanoparticles as a function of potential scanning [26].

The presence of stripping peaks of both AuO and PdO in the voltammogram of Au@Pd NPs confirms the bimetallic nature of the mesoporous substrate. The reduction potentials of the surface oxides were shifted positive *wrt* their monometallic counterparts by 50mV. This shift in potential could be attributed to the interaction of the bimetallic components. The electro-deposition procedures followed in this study involve simultaneous dissolution of the two metals, avoiding the requirement for a layer by layer deposition of the nanoparticles on the substrate. The fact that the stripping peak of gold oxide becomes apparent only after the simultaneous removal of palladium is an electrochemical evidence for the core-shell nature of the nanoparticles with Au constituting the core and Pd, the shell layer.

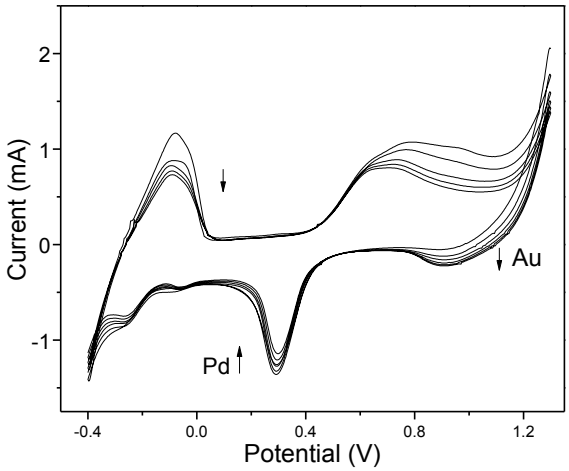

Figure 2. *Cyclic voltammograms of graphite rod modified with nanoparticles of Au@Pd in 0.5M H_2SO_4 at a scan rate of 100mV/sec Vs SCE*

To probe into the morphological features of the electrodeposited nanoparticle modified substrate, SEM images were acquired. The SEM images of the monometallic nanoparticle modified substrates of gold and palladium nanoparticle prepared under identical experimental conditions are shown in Fig.3 a and b respectively.

In comparison to monometallic nanoparticle modified substrate, the coverage of Au@Pd nanoparticle on the surface of graphite was scattered. The bimetallic nanoparticle modified substrates of Au-Pd on graphite is shown in Fig.4a. Even at a lower magnification, it can be observed that the nanoparticles are associated with halo like features. The surface distribution of these clusters is inhomogeneous which leads to the formation of numerous voids on the surface. These voids make the modified surface highly mesoporous. The SEM image of the electrodeposited bimetallic nanoparticles [Fig.4b] shows a brighter metallic component buried within another component, indicative of core-shell morphology. However, an EDAX analysis on the as prepared samples given in Fig.5 indicated the complete absence of gold in the regions scanned. The Pd composition was contributing 51 % (weight %) of the total composition comprising Pd, C and Cl. This observation may be similar to the cyclic voltammogram of the as prepared samples of Au@Pd samples. The thicker Pd shells may hinder the detection of the Au core which is well buried within the shell. To confirm this, SEM and EDAX characterization of the Au@Pd NP modified substrate subjected to electrochemical potential cycling was performed.

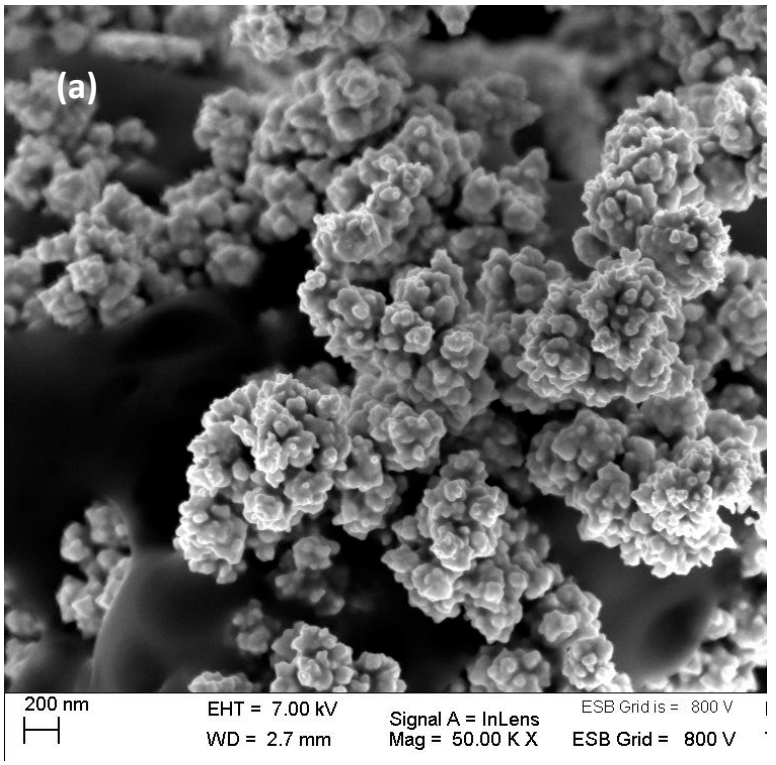

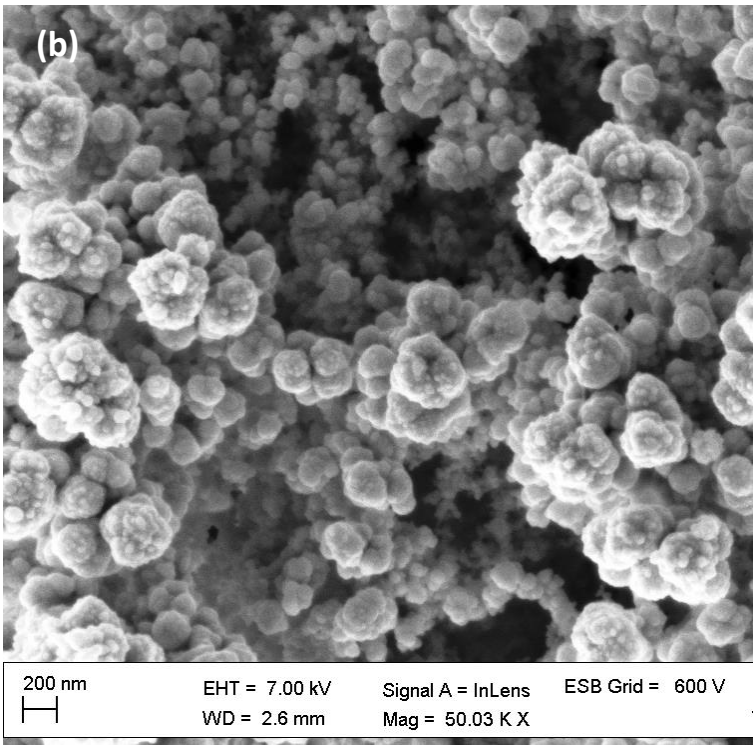

Figure 3. *SEM images of graphite rod modified with monometallic nanoparticles of (a) Au (b) Pd*

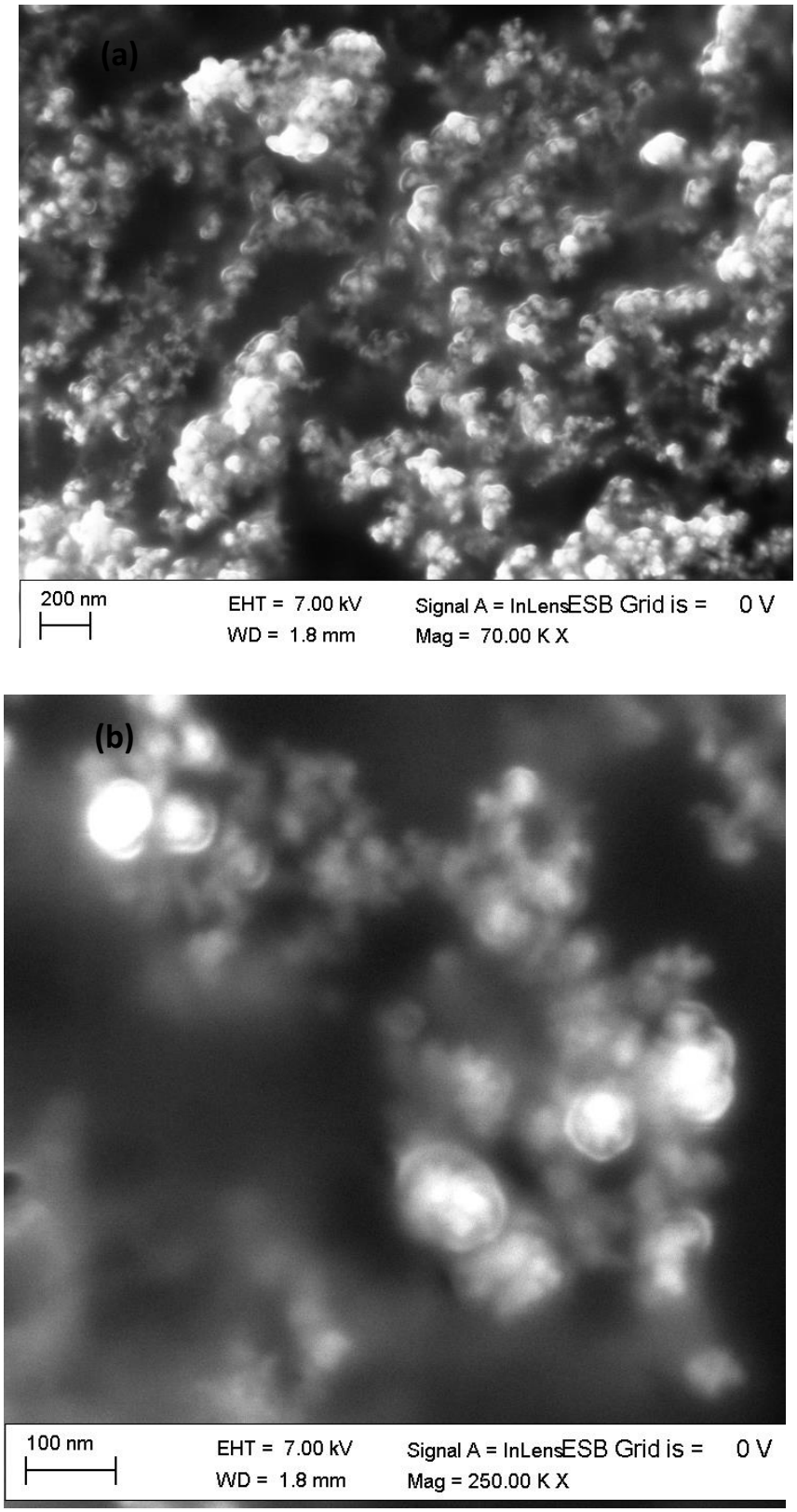

Figure 4. *SEM images of graphite rod modified with Au@Pd NPs*

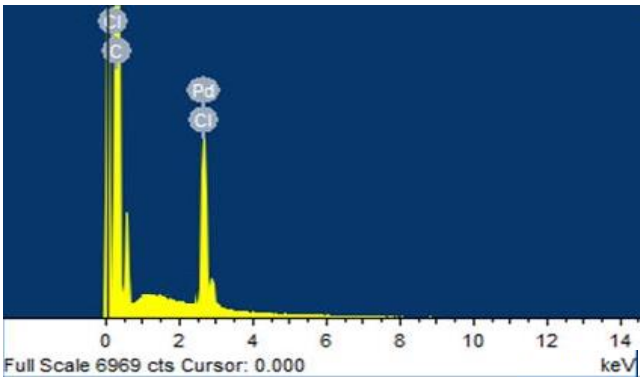

Element	Weight%
C K	37
Cl K	11.33
Pd L	51.60
Totals	100.00

Figure 5. *EDAX of the as prepared Au@Pd NPs on graphite rod*

The morphological analysis of the as prepared samples was compared with that of the samples subjected to electrochemical potential scanning (50 cycles). The SEM images of the electrochemically treated substrate given in Fig.6 revealed a decrease in particle size with the core – shell morphology being preserved.

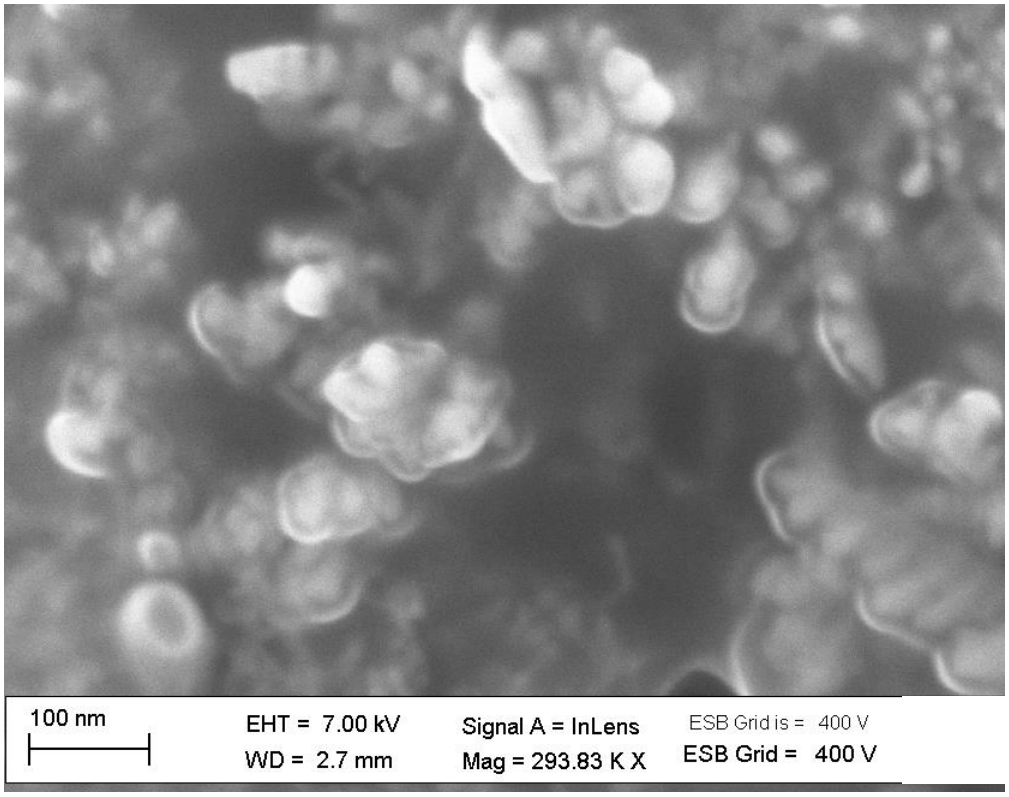

Figure 6. *SEM image of electrochemically treated Au@Pd NPs on graphite*

The EDAX spectrum of the substrate after electrochemical treatment shows the presence of gold [Fig.7a]. The elemental analysis of the electrochemically treated sample provided in showed a decrease in the composition of Pd from 52% to 35%. The decrease in the composition of Pd with that of the corresponding increase in gold (0% to 2.64%) was in accordance with the behavior exhibited in the cyclic voltammogram (Fig.2). The electrochemical analysis together with the morphological characterization confirms the presence of Au@Pd core-shell nanoparticles on the surface of graphite.

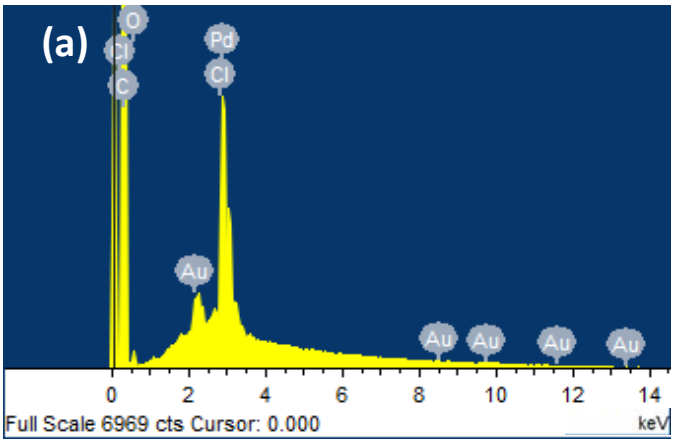

Element	Weight%
C K	60.81
O K	0.43
Cl K	1.18
Pd L	34.94
Au M	2.64

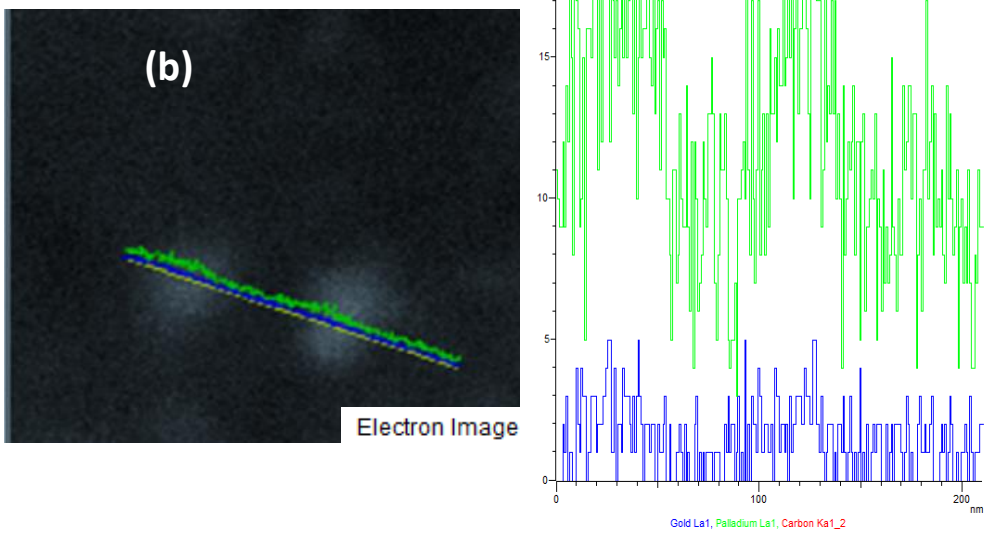

Figure 7. *(a) EDAX of electrochemically treated Au@Pd NPs on graphite (b) EDAX line scan of electrochemically treated Au@Pd NPs on graphite*

The mechanism of electrochemical formation of Au@Pd nanoparticles on the surface of graphite can be described as follows; The application of a constant current density at sacrificial anodes, releases metal ions of Au and Pd to the DES medium. The Pd wire dissolution was observed to be considerably higher than that of Au leading to an increased concentration of Pd ions in the medium. These metals ions instantaneously form complexes with the hydrogen bonded DES components [22]. The standard reduction potentials indicate that the electrochemical reduction of $AuCl_4^-$ is favored over $PdCl_4^-$ (1 V Vs 0.63 V) [19]. Subsequently, the gold atoms associated with higher nucleation rates acts as a nucleic centre for the growth of nanostructured Pd layers. Higher nucleation rate of gold atoms over Pd has been reported earlier in aqueous and reverse miscellar media [27,19]. An increased concentration of Pd ions in the medium causes deposition of several layers of PdNPs on the gold nuclei, which probably accounts for the absence of gold in the EDAX elemental analysis of the as prepared substrate [28-29]. However, gold is shown up by EDAX analysis only after the Pd atoms from the shell of the nanoparticles are electrochemically etched and gold atoms are exposed. EDAX line scan of the electrochemically etched Au@Pd NPs is provided in Fig.7b.

Chirea *et al.* synthesized gold nanowires chemically in ethaline medium using an external reducing agent $NaBH_4$ [22]. The method required excessive amount of $NaBH_4$ for the reduction of the gold - ethaline complex $[HO\text{-}CH_2\text{-}CH_2\text{-}N^+(CH_3)_3]AuCl_4^-.2(HO\text{-}CH_2\text{-}CH_2OH)$. This observation points towards the fact that the DES medium by itself cannot reduce the gold complexes to yield AuNPs in the solution. It therefore indicates that, in this study the AuNPs could have been formed by the electrochemical reduction of the complex on the surface of the cathode. However, the synthesis of palladium nanoparticles utilizing the reducing ability of alcohols especially ethylene glycol have already been studied in detail [30-31]. The ethaline medium comprising of choline chloride and ethylene glycol are weakly bound, increasing the chances of chemical reduction of Pd ions in addition to the electrochemical reduction. The reducing ability of the medium brings about the

formation of PdNPs in the DES medium making the color of the medium turn dark, as observed in the experiment.

Enhanced catalytic activity of Au@Pd bimetallic nanoparticle over monometallic analogues

The electrocatalytic activity of the Au@Pd nanoparticles on graphite was investigated in methanol oxidation in alkaline medium and compared with that of its monometallic counterparts. The electro-oxidation of alcohols largely depends on the coverage of hydroxyl ions adsorbed on the surface of the catalyst from the alkaline medium. However, an optimum control of hydroxyl ion concentration is necessary to ensure the accessibility of electro-active sites for the reactant alcohol molecules and the concentration of NaOH was maintained at 0.5 M in this study. The currents reported here for the electro-oxidation of methanol using the mesoporous substrates were normalized to ECSA and hence can be attributed to the catalytic activity and not to the higher surface area.

6.3.2. Electro-oxidation of methanol in alkaline medium

The electrocatalytic properties in terms of current density and overpotential of the modified electrodes for methanol oxidation were studied by cyclic voltametry. A synergistic effect of Au and Pd, if any was examined by the comparison of voltammetric response of Au@Pd nanoparticle with that of its monometallic counterparts.

The cyclic voltammogram of the mesoporous gold substrate in 2M MeOH given in Fig.8a displays a small hump (-0.1 V) in the anodic scan prior to the intense oxidation peak. The methanol oxidation on gold in alkaline media is known to be occurring at two potential regions. The reaction mechanism on polycrystalline gold in alkaline medium was earlier investigated by Borkowska *et al*. [32]. They obtained two peaks with the first peak at negative potentials being attributed to the oxidation of methanol on hydroxyl ion adsorbed gold surface to yield formate ions releasing four electrons in the process.

$$CH_3OH + 5OH^- \rightarrow HCOO^- + 4H_2O + 4e^-$$

At higher potentials, methanol oxidation proceeds on the surface of gold oxide which results in the formation of carbonates releasing six electrons in the process. The group has confirmed the independent reactions of methanol oxidation on gold hydroxide and gold oxide surfaces by Tafel slope analysis.

$$CH_3OH + 8OH^- \rightarrow CO_3^{2-} + 6H_2O + 6e^-$$

The cyclic voltammograms of methanol oxidation on mesoporous palladium substrate shown in Fig.8b displays a single peak at low overpotentials compared to gold. The palladium based substrates have been known to render superior electrocatalytic activities in alkaline medium based direct alcohol fuel

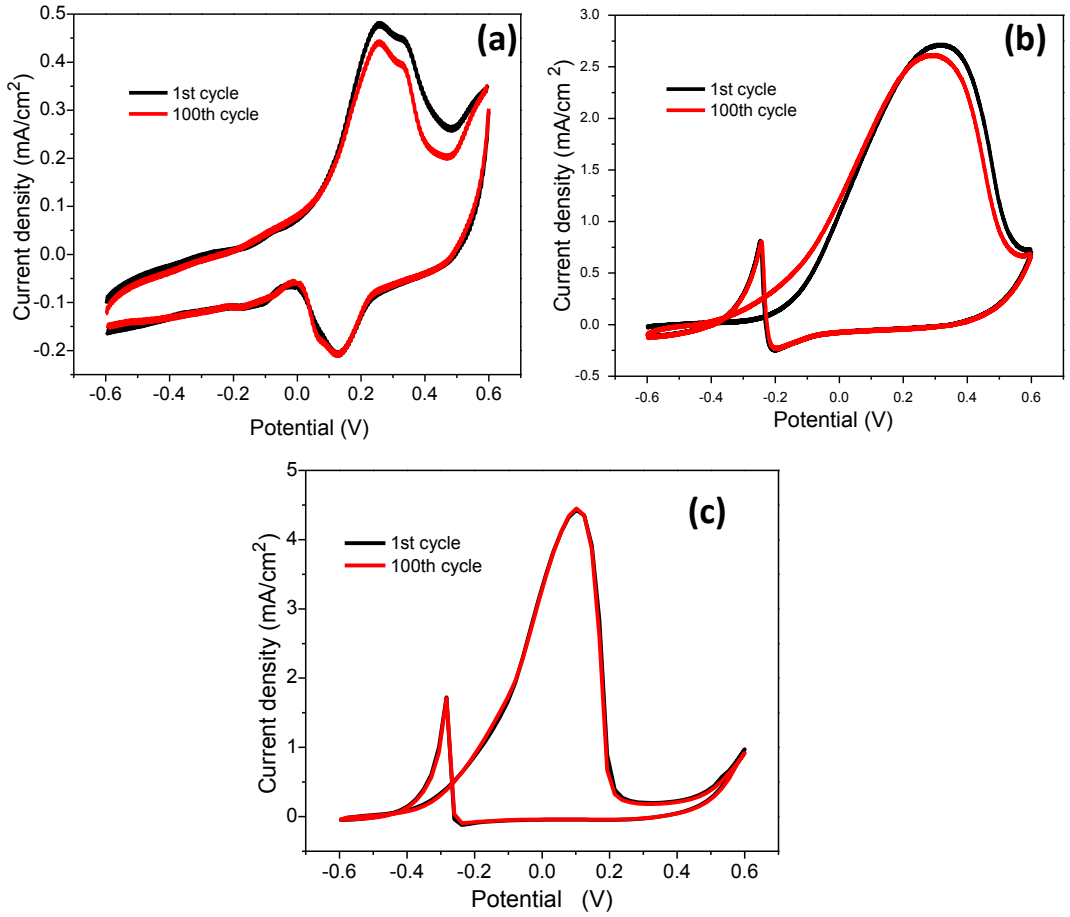

Figure 8. *Cyclic voltammograms of graphite rod modified with nanoparticles of (a) Au (b) Pd (c) Au@Pd in 2M MeOH / 0.5M NaOH at a scan rate of 100mV/sec (Vs MMO)*

cells. The electro-oxidation of methanol on palladium based catalysts yields formate as the main product which was by confirmed by HPLC [33]. However,

ex-situ analytical studies of anode exhaust of methanol oxidation catalyzed by Pd based materials have confirmed the presence of carbonates also along with formats [6].

Fig.8c shows the voltammograms displaying the methanol oxidation on mesoporous Au@Pd modified graphite. The voltammograms exhibit similar features to that of the PdNP modified substrates. The Au@Pd bimetallic substrate shows a single peak in the anodic scan unlike that observed on the AuNP modified substrate. This may be ascribed to the fact that the Au core is well buried within Pd shells and the electro-active sites of the latter are more accessible for the reactant molecules. A synergistic effect of bimetallic components of Au@Pd modified substrates is evident on the comparison of peak potentials and current densities with that of monometallic counterparts.

A comparison of the electrocatalytic properties of hollow Au@Pd, Au and Pd nanoparticles on a glassy carbon electrode by Liu *et al.* indicated that the Au@Pd hollow nanostructures exhibited better catalytic activity in terms of current density (0.6mA/cm^2) at a peak potential of -0.12V Vs Ag/AgCl for a methanol concentration of 0.5M at a scan rate of 50mV/sec [12]. Su *et al.* prepared bimetallic nanoparticles of Au and Pd immobilized onto carbon rods in various compositions and were used as catalysts in the electro-oxidation of methanol, ethanol and isopropanol [34]. At a concentration of 1M, the methanol oxidation currents were in the range of 30 - 42mA/cm^2 (*wrt* geometrical area) for different Au:Pd compositions. The study showed that the stability and poisoning tolerance of Pd was not significantly enhanced by the presence of Au. Lang *et al.* prepared nanoporous substrates of AuPd by a dealloying process and showed that the electrodes displayed high electrocatalytic properties for methanol oxidation (0.4mA/cm^2 at a peak potential of 0.21V Vs Ag/AgCl) [35].

The electrodeposited Au@Pd core shell nanoparticle prepared in this study, exhibited enhanced catalytic properties in terms of a current density of 4.5mA/cm^2 normalized to ECSA (74 mA/cm^2 *wrt* geometrical area) at a peak potential of 76mV (Vs MMO). Table 1 shows the open circuit (E_{OCP}), onset

(E_{Onset}), peak (E_{Peak}) potentials for the three different electrodes studied in this work. It can be seen that the methanol oxidation onset potential and open circuit potentials are quite close in all the cases. This shows that negligible overpotential (40 mV) is required in the case of Pd nanoparticles electrodes whereas the onset potentials are almost matching the OCP in the case of Au@Pd. The onset and peak potentials for methanol oxidation on Au@Pd NP catalysts are comparable to the state of the art electrocatalysts (Pt and Pt-Ru) for methanol electro-oxidation.

Table 1. *Comparison of open circuit (E_{OCP}), onset (E_{Onset}), peak (E_{Peak}) potentials (wrt RHE) of graphite rod modified with nanoparticles of Au, Pd and Au@Pd with literature values* [32, 36, 37]

	E_{OCP} (V)	**E_{Onset} V**	**E_{Peak} V**
AuNP	0.754	0.835	1.131
PdNP	0.516	0.555	1.152
Au@Pd NP	0.441	0.450	0.935
Pt-C/GC [a]	-	0.412	0.92
Pt/GC [b]	-	0.443	1
Pt/Ru[c]	-	0.333	0.914
Pt disc	-	0.4	1

a-chemical deposition of commercial Pt catalyst on glassy carbon , **b**- electrochemical deposition of commercial Pt catalyst on glassy carbon, **c**- Pt/Ru catalyst on high surface area carbon

The stability of nanoparticle modified graphite electrodes (AuNP, PdNP and Au@PdNP) was monitored with continuous potential scans in 2M methanol / 0.5M NaOH. The Au@Pd nanoparticle modified electrodes were extremely

stable to methanol oxidation over continuous scans [Fig.8c]. The stability of monometallic counterparts is also apparent from the Fig. 8a and b.

During the reverse scan, a reduction peak of very low current can be observed at ~ -0.23 V followed by a sharp oxidation peak as in Fig.8b and Fig.8c. The reduction peak corresponds to the stripping peak of PdO similar to that seen earlier in 0.5M H_2SO_4 (Fig.1b). The negative shift in the potential of stripping peak is attributed to the change in the pH of the medium from acidic to alkaline. Such an electrochemical reduction of PdO during the cathodic scan creates fresh Pd atoms that lack lattice stabilization and thereafter are not in equilibrium with the lattice [38-39]. These non- equilibrated Pd atoms are associated with high catalytic activity. Interestingly the Au@Pd NPs associated with Pd shells displayed similar behavior as that of PdNPs.

Manoharan *et al.* studied the changes associated with the reverse oxidation peak current (I_p) of alcohol oxidation on Pt in acidic medium on scanning to high anodic limits [40]. It was observed that this current decreased on extending the anodic limits. It is known that at potentials beyond 1.3V, removal of carbonaceous species via evolution of CO_2 occurs [41]. Such a decrease in peak current confirms that the reverse oxidation peak current is associated with oxidation of residual carbon species of alcohol. Recent studies of alcohol oxidation in alkaline medium on metals such as Pt, Pd are also attributed reverse anodic peak to the same phenomenon [10, 33, 41].

The reverse anodic peak can be also explained in terms of catalytic activity of freshly reduced metal sites. The oxidation peak at -0.3V in the cathodic scan immediately after the stripping peak is due to the methanol oxidation occurring on the surface of freshly prepared Pd atoms as explained by Manzanares *et al.* in the electro-oxidation of formic acid on Palladium in acidic medium [43].

In this study, Pd shell of Au@Pd NP provides catalytic sites for the electro-oxidation of methanol as discussed in previous section. Therefore, PdNP modified graphite electrode were studied for the cyclic voltammetric experiments. Fig.9a shows the cyclic voltammogram of PdNP modified graphite in the absence of methanol. The Pd oxide formation and stripping

peak of PdO is evident in the anodic and cathodic scan respectively. In the presence of 2M methanol (Fig.9b), an intense methanol oxidation peak can be seen during the forward scan and also an anodic peak in the reverse scan. To confirm whether the reverse anodic peak is indeed due to the adsorbed carbonaceous species, the oxidation process was stopped and reversed at the peak potential associated with maximum extent of the methanol oxidation. This would ensure that the carbonaceous impurities are retained on the surface and can undergo oxidation during the reverse scan. However, counter-intuitively no reverse anodic peak was observed as apparent in Fig.9c. Another experiment of extending anodic limit to 1.3V, resulted in a substantial decrease in reverse anodic peak current (Fig.9d), similar to that observed by Manoharan *et al.*. It is evident therefore, that oxidation of residual carbonaceous impurities can occur only in the presence of freshly formed Pd atoms. This is also confirmed from Fig.9c, where on restricting the anodic limit to E_p no stripping peak is observed which

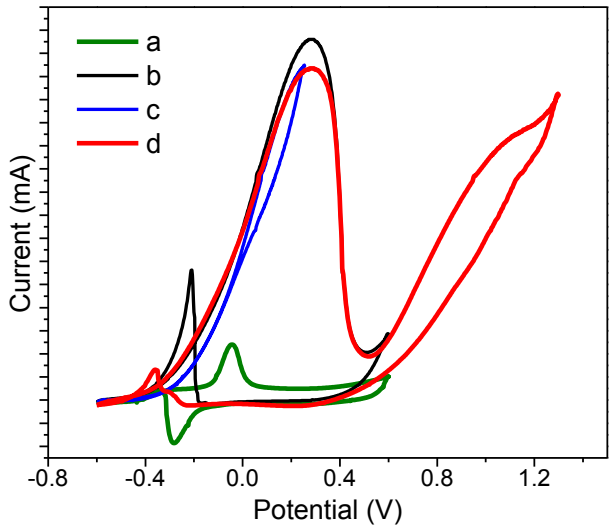

Figure 9. *Cyclic voltammograms of graphite rod modified with Pd NPs in (a) 0M MeOH (b) 2M MeOH, anodic limit 0.6 V (c) 2M MeOH, anodic limit 0.255 V (d) 2M MeOH, anodic limit 1.3 V at a scan rate of 100mV/sec in 0.5M NaOH (Vs MMO)*

indicates that fresh Pd atoms are not formed and residual carbon species do not get oxidized during cathodic scan. Earlier Takamura *et al.* studied the adsorption and oxidation of methanol on Palladium in alkaline medium by specular reflectivity [44].[43] The reverse anodic peak was attributed to electro oxidation of organic entities on freshly formed Pd sites as confirmed by our observation.

6.3.2.1. Kinetics of methanol electro-oxidation

The data obtained from the voltammetric response of nanoparticle modified electrodes towards methanol oxidation reaction were subjected to a detailed kinetic analysis based on Tafel analysis, activation energy measurements and reaction order calculations.

(a) Tafel analysis

Tafel analysis is usually done to get insight into the rate determining step. However in the case of alcohol oxidation, Tafel slopes often show large deviations from ideal values owing to undesired reactions of adsorbed reactive intermediates and excessive coverage of poisoning species on catalytic surface. The decomposition of methanol to CO on Pd in gas phase was studied by Davis *et al.* [45]. The group suggested that methanol adsorption on to the metal site occurs through the oxygen atom which subsequently forms an adsorbed methoxy intermediate. The rate determining step in the decomposition of methoxy intermediate to carbonyl species was the cleavage of –C-H bond. There are several studies on the mechanism of methanol oxidation on Pt in acidic and alkaline media, Au in alkaline medium, MoO_3 in gas phase [46-49]. The sequence of reaction steps proposed was somewhat different in each of these cases. Nevertheless, in all of these systems, the rate determining step was proposed as the –C–H bond scission as in the following reaction, whch yields a Tafel slope of 120mV/dec in the i-V curve.

$$CH_3OH \rightarrow *CH_2OH + H^+ + e^-$$

Recently, Kwon *et al*. studied the mechanism of electro-oxidation of alcohol in alkaline media by establishing the Hammett relationship [50]. Though the studies were performed on a gold surface, the implications of the model could be applied for Pt and Pd based catalyst in alkaline media. The proposed two step pathway involves an initial deprotonation of methanol resulting in an alkoxide ion. This is followed by a second deprotonation step as discussed above to give an aldehyde. The initial deprotonation is base catalyzed while the second deprotonation is characteristic of the electrode material.

The Tafel plots (Fig.10) were obtained by conducting chronoamperometry at various potentials at the foot of the methanol oxidation peak at different

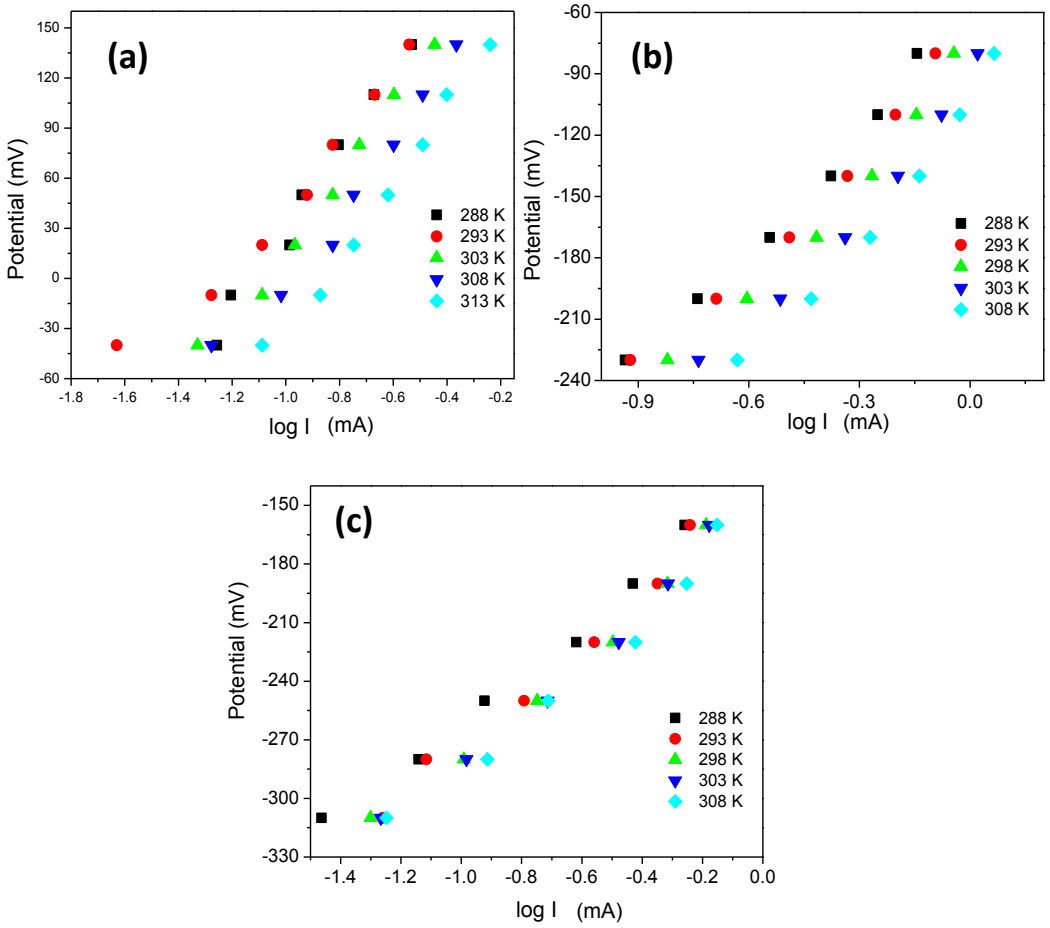

Figure 10. *Tafel plots of (a)AuNP (b)PdNP (c)Au@Pd NP modified graphite rod in 2M MeOH / 0.5M NaOH Vs MMO at various temperatures*

temperatures. The Tafel slopes obtained for all the mesoporous substrates under study are provided in Table 2. Tafel slopes obtained for mesoporous substrates of gold and Pd show deviations from the ideal value of 120 mV. These deviations are attributed to the oxidative intermediates that get adsorbed on to electrode surface and prevent the accessibility of fresh reactant molecules onto the catalytically active sites [47]. Such a reduced accessibility would necessitate excess applied potential to maintain the same defined current. Thus, in general a high Tafel slope, $d\eta / d(\log i)$ hints at the surface contamination owing to the adsorption of intermediates of methanol oxidation.

***Table 2**: Tafel slopes for methanol oxidation on AuNP, PdNP and Au@Pd NPs at various temperatures*

Temperature (K)	Tafel slopes (mV/dec)		
	AuNP	PdNP	**Au@PdNP**
288	241	178	**122**
293	170	163	**135**
298	214	171	**131**
303	203	178	**134**
308	221	193	**131**

The Au@Pd nanoparticle modified graphite exhibit Tafel slopes varying from 122 to 135 mV/dec at a temperature range of 288K-308K. The obtained results are in agreement with the theoretical prediction of 120mV/dec for an electrochemical reaction involving a single electron transfer during the rate determining step. The values were comparable with the Tafel slopes obtained for methanol oxidation on carbon supported Pt/Ru catalyst at a similar temperature range [51]. It is evident from the table that the Au@Pd NPs are

associated with better tolerance to poisoning intermediates. Thus, the catalytic sites are accessible to fresh methanol molecules maintaining the Tafel slopes close to the predicted values.

(b) Activation energy measurements

The activation energy for an electrochemical process is a measure of the catalytic efficiency. Higher activation energy necessitates higher operating temperatures for methanol oxidation. The activation energy (E_a) for the electro-oxidation of methanol was determined from the Arrhenius plot of log I Vs T^{-1} at low overpotential regions. E_a was obtained by equating the slope of the linear fit of the Arrhenius plot to $-E_a/2.303R$, R being gas constant. The

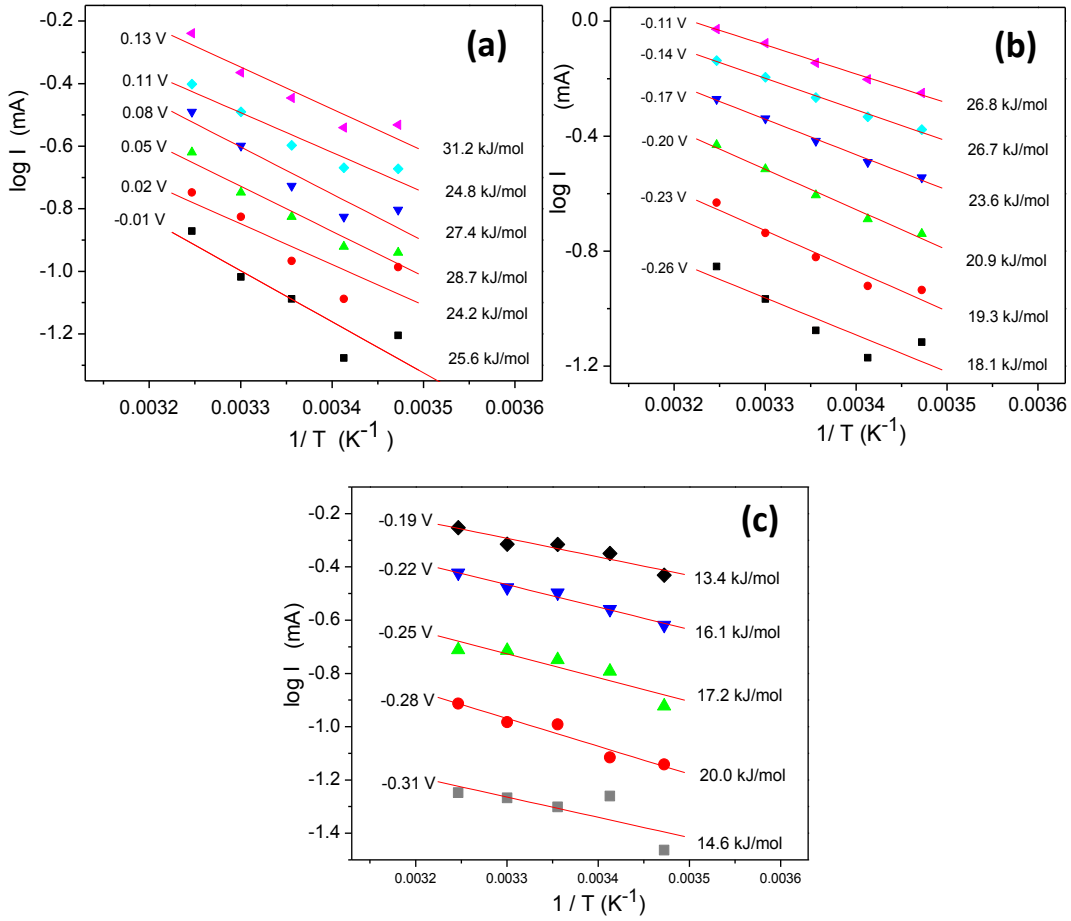

Figure 11. *Arrhenius plots for (a) Au NP (b) Pd NP (c)Au@Pd NP modified graphite rods in 2M MeOH / 0.5M NaOH Vs MMO at different potential ranges*

activation energy plots, as expected show an increase in log I with temperature at any overpotential studied. Such an increase in log I with temperature is attributed to the enhanced adsorption of hydroxyl ions from the alkaline medium, which provides active oxygen species required for electro-catalysis [52].

In an alkaline medium, Pd based catalysts are known to lower the activation energy for methanol oxidations much more than that of Pt/Ru electrocatalyst (40-50 kJ/mol) and are extensively studied as Pt alternatives [53]. The activation energy required for methanol oxidation on a Pd disc electrode was studied by Wang *et al.* in alkaline medium and was found to be ~33 kJ/mol [42]. Recently, for methanol oxidation reaction, the Pd-Ni-Cu-P metallic glass nanowire catalyst in an alkaline media showed improved poisoning resistance and lowered onset potential [54]. The activation energy required for the electro-oxidation process was found to be 22 kJ/mol.

The Arrhenius plots for monometallic substrates of AuNP and PdNP modified graphite rods in our studies at different overpotentials are provided in Fig.11 a and b. The PdNP modified graphite rod exhibited an average E_a of 22.5kJ/mol. The E_a requirement for methanol electro-oxidation on gold nanoparticle modified graphite (~27 kJ/mol) was somewhat higher than that of Pd. An enhanced performance of Au@Pd modified substrate is evident from the very low activation energies (13 – 20 kJ/mol) at a potential range of -0.310 V to -0.160 V giving an average E_a of 16.2 kJ/mol. The Arrhenius plots obtained for the process are provided in Fig.11c. The synergistic catalytic effect for Au and Pd is evident from the very low activation energies for methanol oxidation when compared to their monometallic counterparts and also to other catalytic materials reported in literature.

(c) Reaction order calculations

The reaction order of the methanol oxidation on Au@Pd NPs was calculated from the plot of log I Vs log C by the equation, log I = log nFk + m logC, where F is the Faraday constant, k is the reaction constant, m is the reaction order and C is the concentration of alcohol. A Linear relationship obtained (Fig.12) indicates that the mechanism involved is not affected by the concentration of the reactant. The slope of 0.56 at peak potential (70 mV) indicates that the reaction order is ½ similar to that of Pt in acidic and alkaline media [30,37,49].

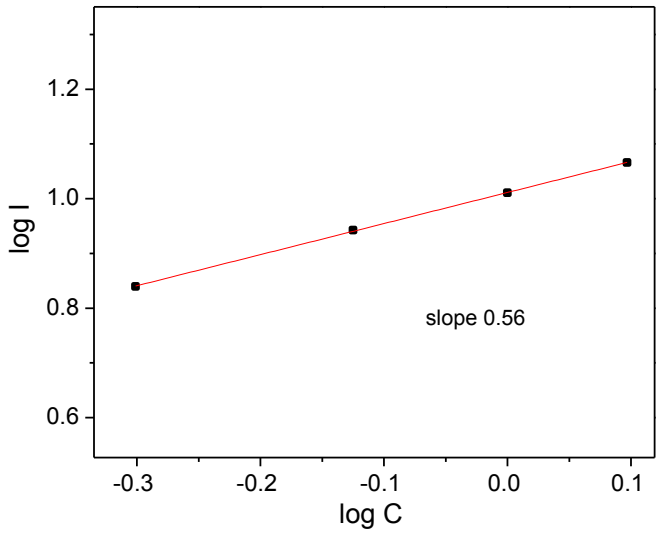

Figure 12*. log C Vs log I plots for electrochemical oxidation of methanol catalyzed by Au@Pd at peak potential of 70 mV*

6.3.3. Electro-oxidation of ethanol in alkaline medium

The electrocataytic properties of the Au@Pd NPs on graphite were studied for ethanol oxidation reaction also. The results were compared with that obtained on monometallic nanoparticle modified substrates of Au and Pd. The onset and the peak potentials for ethanol oxidation were found to be more negative than that of Au and Au@Pd NP modified substrates. However it can be noted from Table 3 that the overpotential required for the ethanol oxidation is comparatively lesser in the case of AuNP and Au@Pd NP modified graphite substrates. Cyclic voltammograms of the electrocatalysts in 0.4M ethanol /0.5M NaOH is given in Fig.13.

***Table 3**. Comparison of open circuit (E_{OCP}), onset (E_{Onset}), peak (E_{Peak}) potentials for ethanol oxidation on graphite rod modified with nanoparticles of Au, Pd and Au@Pd*

Substrates	E_{OCP} V	E_{onset} V	E_{peak} V
Aunp/Graphite	229	235	320
Pdnp/Graphite	564	501	65.88
Au@Pd/Graphite	555	532	32.95

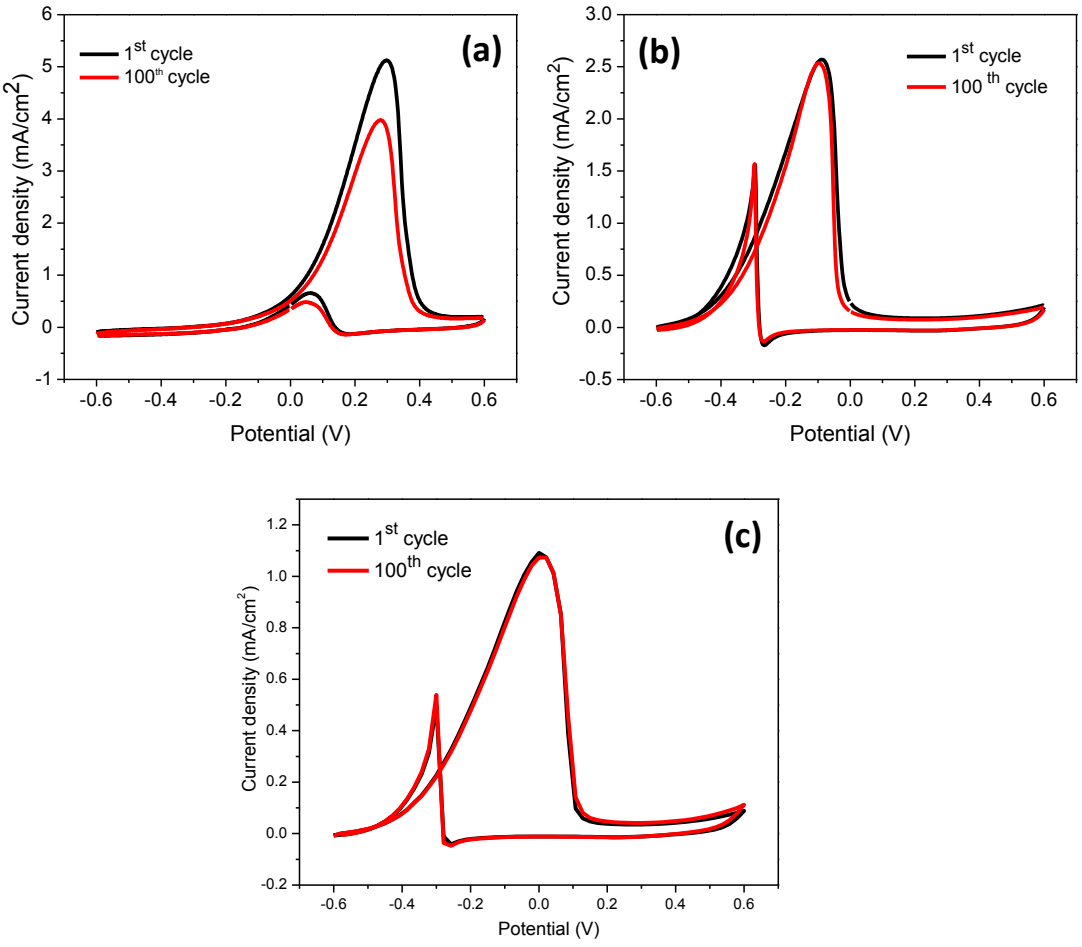

***Figure 13.** Cyclic voltammograms of graphite rod modified with nanoparticles of (a) Au (b) Pd (c) Au@Pd in 0.4M EtOH / 0.5M NaOH at a scan rate of 100mV/sec (Vs MMO)*

Previously Song *et al.* prepared hollow Au@Pd NPs based electrocatalyst by adhering chemically formed Au@Pd nanoparticles on a glassy carbon electrode by means of Nafion [11]. The study showed that the electrocatalytic properties of the nanoparticles of Au@Pd in ethanol oxidation were superior to that of Au@PtNPs prepared under identical conditions. Smiljanic deposited palladium on single crystals of gold and studied their electrocatayltic properties in ethanol oxidation. The peak potentials reported in the study are comparable to that reported in our studies [55].

6.3.3.1. Kinetics of ethanol electro-oxidation

The kinetics of the ethanol oxidation on the prepared electrocatalysts were studied as performed by Tafel analysis and activation energy measurements. The Tafel plots for ethanol oxidation on the electrodeposited nanoparticles of Au, Pd and Au@Pd are

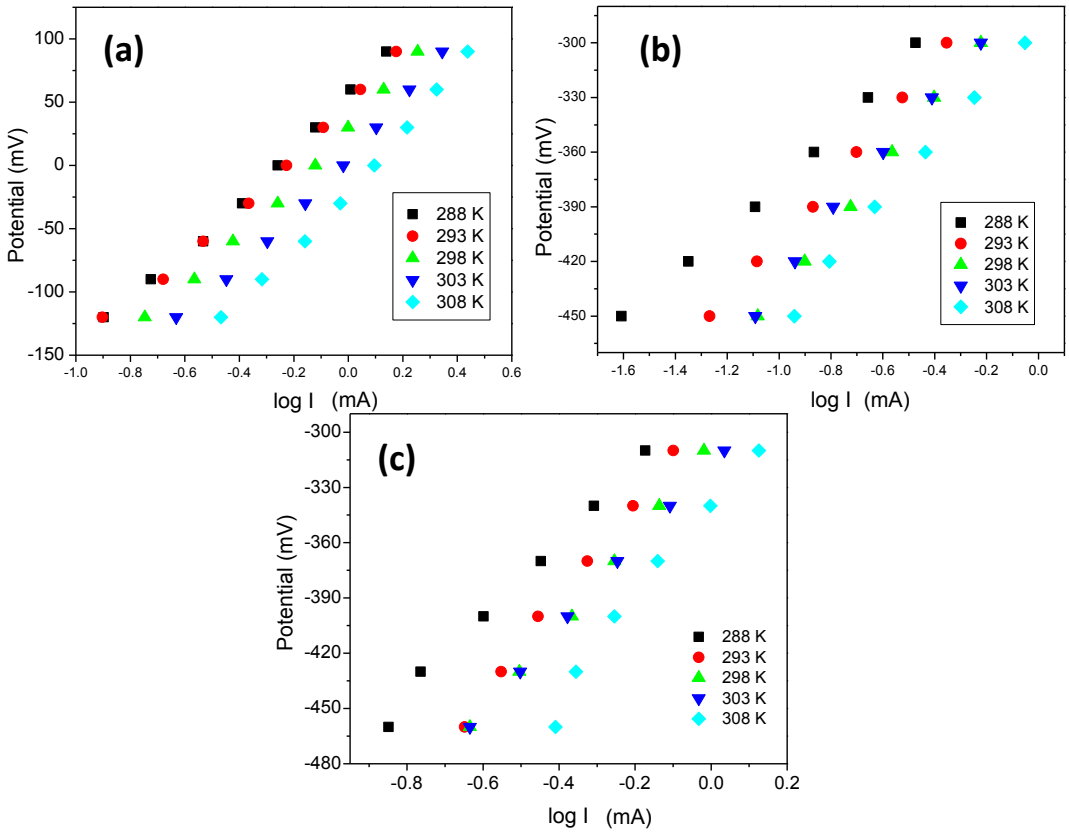

Figure 14. *Tafel plots of (a)AuNP (b)PdNP (c)Au@Pd NP modified graphite rod in 0.4M EtOH / 0.5M NaOH Vs MMO at different temperatures*

***Table 4**: Tafel slopes for ethanol oxidation on AuNP, PdNP and Au@Pd NPs at various temperatures*

Temperature (K)	Tafel slopes (mV/dec)		
	AuNP	PdNP	Au@PdNP
288	204	131	203.3
293	198	163	259.1
298	211	171	249.4
303	217	176	223.0
308	232	165	245.8

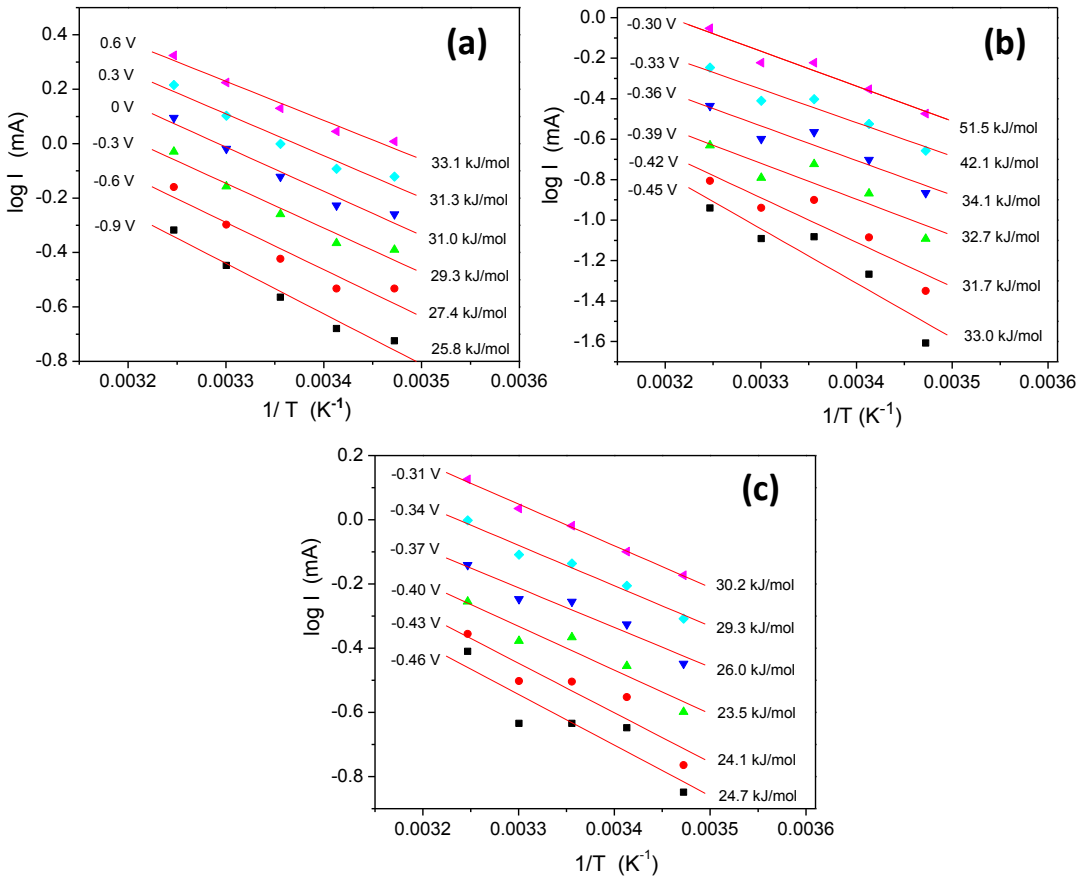

***Figure 15.** Arrhenius plots for (a) Au NP (b) Pd NP (c)Au@Pd NP modified graphite rod in 0.4M EtOH / 0.5M NaOH Vs MMO at different potential ranges*

given in Fig.14. The Tafel slopes (Table 4) of PdNP were less indicating that catalytic poisoning due to alcohol oxidation is minimal. The Tafel slopes of AuNP and Au@PdNPs were comparable.

The Au@Pd NP modified subtrates exhibited superior performance over their monometallic analogues in terms of activation energy requirements as that observed in the methanol oxidation studies. The average activation energy were calculated from the Arrhenius plots given in Fig.15 for AuNP (30.4 kJ/mol), PdNP (37.4 kJ/mol) and Au@PdNP (26 kJ / mol). A comparison of the average activation energies obtained on the nanoparticles of Au, Pd and Au@Pd for methanol and ethanol oxidation reaction is given in Table 5.

Table 5. *Comparison of the average activation energy for methanol and ethanol oxidation reactions*

	Average activation energy (kJ/mol)		
	AuNP	PdNP	Au@PdNP
Methanol	26.9	22.5	**16.2**
Ethanol	30	37.4	**26**

The reaction order for the ethanol oxidation on Au@Pd NPs was calculated by measuring the current at the peak potential (33mV) for different concentrations of ethanol. A slope of 0.46 indicating a half order reaction was obtained from the log I Vs log C plot (Fig.16). The mechanism of the electrochemical oxidation of ethanol was not affected by the concentration of the reactant as indicated by a linear relationship in the plot.

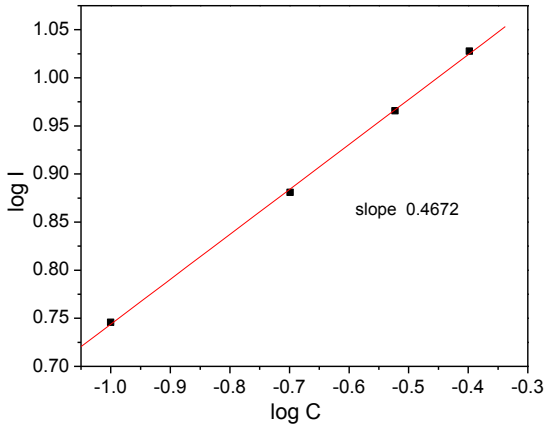

Figure 16. *log C Vs log I plots for the electrochemical oxidation of ethanol catalyzed by Au@Pd NP modified graphite at peak potential of 33mV*

6.4. Conclusions

Robust nanostructures of Au@Pd, Au and Pd nanoparticles were synthesized via novel electrochemical route in a deep eutectic solvent. The method exploits the stabilizing effect of the DES components. The material requirements for the proposed nanoparticle synthesis are minimal and totally eco-friendly. The electrodeposited films were well adherent and stable for continuous electrochemical treatment at varying temperatures and are expected to better than electrocatalysts modified in dispersing medium like Nafion. The fabricated nanoparticle modified substrates were extensively studied as electrocatalyst for methanol and ethanol oxidation in alkaline media. The Au@Pd nanoparticles modified substrates displayed superior performance over their monometallic counterparts in terms of voltammetric response and high CO poisoning tolerance. The Arrhenius plots reveal markedly low activation energy requirements for the Au@Pd NPs. The material developed here can be deposited on any conducting substrate and hence can be developed as potential candidates for fuel cell applications.

References

1. Z. Fan, D. Senapati, A. K. Singh and P.C. Ray, *Mol. Pharmaceutics*, 2013, **10**, 857.

2. Y. Park, S. Yoo and S. Park, *Langmuir*, 2008, **24**, 4370.

3. D. Deng and J. Y. Lee, *Chem. Mater.*, 2008, **20**, 1841.

4. S. Guha, S. Roy and A. Banerjee, *Langmuir*, 2011, **27**, 13198.

5. H. Shin and S. Huh, *ACS Appl. Mater. Interfaces*, 2012, **4**, 6324.

6. C. Bianchini and P. K. Shen, *Chem. Rev.*, 2009, **109**, 4183.

7. L. D. Zhu, T.S. Zhao, J. B. Xu and Z. X. Liang, *J. Power Sources*, 2009, **187**, 80.

8. C. Xu, L. Cheng, P. Shen and Y. Liu, *Electrochem. Commun.*, 2007, **9**, 997.

9. D. F. Silva, A. N. Geraldes, E. Z.Cardoso, M. M. Tusi, M. Linardi, E. V. Spinacé and A. O. Neto, *Int. J. Electrochem Sci.*, 2011, **6**, 3594.

10. M. Zhang, Z. Yan, Q. Sun, J. Xie and J. Jing, *New J. Chem*., 2012, **36**, 2533.

11. H. M. Song, D. H. Anjum, R. Sougrat, M. N. Hedhilib and N. M. Khashab, *J. Mater. Chem*., 2012, **22**, 25003.

12. Z. Liu, B. Zhao, C. Guo, Y. Sun, F. Xu, H. Yang and Z. Li, *J. Phys. Chem. C*, 2009, **113**, 16766.

13. M. J. Kim, K. J. Park, T. Lim, S. Choe, T. Yu and J. J. Kim, *J. Electrochem. Soc.*, 2013, **160**, E1.

14. F. Yang, K. Cheng, T. Wu, Y. Zhang, J. Yin, G. Wang and D. Cao, *Electrochim. Acta*, 2013, **99**, 54.

15. M. T. Reetz, W. Helbig and S. A. Quaiser, *Chem. Mater*., 1995, **7**, 2227.

16. X. Huang, H. Wu, S. Pu, W. Zhang, X. Liao and B. Shi, *Green Chem*., 2011, **13**, 950.

17. J. Hu, Y. Zhang, J. Li, Z. Liu, B. Ren, S. Sun, Z. Tian and T. Lian, *Chem. phys. Lett*., 2005, **408**, 354.

18. S. K. Srivastava, T. Hasegawa, R. Yamada, C. Ogino, M. Mizuhata and A. Kondo, *RSC Adv*., 2013, **3**, 18367.

19. M. Wu, D. Chen and T. Huang, *Langmuir*, 2001, **17**, 3877.

20. K. Richter, P.S. Campbell, T. Baecker, A. Schimitzek, D. Yaprak and A. Mudring, *Phys. Status Solidi B*, 2013, **250**, 1152.

21. L. Wei, Y. Fan, N. Tian, Z. Zhou, X. Zhao, B. Mao and S. Sun, *J. Phys. Chem. C*, 2012, **116**, 2040.

22. M. Chirea, A. Freitas, B. S. Vasile, C. Ghitulica, C. M. Pereira and F. Silva, *Langmuir*, 2011, **27**, 3906.

23. S. Trasatti and O. A. Petrii, *Pure & Appl. Chem*., 1991, **63**, 711.

24. W. Pan, X. Zhang, H. Ma and J. Zhang, *J. Phys. Chem. C*, 2008, **112**, 2456.

25. K. Juodkazis, J. Juodkazyte, , B. Sebeka, G. Stalnionis and A. Lukinskas, *Russ. J. Electrochem.*, 2003, **39**, 954.

26. K. Deplanche, M. L. Merroun, M. Casadesus, D. T. Tran, I. P. Mikheenko, J. A.Bennett, J. Zhu, I. P. Jones, G. A. Attard, J. Wood, S. S. Pobell and L.E. Macaskie, *J. R. Soc. Interface*, 2012, **9**, 1705.

27. Y. W. Lee, M. Kim, Z. H. Kim and S. W. Han, *J. Am. Chem. Soc.*, 2009, **131**, 17036.

28. L. Lu, H. Wang, S. Xi and H. Zhang, *J. Mater. Chem.*, 2002, **12**, 156.

29. H. Chen, G. Wei, A. Ispas, S. G. Hickey and A. Eychmüller, *J. Phys. Chem. C*, 2010, **114**, 21976.

30. N. Toshima and T. Yonezawa, *New J. Chem*., 1998, **22**, 1179.

31. L. Chen, C. Wan and Y Wang, *J. Colloid Interface Sci.*, 2006, **297**, 143.

32. Z. Borkowska, A. T. Zielinska and G. Shul, *Electrochim. Acta*, 2004, **49**, 1209.

33. A. S. Aarnio, Y. Kwon, E. Ahlberg, K. Kontturi, T. Kallio and M. T. M. Koper, *Electrochem. Commun.*, 2011, **13**, 466.

34. Y. Su, M. Zhang, X. Liu, Z. Li, X. Zhu, C. Xu and S. P. Jiang, *Int. J. Electrochem. Sci.*, 2012, **7**, 4158.

35. X. Y. Lang, H. Guo, L. Y. Chen, A. Kudo, J. S. Yu, W. Zhang, A. Inoue and M. W. Chen, *J. Phys. Chem. C*, 2010, **114**, 2600.

36. A. V. Tripkovic, K. Dj. Popovic, J.D. Lovic, V. M. Jovanovic and A. Kowal, *J. Electroanal. Chem.*, 2004, **572**, 119.

37. A. V. Tripkovic, K. D. Popovic and J. D. Lovic, *J. Serb. Chem. Soc.*, 2007, **72**, 1095.

38. W. P. Zhou, A. Lewera, R. Larsen, R. I. Masel, P. S. Bagus and A. Wieckowski, *J. Phys. Chem. B*, 2006, **110**, 13393.

39. V. Mazumder and S. Sun, *J. Am. Chem. Soc*., 2009, **131**, 4588.

40. R. Manoharan and J. B. Goodenough, *J. Mater. Chem*., 1992, **2**, 875.

41. K. Kunimatsu, *J. Electroanal. Chem*., 1983, **145**, 219.

42. D. Wang, J. Liu, Z. Wu, J. Zhang, Y. Su, Z. Liu and C. Xu, *Int. J. Electrochem. Sci*., 2009, **4**, 1672; O. O. Fashedemi and K. I. Ozoemena, *Phys. Chem. Chem. Phys.*, 2013, **15**, 20982; V. Bambagioni, C. Bianchini, A. Marchionni, J. Filippi, F. Vizza, J. Teddy, P. Serp and M. Zhiani, *J. Power Sources*, 2009, **190**, 241; L. Yang, W. Yang and Q. Cai, *J. Phys. Chem. C*, 2007, **111**, 16613.

43. M. I. Manzanares, A. G. Pavese and V. M. Solis, *J. Electroanal. Chem*., 1991, **310**, 159.

44. T. Takamura and Y. Sato, *Electrochim. Acta*, 1974, **19**, 63.

45. J. L. Davis and M. A. Barteau, *Surface Sci.*, 1987, **187,** 387.

46. K. Franaszczuk, E. Herrero, P. Zelenay, A. Wieckowski, J. Wang and R. I. Masel, *J. Phys. Chem.* , 1992, **96**, 8509.

47. J. S. Spendelow, J. D. Goodpaster, P. J. A. Kenis and A. Wieckowski, *Langmuir*, 2006, **22**, 10457.

48. K. A. Assiongbon, D. Roy, *Surface Sci.*, 2005, **594**, 99.

49. S. T. Oyama, R. Radhakrishnan, M. Seman, J. N. Kondo, K. Domen and K. Asakura, *J. Phys. Chem. B*, 2003, **107**, 1845.

50. Y. Kwon, S. C. S. Lai, P. Rodriguez and M. T. M. Koper, *J. Am. Chem. Soc*., 2011, **133**, 6914.

51. S. Lj. Gojkovic, T. R. Vidakovic and D. R. Durovic, *Electrochim. Acta*, 2003, **48**, 3607.

52. R. K. Pandey and V. Lakshminarayanan, *J. Phys. Chem. C*, 2010, ***114***, 8507.

53. J. S. Spendelow and A. Wieckowski, *Phys. Chem. Chem. Phys*., 2007, **9**, 2654.

54. R. C. Sekol, M. Carmo, G. Kumar, F. Gittleson, G. Doubek, K. Sun, J. Schroers and A.D. Taylor, *Int. J. Hydrogen Energy*, 2013, **38**, 11248.

55. M. Smiljanic, Z. Rakocevic, S. Strbac, *Int. J. Electrochem. Sci*., 2013, **8**, 4941.

CHAPTER 7

Oxygen evolution catalysts of graphite modified with Co and Co-Ni alloys prepared in Deep Eutectic Solvents (DES)

7.1. Introduction

Oxygen finds several applications in energy generation devices including that of fuel cells. Oxygen evolution reaction (OER) is the anodic reaction of water electrolysis. The efficiency of water electrolysis is often affected by the high overpotential required for OER. A substantial amount of research has been carried out to develop electrocatalysts capable of decreasing the overpotential required for oxygen evolution reaction. Initially, the research was concentrated on Pt and other noble metal oxides in acidic medium. Over the past years, there has been an increasing interest to develop base metal catalysts as alternatives to the expensive noble metal catalysts. Of these, cobalt oxides and cobalt based materials in their mixed oxidation states have been shown to exhibit superior electrocatalytic activity over other metallic counterparts. These base metal oxide catalysts are usually studied in alkaline medium to prevent problems associated with corrosion. Nocera group has developed the preparation method for cobalt-phosphate based OER electrocatalysts that works effectively in neutral pH [1]. Recently, Graphene-Co_3O_4 nanocomposite prepared by Zhao *et al.* exhibited excellent stability and electrocatalytic activity for OER in both neutral and alkaline medium [2].

Cobalt based electrocatalyst materials are normally prepared by an initial thermal decomposition or freeze drying-vacuum decomposition technique. The materials prepared are later modifed to the required electrode surface. Electrochemical techniques are also employed to obtain stable electrodeposited films of cobalt. The electrochemical reduction of cobalt ion at the cathode leads to the formation of cobalt film. The electrodeposition at the cathode is accompanied by a side reaction of water reduction [3].

$$2H_2O + 2e^- \rightarrow 2OH^- (aq) + H_2(g)$$

The reaction products increases the pH at the cathode interface leading to the formation of $Co(OH)_2$. The formation of $Co(OH)_2$ has been confirmed by EQCM technique [4]. To maintain the pH of the solution at the interface and thereby prevent the formation of $Co(OH)_2$, boric acid is added to the electrodeposition medium. The presence of boric acid ensures the direct electrochemical reduction

of cobalt ions at the cathode. The pH of the aqueous electrodeposition medium of cobalt is usually mildly acidic (pH 4-5).

The electrodeposition of cobalt in aqueous medium is also accompanied by hydrogen evolution at the cathode. The current efficiency of the electrodeposition is often affected by this side reaction. In addition to this, the hydrogen evolution reaction happening at the cathode causes hydrogen to get adsorbed into the electrodeposited cobalt film. The adsorbed hydrogen diffuses into the metal film over a period of time, forming numerous surface defects called hydrogen embrittlement. These problems associated with the aqueous medium can be solved essentially by the use of ionic liquids and deep eutectic solvents (DES). Electrodeposition of cobalt-samarium, cobalt-iron alloys carried out by DC and pulse techniques have already been reported in DES medium [5-6]. Saravanan *et al*. studied in detail, the corrosion resistive properties of cobalt-chromium electrodeposited in DES [7]. The electrochemical properties of Co-Ni alloys have been studied by Lupi *et al.* [8]. A majority of these experiments deals with alloy depositions and were carried out at high temperatures usually greater than 70 ^{0}C.

In this study, the experiments carried out for the electrodepositions of cobalt and cobalt-nickel alloy in three different DES at room temperature are described. The morphological, electrochemical and electrocatalytic properties of these substrates in OER are compared in detail. As pointed out earlier, the electrodeposition of cobalt is carried out at low pH in aqueous medium to decrease the problems associated with the passivation of electrode due to the formation of hydroxide/oxide films. Electrodeposition in DES is not associated with passivation problems of the electrode and apparently a low pH medium is not essential in DES. However, the pH effect on the electrodeposition of Co in DES media has to be carefully studied. The pH of choline chloride based DES depends only on the hydrogen bond donor used in the preparation. In this study, the electrodeposition was carried out in DES media viz., maline, ethaline and reline containing different hydrogen bond donor. While ethaline prepared from ethylene glycol and maline prepared from malonic acid are expected to be neutral and weakly acidic respectively, the slightly alkaline nature of reline has already been confirmed by Li *et al.* [9].

Inspite of the fact that graphite is not catalytically active for OER, it is relatively less expensive and also provides an excellent substrate for Co based catalyst. It is therefore chosen as a substrate for depositing the porous films of Co. The electrocatalytic activity of Co for OER depends on the electronegativity of the substrate material used. Yeo *et al.* observed that the OER electrocatalytic activity of Co decreased with the electronegativity of the substrate metals in the order Au > Pt > Pd > Cu > Co [10]. Thus, carbon (graphite) with an electronegativity of 2.5 is comparable to that of Au (2.4) and hence is expected to be a good substrate material as that of gold. Further, for practical applications, a low cost substrate material such as graphite is considered ideal.

7.2. Experimental

7.2.1. Materials

Deep eutectic solvents of maline, ethaline and reline were used as electrodeposition media.

QAS	HBD	DES	Molar ratio
Choline chloride (Aldrich)	Malonic acid (Merck)	Maline	1:1
	Ethylene glycol (Merck)	Ethaline	1:2
	Urea (Merck)	Reline	1:2

Cobalt chloride and nickel chloride were purchased from Merck. Cobalt wire (0.5mm diameter) of 99 % purity was purchased from Advent research materials (UK). Exfoliated graphite sheets were used as subtrate material.

7.2.2. Electrochemical studies

The electrodeposition was carried out in galvanostatic mode in an electrochemical cell of 10ml capacity. The volume of the DES was kept constant (4ml) in each of the conditions. Graphite sheet of 1mm thickness was used as the cathode for

electrodeposition. The geometrical area of the graphite substrate was kept constant (0.20 cm^2) for all optimization conditions. For monometallic Co deposition, cobalt wire anode of 5mm length was exposed to the medium while the remaining area was masked completely by parafilm and teflon tapes. Nickel strips of 5mm x 5mm were used as anodes for the electrodeposition of Co-Ni alloys.

For cyclic voltammetric studies, while the modified electrode was used as working electrode, a platinum foil of large surface area was used as the counter electrode. Since the electrochemical experiments were carried out in alkaline medium, Hg/HgO/1M NaOH reference electrode was used.

7.3. Results and discussion

7.3.1. Electrocatalysts based on porous films of Cobalt

The experimental conditions for the electrodeposition at room temperature were optimized based on the cyclic voltammograms of the electrodeposited cobalt. The peaks corresponding to the oxidation of cobalt is known from literature and the area under these peaks correspond to the charge consumed during the process and is considered to quantify the surface area of electrodeposited cobalt.

7.3.1.1. Optimization of electrodeposition conditions

The electrodeposition was initially carried out in DES medium using anodic dissolution of Co wire as the only source of metal ions without the addition of any cobalt salt. The DES solution attained a blue colour with the progress of the anodic dissolution of cobalt wire. However, it was observed that the anodic dissolution of cobalt to cobalt ions was not followed by the electrochemical reduction and deposition of Co on the graphite cathode. This was confirmed from cyclic voltammetric studies of the cathode used. It was apparent from the blue colour of the DES that, during dissolution of Co wire there is a release of cobalt ions into the electrolytic solution. To check whether the cobalt ions existed as simple metal salts in reducible form or as stable complexes in irreducible form, a simple test was conducted. This was carried out by adding the reducing agent sodium borohydride of different concentrations to the blue coloured cobalt

solution in DES. However, this addition did not produce any further change in the colour of the solution. A similar experiment carried out in aqueous medium, however initially forms a pink solution corresponding to the formation of an octahedral cobalt (II) complex. The octahedral complex gets reduced to a black coloured solution of Co nanoparticles with the addition of sodium borohydride. This procedure has been used by Liang *et al.* for the wet chemical synthesis of CoNP at room temperature [11]. The absence of any colour change after the dissolution of cobalt in DES even after the addition of reducing agent indicates that cobalt ions in DES exists as stable cobalt complex.

Earlier, the complex formation and electrochemical reduction of cobalt ions was studied in ionic liquids too. The studies carried out in ionic liquids containing excess of Lewis basic chloride anions showed that the cobalt exists as blue coloured tetrachlorocobaltate complex, $CoCl_4^{2-}$ which is electrochemically inactive [12]. It was also shown that the electrodeposition of cobalt is strongly dependent on the $CoCl_2$ concentration when the process is carried out in chloride based ionic liquids.

$$2[C_4mim]\,Cl + CoCl_2 \rightarrow [C_4mim]_2^{+}\,[CoCl_4]^{2-}$$

The reaction shows that for each $CoCl_2$, two chloride anions from ionic liquid is required for the formation of $[CoCl_4]^{2-}$. Thus $[CoCl_4]^{2-}$ can be formed only when $CoCl_2$ concentration is $\geq 33\%$. At a $CoCl_2$ concentration of greater than 33%, the chloride ions from the ionic liquid are insufficient for the formation of electrochemically inactive tetrachloro complexes and hence free cobalt ions are available for the electrochemical reduction and electrodeposition.

DES are a class of chloride rich ionic liquid, with the major difference being the fact that the chloride ions of choline chloride are bound to the hydrogen bond donors such as ethylene glycol, malonic acid, urea through strong hydrogen bonding interactions. However, under equilibrium a small concentration of chloride ions remains unbound in the DES medium. Therefore, the cobalt ions produced during the anodic dissolution can complex with these free chloride ions and remain electrochemically inactive. Hence, the cobalt ions obtained by anodic dissolution alone are not sufficient to cross the threshold concentration as seen in ionic liquids, necessitating the addition of cobalt salts to the DES medium.

However, it is to be noted that in the case of DES, only the unbound chloride ions take part in complexation to form $[CoCl_4]^{2-}$ vis-à-vis the entire chloride ions in ionic liquid and hence the threshold concentration of $CoCl_2$ required for electrodeposition is expected to be considerably lower than the 33% required in ionic liquids.

(a) Electrodeposition in maline

The maline medium is weakly acidic due to the presence of malonic acid component. The acidic components can complex with the oxygen of metal oxides and solubilize them easily, thereby minimizing the passivation problems associated with the anodic dissolution process. Maline medium is associated with a very high viscosity of 1124 cP at room temperature. The high viscosity of the medium can have detrimental affects on the mass transport properties associated with the electrodeposition process. The studies done by Florindo *et al.* showed that a small percentage of water in the DES medium lower the viscosity of the medium much better than raising the temperature [13]. The optimum composition of maline-water mixture was determined from the extent of electrodeposition of Co in different composition of maline:water mixtures. This is because of the fact that at a high maline percentage, the viscosity factors affects mass transport and thereby the deposition process. A low maline percentage increases the gas evolution at the electrodes and decreases the deposition. From the cyclic voltammograms shown in Fig. 1a, it is apparent that the compositions corresponding to 100% maline and 100% water are associated with minimal deposition.

The composition of maline:water was maintained constant at 80:20 for experiments to optimize the current density for electrodeposition and the concentration of $CoCl_2$. The current densities were varied between 9–70 mA/cm^2 at 0.16M $CoCl_2$ in 20% aqueous maline (Fig.1b). It was found that a low current density of $9mA/cm^2$ gave extremely thin deposition, while the electrodepositions carried out at higher current densities resulted in poor adhesion of the cobalt films onto the substrate. The cobalt chloride concentrations were varied between 0.09-0.5M maintaining the other parameters optimized (Fig.1c). The reaction

conditions of solvent composition, current density, $CoCl_2$ concentration and deposition time used for the electrodeposition of cobalt in maline are given in Table -1.

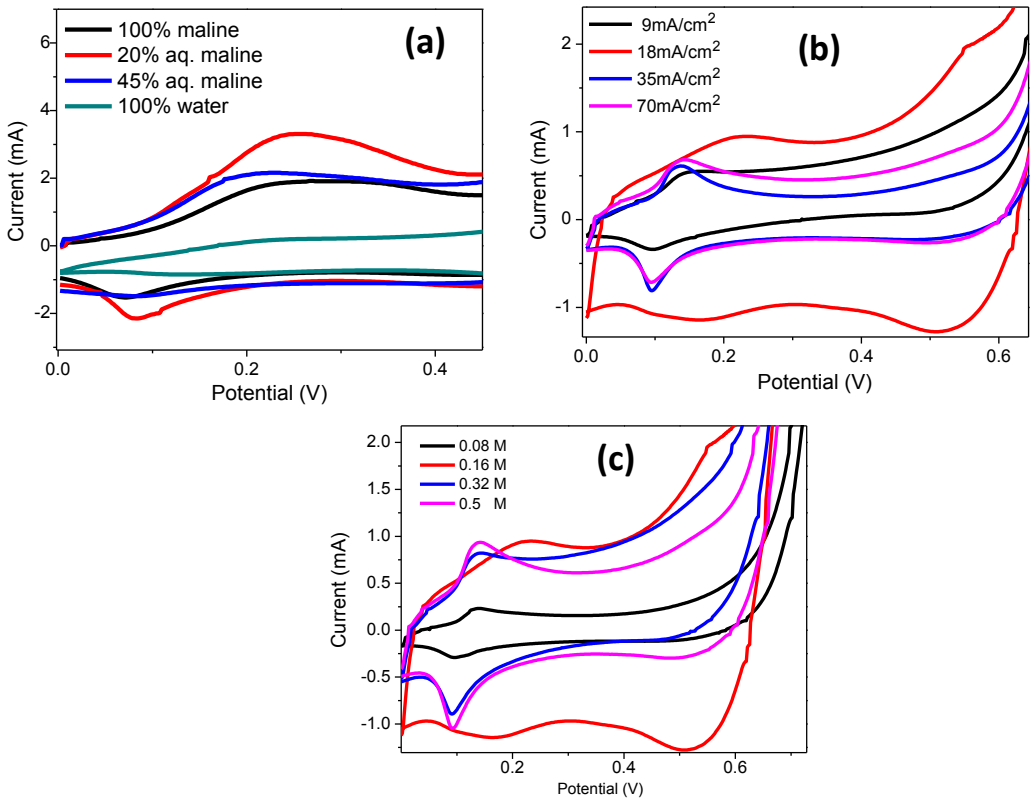

Figure 1. *Cyclic voltammograms of the electrodeposited cobalt prepared in maline at varying composition of water (a), current density (b) and $CoCl_2$ concentration (c) in an alkaline medium of 1M NaOH*

Table 1. *Optimized conditions for the electrodeposition of Co in maline*

Composition of water	20%
Current density	18mA/cm^2
$CoCl_2$ concentration	0.16 M
Electrodeposition time	1 hour

(b) Electrodeposition in ethaline

Ethaline (choline chloride + ethylene glycol) is the one of the most favoured medium for the electrodeposition of nanoparticles owing to its low viscosity and high ionic conductivity (7.61 mS/cm). The deposition of nanostructured materials of Pd, Cu, Pt and Ni have already been reported in ethaline medium [14-17]. The studies involving addition of water was not required for a low viscous medium of ethaline (37 cP) vis-à-vis the highly maline (1124 cP). However, experimental parameters such as current density for electrodeposition, concentration of $CoCl_2$ of the deposition bath have to be optimized for the ethaline medium. The concentration of $CoCl_2$ in the electrodeposition bath depends on the percentage of free chloride ions in the DES medium. In the case of 20% aqueous maline bath discussed in the earlier section, the presence of water in the medium though minimal, disrupts the hydrogen bonding interaction in $Cl^{-} \cdots (HOOC)_2 - CH_2$ thereby increasing the percentage of free chloride ions [18-19]. In contrast to this, in a neat ethaline bath the hydrogen bonding interactions between the Cl^- of choline chloride and ethylene glycol remains intact and hence it is unlikely to possess a high free Cl^- concentration in the medium unlike that of 20% aqueous maline. The concentrations of $CoCl_2$ in ethaline medium were varied between 0.08 - 0.32M and the extent of depositions were observed from the cyclic voltammograms (Fig.2a). Though the thickness of the deposition was found to be higher in the case of higher concentrations, the films were found to peel off with time.

The cyclic voltammograms of the electrodeposited cobalt at various current densities between 9 - 70 mA/cm^2 at a fixed $CoCl_2$ concentration of 0.08M are given in Fig.2b. The absence of water in the medium prevents gas evolution at the electrodes and hence using higher current density for electrodeposition is not a constraint as seen in the case 20% aqueous maline bath. Table 2 contains the optimized conditions for electrodeposition in ethaline medium.

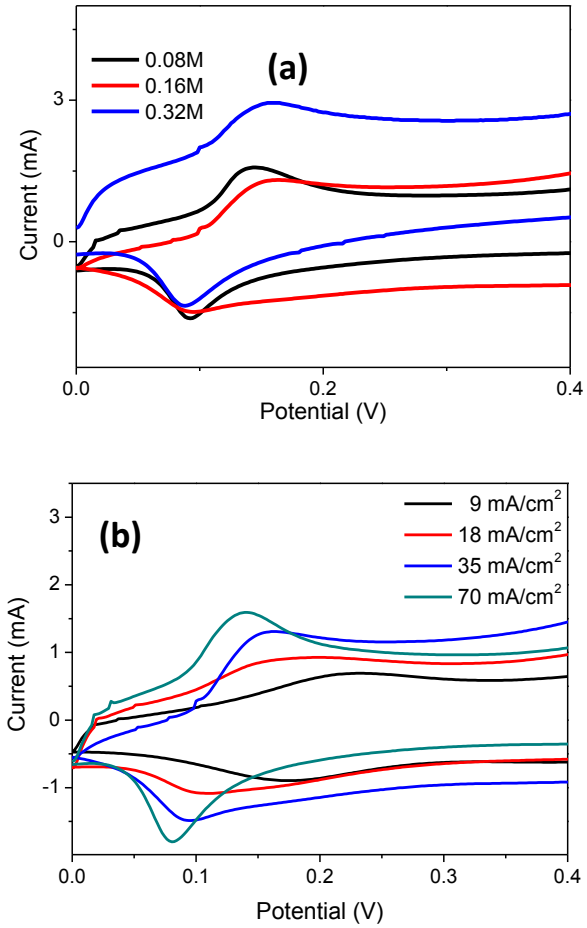

***Figure 2**: Cyclic voltammograms of the electrodeposited cobalt prepared in ethaline at varying $CoCl_2$ concentration (a) and current density (b), in an alkaline medium of 1M NaOH*

***Table 2**: Optimized conditions for the electrodeposition of Co in ethaline and reline*

Current density	70 mA/cm^2
$CoCl_2$ concentration	0.08 M
Electrodeposition time	1 hour

The electrodeposition conditions of cobalt optimized for the neat ethaline medium were maintained for the electrodeposition of reline (Table-2). This is because similar to ethaline, the medium is devoid of water and also the fact that electrodeposition process is not associated with gas evolution. Henceforth, in

what follows the Co films on graphite electrodeposited in 20% aqueous maline, ethaline and reline media are denoted as Co_{Mal}, Co_{Eth} and Co_{Rel} respectively.

7.3.1.2. Characterization of the electrodeposited films of Co

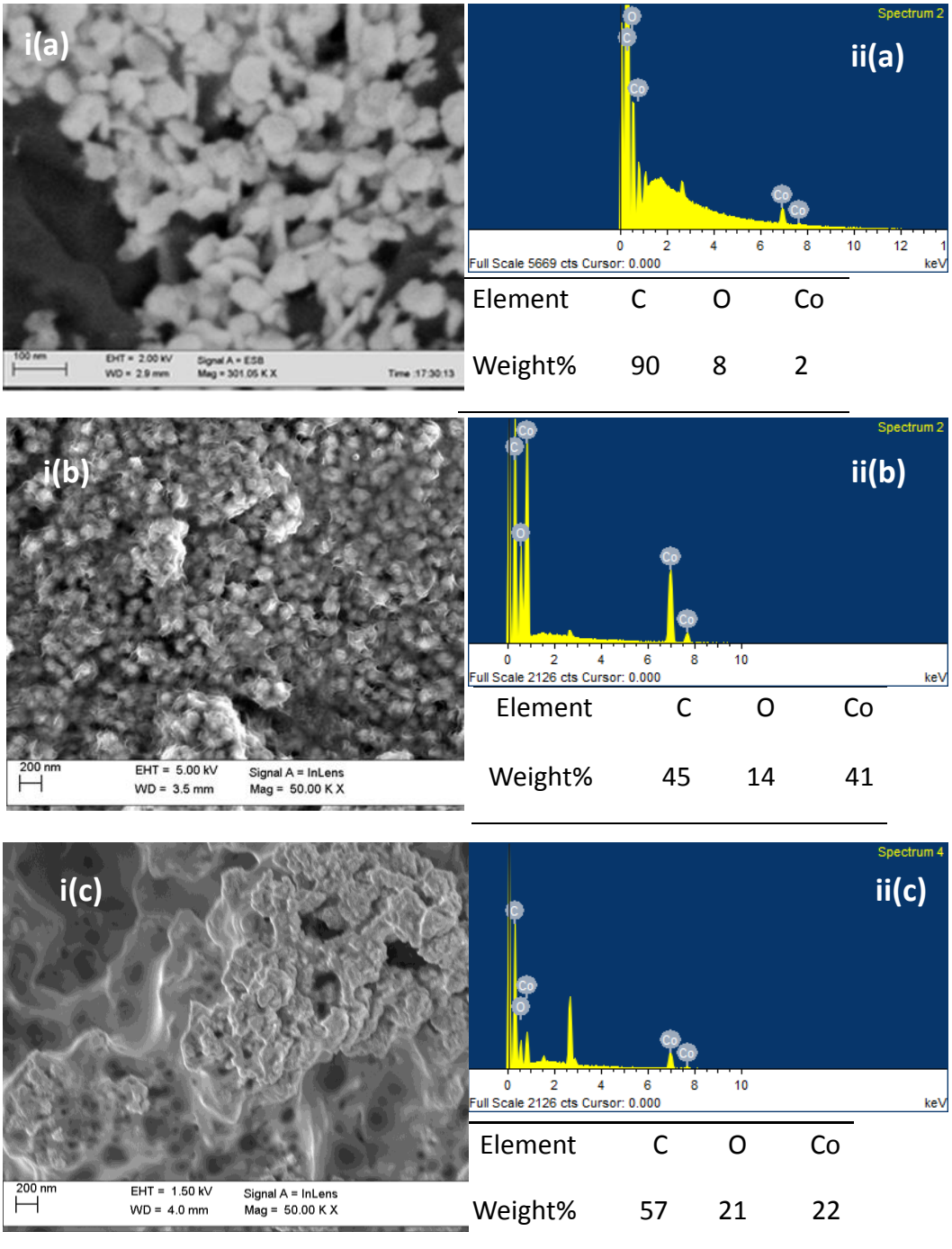

***Figure 3**: SEM images (i) and EDAX (ii) of (a)Co_{Mal} (b) Co_{Eth} and (c)Co_{Rel} prepared in maline, ethaline and reline respectively*

Fig.3 (ia) shows that Co_{Mal} contains disc shaped nanoparticles with diameters ranging between 50-100 nm. The EDAX spectrum of the sample given in Fig.3 (ib) confirms the presence of cobalt and the relative composition of other elements, carbon and oxygen. The morphology of the Co_{Eth} seen in Fig.3(ib) is considerably different from that of Co_{Mal} seen in Fig.3(ia). It is apparent that the Co film is composed of spherical nanoparticles of diameter 150-200 nm. The morphology of the Co_{Eth} exhibits a uniform distribution of tightly packed nanoparticles. The EDAX analysis of the deposit given in Fig.3(iib) indicates that the composition of Co on the graphite is found to be higher in Co_{Eth} (41%) compared to that of Co_{Mal} (2%). Fig.3(ic) shows that the cobalt films prepared in reline medium (Co_{Rel}) does not exhibit any nanostructured features. However, the presence of cobalt in the substrate with a fairly high Co content of 22% is confirmed from the EDAX [Fig.3(iic)].

7.3.1.3. Cyclic voltammetric studies of the electrodeposited Co films

In this section, the mesoporous Co films deposited onto the graphite sheet is studied as an oxygen evolution catalyst in alkaline medium. The oxidation of cobalt begins with the formation of a passive Co (II) oxide film at negative potentials of about -0.8V Vs Hg/HgO. The cyclic voltammogams (Fig.4) shows the formation of Co (III) and Co (IV) oxidation states at 0.24V and 0.55V respectively. The oxidised species Co (IV) acts as adsorption sites for the hydroxyl anions leading to the formation of an intermediate $Co^{IV}(OH)_{ad}$. The presence of Co (IV) at high overpotentials was earlier confirmed by Mossbauer spectroscopy [20]. It is apparent from the figure that the oxygen evolution reaction begins immediately after the formation of the Co (IV) oxidation.

The onset potential for OER is 0.65V Vs Hg/HgO (0.815V Vs NHE) for the Co catalysts prepared in maline and ethaline. Cobalt oxides with spinel structure such as Co_3O_4 prepared by Nikodov *et al.* was associated with an onset potential of 0.63V Vs Hg/HgO [20]. The cobalt phosphate (Co-Pi) electrocatalysts prepared by Nocera *et al.* for OER in neutral medium exhibited an onset of 1.1V Vs NHE [21]. The oxygen evolution on electrodeposited cobalt oxides deposited on nickel susbtrates commenced at 0.6V Vs Hg/HgO [22].

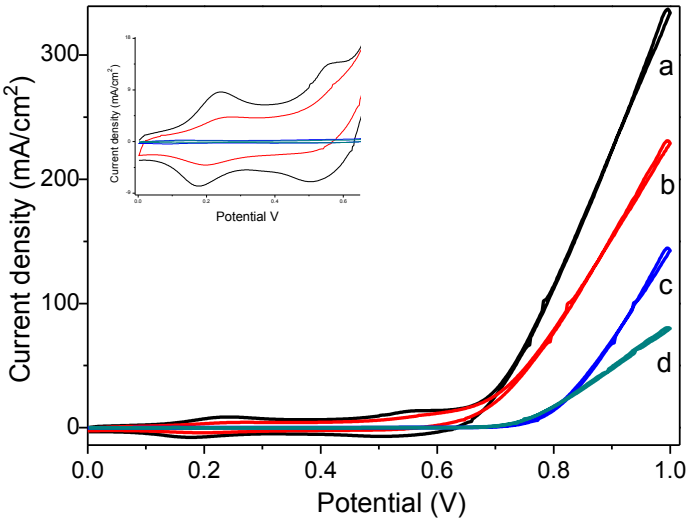

Figure 4. *OER on (a)Co_{Mal} (b)Co_{Eth} and (c)Co_{Re} (d)Co wire in 1M NaOH at a scan rate of 100 mV*

At higher overpotentials, OER current normalized to the corresponding geometrical area increases sharply and follows the trend Co_{Mal} > Co_{Et} > Co_{Rel} > Co wire. It is striking to note that the Co_{Mal} associated with least Co content as per EDAX exhibits the maximum OER current density *wrt* geometrical area. This could be attributed to the morphological features and smaller size of the nanoparticles observed in SEM. Due to this, the reactants can access catalytic active site more readily in Co_{Mal} than in Co_{Et} and $Co_{Rel.}$

The catalytic activity due to the nanostructured features of the subtrate can be understood only from the calculation of electroactive surface area. However, there are no reports on the precise calculation of electroactive surface area (ECSA) from the charge obtained in cyclic voltammogram. Hence in our studies, the calculation is done by assuming the charge associated with the formation of α-hydroxide layer of Co to be 514 μC/cm^2 as that used for the calculation of ECSA of Ni. The current measured at 1V during OER is normalized *wrt* to geometrical area and ECSA and given in Table 3. It is evident that the high OER currents obtained on Co_{Mal} despite the low Co composition shown in EDAX (*wrt* to other substrates) is only due to the high surface area.

Table 3. *Current densities obtained for OER on Co_{Mal}, Co_{Eth}, and Co_{Rel} at 1 V*

	Actual Current at 1V mA	**Current normalized to GA (mA/cm^2)**	**Current normalized to ECSA (mA/cm^2)**
Co_{Mal}	67.2	336	9.28
Co_{Eth}	46.2	231	14.7
Co_{Rel}	28.8	144	20.36

7.3.1.4. Mechanism of OER on the electrodeposited Co films

The mechanism of OER on Co is reported to be similar in both alkaline and neutral media by various groups [23-25]. The electrochemical oxidation of cobalt leading to the formation of Co^{IV} occurs through multiple steps of single electron transfer. The Co (IV) species is known to be crucial in catalysing the oxygen evolution reaction.

Tafel polarization studies were carried out at a potential range of 600-900 mV on a fresh cobalt wire at 298K (Fig.5). At low overpotentials, the Tafel slopes obtained were almost equal to 60mV/dec. This value of Tafel slope implies that the mechanism of oxygen evolution involves an initial single electron transfer step which is followed by a rate determining chemical step [26]. The first step as proposed by Nocera *et al.* is given below [21],

$$[Co_{III}\text{-}OH] \leftrightarrow [Co_{IV}\text{-}O] + H^+ + e^-$$

This is followed by the rate determining chemical step which involves the coupling of the Co_{IV}-O species forming O-O bonds that spontaneously leads to oxygen evolution [27].

At low overpotentials, the Tafel slopes of the electrodeposited Co films Co_{Mal}, Co_{Et}, Co_{Rel} differ from that of a cobalt wire by 15-20 mV/dec as can be seen in Table 4. The larger Tafel slope values observed on the graphite substrates can be attributed to the oxygen evolution occurring on graphite surface in addition to cobalt nanoparticles. The mechanism of electrocatalysis on Co has been found to be dependent on the nature of the substrate material used. For example, Tafel

slope for OER on Co_3O_4 nanoparticles on silicate based substrate was found to be 108 mV/dec [28]. The OER studied on Co_3O_4/MWCNT modified ITO subtrates exhibited a Tafel slope of 104 mV/dec [29]. OER electrocatalysts based on graphene-CoO and nitrogen doped graphene-CoO prepared by Mao *et al.* exhibited Tafel slopes of 75 and 71mV/dec respectively [30].

At high overpotentials, the Tafel slopes deviate from its corresponding value at low overpotential for all the materials studied here. These variations are observed for all the Co based substrates reported elsewhere and is attributed to ohmic resistivity of oxide films formed at high overpotentials and also to the increased

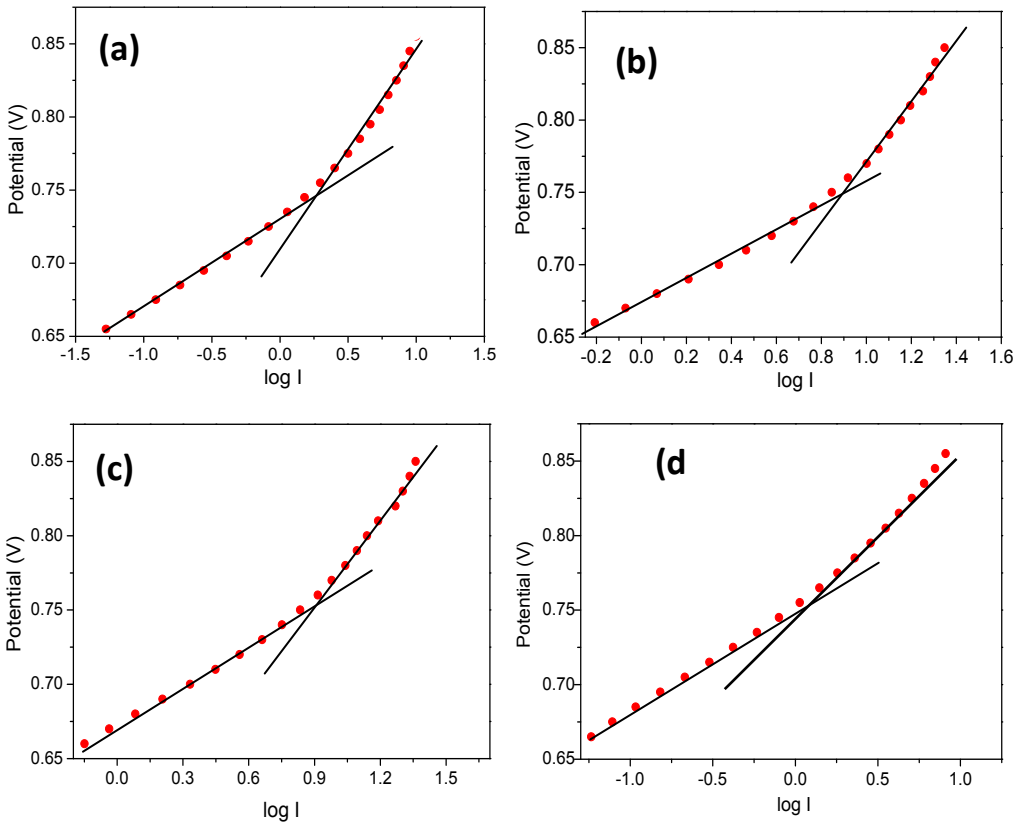

Figure 5*. Tafel plots for OER on (a) Co wire (b) Co_{Mal} (c) Co_{Et} (d) Co_{Rel} at 298K*

gas evolution occurring at high overpotentials. To confirm which of these factors affects the Tafel slope, Kessler *et al.* compared the Tafel slopes of a Co based substrate and also an oxide coated Co based substrate [31]. The results obtained were identical in both the cases and hence it was concluded that ohmic resistivity was not the contributing factor. Further, it was found that the deviation in Tafel slope was observed at the threshold potential for gas evolution. The gas bubble formation decreases the electroactive surface area causing an additional

resistance. The additional resistance alters the rate determining characteristics and brings about a change in the Tafel slope. A comparison of the cyclic voltammograms and Tafel plots (Fig.4 and 5) show that the Tafel slope deviates at about 0.75V where OER becomes significant.

Table 4*. Tafel slopes at low and high overpotentials of the OER electrocatalysts studied at 298K*

	low η (mV/dec)	**high η (mV/dec)**
Co wire	61	136
Co_{mal}	76	183
Co_{eth}	83	186
Co_{rel}	79	194

7.3.1.5. Activation energy measurements

The determination of activation energy for a process is important for designing and fabricating electrocatalysts aimed for fuel cell applications. This is because lower the activation energy for a reaction, lower will be operating temperature of the fuel cell. Till date, there has been very few literature reported on activation energy calculations for OER on Co substrates. Hence in this study, the OER activation energy requirements for the electrodeposited cobalt substrates were compared with that required for a fresh cobalt wire. The Arrhenius plots of the electrodeposited Co catalysts Co_{Mal}, Co_{Eth}, Co_{Rel} and Co wire at various overpotentials are shown in Fig. 6. The slope obtained from the Arrhenius plot was equated to 2.303/RT to get the activation energy of the OER on different substrates. The values obtained are given in the Table 5.

The activation energy requirements on Co wire is quite high compared to the other electrodeposited Co films on graphite. Earlier Nikdov *et al.* prepared Co based OER catalysts by the thermal decomposition of their respective nitrate salts at different temperatures. The activation energies requirements for the prepared Co_3O_4 were found to vary between 75 – 81kJ/mol [20].

It can be seen from the figure that the Co substrates prepared in maline and ethaline media exhibit significantly lower activation energy despite the low composition of cobalt on the graphite surface as shown in Fig. 3 (EDAX). The nanostructured features of Co_{Mal} and Co_{Eth} were apparent from the SEM and also the true surface area. The high ECSA contributes to the increase in the catalytic active sites available on the substrate, which lowers the activation energy of the process. Further, the thin films of cobalt electrodeposited on a graphite substrate are more economically viable for practical applications.

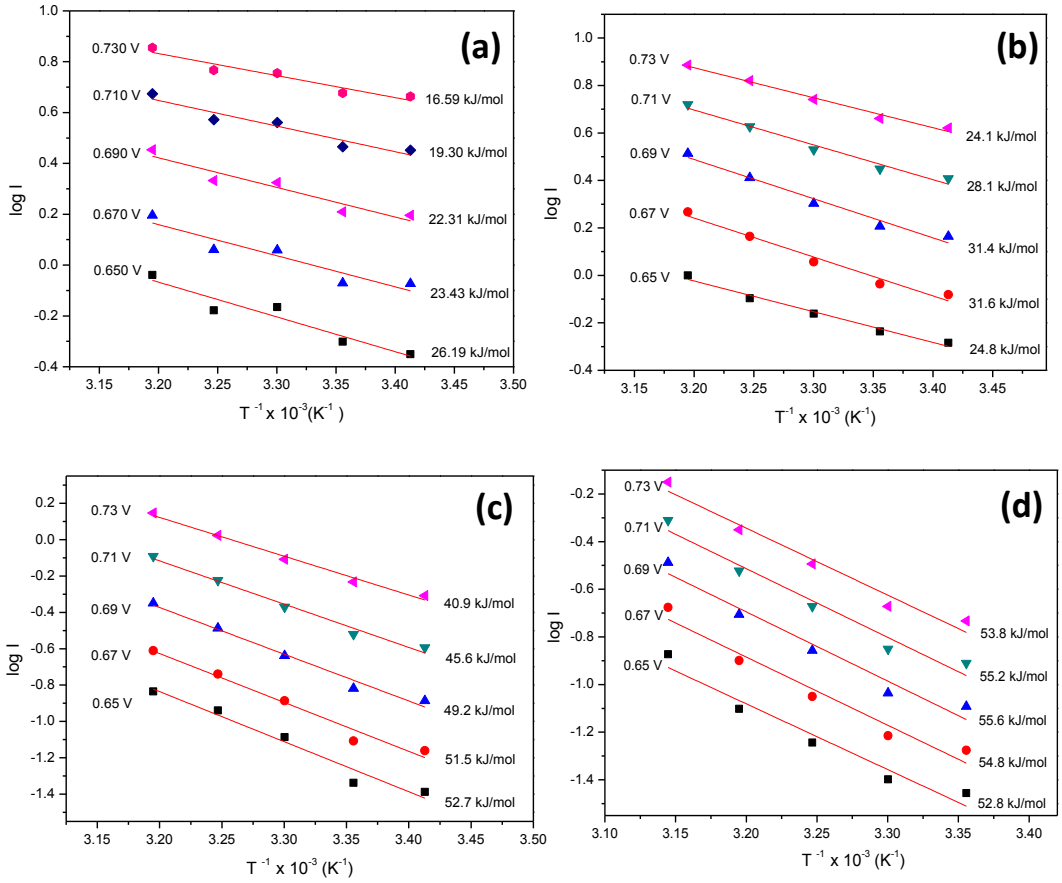

***Figure 6**. Arrhenius plots for OER on (a)Co_{Mal} (b) Co_{Eth} (c) Co_{Rel} (d) Co wire at different overpotentials*

Table 5. *Comparison of the average activation energies determined for OER on different substrates*

Substrate	Average Activation energy (kJ/mol)
Co wire	54.44
Co_{Mal}	21.56
Co_{Eth}	28.0
Co_{Re}	47.98

7.3.2. Electrocatalysts based on porous films of Cobalt – Nickel alloy

The electrocatalytic activity of Co based alloys has been found to increase by doping the material with other metals. Rasiya and Tseung observed an enhanced electrocatalytic activity of $Li_xCo_3O_4$ over Co_3O_4 due to the extra stabilization of Co^{n+} ions by the Li^{n+} ions [32]. Jasem and Tseung showed that $NiCo_2O_4$ exhibited the highest OER activity with very low activation energy over its counterparts [33]. The alloy components are usually optimized based on the availability, cost, thermodynamic stability and corrosion resistance of the material.

7.3.2.1. Electrodeposition of Co-Ni alloys on graphite

The electrodeposition of Ni-Co alloy films was carried out in ethaline and maline medium. The current density for electrodeposition and concentration of $CoCl_2$ in the medium were maintained as that optimized for Co deposition. The cobalt wire used as anode in the electrodeposition of Co was replaced by nickel strips for Co-Ni deposition. However, the use of nickel strips alone as metal ion source did not result in nickel deposition on graphite. Therefore nickel salts ($NiCl_2$) were also added to the DES media in addition to the $CoCl_2$. The concentration of the nickel salts were optimized based on the solubility of the metal salt in DES and also on the adhesion of the electrodeposited film onto the substrate. Based on these factors, the nickel chloride concentration was optimized as 0.08M in maline and 0.3M in ethaline.

7.3.2.2. Characterization of the electrodeposited films

The SEM images of the electrodeposited Co-Ni films on graphite were acquired for morphological studies. Fig.7a shows that the SEM image of the Co-Ni films prepared in 20% aqueous maline medium. The Co-Ni film covered almost the entire surface of the graphite, exhibiting sharp features with a hexagonal platelet morphology. Earlier, Liu *et al.* had attained the hexagonal platelet morphology with α and β - cobalt hydroxides using homogeneous precipitation method [34]. The electrodeposited films of Nickel in DES media reported by You *et al.* also exhibited a similar morphology [35].

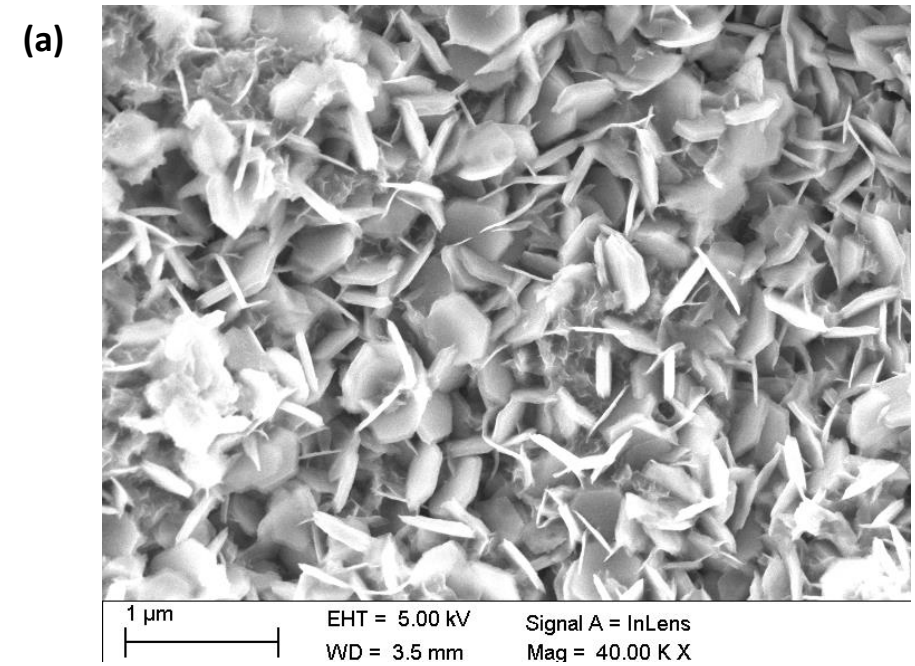

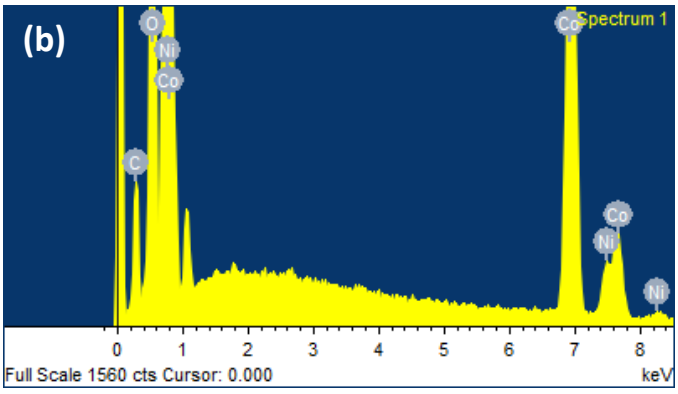

Element	Weight%
C K	7.62
O K	23.42
Co K	62.50
Ni K	6.46
	100

Figure 7. *(a) SEM images (b)EDAX spectra of porous Co-Ni$_{Mal}$ film deposited on graphite.*

The EDAX spectra of the film shown in Fig.7b confirmed the presence of both the metals Co and Ni on the substrate. The ratio of the Co composition was almost 10 times that of Ni. EDAX spectra also confirmed that cobalt and nickel are uniformly distributed across the entire surface.

The SEM image of the Co-Ni films deposited in ethaline medium is shown in Fig.8a. The morphology of the films is considerably different from that of Co-Ni_{Mal}. The crystallite textures with a leafy morphology of cobalt and nickel are distributed uniformly throughout the sample surface. The EDAX spectrum indicates (Fig.8b) that the oxide content of the film is very high, making the percentage of Co and Ni to be very low. The relative ratio of Co:Ni in the film is almost equal to 1:2.

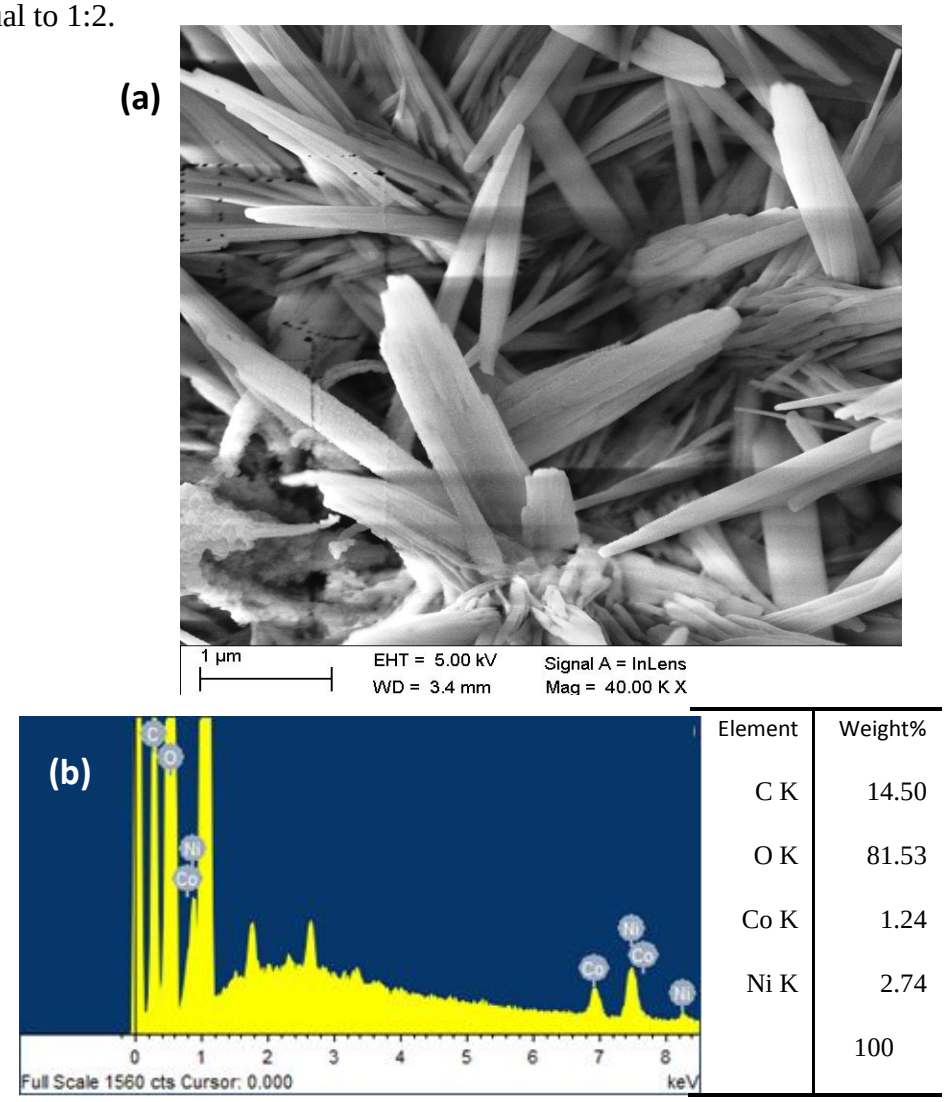

Element	Weight%
C K	14.50
O K	81.53
Co K	1.24
Ni K	2.74
	100

Figure 8. *(a) SEM images (b)EDAX spectra of porous Co-Ni_{Eth} film deposited on graphite.*

7.3.2.3. Cyclic voltammetric studies of Co-Ni alloys films

The cyclic voltammogram in Fig.9a and 9b shows that there are no well resolved individual redox peaks of the metallic components of Co and Ni. The appearance of as single redox peak further points to the possibility of a Co-Ni alloy formation. If the graphite substrate contained uniformly distributed individual particles of Co and Ni, the cyclic voltammograms is likely to exhibit independent

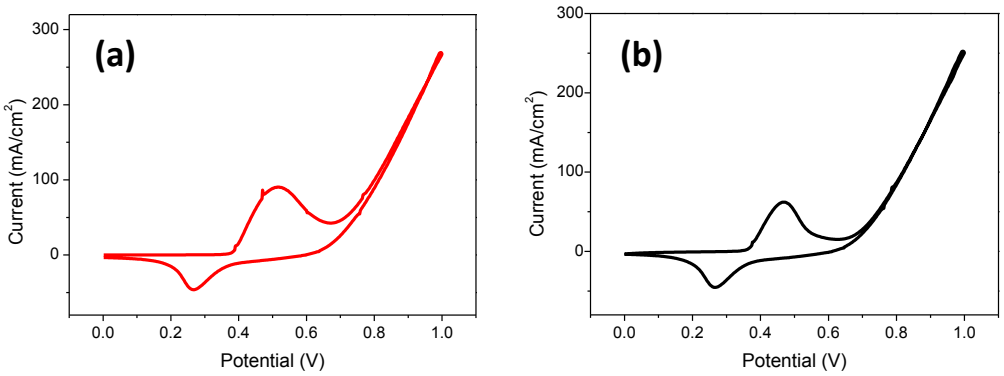

Figure 9. *Cyclic voltammograms of porous films of (a)Co-Ni$_{Mal}$ (b)Co-Ni$_{Eth}$ on graphite in 1M NaOH at a scan rate of 100 mV.*

redox peaks. It can also be considered that the SEM images of Co-Ni film exhibited a single uniform morphology all through the graphite substrate. Earlier, the Nikdov *et al.* observed unresolved peaks of Co and Ni in the cyclic voltammograms of nickel cobaltites, $Ni_xCo_{3-x}O_4$ [20]. The onset potentials for OER on Co-Ni films of Co-Ni_{Mal} and Co-Ni_{Eth} was shifted positive 20-30 mV compared to their respective monometallic Co counterparts. The current densities for OER at 1V obtained in both the cases Co-Ni_{Mal} and Co-Ni_{Eth} were also found to be comparable.

7.3.2.4. Mechanism of OER on Co-Ni films

The mechanism of cobalt, nickel and cobalt-nickel alloy are usually known to proceed with the same mechanism. To understand the mechanism of OER on Co-Ni films, Tafel analysis of the plot of log I Vs E was carried out. It can be seen from Fig. 10 that the Tafel plots exhibited two slopes at low and high overpotentials similar to that observed on Co films on graphite. The Tafel slopes at high overpotential are almost double (Table 6) that of the values at low overpotential which can be described to the enhanced oxygen evolution occurring

at higher overpotential as explained before. The values seem to deviate from the ideal value of 60 mV/dec as per the mechanism obtained on a fresh Co wire. The departure from the Tafel slope may be ascribed to the nickel content in the electrodeposited film compared to a fresh cobalt wire. The deviation in Tafel slope is more pronounced in the Co-Ni films prepared in ethaline medium. It was observed in the EDAX spectra (Fig.8b) that the composition of Co and Ni was very much less (1.2% and 2.7%) when compared to the oxide content (81%) on the graphite substrate. Further, the composition of Ni was almost double than that of Co. These factors might contribute to the increased Tafel slopes of Co-Ni_{Eth} compared to the Tafel slope of a fresh Co wire and Co-Ni_{Rel}.

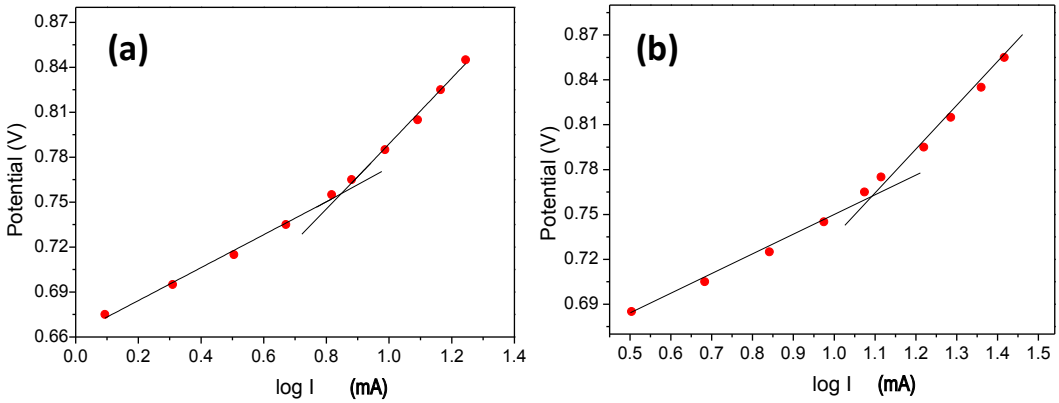

***Figure 10**. Tafel plots for OER on (a)Co-Ni_{Mal} (b)Co-Ni_{Eth} at 298 K*

***Table 6**. Tafel slopes at low and high overpotentials for OER on Co-Ni electrocatalyts studied at 298 K*

	low η (mV/dec)	**high η (mV/dec)**
Co-Ni $_{Ma}$	109	219
Co-Ni $_{Eth}$	138	265

7.3.2.5. Activation energy measurements

The activation energy for the oxygen evolution on Co-Ni films on graphite was determined from the Arrhenius plots (Fig.11). The average activation energy obtained for both the substrates Co-Ni_{Mal} and Co-Ni_{Eth} were very close to each

other as seen in Table 7. These values obtained are very much lesser than the activation energy required by Nickel cobaltites (64 kJ/mol) prepared by thermal decomposition of the corresponding metal salts [20]. The Co-Ni film prepared in maline medium exhibited slightly higher activation energy than the corresponding Co film prepared in maline medium. However, the activation energy requirements of Co-Ni_{et} and Co_{Et} films were comparable.

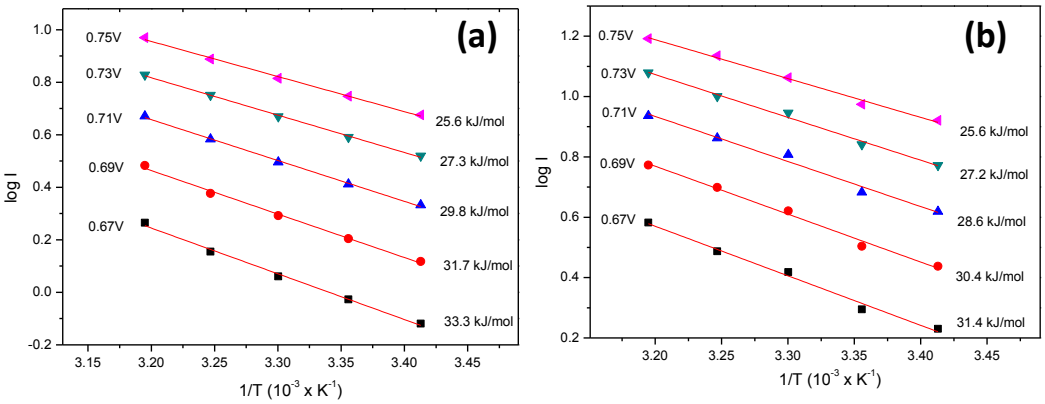

***Figure 11**. Arrhenius plots for OER on (a)Co-Ni_{Mal} (b) Co-Ni_{Eth} studied at different over potentials*

***Table 7.** Comparison of the average activation energies determined for OER on Co-Ni alloys*

Substrate	Average Activation energy (kJ/mol)
Co-Ni_{Mal}	29.54
Co-Ni_{Et}	28.64

7.4. Conclusions

The electrodeposition of cobalt nanostructures onto graphite sheets as substrate material was studied in different DES systems. The studies show that electrodeposition of Co could be achieved only above a threshold concentration of cobalt ions. In other words, electrodeposition could not be carried out with anodic dissolution of Co wire as the sole source of metal ions. The nature of the electrodeposit prepared in ethaline and reline showed that a low pH was not crucial for the electrodeposition of Co in DES unlike that in aqueous medium. Further, a fairly good deposition was achieved in DES without the use of any

additives. A set of experiments were also carried out to study the bimetallic electrodeposition of Co-Ni in DES medium. The catalytic activity of the electrodeposited Co and Co-Ni films in oxygen evolution reaction was studied from cyclic voltammetry and activation energy measurements. It was observed that the Co films with a nanostructured morphology exhibited enhanced catalytic activity compared to the other systems. Inspite of the fact that the activation energy requirements of the Co-Ni films are slightly higher than (~ 8kJ/mol) that of the Co films, the Co-Ni alloy film will be more cost effective in any practical application.

References

1. M. W. Kanan and D. G. Nocera, *Science*, 2008, **321**, 1072.
2. Y. Zhao, S. Chen, B. Sun, D. Su, X. Huang, H. Liu, Y. Yan, K. Sun and G. Wang, Nature-Scientific reports, 5, 7629.
3. E.M. Garcia, J.S. Santos, E.C. Pereira and M.B.J.G. Freitas, J. Power Sources, 2008, **185**, 549.
4. T. Matsushima, F.T. Strixino and E.C. Pereira, *Electrochim. Acta*, 2006, **51**, 1960.
5. E. Gomez, P. Cojocaru, L. Magagnin and E. Valles, *J. Electroanal. Chem.*, 2011, **658**, 18.
6. S. E. Wulfa, R. Bocka and C. Jakob, Internationales Wissenschaftliches Kolloquium; proceedings, 2009, ISBN 978-3-938843-45-1
7. G. Saravanan and S. Mohan, *J. Alloy Compd*., 2012, **522**,162.
8. C. Lupi, A. D. Era, M. Pasquali and P. Imperatori, *Surf. Coating Tech*., 2011, **205**, 5394.
9. W. Li, Z. Zhang, B. Han, S. Hu, J. Song, Y. Xie and X. Zhou, *Green Chem*., 2008, **10**, 1142.
10. B. S. Yeo and A. T. Bell, *J. Am. Chem. Soc*. 2011, **133**, 5587.
11. X. Liang and L. Zhao, *RSC Adv*., 2012, **2**, 5485.

12. C. L. Hussey and T. M. Laher, *Inorg. Chem*., 1981, **20**, 4201.

13. C. Florindo, F. S. Oliveira, L. P. N. Rebelo, Ana M. Fernandes and I. M. Marrucho, *ACS Sustainable Chem. Eng*., 2014, **2**, 2416.

14. J. A. Hammons, T. Muselle, J. Ustarroz, M. Tzedaki, M. Raes, A. Hubin and H. Terryn, *J. Phys. Chem. C*, 2013, **117**, 14381.

15. Q. B. Zhang and Y. X. Hua, *Phys. Chem. Chem. Phys*., 2014,**16**, 27088.

16. L. Wei, Y. Fan, N. Tian, Z. Zhou, X. Zhao, B. Mao and S. Sun, *J. Phys. Chem. C*, 2012, **116**, 2040.

17. C. Gu and J. Tu, *Langmuir*, 2011, **27**, 10132.

18. A. Yadav, S. Trivedi, R. Rai and S. Pandey, *Fluid Phase Equilib*., 2014, **367**, 135.

19. Q. Zhang, K. De O. Vigier, S.Royer and F. Jerome, *Chem. Soc. Rev.*, 2012, **41**, 7108.

20. I. Nikdov, R. Darkaoui, E. Zhecheva, R. Stoyanova, N. Dimitrov and T. Vitanov, *J. Electroanal. Chem*., 1997, **429**, 157.

21. Y. Surendranath, M. W. Kanan, and D. G. Nocera, *J. Am. Chem. Soc.*, 2010, **132**, 16501.

22. E. B. Castro, C. A. Gervasi and J. R. Vilche, *J. Appl. Electrochem*., 1998, **28**, 835.

23. G. Mattioli, P. Giannozzi, A. A. Bonapasta and L. Guidoni, *J. Am. Chem. Soc*., 2013, **135**, 15353.

24. M.R.G. Chialvo and A.C. Chialvo, *Electrochim. Acta*., 1990, **35**, 437.

25. M.E.G. Lyons and M.P. Brandon, *J. Electroanal. Chem*., 2010, 641, 119.

26. R. L. Doyle, I. J. Godwin, M. P. Brandon and M. E. G. Lyons, *Phys. Chem. Chem. Phys*.**,** 2013, **15**, 13737.

27. G. Mattioli, P. Giannozzi, A. A. Bonapasta and L. Guidoni, *J. Am. Chem. Soc.*, 2013, **135**, 15353.

28. S. A. Khan, S. B. Khan and A. M. Asiri, *New J. Chem*., 2015, **39**, 5561.

29. J. Wu, Y. Xue, X. Yan, W. Yan, Q. Cheng and Y. Xie, *Nano Res*., 2012, **5**, 521.

30. S. Mao, Z. Wen, T. Huang, Y. Houa and J. Chen, *Energy Environ. Sci*., 2014, **7**, 609.

31. T. Kessler, W. E. Triaca, A. J. Arvia, *J.* Appl. Electrochem., 1994, **24**, 310.

32. Rasiya and A.C.C. Tseung, *J. Electrochem. Soc*., 1983, **130**, 365.

33. M. Jasem and A.C.C. Tseung, *J. Electrochem. Soc*., 1979, **126**, 1353.

34. Z. Liu , R. Ma, M. Osada, K. Takada and T. Sasaki**,** *J. Am. Chem. Soc.*, **2005**, *127*, 13869.

35. Y. H. You, C. D. Gu, X.L. Wang and J. P. Tu, *Surf. Coat.*Tech**.,** 2012, **206** 3632.

CHAPTER 8

A novel colloidal suspension of TBA^+ BF_4^- - EG and its applications as a soft solid electrolyte

8.1. Introduction

In this chapter, the preparation and applications of a novel ionically conducting colloidal suspension of tetrabutyl ammonium tetrafluoroborate in ethylene glycol is discussed. A systematic characterization of the colloidal suspension in terms of thermal, rheological and ionic conductivity properties was carried out. The electrochemical technique using the novel material is being explored as a potential medium for a simple automated enzyme based biosensor device. Since for the development of any enzyme based biosensor an investigation of the enzyme kinetics in the medium is desirable, the enzyme-substrate reactions were carried out in the media using urease – urea, glucose oxidase – dextrose and alkaline phosphatase - pNPP as model systems.

Electrochemical techniques have been widely accepted in biosensing applications due to the fact that some of the complex biological information can be converted to more easily processable electrical signals using appropriate surface modification strategy on the electrode. This provides a rather straight forward route for the development of electrochemical biosensors which are powerful tools for quantifying the biological analytes in terms of electrochemical responses such as charge transfer resistance in ac techniques and redox current in dc measurements [1,2]. It is therefore important to ensure that the electron transfer between the electrode surface and the redox active bio-recognition element is facilitated for attaining high selectivity and sensitivity. Unfortunately, in the case of enzymes, the direct electron transfer process on the electrode surface is largely inhibited since the redox active sites of the enzyme are normally buried well within its bulk.

In order to facilitate the electron transfer process in enzyme – electrode systems, several strategies are being devised. One of the commonly adopted methods to enable facile electron transfer process is by using diffusional redox mediators such as ferrocyanide or ferrocene along with the redox enzyme. In recent times there are several reports of nanomaterials being employed as charge transporters between the redox enzymes and the electrode surface [3,4]. For example, the glucose oxidase

enzyme after being bound to carbon nanotubes can undergo electron transfer on carbon nanotube surfaces as reported earlier by other workers [5,6]. In these cases carbon nanotubes (CNT) act as nanowires bridging the electrode surface and redox part of the enzymes, thereby enhancing the electron transfer rate. Zhou *et al.* utilized a molecular hydrogel as a surrounding matrix to stabilize the enzyme and also to facilitate the electron transfer process [7]. An aqueous organic gel interface has also been demonstrated as an amperometric detector of ions that are produced as a result of an enzymatic process [8]. A combination of these strategies has also been attempted by various groups to achieve highly efficient electrochemical biosensors.

There have also been several approaches towards the immobilization of nanomaterials together with the enzyme onto the electrochemical surface. Xiao *et al*., (2003) used gold nanoparticles to wire the redox enzyme glucose oxidase for enhancing the sensitivity of glucose determination [9]. A simple and straightforward method facilitating direct electron transfer of enzyme - electrode was achieved by immobilizing glucose oxidase (GOx) – colloidal gold mixture onto a carbon paste electrode [10]. A similar strategy was adopted by the immobilization of GOx/colloidal gold nanoparticles on a glassy carbon electrode by means of a Nafion film [11]. Mahmoud *et al*., showed that a composite matrix of cellulose nanocrystals functionalized by gold nanoparticles can serve as excellent support for enzyme immobilization [12]. Crespilho *et al*., immobilized an enzyme onto an ITO surface modified by a layer- by- layer assembly of polymeric dendrimers and gold nanoparticles for the preparation of amperometric biosensors [13].

Through this work, it is shown that the application of an appropriate high frequency ac potential, as determined from electrochemical impedance spectroscopy and simultaneous measurement of the current response can provide information on the enzyme – substrate reaction. Any transformation that arises due to progress of the enzyme-substrate reaction brings about changes in the bulk ionic characteristics which can very well be monitored by impedance. It can be shown that by choosing appropriate high frequency measurements, the observed changes during the course of the reaction can be attributed to the changes in the bulk solution resistance. Since the

process is happening in bulk, the accessibility of the active redox centers of the enzyme to the electrode surface is not essential thereby providing an alternative to the method of complex surface modifications of the electrodes. The method however is limited at present to the systems which show changes in the ionic constitution of the product vis-à-vis the substrate during the reactions.

The work being reported here provides a possibility of designing an electrochemical device that works with an integrated real-time monitoring of an enzyme – substrate reaction that utilizes only a few microliters of reaction media. This is beneficial in terms of minimal volume requirements and also due to the fact that the reaction happens close to the electrode surface. However, the minimal volume of a solution-based medium can cause errors due to solvent evaporation and solvent seepage. This problem can however be overcome, by employing an ionic conducting soft matter as a medium for the study. The soft matter would provide an environment that mimics a biological medium and this may be preferred over an aqueous buffer solution normally used in such studies. Incidentally, the study will provide information on the influence of soft matter medium on the kinetics of enzyme – substrate reaction.

There are several reports of biocompatible synthetic sol-gel materials being studied as a matrix for protein storage, enzyme catalyzed organic reactions and enzyme kinetics [14-16]. It was also shown by various experiments that the structure of the protein in its native state is very well preserved in a gel matrix compared to that in the molecular solvents [17]. Till date, only polyacrylamide, gelatin and silica based gel matrices have been employed for enzymatic studies. With the advent of designer solvents, application oriented preparation of non-polymeric soft solid materials with controlled ionic and mechanical properties have become possible [18]. Soft solids are prepared by the quasi-solidification process of ionic liquids and organic solvents with various additives such as polymers, inorganic nanoparticles and low molecular weight gelators [19-22].

The application of the colloidal suspension in dispersing nanoparticles is also demonstrated here. The aggregation of nanoparticles in solvent matrices is an

important issue that can adversely affect their use in potential applications. The problem can be circumvented using a suitable dispersing medium. The nanoparticle dispersions have been prepared earlier in molecular solvents through proper control of surface potentials and surface forces of nanoparticles, yet highly loaded nanoparticle suspensions were found to be difficult to achieve.

8.2. Experimental section:

8.2.1. Materials

Tetrabutylammonium tetraflouroborate ($TBABF_4$) Tetrabutylammonium hexafluorophosphate ($TBAPF_6$) from Aldrich and Ethylene glycol, Ethanol, Acetonitrile, Glycerol from Merck were used as received.

Urease from Canavalia ensiformis (Sigma Aldrich), glucose oxidase from aspergillus niger, alkaline phosphatase (Sigma Aldrich) were used as enzymes while urea, dextrose and para-Nitrophenylphosphate (pNPP) were used as their respective substrates. Pt foils (0.5mm thickness) were purchased from Advent research materials as electrodes for the ionic conductivity measurements.

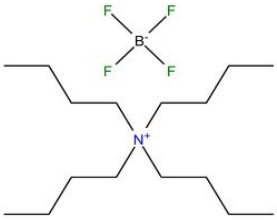

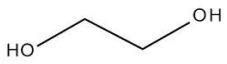

$[TBA]^+ [BF_4]^-$ Ethylene Glycol

Scheme-1. *Chemical structure of the components of the colloidal suspension*

8.2.2. Preparation of the colloidal suspension

The two components shown in scheme-1 were mixed in a molar ratio of 1:8 and heated at 80 ^{0}C under magnetic stirring till a homogeneous colorless solution was obtained. The solution attains a soft solid state as the temperature decreases below 50 ^{0}C.

8.2.3. Instrumentation

All the rheological measurements were performed in a commercial modular compact rheometer Anton Paar MCR 501 after loading a fresh sample for every run in concentric cylinder geometry CC17. This geometry has a gap of 0.71 mm, an effective length of 24.99 mm and requires a sample volume of 4.72 ml for every run. The sample temperature was controlled by a water circulation unit Viscotherm VT2. The rheological data was acquired using the Rheoplus software (version 3.40) provided by the manufacturer.

For the cryo-SEM experiments, the samples are transferred to a PP3000T cryo unit (Quorum Technologies) and freeze fractured with a cold knife. The fractured and cut samples are sublimated at -130 ^{0}C for 5 minutes and then sputtered with platinum inside the unit. Imaging of the samples were performed using Zeiss Ultra Plus cryo-SEM setup at a temperature of -160 ^{0}C.

The transition temperature of the material developed was determined by differential scanning calorimetry (DSC) using Perkin-Elmer, Model Pyris-1 at a heating rate of 5 ^{0}C/min. The texture of the colloidal suspension was observed using a polarising optical microscope (POM) (Olympus BX50) equipped with a heating stage (Mettler FP82HT) and a central processor (Mettler FP90).

The electrochemical characterization of the developed medium was performed by electrochemical impedance spectroscopy in a frequency range of 0.1 to 10^5 Hz. The kinetics of enzyme–substrate reaction was monitored by a Lock in amplifier (model SR830 DSP, Stanford research systems) using Labview 2012, Stanford research-830 constant frequency.

8.2.4. Cell design

A teflon cell containing ‘H’ shaped grooves as shown in scheme-2a was designed and prepared in our lab. Two platinum foils (10 x 6 x 0.5mm) were placed within the vertical segments of the grooves. The Pt foils were placed parallel at a distance of 3mm. The rear sides of the Pt foils were masked by means of teflon tapes. The vertical segments of the ‘H’ shaped groove facilitates Pt foils to be placed in a constricted way while the gap formed amidst the Pt foils serves the purpose of a

sample well (scheme-2b). The sample well can hold a colloidal volume of 110µL.

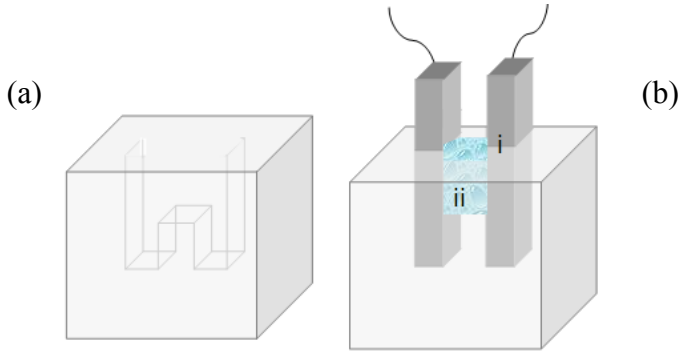

Scheme-2. *(a) Teflon container (b) components of the electrochemical cell (i) Pt foils (ii) colloidal matrix in the teflon container used for the electrochemical monitoring of enzyme-kinetics.*

8.2.5. Electrochemical procedure followed for monitoring enzyme – substrate reaction

The progress of the enzyme - substrate reaction was electrochemically monitored as follows. A known weight of the substrate was dissolved in the colloidal matrix at temperatures greater than 50 ^{0}C to prepare different concentrations of substrates. From each concentration, 110µL is pipetted into the sample well. The colloidal matrix was allowed to equilibrate in the electrochemical cell. The enzyme (1µL of 1mg/ml aqueous solution) was added to the matrix and the real time monitoring of ionic conductivity with the progress of the reaction was carried out.

8.3. Results and discussion

8.3.1. Optimization of the gel components

The components of the colloidal suspension were chosen such that they possess optimal mutual interactions. This is because of the fact that any excessive mutual interactions among them would lead to the formation of a room temperature liquid which is not desirable [23]. In view of this, the cation, anion and the organic solvent were optimized from the experiments carried out as well as from the literature reports of similar systems.

The quaternary ammonium cation used here is symmetric with an alkyl chain of C_n = 4. This bulky cation is devoid of any polar functional groups. It is thus least expected for the cation to have any significant secondary interactions with the other components ie., $[BF_4]^-$ and ethylene glycol (EG). However, recent reports on eutectic solvents prepared from tetra butyl ammonium chloride (TBA^+Cl^-) and EG as well as tetrabutyl ammonium bromide (TBA^+ Br^-) and EG show that a strong hydrogen bonding interaction between the Cl / Br anion and EG is sufficient for the formation of a room temperature liquid [24]. Thus, together with a symmetric tetrabutyl ammonium cation, a poorly interacting anion also needs to be selected so as to ensure the formation of a soft solid. Abbott *et al*. studied depressions in freezing point of mixtures containing hydrogen bond donor (HBD) and choline salts with different anions such as Cl^-, $[BF_4]^-$, $[NO_3]^-$ and F^- [23]. The studies showed that the mixtures containing $[BF_4]^-$ were associated with least depression in freezing point and this was correlated with weak hydrogen bonding interactions between the anion and HBD. The experiments carried out in this work also shows that TBACl and TBABr form corresponding liquids with EG while $TBABF_4$ and $TBAPF_6$ form soft solid with EG. The studies on $[C_4mim]$ $[BF_4]$ assisted gelation of DMSO also reported the crucial role of tetraflouroborate anion in gelating the solvent [25].

The effect of solvent on the physical state of the salt on mixing was also studied by the inverted vial experiment. The quaternary ammonium salt $[TBA]^+$ $[BF_4]^-$ was fixed at the same mole fraction and EG (ε -37) was replaced with other molecular solvents such as acetonitrile (ε - 37.5), glycerol (ε - 42.5) and ethanol (ε - 24). $[TBA]^+$ $[BF_4]^-$ dissolved completely in acetonitrile and ethanol while it gelated in glycerol. The results suggest that a structured/associated solvent has greater influence on the physical state of the mixture rather than its dielectric constant. It is also known that the viscosities of EG and glycerol are considerably greater than that of acetonitrile and ethanol. Thus the viscosity of the solvent can be a crucial factor on the formation of gel rather than its dielectric constant.

Based on all these observations, the components were chosen as $[TBA]^+$ $[BF_4]^-$ and EG (scheme -1). A weak hydrogen bonding interaction between hydroxyl protons of

EG and BF_4^- has been earlier confirmed in literature by fluorescence spectroscopy and NMR [26]. Thus the symmetric tetrabutyl ammonium cation and the weak hydrogen bonding interactions of BF_4^- and EG would render a delicate balance of polar-non polar characteristics to the medium and thus promote the formation of a stable colloidal suspension of $[TBA]^+ [BF_4]^-$ in EG.

Figure 1. *Photographs of the vial containing the colloidal suspension and a teflon coated magnetic pellet at (a) T > 60^{0}C and (b) RT*

8.3.2. Characterization of the colloidal suspension

As a preliminary test, a vial inversion experiment was carried out on the colloidal suspension. The ability of the suspension to resist flow under its own weight is observed by the vial inversion experiment. A set of vial inversion experiments were conducted with different ratios of $TBABF_4$: EG. A ratio of 1:8 was optimized as the composition exhibited a fine balance in rigidity and fluidity. Photographs of the suspension in an inverted vial are shown in Fig.1a. The mechanical strength of the composition corresponding to 1:8 was sufficiently high enough that a colloidal volume corresponding to 1.5ml could hold a teflon coated magnetic pellet (0.76 gm) in an inverted vial as shown in Fig.1b.

8.3.2.1. Phase transition studies

The sol-gel transition of the colloidal suspension was monitored by differential scanning calorimetry (DSC) given in Fig.2a. The gel → sol conversion was observed at 60 ^{0}C while the reverse transition corresponding to sol → gel occurred at 51 ^{0}C. The gelation and melting processes are accompanied by

exothermic and endothermic peaks respectively as usually observed for any freezing or melting process. However, the sharp calorimetric peaks of the colloid observed in DSC reveal a first order transition which indicates that all molecules undergo the transition in unison [27]. The driving force for the gelation of the colloid can be attributed to the aggregation of the salt components so as to favor the hydrogen bonding interactions within the solvent EG. Fig.2b shows the variation in the viscosity of the colloidal suspension within a temperature range of 25 ^{0}C – 65 ^{0}C. A sharp change in viscosity (almost 10^4) characteristic of sol-gel transition of the colloid was observed at a temperature close to 55 ^{0}C. The temperature associated with the sudden change in the viscosity values corresponds closely with the transition temperature observed in DSC both on heating and cooling.

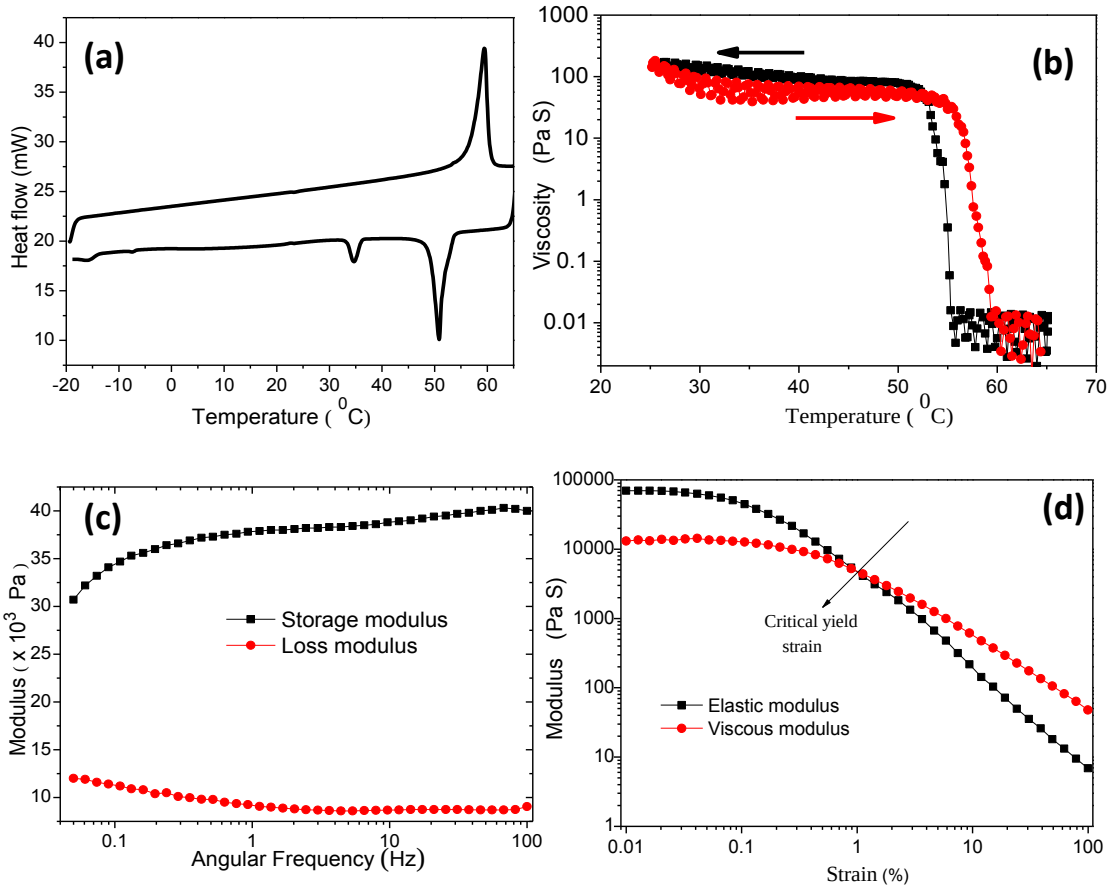

Figure 2.*(a) DSC plot (b) variation in viscosity with temperature (c) frequency response of the gel at 0.05% (d) strain response at 0.5rad/s of the colloidal suspension*

8.3.2.2. Rheological studies

The mechanical properties of the prepared colloidal suspension were analyzed from the frequency response measurements at room temperature at a strain amplitude of 0.05% (Fig.2c). The loss modulus and storage modulus shown in figure signifies the fluid and solid phase behavior respectively. The moduli exhibit least dependence to the frequency as is evident from the figure. The loss modulus is lower than that of the storage modulus at all the frequencies studied. These characteristic features observed in the frequency sweep measurements confirm the soft solid behavior of the suspension [28]. The elastic and viscous moduli of the suspension at room temperature were measured from the strain amplitude measurements at a constant angular frequency of 0.5rad/s as given in Fig.2d. There is no linearity in the response over a range of strain amplitude between 0.1 to 100%. The elastic modulus lags behind the viscous modulus beyond the critical yield strain of 1% amplitude, indicating a permanent deformation of the structure.

8.3.2.3. Morphological studies

The cryo -SEM image of the colloidal suspension was obtained to examine the morphology. Fig.3 (a) shows the evenly distributed spherical aggregates of ~50 nm. The spherical features could have formed by the aggregation of $TBABF_4$ in EG These spherical aggregates of $TBABF_4$ can be stabilized by the weak hydrogen bonding interactions between BF_4^- with –OH groups of EG. The aggregation behavior of $[C_4mim][BF_4]$ have been studied by many groups. Bowers *et al.* observed that these ionic compounds form spherical aggregates in aqueous solution above its critical aggregation concentration [29]. Dorbritz *et al.* observed the aggregation behaviour of $[C_4mim][BF_4]$ in methanol, 2-propanol, and ethyl acetate by electrospray ionization mass spectrometry [30]. The group observed that on decreasing the polarity of the solvent and increasing the concentration of the salt, the size of the aggregates could be increased. The three dimensional network structures characteristic of gel structure was absent in the cryo-SEM images. The birefringence observed in polarizing optical microscope (POM) images shown in Fig.3b at room temperature further confirms the crystallinity of the suspension.

8.3.2.4. XRD studies

X ray diffraction studies were carried out to probe into the nature of the suspension at different temperatures and also with respect to the components. The room temperature XRD patterns of the suspension exhibited additive features of both the components viz., sharp diffraction peaks corresponding to $[TBA]^+$ $[BF_4]^-$ throughout the spectra and the broad peak of ethylene glycol in the wide angle region.

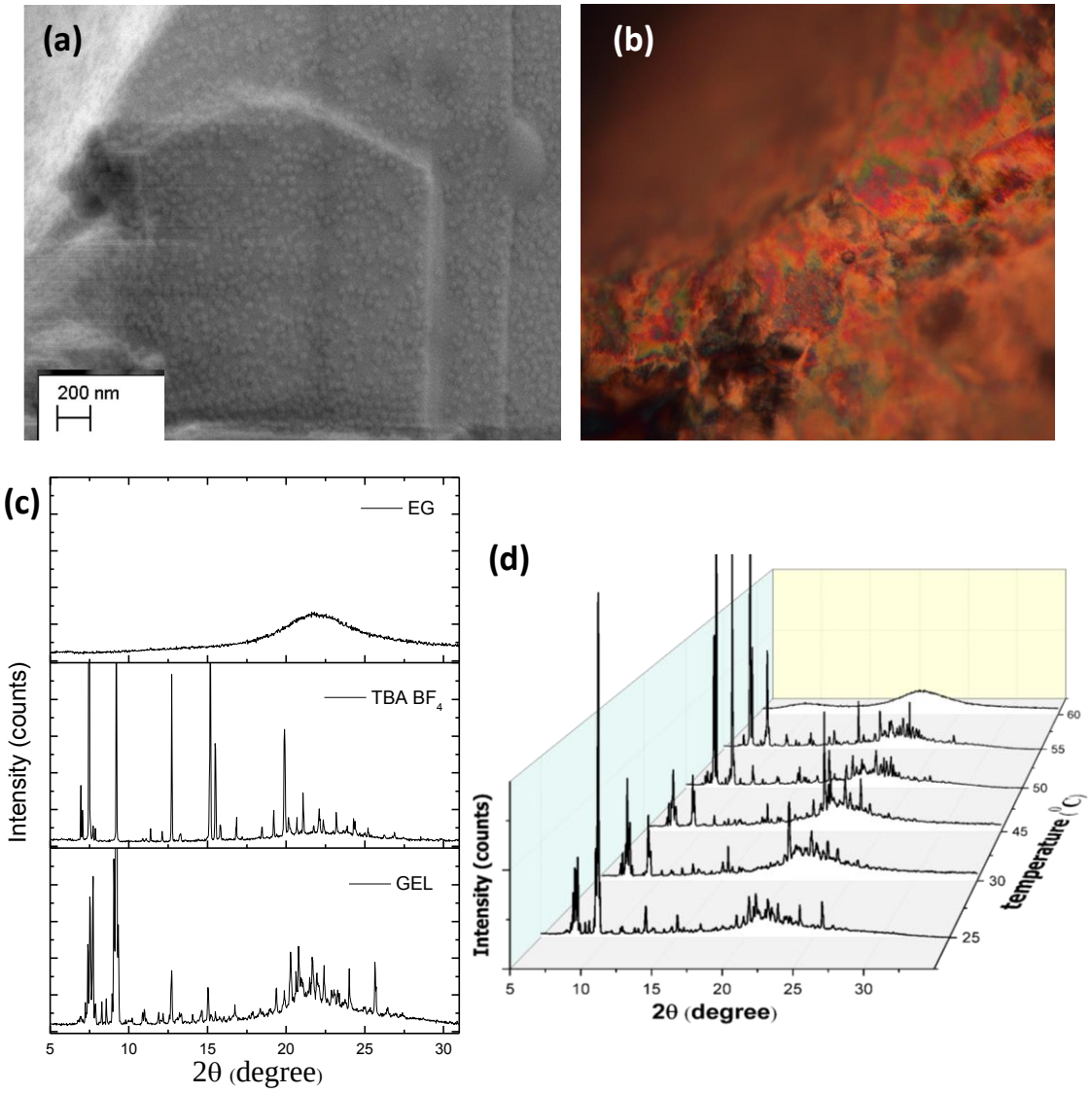

Figure 3 *(a) Cryo-SEM images of the freeze fractured surface at -160 ^{0}C (b) POM image at RT of the colloidal suspension (c) XRD of the colloidal suspension and its components (d) XRD of the colloidal suspension at different temperatures*

A comparison of the XRD spectra of the colloidal suspension and its components, viz., $[TBA]^+$ $[BF_4]^-$ and EG is shown in (Fig.3c). There was no significant shift in peaks or absence of any peak as compared to $[TBA]^+$ $[BF_4]^-$ which indicate that the secondary interactions of $[BF_4]^-$ with EG do not hinder the crystallinity of the salt. It can also be noted that beyond the gel → sol transition temperature of the colloid, the entire set of sharp peaks of the suspension disappears due to the melting of salt as observed in Fig.3d.

8.3.2.5. Ionic conductivity measurements

The ionic conductivity measurements of the colloidal suspension were carried out by considering the electrode - gel interface analogous to a simple Randles equivalent circuit with a parallel combination of double layer capacitance and charge transfer resistance in series with the solution resistance (scheme 3).

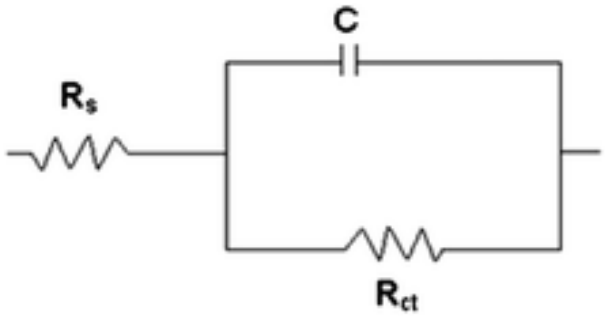

Scheme 3. *Randles circuit with a resistor and capacitor in parallel*

For a Randles circuit with a resistor and capacitor in parallel, [31],

$$Z_{re} = R_s + \frac{R_{ct}}{1 + \omega^2 C_d^2 R_{ct}^2} \qquad (1)$$

$$Z_{Im} = \frac{\omega C_d R_{ct}^2}{1 + \omega^2 C_d^2 R_{ct}^2} \qquad (2)$$

At high frequencies > 6 kHz,

$$\frac{1}{\omega C_d} \longrightarrow 0,$$

Hence, $Z_{re} = R_s$ and $Z_{Im} = 0$ according to eqn (1) and (2) respectively.

The ionic characteristics were measured by eletrochemical impedance spectroscopy (EIS) using two parallel planar Pt electrodes at the open circuit potential. The ionic conductivity of the colloidal matrix was determined at a frequency of 10kHz where the capacitive contribution is negligible. The system exhibits only solution resistance at this frequency. This can very well be observed from the Bode phase diagram Fig.4a, where the phase angle tends to zero at frequencies greater than 6kHz. The ionic conductivity is calculated from $\sigma = L / A R_s$ where A and L represent the cross sectional area and distance between the between the Pt plates. R_s denotes the solution resistance at 10 kHz measured from the Bode plots at different temperatures. The Bode plots of the gel in a temperature range of 25-60 ^{0}C is given in Fig.4b. The ionic conductivity values varied between 0.5 – 12.67 mS/cm in the temperature range. The values are 2 - 4 orders of magnitude greater than those reported on

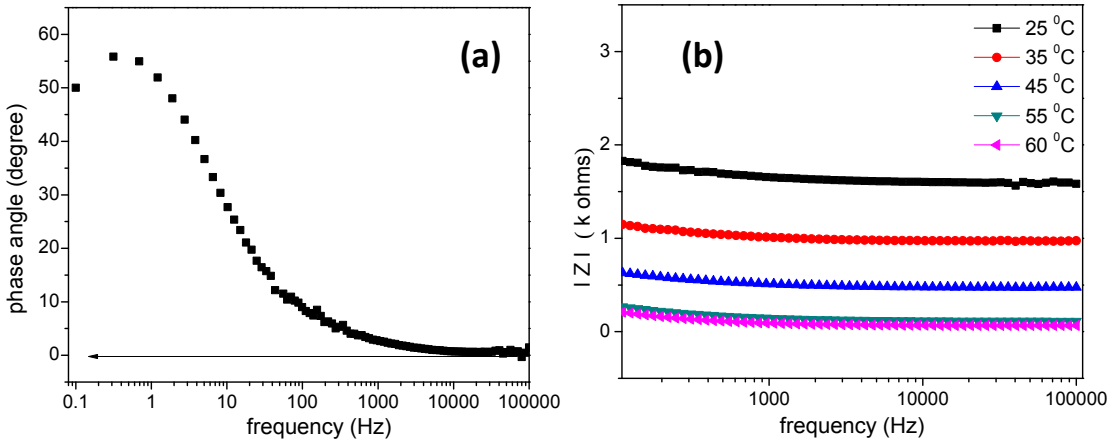

Figure 4.*(a) Phase angle Bode plot at room temperature (b) Bode plots of the colloidal suspension at different temperatures*

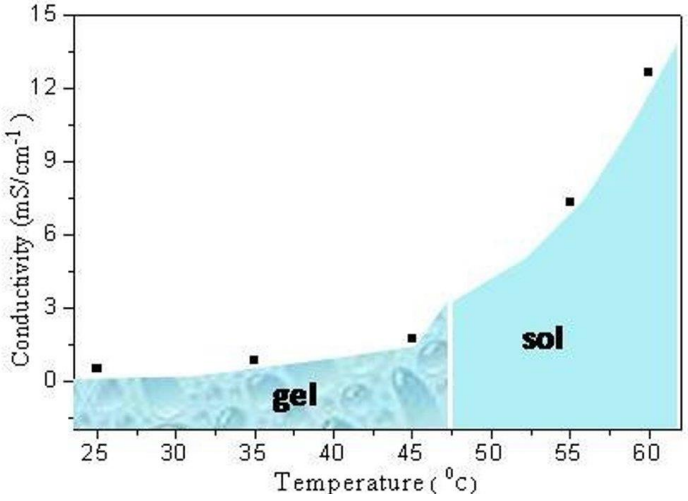

Figure 5. *Variation in the ionic conductivity of the colloidal suspension with temperature*

polymeric ionic gels (PEG or PEO) [32]. Sekhon *et al.* reported an ionic conductivity of the order 10^{-4} S/cm for ionic gels formed from a mixture of ternary solvent, salt and a polymer (PVdF) [33]. The ionic gels prepared by the gelation of DMSO were associated with an ionic conductivity of ~15 mS/cm. However the study showed that there was no decrease in ionic conductivity before and after the phase transition. This was attributed to the fact that ions were not part of gel network [25]. The ionic conductivity of the gels formed from ionic liquid compatible cyclic carbonate network varied from 7μS/cm to 3.2 mS/cm with increase in ionic liquid composition [34]. It is evident from Fig.5 that the phase transition corresponding to gel → sol of the colloidal suspension at 55 ^{0}C, is associated with a seven fold increase in the ionic conductivity. This can be explained by the collapse of the spherical aggregates of quaternary ammonium salt at temperatures above 55 ^{0}C, causing the release of a large number of ions. Further, it was also observed from the rheological characteristics that the viscosity decreases drastically at the phase transition temperature, which also contributes to an increase in ionic mobility.

8.3.2.6. Schematic model of the colloidal suspension

The proposed models of the colloidal suspension at the sol and gel phases are provided in scheme-4. At room temperature, the crystalline features of the colloidal suspension were evident from the XRD and POM textures. Further, the XRD of the colloidal suspension was observed to be exactly similar with that of the $TBABF_4$ salt. Thus in the model, it is proposed that the crystal structure of $TBABF_4$ is preserved in the colloidal suspension at room temperature. The hydrogen bonding interactions between ethylene glycol and BF_4 as mentioned earlier is represented by the dotted lines. At temperatures beyond the phase transition ($T > 50\ ^0C$), the crystal structure of $TBABF_4$ is shown to collapse to tetrabutyl ammonium cations and BF_4 anions. These changes are confirmed by the isotropic phase obtained in the XRD of the colloidal suspension at high temperatures. Such a collapse can explain the sudden increase in ionic conductivity on phase transition.

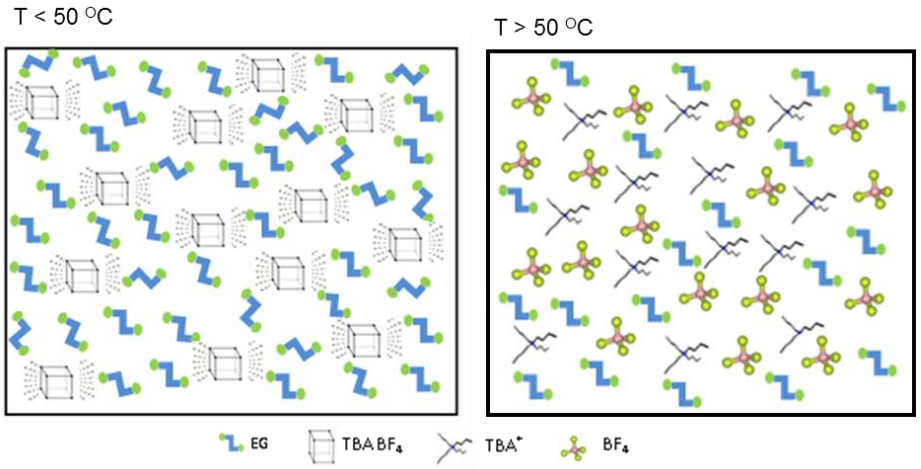

Scheme 4*. Proposed model of the colloidal suspension (dotted lines around the cube denote the hydrogen bonding interactions in sol and gel phase)*

8.4. Applications of the $TBABF_4$ – EG colloidal suspension

The colloidal suspension is associated with a fine balance of polar and non-polar components and is expected to have excellent solvent properties. The ambient

temperature isotropic phase exhibited by these soft solids helps in solvent free processing of the suspension for experimental studies. The sharp reversible sol-gel transition of the colloid can also be utilized for dispersing nanoparticles. In addition, the inherent ionic conductivity of these soft solids makes it an ideal medium for the electrochemical studies of biomolecules especially enzymatic processes. The experiments involving enzyme-substrate reaction usually require immobilization of the enzyme. This is done either by the covalent attachment of the enzyme onto an insoluble carrier molecule or entrapment onto a gel matrix. The entrapment onto the gel matrix (usually polyacrylamide or crosslinked gelatin gel) is frequently used owing to the simplicity of the method. To the best of our knowledge, enzyme – substrate reaction has not been monitored in a non-polymeric gel electrolyte. To explore this possibility, we have made an attempt to utilize these soft solids as a medium for monitoring enzyme kinetics.

8.4.1. Dispersing medium for nanoparticles

The sharp reversible sol-gel phase transition of the colloid can be utilized as a matrix for dispersing nanomaterials such as CNT, graphene and metal nanoparticles. A few of such dispersions of nanoparticles (CNT, Graphene, Fe_3O_4 NP, AgNP) in the colloid are shown in the Fig.6. A vial containing 0.5 mg /ml nanoparticles in sol were initially sonicated at a temperature of about 50-60 ^{0}C. As soon as a stable dispersion of nanoparticles was achieved, the nanoparticle matrix was plunged into cold water. The sudden drop in temperature brings about the phase transition of sol → gel, thus freezing the well dispersed state of nanoparticles brought about by sonication. The nanoparticles dispersion in the colloid by the method has the potential for use in electrochemical biosensors, electronic and optoelectronic applications.

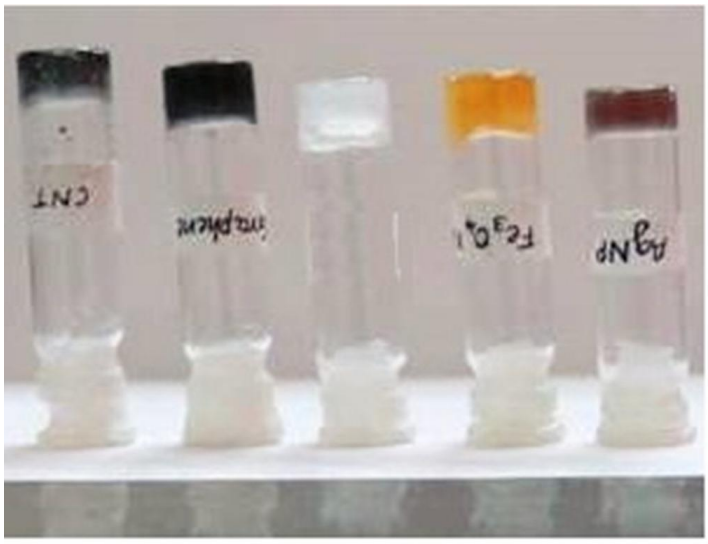

Figure 6. *Inverted vial containing colloidal dispersions of CNT, graphene, Fe_3O_4 NP and AgNP [blank colloid in the centre)*

8.4.2. Electrochemical monitoring of enzyme kinetics in the gel matrix

8.4.2.1. Urea - urease reaction

The urea - urease reaction is usually studied in a buffered media by spectrophotometry [27], calorimetry [28], titrimetry or conductivity measurements [35-37]. Osakai *et al*., developed an amperometric sensor based on direct detection of ammonium ion transferred across a gel-solution interface [38]. Recently, changes in the imaginary component of electrochemical impedance spectroscopy were utilized to monitor enzyme kinetics [39]. In this experiment, a small volume (110µL) of the sol containing a known concentration of urea was injected amidst two parallel Pt electrodes kept at a distance of 3mm (Scheme-2). The sol solidifies immediately to form the gel and the corresponding enzyme urease (1µL of 1mg/ml aqueous solution) was added to the gel. The enzyme-substrate reaction was allowed to take place in the gel matrix.

The urea- urease reaction is given as

$$(NH_2CO\ NH_2) + 2H_2O \rightarrow 2\ NH_4^+ + CO_3^{2-} \qquad (3)$$

As is evident from equation (1), the reaction yields ammonium ions and carbonate

ions. The progress of the reaction is expected to increase the ionic conductance of the medium. The real time monitoring of ionic conductance was carried out by impedance spectroscopy at open circuit potential.

To optimize the frequency at which the measurements were to be performed, Bode phase plot of the gel matrix containing the substrate was studied over the entire range of frequencies from 100 kHz to 100 mHz at the open circuit potential (Fig.7a). It was observed that at frequencies greater than 1 kHz, the impedance is contributed only by the resistance of the medium. A frequency of 20 kHz is optimized for the study as the phase angle is zero at this frequency.

The kinetics of urea-urease reaction was monitored at various concentrations of urea ranging from 0.5 mM – 5mM. The observed changes in the ionic conductance with

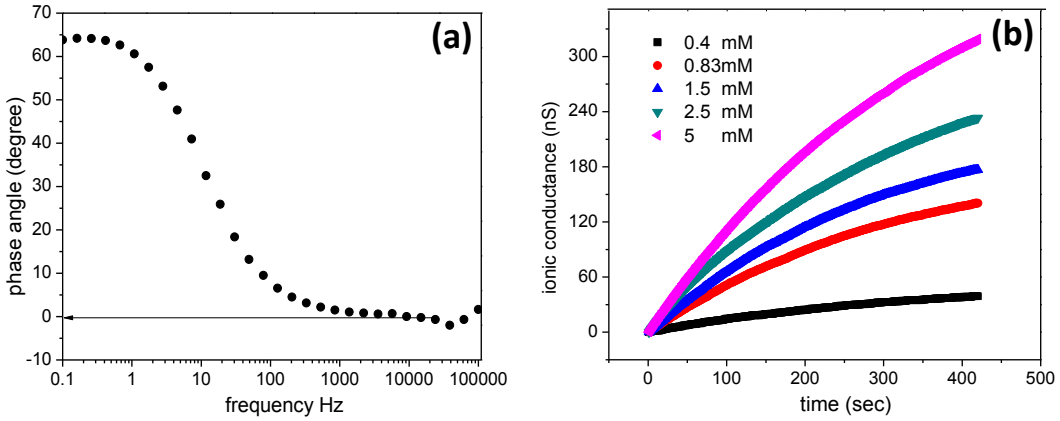

Figure 7.*(a) Phase angle Bode plot of the colloidal suspension used for enzyme kinetics studies under experimental conditions (b) Electrochemical monitoring of the variation in ionic conductance with the progress of urea-urease reaction at different urea concentrations (baseline subtracted)*

time were baseline corrected to remove the inherent ionic conductance of the gel-urea mixture. An increase in the ionic conductance with time was observed indicating that ions are generated with the progress of the reaction (Fig. 7b). It can be seen that for each concentration, the initial increase in ionic conductance is linear while it plateaus with time due to the saturation of the enzyme sites.

The initial rate of the reaction was obtained from the slope of the linear segment of t = 0 to t = 80 sec. Hence the initial rate of the reaction is plotted in terms of change in ionic conductance of the medium with time (S/min). The plot of initial rate of the reaction Vs urea concentration (Fig. 8) was found to follow Michaelis-Menten equation (2) with an Adj. R^2 of 0.96.

$$\nu = \frac{V_{max}[S]}{K_m + [S]} \qquad (4) \qquad (2)$$

Where V_{max} represents the maximum velocity achieved by the system, [S] is the substrate concentration and K_m is the Michaelis constant.

For an enzyme – substrate reaction,

$$E + S \underset{k_{-1}}{\overset{k_1}{\rightleftharpoons}} [ES] \xrightarrow{k_2} E + P$$

$$K_m = \frac{k_{-1} + k_2}{k_1} \qquad (5)$$

K_m is determined from the concentration of the substrate at which the rate of the reaction is exactly half of V_{max}. Thus, a lower K_m indicates that the maximum velocity of the reaction V_{max} is attained at small substrate concentrations. K_m is also a measure of enzyme – substrate binding affinity. It is evident from the eqn (5) that a low K_m signifies a high binding affinity in the medium. The experiment was repeated to check the consistency of measurements and was averaged which gives a K_m of 2.1 mM with a standard deviation of 0.1621. The K_m values for the urea-urease reaction monitored under different experimental conditions were compared earlier by Qin & Cabral [40]. In an unbuffered neutral medium, K_m varied between 1.25 - 3.28 mM whereas the values were in the range of 9.5 - 20 mM in phosphate buffer and 1.2 - 3.8mM in a citrate buffer. The value obtained in our studies is very much close to that obtained (K_m=1.8mM) for the urea-urease reaction done in an unbuffered gel matrix of polyacrylamide [16].

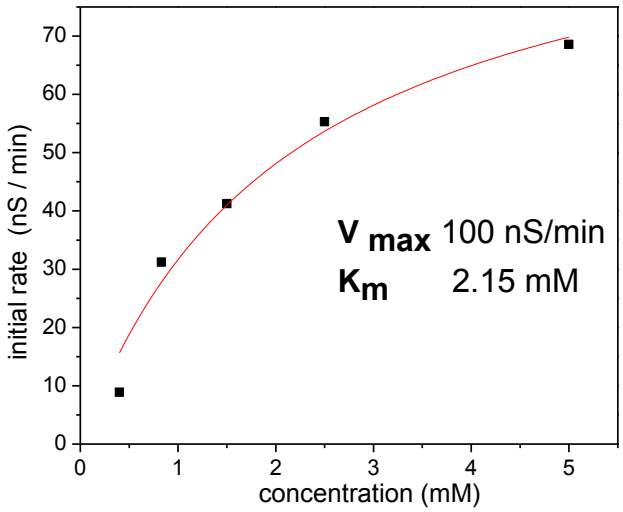

Figure 8. *Michaelis –Menten plots for the urease-urea reaction carried out in the colloidal suspension*

8.4.2.2. Glucose oxidase – dextrose

Electrochemical glucose biosensors are mainly based on glucose oxidase (GOx) and are of great importance in the diagnosis and therapy of diabetics. The conventional electrochemical amperometric and impedimetric biosensors measures the changes in the redox current and charge-transfer resistance, R_{ct} respectively from the reaction,

$$\text{Glucose} + O_2 \xrightarrow{\text{GOx}} \text{Gluconic acid} + H_2O_2 \qquad (6)$$

The GOx - dextrose reaction was allowed to take place in the gel matrix and the reaction was monitored continuously at a constant frequency of 20kHz as in the case of urease - urea. The increase in ionic conductance observed with the progress of the reaction can be attributed to the formation of gluconic acid and its subsequent self-dissociation (Fig.9a). The gluconic acid with a pK_a of 3.6, freely dissociate to give a gluconate anion and a proton. Earlier Periera *et al*., (2004) developed an amperometric glucose biosensor based on the protons formed by the self-dissociation of gluconic acid [41].

The kinetics of the enzyme-substrate reaction is found to be affected by the immobilization method and also the matrix. Attempts are made so as to decrease the

K_m value and increase the sensitivity of measurements. The K_m values vary considerably with the medium and tend to decrease by the use of nanomaterials. The apparent Michaelis–Menten constant K_m calculated for the GOx immobilized in sol–gel chitosan/silica hybrid composite film was found to be 3.2mM [42]. Earlier, GOx

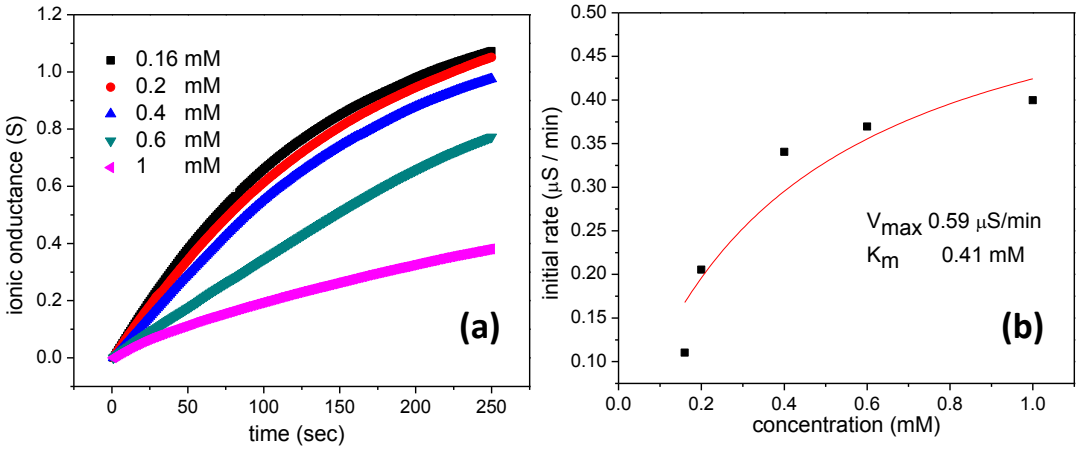

Figure 9. (a) *Electrochemical monitoring of variation in ionic conductance (baseline substracted) with the progress of (a) GOx – dextrose reaction at different dextrose concentrations (b) Michaelis –Menten plots for the GOx – dextrose reaction carried out in the colloidal suspension*

was entrapped in a thin film of sol-gel composite composed of multi walled carbon nanotubes (MWCNTs) and Celestin blue gave a K_m of 2.4 mM [43]. The K_m value obtained for GOx modified electrodes obtained by entrapping the enzyme and ferrocene (Fc) in chitosan membrane was found to be 1.67 mM [44]. Lan *et al.* observed that the apparent Michaelis–Menten constant of GOx in a Tetraethyl orthosilicate based sol–gel (2mM) was found to decrease to a value of 0.3mM with the addition of gold nanoparticles in the matrix [45].

The initial rate of the reaction Vs dextrose concentration obtained in this study was found to fit the Michaelis – Menten equation with an Adj. R-Square of 0.86 (Fig.9b). A detailed analysis of the effect of gluconic acid and its dissociation on the gel electrolyte has to be done to explain the slight deviation from a perfect fit. The K_m value for GOx –dextrose system in the gel matrix is calculated to be 0.41 mM which is significantly lower than that of a free GOx enzyme reported in any solution.

8.4.2.3. Alkaline Phosphatase – p-nitrophenyl phosphate

In the case of ALP – p-NPP system, the increase in ionic conductivity is only marginal compared to the other enzyme systems (Fig.10a). This may be attributed to the fact that while the progress of the reactions URS-urea and GOx-dextrose leads to the formation of ions, in the case of ALP-pNPP the bulky nitrophenyl phosphate anion decomposes to give smaller phosphate ion. Thus any increase in ionic conductivity is only due to a change in the ionic mobility owing to the decrease in size and not due to any increase in the ions formed.

The kinetics of the ALP - p-NPP system was also found to obey Michaelis-Menten equation (Fig.10b). The K_m value was found to be 0.74 mM in the gel matrix measured using the proposed method. The value is higher than that observed for the kinetics of free enzyme in solution. K_m values of the ALP in bulk solution obtained by spectroscopic methods are reported to be 0.467mM [39]. Faure *et al.* monitored the hydrolysis of 4-nitrophenylphosphate (pNPP) by alkaline phosphatase (ALP) bound on paramagnetic-beads by ionic conductivity measurements [46]. The K_m value obtained was found to be 0.3mM. The decrease in

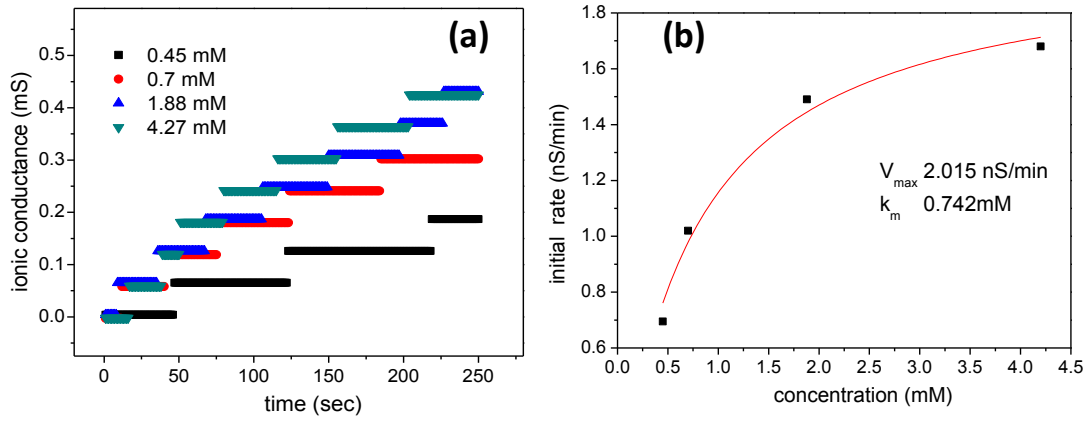

Figure 10. (a) *Electrochemical monitoring of variation in ionic conductance (baseline substracted) with the progress of (a) ALP - pNPP reaction at different pNPP concentrations (b) Michaelis –Menten plots for the ALP - pNPP reaction carried out in the colloidal suspension*

the sensitivity of the ALP- pNPP measurements in our studies could be accounted by the fact that the enzyme is most stable in a pH range of 7.5–9.5. Though experiments to understand the effect of pH on the gel matrix were not carried out in this work, it is known that the pH of the gel will be influenced only by the protic component viz., ethylene glycol which is neutral (pH : 6 – 7 as per the product information). The enzyme systems URS and GOx are stable in the neutral pH range.

8.5. Conclusion

A simple and efficient technique of studying enzyme kinetics based upon the real time monitoring of the ionic conductance changes was demonstrated. For this application, a novel gel electrolyte with soft solid properties and inherent ionic conductivity was custom made. The gel electrolyte was thoroughly characterized in terms of its thermal, rheological and ionic conducting properties. The enzyme-substrate reaction was allowed to happen in the prepared gel electrolyte without any additives or electrode modifications. The studies showed that the gel electrolyte has ample scope as a soft solid media for dispersing nanoparticles and also in electrochemical applications. The enzyme kinetics of urease-urea, GOx-dextrose and alkaline phosphatase – p NPP was found to follow Michaelis-Menten equation. The K_m values of urease-urea, GOx-dextrose and ALP- pNPP determined were found to be 2.1mM, 0.42mM and 0.74 mM respectively. The technique can be extended to for a large range of enzyme systems that are stable in a neutral pH medium.

References

1. J. G. Guan, Y. Q. Miao and Q. J. Zhang, *J. Biosci. Bioeng.*, 2004, **97**, 219–226.
2. J. Wang, 2008, *Chem. Rev.*, **108**, 814.
3. J. R. Mor and R. Guarnaccia, *Anal. Biochem.*, 1977, **79**, 319.
4. W. Schuhmann, T. J. Ohara, H. L. Schmidt and A. Heller, *J. Am. Chem. Soc.*, 1991, **113**, 1394.
5. C. X. Cai and J. Chen, *Anal. Biochem*., 2004, **332**, 75–83; A. Guiseppi-Elie, C.H. Lei, R. H. Baughman, *Nanotechnology*, 2002, **13**, 559.

6. A. Guiseppi-Elie, C.H. Lei and R.H. Baughman, *Nanotechnology*, 2002, **13**, 559.
7. J. Zhou, C. Liao, L. Zhang, Q. Wang and Y. Tian, *Anal. Chem*., 2014, **86**, 4395.
8. F. Silva, M. D. Sousa and C. M. Pereira, *Electrochim. Acta*, 1997, **42**, 3095.
9. Y. Xiao, F. Patolsky, E. Katz, J. F. Hainfeld and I. Willner, *Science*, 2003, **299**, 1877.
10. S. Liu and H. Ju, *Biosens. Bioelectron.*, 2003, **19**, 177.
11. S. Zhao, K. Zhang, Y. Bai, W. Yang, and C. Sun, *Bioelectrochemistry,* 2006, **69**, 2158.
12. K. A. Mahmoud, K. B. Male, S. Hrapovic and J. H. T. Luong, *ACS Appl. Mater. Interfaces*, 2009, **1**, 1383.
13. F. N. Crespilho, M. E. Ghica, M. Florescu, F. C. Nart, O. N. Oliveira Jr., and C. M. A. Brett, *Electrochem. Commun.,* 2006, **8**, 1665.
14. H. F. Mullerad and D. Avnir, *J. Am. Chem. Soc.,* 2005, **127**, 8077.
15. S. Wu, J. Lin and Sl. Chan, *Appl. Biochem. Biotechnol.*, 1994, **47**, 11.
16. B. Atkinson and I. Rousseau, *Biotechnol. Bioeng.*, 1977, **19**, 1065.
17. M. Yan, J. Ge, Z. Liua and P. Ouyang, *J. Am. Chem. Soc*., 2006, **128**, 11008.
18. M. Freemantle, *Chem. Eng. News,* 1998, **76**, 32.
19. S. Washiro, M. Yoshizawa, H. Nakajima and H. Ohno, *Polymer*, 2004, **45**, 1577.
20. P. Wang, S. M. Zakeeruddin, P. Comte, I. Exnar and M. Gratzel, *J. Am. Chem. Soc.*, 2003, **125**, 1166.
21. K. Hanabusa, H. Fukui, M. Suzuki and H. Shirai, *Langmuir*, 2005, **21**, 10383.
22. J. C. Ribot, C. G.Sanchez, R. Hoogenboom and U. S. Schubert, *J. Mater. Chem*., 2010, **20**, 8279.
23. A. P. Abbott, G. Capper, D. L., R. K. Rasheed and V. Tambyrajah, *Chem. Commun*., 2003, 70.
24. (a) F. S.Mjalli, J. Naser, B. Jibril, V. Alizadeh and Z. *J.* Gano, *Chem. Eng. Data,* 2014, **59**, 2242; (b) R. Yusof, E. Abdulmalek, K. Sirat and M. B. A. Rahman, *Molecules*, 2014, **19**, 8011.

25. N. W. Smith, J. Knowles, J. G. Albright and S. V. Dzyuba, *J. Mol. Liq.*, 2010, **157**, 83.
26. T. Singh, K. S. Rao and A. Kumar, *Chem. Phys. Chem.*, 2011, **12**, 836.
27. Weiss, R.G.; Terech, P. (eds.), Molecular Gels: Materials with Self-Assembled Fibrillar Networks, 233.
28. Y. Hea and T. P. Lodge, *Chem. Commun*., 2007, 2732.
29. J. Bowers, C. P. Butts, P. J. Martin, M. C. Vergara-Gutierrez and R. K. Heenan, *Langmuir*, 2004, **20**, 2191.
30. S. Dorbritz, R. Wolfgang and U. Krag, *Adv. Synth. Catal.* 2005, **347**, 1273.
31. A. J. Bard, L. R. Faulkner, *Electrochemical Methods Fundamentals and Applications*, John Wiley and Sons, Noida, 2nd edn., 2004.
32. S. S. Soni, K. B. Fadadu and A. Gibaud, *Langmuir*, 2012, **28**, 751.
33. S. S. Sekhon and H. P. Singh, *Solid State Ionics*, 2002, **152–153**, 169.
34. S. Jana, A. Parthiban and C. L. L. Chai, *Chem. Commun.*, 2010, **46**, 1488.
35. F. Lespinas, G. Dupuy, F. Revol and C. Aubry, *Clin. Chem*., 1989, **35**, 654.
36. M. J. Todd and J. Gomez, *Anal. Biochem*., 2001, **296**, 179.
37. D. D. Van Slyke and R. M. Archibald, *J. Biol. Chem*.,1944, **154**, 623.
38. T. Osakai, T. Kakutani and M. Senda, *Anal. Sci*. 1988, **4**, 529.
39. S. Shrikrishnan, K. Sankaran and V. Lakshminarayanan, *J. Phys. Chem.* C, 2012, **116**, 16030.
40. Y. Qin and J.M. S. Cabral, *Appl. Biochem. Biotech*.,1994, **49**, 217.
41. C. M. Pereira, J. M. Oliveira, R. M. Silva and F. Silva, *Anal. Chem*., 2004, **76**, 5547.
42. X. C.Tan, Y. X. Tian, P. X. Cai, X. Y. Zhou, Anal. *Bioanal. Chem*., 2005, **381**, 500.
43. A. Noorbakhsh, A. Salimi and E. Sharifi, *Electroanalysis*, 2008, **20**, 1788.
44. S. Y. Lee and H. H. Yoon, *Mol. Cryst. Liq. Cryst.*, 2012, **566**, 38.
45. D. Lan, B. Li. and Z. Zhang, *Biosens. Bioelectron*., 2008, **24**, 934.
46. M. Faure, B. Sotta and J. Gamby, *Biosens. Bioelectron*., 2014, **58**, 61.

CHAPTER 9

Summary and Future works

In this chapter, the highlights of the thesis work and some of the important findings are summarized, in addition to briefly discussing the scope of future work.

1. Electron transfer studies of some redox active species (cationic, anionic, neutral) in Deep Eutectic Solvents

The electron transfer studies of a set of standard redox species such as potassium ferrocyanide, hexammine ruthenium chloride, methyl viologen (MV), ferrocene (Fc) and its derivatives in DES were carried out for the first time. Such a study is important in understanding the fundamental processes of electron transfer reaction in a medium such as DES which is different from that of molecular solvents in terms of high viscosity, ionic composition and solvation mechanism. The peak separation values observed in the cyclic voltammograms of redox species in DES medium indicated that the reactions are reversible. The half peak potentials ($E_{1/2}$) provide information on the extent and nature of solvation by the DES components on the oxidized/ reduced species. It was found that while there was no preferential solvation for the charged redox complexes [$Fe(CN_6)^{4-/3-}$, $Ru(NH_3)^{2+/3+}$] in DES, the reduced species of the neutral/non polar complexes [Fc and MV] are preferentially solvated by DES. In terms of diffusion of the redox species in DES, the peak currents varied with the scan rate according to the Randles-Sevcik equation for a diffusion controlled reaction. The high viscosity of DES causes a significant decrease in the peak current when compared to that in molecular solvents. The diffusion coefficients (D) of the redox species in DES were calculated from electrochemical impedance spectroscopy and cyclic voltammetry. The $D^{1/2}$ values obtained for all the redox species were almost an order of magnitude lower in DES compared to that in molecular solvents.

2. Electrochemically prepared SERS substrates of Ag by anodic dissolution in DES

Electrochemical synthesis and *in situ* deposition of silver nanoparticles were carried out in DES by anodic dissolution technique. The anodic dissolution of silver and simultaneous deposition of nanoparticles on the cathode surface cannot

be carried out in aqueous medium owing to the formation of passive silver oxide film on the anode surface. It is shown in this work, that the passivation problems associated with the anode could be resolved in DES due to the inherent oxide solubilizing ability of DES components. The silver film electrodeposited onto a Pt/Rh wire in the DES medium was highly porous and well adherent. The substrates were calcined to remove the organic stabilizers present on the substrate so as to provide a pristine surface ideally suited for surface enhanced Raman spectroscopy (SERS) applications. The enhancement factor calculated for methylene blue used as an analyte on the calcined mesoporous Ag substrate was found to be 10^6.

3. Electrochemically grown mesoporous metallic substrates of Ag, Au and Pd by anodic dissolution in Deep Eutectic Solvents; Synthesis, characterization and electrocatalytic studies

The DES was used as a medium for the *in situ* preparation and electrodeposition of nanoparticles of Ag, Au and Pd on to metallic substrates. The studies were carried out both in the presence and absence of the reducing agents and organic stabilizers as per the nature of the metal ions generated during anodic dissolution. It was observed that under certain conditions, the components of DES could effectively stabilize the metal nanoparticles formed. The electrodeposition in DES medium has a decisive advantage as it is not associated with vigorous gas evolution unlike that in aqueous medium. Thus the electrodeposition was found to be more efficient in DES medium producing more adherent mesoporous films compared to that in aqueous medium. The prepared mesoporous substrates (Ag, Au and Pd) exhibited excellent electrocatalytic activity for hydrogen evolution reaction (HER). The mechanisms of HER on the mesoporous substrates were proposed based on chronoamperometry and electrochemical impedance studies.

4. One step preparation of 'ready to use' Au@Pd nanoparticle modified surface using Deep eutectic solvents and its electrocatalytic properties in alcohol oxidation reaction

A novel electrochemical route was proposed for the single step preparation of Au@Pd core shell nanoparticles in DES. The electrochemical

method following anodic dissolution process proposed in this work is simple and effective with minimal requirement of materials. The characterization by SEM, EDAX and cyclic voltammetry studies confirmed the core shell morphology of the nanoparticles. The electrocatalytic properties of the Au@PdNPs in alcohol oxidation were compared with their monometallic counterparts (AuNPs and PdNPs) prepared under identical conditions. The Au@PdNPs exhibited superior performance in alcohol oxidation in terms of activation energy and low overpotentials.

5. Oxygen evolution catalysts of graphite modified with Co and Co-Ni alloys prepared in DES

The porous films of cobalt and cobalt-nickel alloys were electrodeposited on to graphite substrate in DES medium. While cobalt is known to exhibit good electrocatalytic activity in oxygen evolution reaction, graphite is an excellent substrate for many practical applications such as batteries and fuel cells. The electrodeposition was carried out in ethaline (choline chloride + ethylene glycol), reline (choline chloride + urea) and maline (choline chloride + malonic acid) media. It was found that the anodic dissolution of Co in DES could not provide sufficient metal ions in electrochemically reducible form and hence electrodeposition could be carried out only by the addition of metal salts as metal ion sources. The electrodeposition conditions were optimized by varying current density, electrodeposition time and cobalt chloride concentration. To minimize the high viscosity of maline (1124 cP) at room temperature, an optimized quantity of water was added to the electrolytic medium. The electrocatalytic performance of porous Co and Co-Ni films prepared in maline, ethaline and reline were studied by cyclic voltammetry and chronoamperometry by measurement of Tafel slopes and activation energy. The Co catalysts prepared in aqueous maline medium exhibited excellent electrocatalytic activity despite a very small percentage of Co (2%) deposited on the graphite substrate.

6. A novel colloidal suspension of TBA^+ $BF4^-$ - EG and its applications as a soft solid electrolyte

A colloidal suspension possessing inherent ionic conductivity was designed and prepared for applications requiring soft solid media. For optimizing the components of the material, conditions leading to the formation of a liquid were avoided by considering various factors such as symmetry, viscosity, polarity and ionic composition of the potential components. The prepared colloidal suspension exhibited sharp sol – gel transitions at ambient temperature and was demonstrated as an ideal medium for preparing and storing stable nanoparticles as dispersions.

The soft solid nature combined with the inherent ionic conductivity makes the matrix an ideal medium for electrochemical studies of biomolecules. The evaluation of the material as a medium for real time monitoring of enzyme kinetics was carried out by electrochemical impedance spectroscopy. The enzyme kinetics of urea-urease, glucose-glucose oxidase and p-NPP- alkaline phosphatase were found to follow Michaelis-Menten equation. The Michaelis-Menten constant K_m for the enzymatic reactions in the colloidal matrix was found to be low compared to that carried out in molecular solvents.

Scope for future studies

In this work, the electron transfer properties for a set of redox species were studied using cyclic voltammetry, electrochemical impedance spectroscopy (EIS). For a better understanding of the potential shifts of the redox species in DES *wrt* molecular solvents, a set of theoretical calculations by molecular simulations can be carried out and compared with the experimental findings. The studies can account for the observed shifts based on free energy changes associated with the redox reactions in DES. This can also provide a realistic solvation model of redox species in DES medium.

Our studies have shown that the mesoporous films of silver prepared by a simple electrochemical technique can provide excellent well adherent stable substrates for SERS with a reasonably good enhancement factor. The studies were carried out using a standard analyte of methylene blue. The substrates have the potential to be used for the detection of trace quanitities of vapors and other

chemicals in atmosphere as well as biomolecules in biological samples for medical diagnostics.

The electrocatalytic activities of a set of mesoporous metallic films in hydrogen and oxygen evolution reactions, alcohol oxidation reactions have been studied. The studies till date have shown that the underlying substrate influences the electrocatalytic activity. Hence studies in this direction by varying the underlying substrates will be useful to design novel and efficient electrocatalysts.

The activation energy requirements of the mesoporous films were found to be low for the electrocatalytic processes and hence these materials have the potential to be used in fuel cell applications. However prior to the use in practical applications, these materials have to be studied under the extreme conditions of pH, temperature and chemical compositions. The mesoporous Pd has excellent potential for use as a hydrogen storage material.

The wide acceptance of DES and ionic liquids has opened up ample scope for designing novel media custom made for specific applications. The studies carried out here on the preparation of the colloidal suspension demonstrate the design of an ionic conducting soft solid. By varying the symmetry and alkyl chain length of the quaternary ammonium salts and hydrogen bond donors, a spectrum of novel ionic liquids, ionic gels, liquid crystals and DES can be designed.